Politecnico di Milano
Department Chemistry, Materials and Chemical Engineering
"Giulio Natta"
Doctoral Programme In SCIENCE AND TECHNOLOGY OF MATERIALS

Raman and IR spectroscopy for applications in molecular electronics

Doctoral Dissertation of:
Ali Maghsoumi

Supervisor:
Prof. Matteo Tommasini

Tutor:
Prof. Chiara Castiglioni

The Chair of the Doctoral Program:
Prof. Chiara Castiglioni

2015 – XXVIII

Acknowledgement

I had the good fortune of having more than one good teacher who shaped my thoughts. The lessons of a good teacher remain etched in my soul. With these emotions and feelings, I would like to thank them all. I would like to offer my sincere gratitude to my supervisors, Matteo Tommasini, who has and will always be a friend to me. I learned immensely during my studies from him. His support and encouragement helped me reach my educational goals and are truly appreciated. I would like to thank Chiara Castiglioni, who has guided me and even paved the path for me, showing me the rights and wrongs. My genuine and heartful thanks to Giuseppe Zerbi, Luigi Brambilla, Mirella Del Zoppo and Andrea Lucotti. My beloved wife, Sogol, who has let up my life with her warm present. The loving support of my family can not be underestimated. These individuals provide the fun and enjoyment essential for a balanced and healthy life. Thanks to my awesome friends, Foad, Reza, Alireza, Ashkan, Mehdi and Lohith who made my everyday life in Italy happy and joyful. While I was so far from home, they have brought home here to me.

Abstract

This thesis focuses on the use of vibrational spectroscopy for the characterization of advanced molecular materials appealing for applications in molecular electronics due to the electronic and optical properties imparted by the presence of conjugated π-electrons. Several molecular systems have been considered, belonging to two broad classes of great current interest in the development of advanced molecular materials, namely: (i) graphene molecules (synthesized in Prof. Klaus Müllen group – Max Planck Institute for Polymer Research, Mainz, Germany) and (ii) thiophene derivatives (synthesized in Prof. C. Bertarelli group – Dipartimento di Chimica, Materiali e Ingegneria Chimica, Politecnico di Milano, Italy).

Resonance Raman (RR) spectroscopy of π-conjugated materials is an effective probe of both the electronic and the vibrational properties, due to the strong electron-vibration coupling typical of π-electrons. The experimental pre-resonance / resonance Raman spectra of several graphene molecules have been investigated in details and rationalized based on Peticolas-Nafie-Stein theory. For selected wavelengths, which better match resonance condition, it is possible to observe clear Raman signals ascribed to the first overtone of the characteristic (G, D) Raman markers of graphitic materials. Interestingly, G+D combinations are also evident in the Raman spectra. These can be taken as a signature of confinement of π-electrons over the molecular dimensions, since this kind of combination is not expected in perfect graphene. Further markers of molecular size are given by interesting features at lower wavenumber than D and G (below 1000 cm^{-1}), which are reminiscent of acoustic-like collective vibrations. IR spectroscopy was also used to investigate and find different edge-markers (zigzag *vs.* armchair) or functionalisation markers (*e.g.*, phenyl caps, iodination, chlorination, hole). From this point of view, IR is complementary to Raman spectroscopy for which the signals are mostly due to the collective motions involving the molecular π-conjugated core and usually carry less information on functional groups.

Two different thiophene derivatives (phenoquinones) with peculiar radicaloid character have been also investigated with vibrational spectroscopy. Raman spectroscopy confirmed their radicaloid character, while IR spectroscopy and DFT calculations revealed a very strong C=O stretching at the phenoquinones moiety.

By comparison with DFT calculations on isolated phenoquinone, it was possible to relate the strong enhancement of the C=O stretching vibration with the peculiar electronic structure of both thiophene derivatives.

Finally, vibrational spectroscopy was used to investigate orientational properties and intermolecular interactions in selected molecular materials. In particular, IR spectroscopy was used to analyze strain induced crystallization and orientation in natural rubber, polybutadiene rubber and their blend. Crystallization is important for different types of rubbers because it highly affects their mechanical properties (tensile strength, fracture and fatigue resistance). IR spectroscopy, compared with results from X-ray diffraction, revealed several markers of strain-induced crystallization. The X-ray diffraction and mechanical characterization parts of this work were done in collaboration with the group of Prof. C. Marano (Dipartimento di Chimica, Materiali e Ingegneria Chimica – Politecnico di Milano, Italy). On the other hand, Resonance Raman spectroscopy was used for monitoring aggregation of **AmB** (a π-conjugated polyene macrocycle widely used as antibiotic) in solution state. It turned out that Raman intensity is a useful marker of aggregation processes in solution state as a function of concentration. Since **AmB** aggregates by π-stacking (similarly to many advanced π-conjugated materials), these results may find application in characterizing the experimental conditions leading to the controlled production of films for applications in molecular electronics.

Abstract

Questa tesi sviluppa l'applicazione della spettroscopia vibrazionale alla caratterizzazione di materiali funzionali avanzati, di interesse per applicazioni di elettronica molecolare, a causa delle proprietà elettroniche e ottiche impartite da elettroni π-coniugati. Sono state considerate diverse molecole appartenenti a due classi di interesse attuale nel campo dei materiali avanzati: (i) molecole grafeniche (sintetizzate nel gruppo del Prof. Klaus Müllen group – Max Planck Institute for Polymer Research, Mainz, Germany) (ii) derivati tiofenici chinoidi (sintetizzati nel gruppo della Prof.ssa C. Bertarelli – Dipartimento di Chimica, Materiali e Ingegneria Chimica, Politecnico di Milano, Italy).

Per i materiali π-coniugati la spettroscopia Raman risonante sensibile sia alla struttura vibrazionale che a quella elettronica a causa del forte accoppiamento elettrone-vibrazioni, tipico degli elettroni π. Diverse molecole grafeniche sono state studiate con la spettroscopia Raman in condizioni di pre-risonanza e risonanza. I risultati sono stati interpretati attraverso l'uso della teoria del Raman risonante introdotta da Peticolas-Nafie-Stein. In condizioni di risonanza, oltre ai picchi caratteristici dei materiali grafenici (G,D) è stato possibile osservare overtones (2D, 2G) e combinazioni (G+D). Queste ultime, solitamente assenti in grafeni ad alta perfezione strutturale, possono essere prese come indicatore di confinamento degli elettroni π in regioni limitate corrispondenti alle molecole considerate. Altri indicatori delle dimensioni molecolari sono stati registrati a numeri d'onda inferiori alla regione (G, D) e sono stati assegnati a vibrazioni con caratteristiche simili a quelle di fononi acustici di corrispondenti strutture estese.

La spettroscopia IR spectroscopy è stata utilizzata per evidenziare indicatori strutturali relativi ai bordi delle molecole grafeniche (zigzag *vs.* armchair), alla loro funzionalizzazione chimica con gruppi fenilici, atomi di cloro o di iodio, nonché alla presenza di buchi in regioni grafeniche estese. La spettroscopia IR è risultata complementare alla spettroscopia Raman, in quanto quest'ultima è soprattutto sensibile ai moti collettivi che coinvolgono il centro π-coniugato di queste molecole e solitamente non mostra segnali facilmente osservabili dovuti a gruppi funzionali.

La spettroscopia Raman è stata anche applicata a composti tiofenici con struttura chinoide (terminati con fenochinoni). Questi sistemi sono caratterizzati da

una particolare struttura elettronica radicaloide, confermata dai risultati Raman. Inoltre l'utilizzo della spettroscopia IR ha permesso di evidenziare un segnale di C=O stretching particolarmente intenso, originato dai fenochinoni terminali. L'uso di calcoli DFT di confronto su di un fenochinone isolato ha permesso di mostrare che l'innalzamento dell'intensità IR è correlato alla particolare struttura elettronica radicaloide di questi composti tiofenici.

Infine la spettroscopia vibrazionale è stata impiegata per studiare le proprietà di orientazione e di interazioni intermolecolari in due materiali molecolari rappresentativi.

La tecnica IR è stata impiegata per analizzare i fenomeni di orientazione molecolare e cristallizzazione sotto stiramento in campioni di gomma naturale, gomma polibutadienica e loro mescole. La cristallizzazione è un fenomeno rilevante in diverse gomme a causa delle modificazioni che induce nelle proprietà meccaniche (carico di rottura, resistenza a fatica e comportamento a frattura). E' stato possibile identificare diversi segnali IR caratteristici sensibili alla cristallizzazione indotta da stiramento, determinata da esperimenti paralleli di diffrazione X condotti in collaborazione con il gruppo della Prof.ssa C. Marano (Dipartimento di Chimica, Materiali e Ingegneria Chimica – Politecnico di Milano, Italy). La spettroscopia Raman risonante è stata utilizzata per seguire lo stato di aggregazione in soluzioni di **AmB**, un macrociclo polienico di ampio utilizzo come antibiotico. I risultati hanno mostrato che l'intensità Raman di segnali caratteristici di AmB è un indicatore sensibile dei processi di aggregazione in funzione della concentrazione. Poiché **AmB** aggrega per effetto di π-stacking (in modo simile a molti materiali π-coniugati avanzati), questi risultati possono trovare applicazione nella caratterizzazione delle condizioni sperimentali per la produzione controllata di film nell'ambito dell'elettronica molecolare, ove il controllo delle interazioni molecolari è essenziale per l'ottenimento delle proprietà desiderate.

Summary

This thesis focused on the use of vibrational spectroscopy for the characterization of advanced molecular materials appealing for applications in molecular electronics due to the electronic and optical properties imparted by the presence of conjugated π-electrons. Several molecular systems have been considered, belonging to two broad classes, namely (i) graphene molecules and (ii) thiophene derivatives.

(i) Graphene molecules constitute effective models of graphene confined over a limited region. Due to confinement, the electronic and vibrational properties of graphene molecules can be modulated,[1] leading to functional molecules optimized for specific applications. For instance, in photovoltaics it is important to design systems with a good control of the optical gap (for efficient photon harvesting) and of the electronic properties (to support exciton dissociation and electron transfer). Polycyclic Aromatic Hydrocarbons (PAHs) is just the alternative name of graphene molecules. They inspired scientific research for several reasons and have provided models to develop and test elementary π-bond theory.[2] Their extended π-conjugation and self-organizing properties are important for molecular electronics.[3] They are of high interest not only in organic chemistry but also for various applications, including sensing, (opto-)electronics and catalysis.[4–6] PAHs are well-defined cutouts or model compounds of graphene (nanographene) and graphene nanoribbons (GNRs-nanometer-wide strips of graphene).[7] When chemically functionalized with aliphatic chains at their edges they form π-stacked discotic liquid crystals[8] that may yield useful electron transport properties.[3]

π electrons of conjugated materials are the key actor in Resonance Raman (RR) spectroscopy, which is an effective probe of both the electronic and the vibrational properties. From a physical point of view, this is due to the strong coupling existing between π-electrons and nuclear coordinates, especially those associated to the stretching of CC bonds.[1,9] Hence the experimental pre-resonance/resonance Raman response of a representative graphene molecule (**C78** - see Chapter 3) has been investigated in details based on the recently developed approach to the calculation of RR response of π-conjugated molecules.[10] For selected wavelengths, which better match resonance condition, it is possible to observe clear Raman signals ascribed to the first overtone of the characteristic Raman markers of graphitic

materials (*i.e.*, the G- and D-line[1]). Interestingly, G+D combinations are also evident in the Raman spectra.[11] This feature is a specific signature of confinement and it is usually absent in graphene.[12] The multi-wavelength Raman spectra of **C78** also display important features at lower wavenumber than D and G (*i.e.*, below 1000 cm^{-1}). Some of these features can be associated to in-plane acoustic-like vibrations that depend on the molecular size[13] and can be used as a further marker of confinement. The outcomes of this analysis can be extrapolated to graphene, for which Raman spectroscopy is one of the more commonly used characterization techniques.[12]

Among graphene molecules, Hexa-peri-hexabenzocoronene (**HBC**) is one the most important examples of the fully benzenoid PAHs: it is very stable and it can form columnar structures through self-assembly promoted by the strong π-stacking interactions.[14] HBCs are characterized by their unique opto-electronic behavior, which can be tuned by suitable chemical modification at the molecular edge. PAHs with K-regions or zigzag periphery are more unstable, but demonstrate interesting properties such as lower bandgaps.[15] Raman and IR spectroscopies have been used to characterize and prove the chemical structure of **tetra-zigzag-HBC**, selected graphene nanoribbons (GNRs) and their monomers (see Chapter 3), chlorinated molecular graphenes (**HBC-Cl** and **C96-Cl** – see Chapter 4) and a model molecule of a "hole" in graphene (**C216** – see Chapter 5). In the case of **tetra-zigzag-HBC**, Clar's annellation theory[2,16] was successfully used to rationalize the electronic structure, which implies a sizable (179 nm) redshift of the para-absorption band in the UV-Vis spectrum of **tetra-zigzag-HBC** compared to that of **HBC**.

Furthermore, IR spectroscopy was used to investigate and find different edge-markers (zigzag *vs.* armchair) or functionalisation markers (phenyl caps, iodination, chlorination, hole). From this point of view, IR spectroscopy is complementary to Raman spectroscopy for which the signals are mostly due to the collective motions involving the molecular π-conjugated core and usually carry less information on functional groups. Results from the RR spectroscopy of the **C78** have been extended to other molecular graphenes: **C84** necklace GNR,[17] **tetra-zigzag-HBC**, graphene nanoribbons with partially zigzag edge structures (**M** samples), **C96-Cl** and **C216**. This allowed testing the resonance Raman theory for molecular graphenes, which was developed for C78, and confirming it in terms of observed lines, relative intensities, and resonance behavior. All of the graphene molecules investigated in this thesis were synthesized in Prof. Klaus Müllen group (Max Planck Institute for Polymer Research, Mainz, Germany).

(ii) Two different thiophene derivatives (**QBT** and **QDTT** phenoquinones) have been also investigated with vibrational spectroscopy, leading to the results presented in Chapter 6. These molecules present an interesting radicaloid character; when used as third components in bulk-heterojunction solar cells, they improve the performance of the cell. Raman spectroscopy confirmed the radicaloid character of both **QBT** and **QDTT**, while IR spectroscopy and DFT calculations revealed a very strong C=O stretching at the phenoquinones moiety. By comparison with DFT calculations on isolated phenoquinone, it was possible to relate the strong enhancement of the C=O stretching vibration with the peculiar

electronic structure of **QBT** and **QDTT**. These thiophene derivatives were synthesized by Dr. L. Colella in the group of Prof. C. Bertarelli (Dipartimento di Chimica, Materiali e Ingegneria Chimica – Politecnico di Milano, Italy).

Finally, vibrational spectroscopy has been used to investigate orientational properties and intermolecular interactions in selected molecular materials.

In particular, IR spectroscopy has been used to analyze strain induced crystallization and orientation in natural rubber (**NR**), polybutadiene rubber (**BR**) and their blend (**NR/BR**). Crystallization is really important for different types of rubbers and it highly affects their mechanical properties (*e.g.* tensile strength, fracture and fatigue).[18] IR spectroscopy, compared with results from X-ray diffraction, revealed several markers of strain-induced crystallization, which were not known for the **NR/BR** blend. The X-ray diffraction and mechanical characterization parts of this work were done in collaboration with Dr. Shahram Mohammad Poor in the group of Prof. C. Marano (Dipartimento di Chimica, Materiali e Ingegneria Chimica – Politecnico di Milano, Italy).

Resonance Raman spectroscopy has been used for monitoring aggregation of **AmB** (a bio-relevant molecule π-conjugated polyene macrocycle widely used as antibiotic) in solution state as a function of concentration. It turned out that Raman intensity is a useful marker of aggregation processes in solution state as a function of concentration. These results may find application in characterizing the experimental conditions leading to the controlled production of films for applications in molecular electronics. In fact, similarly to many π-conjugated materials used in molecular electronics, **AmB** aggregates by π-stacking.

Contents

List of Figures

List of Tables

CHAPTER 1

Introduction

Vibrational spectroscopy is a characterization technique with many useful applications in Material Science whenever molecular sensitivity is required. For instance, in developing novel molecular materials, one would like to experimentally assess the successful synthesis of the designed compound. In other cases one would like to obtain information about the molecular structure in space, *i.e.*, the conformation of the molecule. Since properties of molecular materials depend also on the arrangement of the active molecules in the sample, clearly vibrational spectroscopy offers a very convenient probe for molecular orientation and may provide some hints about molecular packing when specific inter-molecular interactions are the driving force (*e.g.*, π-π interactions in advanced functional materials). In this Ph.D. thesis several molecular materials have been investigated by vibrational spectroscopy, which proved useful in elucidating chemical composition of novel molecular graphenes and thiophene derivatives, orientation and crystallization phenomena in rubber systems. A part of the work was also devoted to the use of DFT calculations for the detailed assignment of the unprecedented Raman and IR spectra of novel molecules which were synthesized in Prof. Chiara Bertarelli (Dipartimento di Chimica, Materiali e Ingegneria Chimica – Politecnico di Milano, Italy) and Prof. Klaus Müllen group (Max Planck Institute for Polymer Research, Mainz, Germany). In the following paragraphs the research carried out in this thesis work will be introduced.

1.1 PAHs and molecular graphene

Polycyclic aromatic hydrocarbons (PAH) are compounds with multiple fused rings and much scientific research has been inspired by them for several reasons. They

are of high interest not only in organic chemistry but also for various applications, including sensing[4,30] (opto-)electronics[5,31] and catalysis.[32] They have been provided models to develop and test elementary π-bond theory and they have important properties useful in molecular electronics such as extended π-conjugation and self-organizing properties.[2,3] PAHs occur as intermediate combustion products upon soot formation and they are drawing attention also because on their carcinogenic activity.[33] In addition, PAHs represent an important research field in astrophysics because they are organic molecular species present in interstellar space.[34]

PAHs which can be drawn with a Kekulé-structure without isolated double bonds are well-known as kinetically very stable and thermodynamically favored substances, and called fully benzenoid.[2,35] E. Clar extensively studied such fully benzenoid PAHs and assigned their high stability to the localization of aromatic sextets within the molecules.

Hexa-*peri*-hexabenzocoronene (HBC) is one the most important examples of the fully benzenoid PAHs which can be regarded as "superbenzene" for its extended benzene-like structure with D_{6h}-symmetry.[3] It is very stable and it can form columnar structures through self-assembly promoted by the strong π-stacking interactions.[14] HBCs are characterized by their unique opto-electronic behavior, which can be tuned by suitable chemical modification at the molecular edge, e.g., with electron-donating or -withdrawing groups.[15,36]

PAHs with K-regions, or zigzag periphery, show benzenoid structures only in a limited areas of the molecules, on the contrary to the fully benzenoid compounds. Such not-fully benzenoid PAHs demonstrate interesting properties such as lower bandgaps, higher chemical reactivity, and even open-shell biradical characters, depending on their structures, but they are more unstable.[37–39]

By bridging the bay regions with C_2 units, the fully benzenoid HBCs can be converted to not-fully benzenoid HBC derivatives with zigzag peripheries. Till now, HBCs with one to three extra "double bonds" (K-regions) have been synthesized and have been demonstrated the varying symmetry and modulating opto-electronic properties.[40–42] But, HBCs with more than three K-regions have remained elusive. However a characterizations of a novel HBC derivative with four K regions, namely zig-zag peripheries have been reported in Section 3.4 and synthesis procedure has been described in detail by Dumslaff *et al.*[43]

HBCs and other large PAHs can also be considered as a cutout or "model compound" of graphene and graphene nanoribbons (GNRs) whose structure can be essentially described as a PAH extending periodically along one direction.[44,45] Research on such large PAHs, namely defined nanographene molecules, provides better insights into the physical properties and reactivity of infinite graphene and GNRs. The physical properties of the GNRs are completely dependent on their edge structures.[46,47] While zigzag-edge GNRs are predicted to have very small bandgaps with localized states at both edges, which can show an antiferromagnetic interaction, GNRs with armchair edges are semiconducting with relatively larger bandgaps.[14,48,49] There are only limited examples of PAHs that can serve as model compounds of zigzag-edge GNRs, although a number of nanographene molecules corresponding to armchair-type GNRs have been reported.[39,50,51] Also,

nanographene molecules with zigzag edges such as anthenes are usually highly unstable, hindering the studies under various conditions and their device applications.[52]

Also GNRs (nanometer-wide strips of graphene), whose structure can be essentially described as a PAH extending periodically along one direction, are attracting an increasing attention for their appealing electronic properties.[53] They are ribbon-shaped graphene segments characterized by structure-dependent non-zero band gaps. Compared to zero band gap graphene, the gap opening in GNRs is induced by the lateral quantum confinement. They are promising for nano- and opto-electronic applications, being systems with tunable properties complementary to those of graphene.[54] Top-down methods such as lithographic patterning of graphene[55] and unzipping of carbon nanotubes[56] have been considered for the production of GNRs. However, these methods suffer from the lack of a good control in the structural precision and reproducibility of the synthesized GNRs. On the other hand, bottom-up chemical synthesis approaches have demonstrated the possibility to synthesize in a reproducible way GNRs with chemically defined and uniform structures. These chemical synthesis methods are based on solution-mediated[57] or surface-assisted[58] cyclodehydrogenation of carefully designed precursors. In this way it has been experimentally shown that the optoelectronic properties of the GNRs, such as the band gap, are affected by the width and the edge configuration, as theoretically predicted.[59,60] Moreover, through chemical synthesis in solution phase, it is possible to prepare sizable quantities of materials which can be then processed from the liquid phase for the fabrication of nano-electronic devices.[61]

Most of the studies on the structure-property connection of the GNRs have been limited to specific edge structures such as armchair, zigzag and their hybrids, and the effect of the edge configuration is still under-explored. Vibrational analysis of a GNR with an unprecedented "necklace-like" structure which features an armchair edge configuration has been reported in Section 3.3.

Raman spectroscopy is a popular and convenient method for analyzing PAHs, graphenes and Graphene Nanoribbons (GNRs).[1,12,13,17,62] It is a fast and non-destructive technique which may provide structural and electronic information. It can be used not only in academic laboratories but also, as a perspective, for the characterization of graphene materials in industrial production frameworks.

The Raman spectroscopy of graphene, graphite and PAHs has been studied extensively. The first-order Raman spectra of these materials exhibit a characteristic shape recognized by two strong bands located at around 1600 cm^{-1} and 1300 cm^{-1}. These bands are a characteristic feature of sp^2 carbon materials and have been called G and D bands, respectively. These Raman signals are structured in PAHs and they show several components.[1,12,13,17,19,62,63]

The D band appears in graphitic systems when some kind of disorder or discontinuity of the lattice occurs. It comes from TO (Transversal Optical) phonons around the Brillouin zone corner (q = K, where q is the phonon wave vector; see Figure 1.1 for the representation of the phonon dispersion curve of graphene). The D label comes from "disorder". In fact, the Raman intensity of the D peak vanishes by symmetry in structurally perfect graphene while it becomes sizable upon the breaking of translational symmetry, which may be caused by the pres-

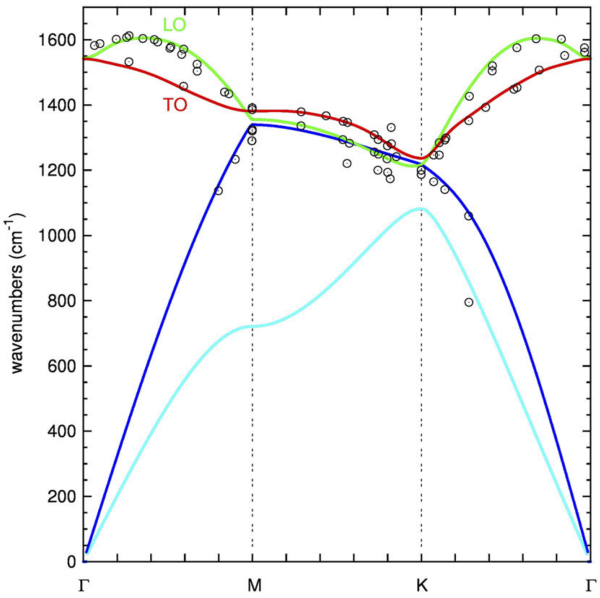

Figure 1.1: *Phonon dispersion curves computed for graphene according to Mapelli et al.[19] Dots are experimental data taken from Maultzsch et al.[20] The figure has been adapted from Ferrugiari et al.[21] For further details see also the cited works by Ferrari et al.[12] and references therein.*

ence of defects or edges in the graphene flake.[12] The D peak is an intrinsic feature of the confinement of π electrons in finite size PAHs,[1] which is why in the Raman spectra of amorphous carbon systems with mixed sp^2/sp^3 content it is possible to observe broad D Raman signals. The intrinsic D peak of PAHs can be also considered the signature of the relaxation of the molecular structure with respect to the characteristic equalized CC bonds of graphene/graphite, driven by the confinement of π-electrons in a finite molecular domain. The D peak is assigned to a specific vibrational mode that can be defined as a cooperative breathing of alternated hexagonal rings in the molecule (see Figure 1.2 for representation of nuclear displacement of D mode of graphene).[12,13,63]

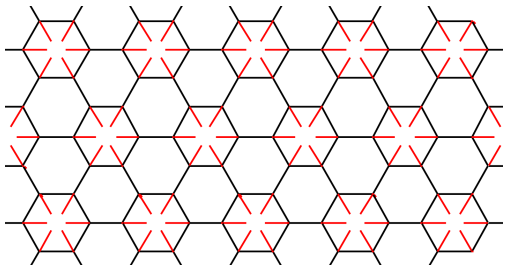

Figure 1.2: *Representation of nuclear displacement of D mode in graphene. It is due to the breathing modes of six-atom rings and will be activated by symmetry breaking.*

It is worth mentioning that, for a better characterization of graphene itself, it is possible to use information that is provided by the Raman investigation of graphene molecules (*i.e.*, PAHs as oligomers of graphene). For instance, when the origin of the Raman D peak was debated in the past,[1,64,65] this actually

happened: the result of calculations originated from molecular models led to the right early assignment of the phonon dispersion curves of graphene[19,66,67] which was later confirmed by first principles calculations.[12,68] Hence, due to the importance of graphene as a novel material,[69,70] investigations on graphene molecules may disclose significant practical applications.

The G Raman line of graphite (G from "graphite") is assigned to the degenerate optical phonon of E_{2g} symmetry of the graphene lattice at the Γ point ($q = 0$; see Figure 1.1 for the phonon dispersion curve of graphene and Figure 1.3 for the representation of the nuclear displacements associated to the G mode).[12,13,19]

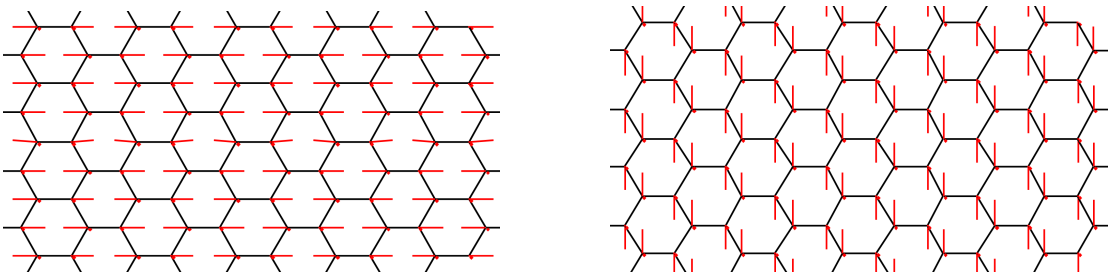

(a) *Longitudinal* **(b)** *Transversal*

Figure 1.3: *Representation of the nuclear displacement associated to the doubly degenerate G mode of graphene (E_{2g} symmetry species).*

1.2 Thiophene-based heterophenoquinones

Conjugated quinoidal molecules are used for a wide range of applications in molecular electronics and optoelectronic devices because of their appealing electronic properties.[71] For example, in an organic photodetector for polymer optical fibers, they have been used as a hole donor.[72] Impressively, photovoltaic activity has been enhanced by the use of thiophene-based heteroquinones: Kan *et al.* reported 47% increase in power conversion efficiency of classical bulk heterojunction poly-3-hexylthiophene:fullerene (P3HT:PCBM) by adding a 0.6 wt% of **QBT**[1].[73] In another case, by adding the 3 wt% of galvinoxyl radicals as a third active component in a standard poly(3-hexylthiophene)/1-(3-(methoxycarbonyl)propyl)-1-1-phenyl)-(6,6)C_{61} solar cell, a relevant improvement of the photovoltaic performance was observed (the efficiency increased by 18%). This enhancement was ascribed to a conversion from singlet to triplet of the polaron pair spin state, interceded by the paramagnetic molecule.[74] In both examples, since an unexpected radicaloid character was reported for **QBT** and its derivatives, the third active component is characterized by the presence of unpaired electrons.[73–75]

Open shell state molecules with an odd number of electrons are generally high-energy reactive species.[76] It is however possible to generate open shell states with two unpaired spins by the promotion of one electron from one electronic state to another; this is an energy-demanding process which can be driven by photoexcitation with visible or UV light. On the other hand, it is possible to

[1] Chemically named: 5,5'-bis(3,5-di-tert-butyl-4-oxo-2,5-cyclohexadiene-1-ylidene)-5,5'-dihydro-2,2'-bithiophene

find a few cases of open-shell molecules in their ground-state, such as non-Kekulé molecules, carbenes, nitrenes.[77] These systems are named diradicals.[76]

Two states can occur when two unpaired spins ($S = 1/2$) localized on the same molecule couple by electron-electron interaction. These states are a singlet and a triplet state. Their energy difference equals twice the spin exchange interaction, J,[78] which also enters an effective spin Hamiltonian,[79] written as $H = -2JS_1S_2$.

To overcome the stability problem of open shell molecules while at the same time limiting the exchange interaction, molecules can be formed by connecting two radicals with a spacer. The spacer keeps the radicals apart and this type of molecules are termed biradicals. In biradicals a closed shell ground state is not formed because the pairing of the two electrons in one of the two singly occupied molecular orbitals (SOMO) would increase the system energy due to strong electron-electron interaction.

The singlet and triplet states can be assumed degenerate when the interaction among two electrons is nearly negligible. The behavior of molecule in this situation is equal to that of two independent radicals (the degeneracy of the state is four in this case).

Diradicaloid molecules have been seen in some systems such as polyaromatic hydrocarbons, graphene and hydrocarbons with non-Kekulé structures.[80] Oligothiphenes have been reported to show a real biradical character.[81] Thiophene-based heterophenoquinones with unusual non-trivial behavior have been studied in this thesis with vibrational spectroscopy. These systems were synthesized by Takahashi *et al.*[82] for the first time and they possess biradical character in the excited state but they are closed-shell molecules in the ground state. This is an unusual property related to the relatively low energy of open-shell state and because the state is not a diradical state (for further details see the Appendix – Tampieri *et al.*[83]).

These materials are characterized by a very low band gap despite their short length. By increasing the number of dihydrothiophenediylidenes the effective conjugation increases; the maximum number of thienylene rings obtained so far is four.[82] Within a homologous series of thiophene-based heterophenoquinones, the role of the π-conjugation length on the occurrence of a biradical ground state has been demonstrated by Fazzi *et al.*: it was shown that by increasing the number of thiophenes from one to two rings, a biradicaloid character was stabilized.[84] Later, by following the same approach, it has been shown that this electronic character could be tuned also by the presence, nature, and position of electron donor/acceptor groups linked to the molecular skeleton.[85] Hence, it is possible to have a separate control over the optical band gap and the electronic character of the ground state.

Selected thiophene-based heterophenoquinones have been characterized by quantum chemical calculations and vibrational spectroscopy in Chapter 6. Further characterization techniques such as electron paramagnetic spectroscopy, NMR and X-ray diffraction have been also carried out and are described in details by Tampieri *et al.*[83] (see Appendix).

1.3 Rubbers

1.3.1 Natural rubber

Natural rubber (**NR**) is a polymer which is obtained from the latex of the *Hevea brasiliensis* tree.[86] The main chemical structure of **NR** corresponds to *cis*-1,4-polyisoprene, which is shown in Figure 1.4. **NR** also contains around 6% of impurities, which include lipids, proteins and other low molecular weight carbohydrates. The molecular weight of **NR** is in the range of 10^4-10^7 g/mol.

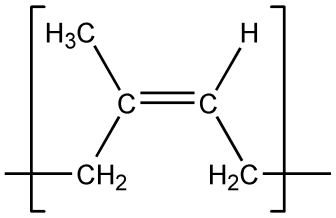

Figure 1.4: *Chemical structure of natural rubber (cis-1,4-polyisoprene).*

NR can crystallize both in the quiescent state and upon stretching due to high stereoregularity (high *cis* content). Crystallization of **NR** also occurs in the vulcanization process and the maximum crystallization rate is observed[87] at $-25°C$. Moreover, in vulcanized rubber, strain induced crystallization is responsible for remarkable high tensile and tear strength.[87–90]

Polybutadiene or butadiene rubber (**BR**) is a synthetic rubber where the monomeric unit may have three different molecular configurations (see Figure 1.5). The properties of **BR** are affected by the molecular configurations of the monomeric units.

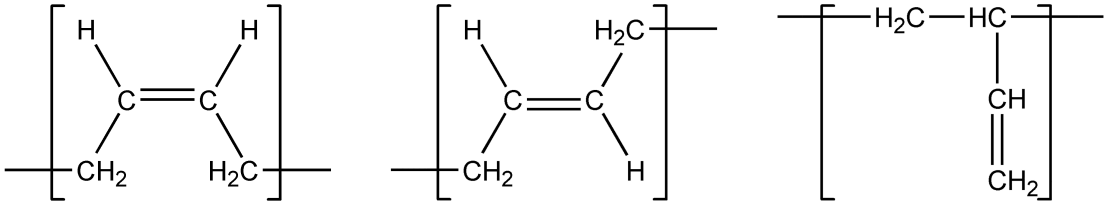

(a) *cis-**BR*** **(b)** *trans-**BR*** **(c)** *vinyl-**BR***

Figure 1.5: *The three configurations of the monomeric unit of **BR**.*

BR with a large content of *cis*-1,4-units (higher than 95%) is widely used in tires production related to the capability of this material to crystallize under stretching as a result of its high stereoregularity.[91] It is known that strain-induced crystallization affects the mechanical behavior of materials such as improving tensile strength, fracture and fatigue behavior. Moreover, vulcanized high-*cis*-**BR** displays high elasticity and resilience, good flexibility at low temperatures, high resistance to abrasion and to cut growth, low heat buildup and high fatigue cracking resistance. Compared to **NR** it is possible to mix **BR** with a higher level of carbon black and oil. However **BR** has low skidding resistance and the synthesis

process is more difficult. Hence polymer factories need to improve the processability of **BR** for producing high performance tires. These improvements include the reduction of rolling resistance, the enhancement of wet grip and abrasion-resistance. The microstructure of **BR** affects the rubber performance during processing and also the final properties of the products, and this microstructure is related to the different monomer configurations of the polymer chain. For example, processing high *cis*-**BR** (95-98 % *cis* content) is more difficult than low *cis*-**BR**, but high *cis*-**BR** have a higher abrasion resistance. **BR** with 35% *cis* content (55% *trans* and 10% *vinyl*) is processed easily but it has really low resilience and it is not possible to crystallize it by stretching; filler addition is required to improve its fracture behavior.[92]

Dissimilar rubbers are not generally miscible. The phases of an immiscible blend will be co-continuous, or one phase will be dispersed inside a continuous matrix of the other phase. Most blends consist of separate particles in a continuous phase. Domains of the material with lower viscosity deform and encapsulate the materials with higher viscosity and "globular" morphology is produced during mechanical mixing. However the morphology is never at equilibrium for an immiscible blend (this would correspond to macroscopic phase separation). Smaller and more interconnected phases can be formed by improving the compatibility of the components of the blend, which can improve the properties of the blend.

The blend of **NR** and **BR** (**NR/BR**) is considered heterogeneous. It is characterized by the presence of two-phases; however, the detailed morphology is not well known. The rheological behavior of these materials has been recently analyzed by Bacchelli *et al.*[93] They have analyzed the rheological properties of two different **NR/BR** blends (different **BR** with respect to molecular weight distribution and degree of branching) over a wide temperature range ($30-110°C$). It was reported that high *cis*-**BR** with a low polydispersity and a low degree of branching lead to an easier mixing process, with the final cured compound showing a lower rolling resistance.

In Chapter 7 the strain induced crystallization of different rubbers has been analyzed by FT-IR spectroscopy in order to relate the mechanical properties with changes occurring at the molecular structure level.

Finally in Chapter 7 it is reported the investigation on the aggregation of Amphotericin B (antifungal drug with 7 conjugated C=C bonds) in solution state as a function of concentration. It found that Raman intensity is a clear marker of the aggregation phenomenon which is driven by π-stacking interactions. This approach may be extended to the investigation of the aggregation phenomena in a wide range of advanced π-conjugated materials which are known to strongly interact by π-stacking (*e.g.*, graphene molecules).

CHAPTER 2

Structure of the graphene molecules investigated

This Chapter is meant to help the reader with a complete list of the graphene molecules and graphene nano ribbons (GNRs) considered in this thesis. All chemical structures and naming conventions are stated here below. These novel molecules were all synthesized in Prof. Klaus Müllen group (Max Planck Institute for Polymer Research, Mainz, Germany) and they have been characterized in next three Chapters.

1) **C78**: $C_{78}H_{26}$ is a PAH with D_{2h} symmetry point group resembling a longitudinally confined graphene ribbon with armchair edge.

2) **HBC**: $C_{42}H_{18}$ is one the most important fully benzenoid PAHs which can be regarded as "superbenzene" for its extended benzene-like structure with D_{6h}-symmetry.

3) **tetra-zigzag-HBC**: $C_{90}H_{62}I_4$ is a novel **HBC** derivative PAH with four zig-zag peripheries. It can be considered as a cutout of an $N = 6$ zigzag GNR.

4) **C84**: $C_{156}H_{70}$ is a PAH with 84 sp^2 carbon atoms. It is a model compound of a **GNR1** with an necklace-like structure.

5) **GNR1**: **GNR1** is a graphene nanoribbon with an necklace-like structure closely related with that of the **C84** graphene molecule.

6) $\mathbf{M}_0$: $C_{60}H_{70}$ is a model PAH of a GNR with a hybrid edge structure formed by zigzag and gulf sections.

7) $\mathbf{M}_1$: $C_{72}H_{74}$ is another model PAH of a GNR with a hybrid edge structure formed by zigzag and gulf sections.

8) $\mathbf{M}_P$: M_P is a GNR with a hybrid edge structure formed by zigzag and gulf sections.

9) **C222**: $C_{222}H_{42}$ is a large graphene molecule with D_{6h} symmetry.

10) **C216**: $C_{216}H_{48}$ is the analogue of the **C222** molecular graphene with the missing central ring (hole). This type of functionalization may alter the planarity of the molecule and the presence of a hole in this molecular graphene alters the conjugation pattern and affects significantly the HOMO-LUMO gap.

11) **HBC-Cl**: $C_{42}Cl_{18}$ is a chlorinated **HBC** and the edge chlorination significantly alters the planarity of the molecules. This structural distortion does not significantly impair the inherent π-conjugation of this graphene molecules.

12) **C96-Cl**: $C_{96}H_3Cl_{27}$ is a chlorinated analouge of large graphene molecule with D_{3h} symmetry. The edge chlorination significantly alters the planarity of the molecules.

2.1 HOMO and LUMO

In this section the HOMO and LUMO of some analyzed structures have been displayed. By comparing them with benzene, the Clar's aromatic sextets are evident and it is possible to observe Clar's rings.

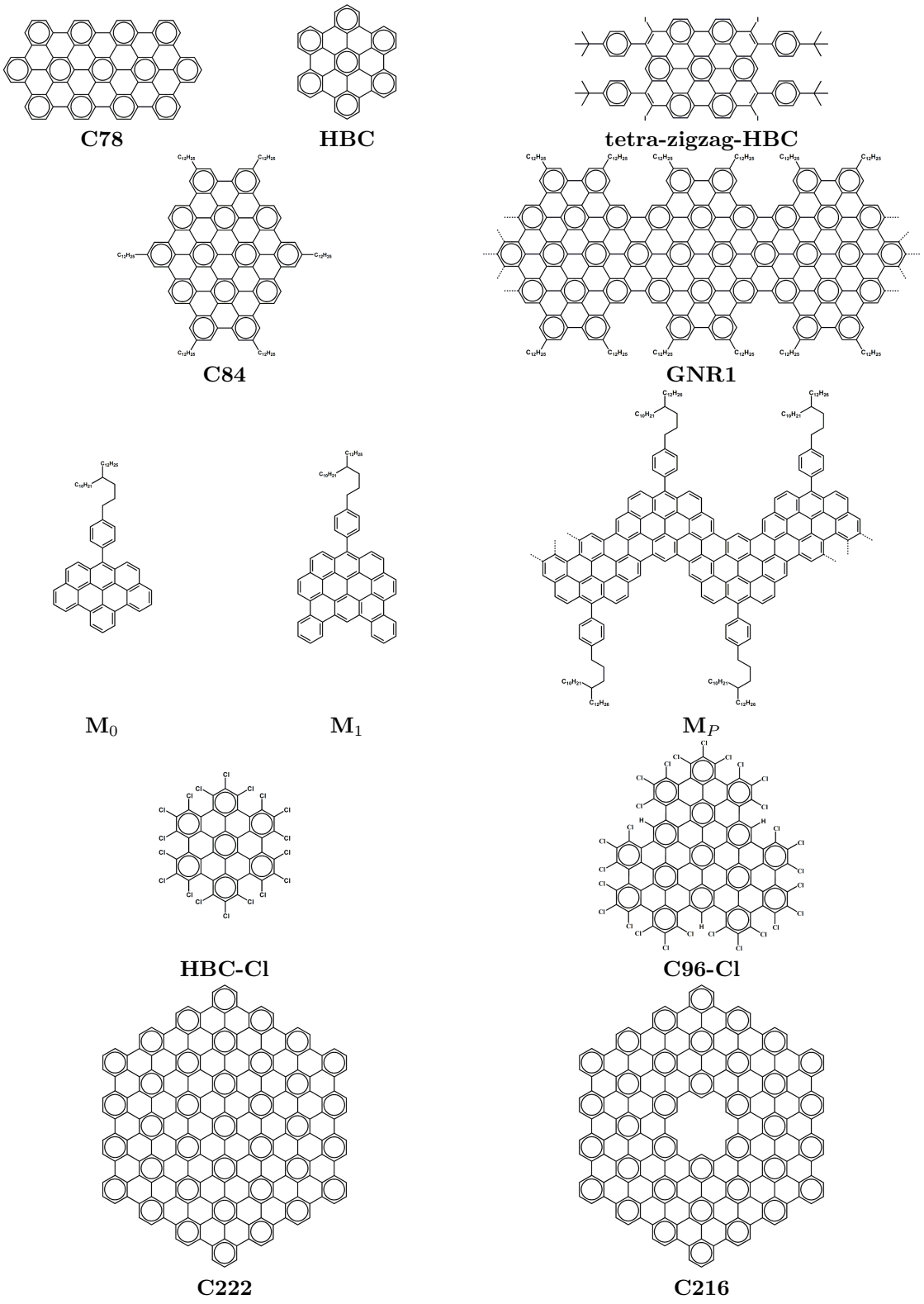

Figure 2.1: *Chemical structure of the graphene molecules and graphene nanoribbons investigated in this thesis.*

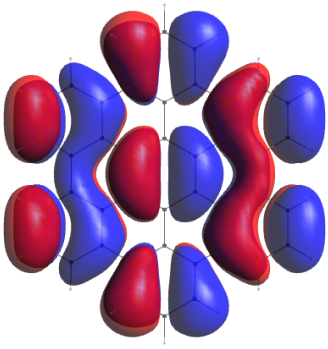

(a) *HOMO: -5.25 eV*

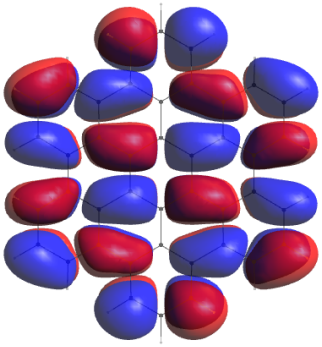

(b) *LUMO: -1.66 eV*

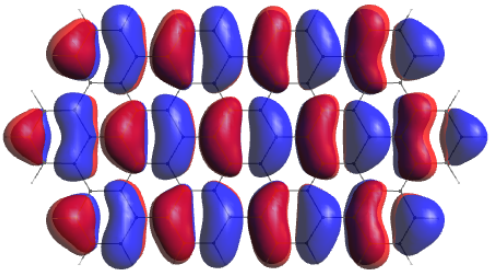

(c) *HOMO: -4.77 eV*

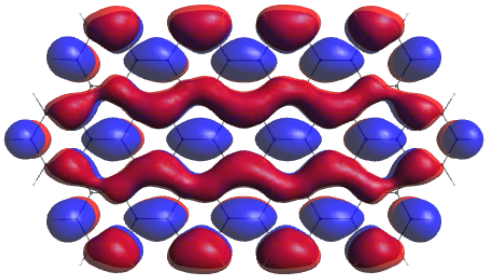

(d) *LUMO: -2.24*

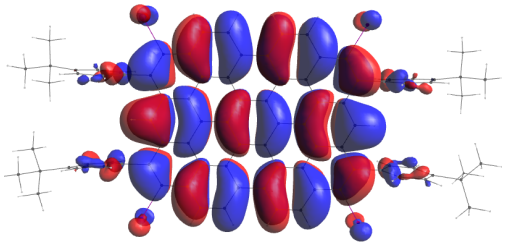

(e) *HOMO: -4.97 eV*

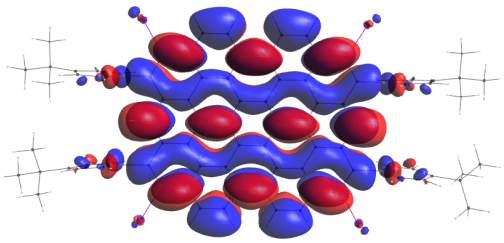

(f) *LUMO: -2.47 eV*

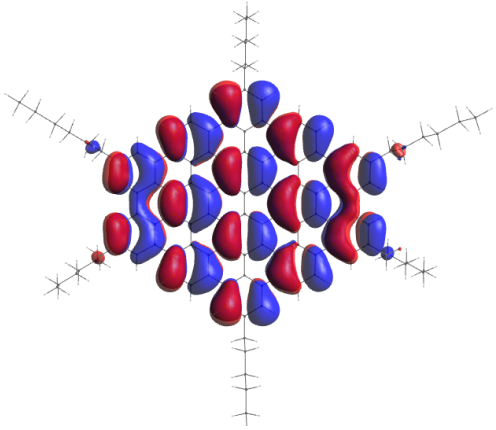

(g) *HOMO: -4.66 eV*

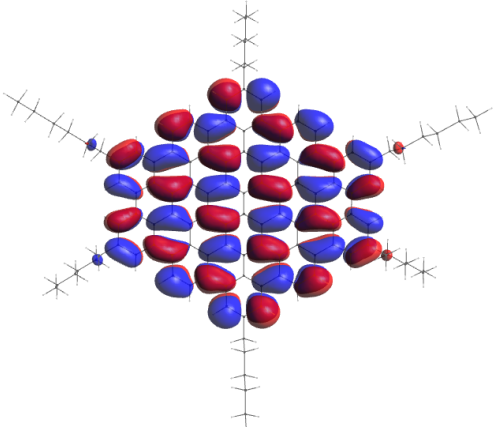

(h) *LUMO: -2.10 eV*

Figure 2.2: *HOMO and LUMO levels of* ***HBC***, ***C78***, ***C84*** *and* ***tetra-zigzag-HBC*** *calculated by DFT at the B3LYP/6-31G(d,p) level.*

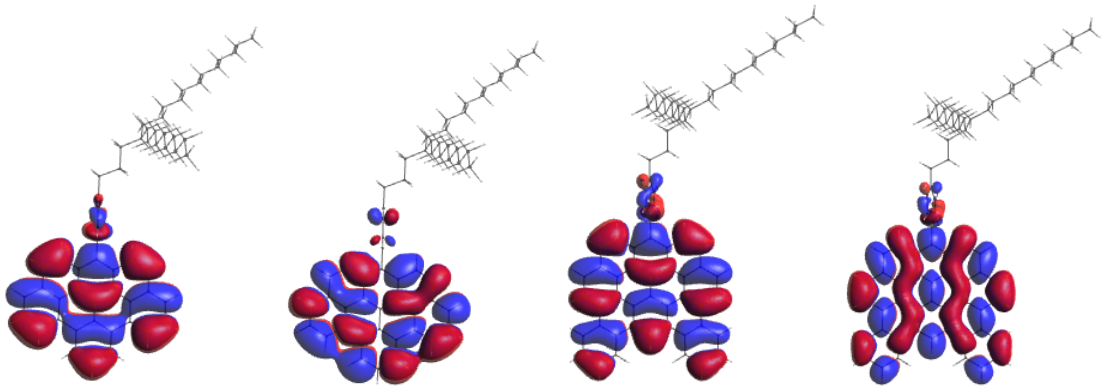

(a) *HOMO: -5.20 eV* **(b)** *LUMO: -1.56 eV* **(c)** *HOMO: -4.95 eV* **(d)** *LUMO: -1.88*

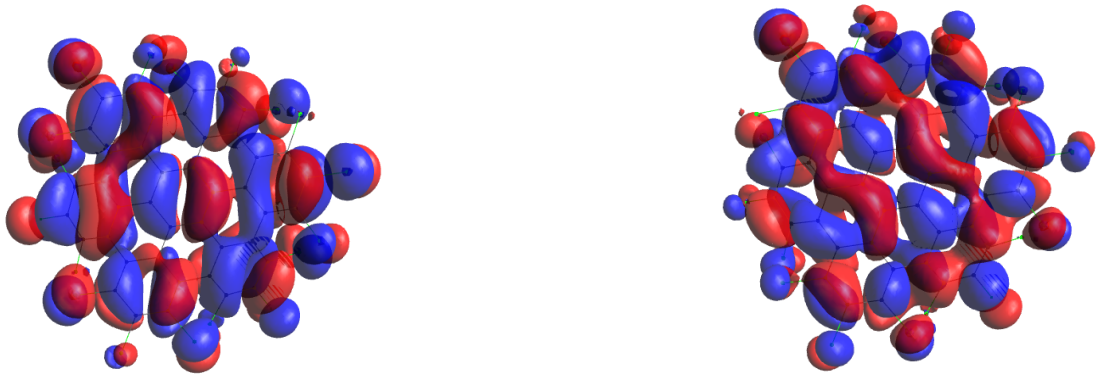

(e) *HOMO: -6.30 eV* **(f)** *LUMO: -3.13 eV*

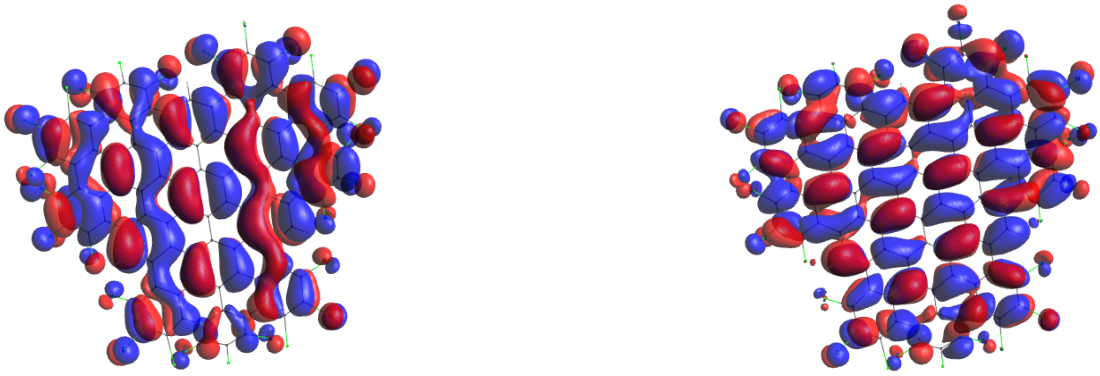

(g) *HOMO: -5.81 eV* **(h)** *LUMO: -3.32 eV*

Figure 2.3: *HOMO and LUMO levels of* $\boldsymbol{M}_0$, $\boldsymbol{M}_1$, ***HBC-Cl*** *and* ***C96-Cl*** *calculated by DFT at the B3LYP/6-31G(d,p) level.*

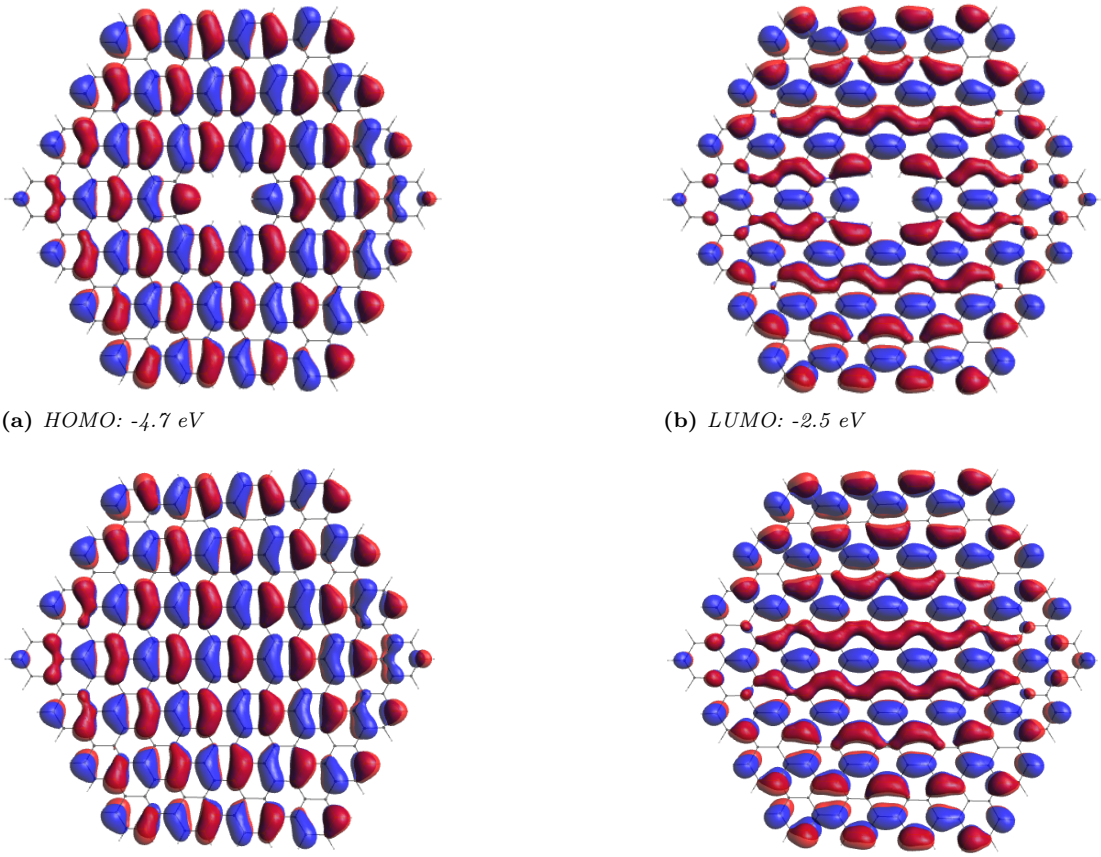

(a) *HOMO: -4.7 eV*

(b) *LUMO: -2.5 eV*

(c) *HOMO: -4.5 eV*

(d) *LUMO: -2.7*

Figure 2.4: *HOMO and LUMO levels of* ***C216*** *and* ***C222*** *calculated by DFT at the B3LYP/6-31G(d,p) level.*

CHAPTER 3

Raman and IR spectroscopy of graphene molecules

3.1 Introduction

This Chapter presents the results obtained applying the methods of vibrational spectroscopy to a class of compounds of great current interest in materials science for applications in molecular electronics.[5,31] Large Polycyclic Aromatic Hydrocarbons (PAHs) constitute effective models of graphene systems with controlled size and chemical structure. They allow investigating the effects of selected chemical substitution and edge topology. These details are not easily controlled with ordinary graphene production methods (*e.g.*, mechanical exfoliation). On the other hand, by controlling molecular structure and end-groups, chemical synthesis may also provide systems with specifically tuned properties, optimized for selected applications.[94,95] Within this framework, being vibrational spectroscopy inherently molecular-structure dependent, it can be profitably used to characterize novel molecular materials, providing specific markers of the molecular structure. In perspective these markers could be used to probe subtle effects which may occur when the material is employed in its target device and/or subject to different environmental conditions (*e.g.*, mechanical stress, doping, temperature change, etc.).

Here are presented the results obtained on several hydrogen-terminated graphene molecules, also functionalized with alkyl chains, namely (1) **C78**, (2) **C84** and its associated graphene nano ribbon (GNR) with necklace shape **GNR 1**, (3) **tetra-zigzag-HBC**, (4) partially-zigzag GNR $\mathbf{M}_P$ and the related oligomers $\mathbf{M}_0$, $\mathbf{M}_1$. The next Chapter is devoted to the class of chlorinated graphene molecules.

All the systems reported in these two related Chapters have been synthesized in the group lead by Prof. Klaus Müllen in Mainz (Max Planck Institute). Details on the structures and commented results from DFT calculations are reported in

Chapter 9.

3.2 C78

The investigation of the multi-wavelength Raman spectroscopy of **C78** has been reported in a paper[11] which can be also found in the Appendix of this Thesis. In the following will be highlighted some details of the Raman characterization of this graphene molecule and will be summarized the main outcomes of the published work.[11]

By considering multi wavelength excitation (namely 325, 458, 514, 632, 785 nm) it is possible to probe changes in the spectral profiles of the characteristic G and D features of **C78**, which can be taken as a representative graphene molecule. As depicted in Figure 3.1 by changing the excitation, the Raman spectrum display changes both in the fundamental and overtone/combination region. The overtone and combination Raman signals in resonance conditions can be analyzed based on Peticolas-Nafie-Stein theory, as recently discussed in the case of β-carotene.[10] It can be shown that the Raman intensity of a combination (or overtone) is proportional to the product of the Raman intensities of the corresponding fundamentals. It is possible to prove this by recalling the equations for fundamental Raman transitions and combinations (see Appendix[11]):

$$I_h \propto \left(\frac{1}{2\hbar\Omega_h}\right)\left|\frac{\hbar\mathbf{g}\cdot\mathbf{L}_h}{i\Gamma(i\Gamma+\hbar\Omega_h)}\right|^2 \tag{3.1}$$

for the overtone case, same normal modes is considered in Equation 3.2 (*i.e.* $h=k$).

$$\begin{aligned} I_{h+k} \propto & \left(\frac{1}{2\hbar\Omega_h}\right)\left(\frac{1}{2\hbar\Omega_k}\right)\times \\ & \left|\frac{(\hbar\mathbf{g}\cdot\mathbf{L}_h)(\hbar\mathbf{g}\cdot\mathbf{L}_k)}{i\Gamma(i\Gamma+\hbar\Omega_h)(i\Gamma+\hbar\Omega_h+\hbar\Omega_k)}+\frac{(\hbar\mathbf{g}\cdot\mathbf{L}_k)(\hbar\mathbf{g}\cdot\mathbf{L}_h)}{i\Gamma(i\Gamma+\hbar\Omega_k)(i\Gamma+\hbar\Omega_k+\hbar\Omega_h)}\right|^2 \end{aligned} \tag{3.2}$$

where $\hbar\Omega_k$ represents the vibrational quantum of the k-th normal mode and the $(\hbar\mathbf{g}\cdot\mathbf{L}_h)$ represents the electron-phonon coupling expressed for the h-th normal mode. The vectors $\mathbf{g}$ and $\mathbf{L}_h$ have $3N$ components, with N representing the number of atoms. Provided that the typical vibrational quantum ($\hbar\Omega$) is much smaller than the resonance broadening parameter Γ ($\hbar\Omega \ll \Gamma$), then by comparing Equation 3.1 with 3.2, it is possible to straightforwardly obtain the following result:

$$I_{h+k} \propto I_h \times I_k \tag{3.3}$$

Through Equation 3.3 one can rationalize the experimental results presented in Figure 3.1 when comparing the first order Raman signal with its second order. In particular, it is possible to observe that the relative intensity changes within the D region are reflected also in the second-order region, and this holds for all the different excitations considered. For instance, when a D component becomes weaker, this will imply a decrease in its overtone and also a decrease in its related

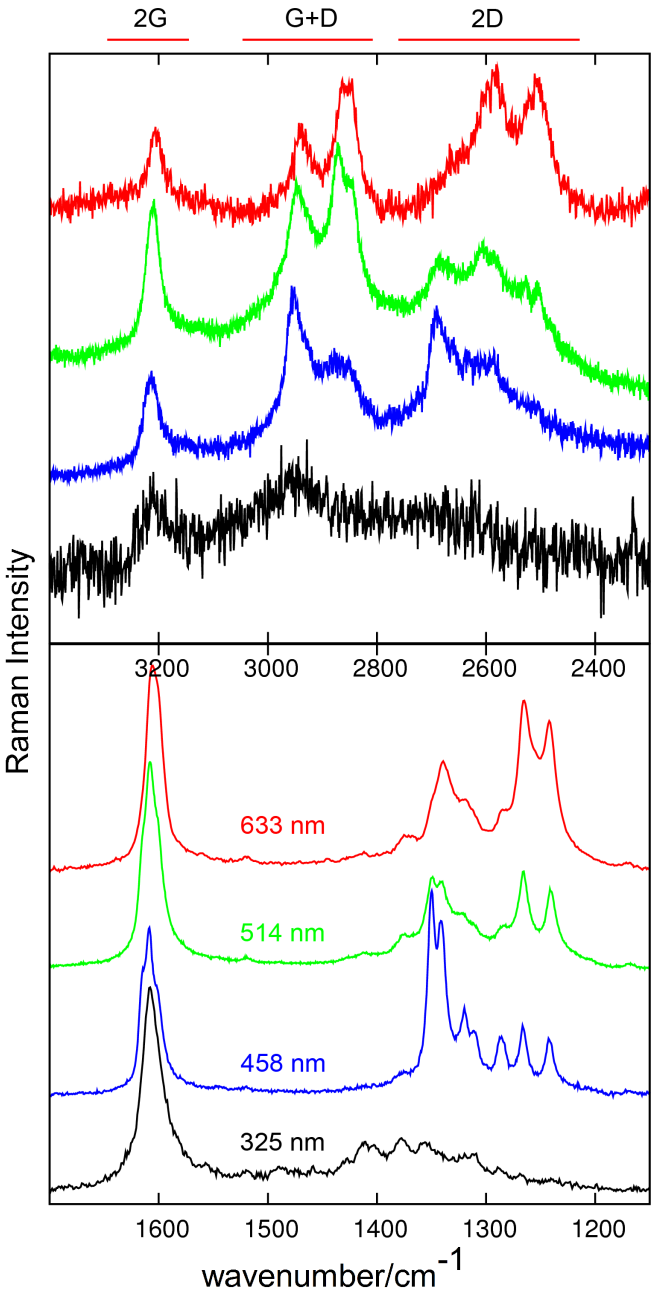

Figure 3.1: *Multi-wavelength first-order Raman spectra of* ***C78*** *compared with the corresponding second-order part where overtones (2G, 2D) and combination lines (G+D) are observed.*

combination with the G peak. Simulations based on the application of this theory (*i.e.*, through Equations 3.1 and 3.2) have been reported (see Appending[11]) and help rationalizing the intensity redistribution observed in the D region. In particular it is possible to simulate, as a function of the excitation wavelength, the relative intensity of the cluster of D peaks in the higher wavenumber tail *vs.* that of the cluster of D peaks in the lower wavenumber tail. This remarkable spectral changes are systematic and experimentally they follow the trend shown

in Figure 3.2, where the I_D/I_G ratio is also shown for completeness. The latter demonstrates that higher D intensities are observed for lower excitation energies, in agreement with well-known multi-wavelength Raman experiments carried out by Pocsik et al.[96] on micro-crystalline graphite. DFT calculations have been car-

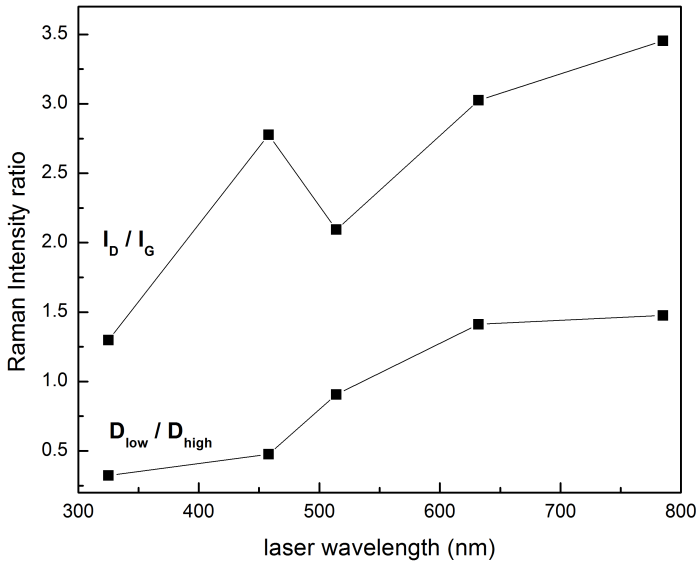

Figure 3.2: *Raman intensity changes as a function of wavelength. For computing the I_D/I_G ratio, I_G includes the Raman signal between 1550 and 1650 cm^{-1} (i.e., G_1, G_2 and G_3 components) while I_D is the integrated Raman signal from 1050 to 1550 cm^{-1}. D_{low} represents the part of the D signal integrated from 1200 to 1300 cm^{-1} (i.e., D_2, D_3 and D_4 components). D_{high} represents the D signal integrated from 1300 to 1400 cm^{-1} (i.e., D_5, D_6, D_7, D_8 and D_9 components).*

ried out on **C78** to assign the many observed Raman spectral features, not only over the D and G range, but also in the low wavenumber region. The results of this analysis are presented in the following sections.

Low wavenumber region The Raman spectrum of **C78** excited with 633 nm laser is shown in Figure 3.3 in the 130 – 1000 cm^{-1} range and compared with the results from DFT calculations and the application of Peticolas-Nafie-Stein theory (see Appendix[11]). The presence of interesting signals in this region and their nature was already pointed out by Di Donato *et al.* in the past.[13] Compared to the previous results,[13] the signal to noise ratio in the present experiments is much improved, which allows detecting more signals than before (just A_1 and A_4 were reliably detected in the past). Several rather sharp Raman lines can be observed in Figure 3.3 which have been listed in Table 3.1. The correspondence with results from DFT calculations in resonance condition with the lowest excited state are remarkably good and allow establishing the peak assignment proposed in Table 3.1. The nuclear displacements of all the modes assigned in Table 3.1 are reported in Figure 3.4. These are all collective in-plane vibrations, with a few

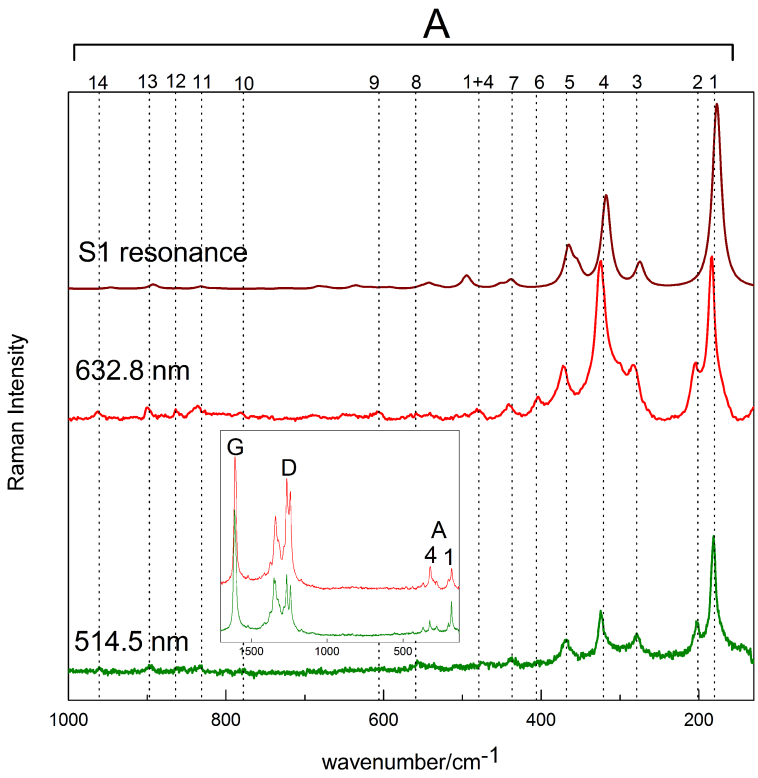

Figure 3.3: *Raman spectra of **C78** recorded with 633 nm laser excitation in the low wavenumber range compared with simulations (see text and Appendix[11]).*

	Computed wavenum.		Scaled wavenum.	Expt. (514.5 nm)	Expt. (632.8 nm)
	A_g	B_{3g}			
A_1	181	-	177	181	180
A_2	-	202	198	203	201
A_3	281	284	275 | 278	279	281
A_4	324	-	317	324	321
A_5	373	-	365	368	369
A_6	-	414	405	-	401
A_7	447	-	438	437	437
A_1+A_4	505	-	494	477	479
A_8	565	-	553	557	556
A_9	616	-	603	-	606
A_{10}	790	-	774	776	779
A_{11}	849	-	831	831	833
A_{12}	-	874	856	854	864
A_{13}	911	-	892	898	897
A_{14}	966	-	946	961	960

Table 3.1: *Experimental and theoretical (DFT) wavenumbers of the Raman features of **C78** found in the low wavenumber region. Experimental data have been recorded with 514.5 and 632.8 nm laser excitations.*

notable markers of molecular size, namely the longitudinal molecular stretching (A_1) and the transversal molecular stretching (A_4).

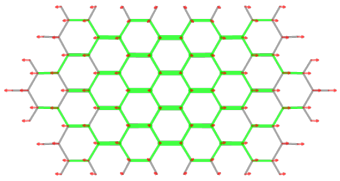

A_1 *longitudinal stretching* (A_g, *181* cm^{-1})

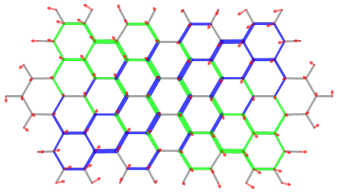

A_2 *shear-like deformation* (B_{3g}, *202* cm^{-1}, *this mode is absent in the spectrum calculated in perfect resonance with* S_1)

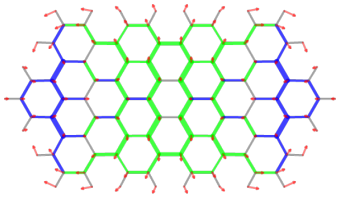

A_3 *collective bending* (A_g, *281* cm^{-1})

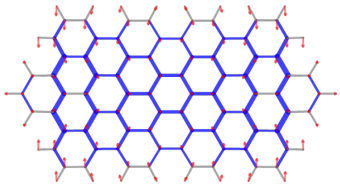

A_4 *transversal stretching* (A_g, *324* cm^{-1})

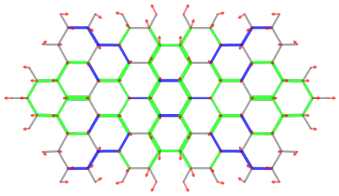

A_5 *collective bending* (A_g, *373* cm^{-1})

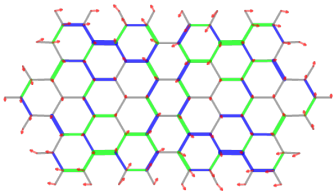

A_6 (B_{3g}, *414* cm^{-1})

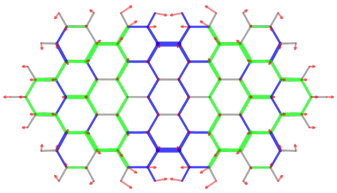

A_7 (A_g, *447* cm^{-1})

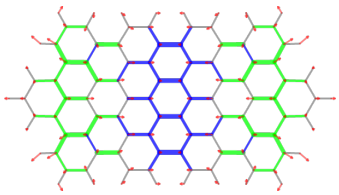

A_8 (A_g, *565* cm^{-1})

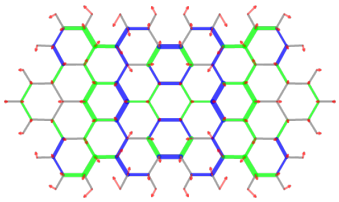

A_9 (A_g, *616* cm^{-1})

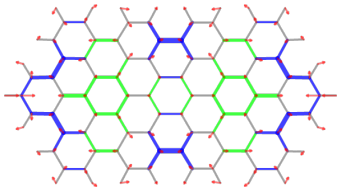

A_{10} (A_g, *790* cm^{-1})

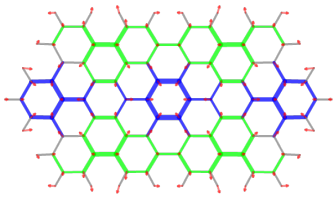

A_{11} (A_g, *849* cm^{-1})

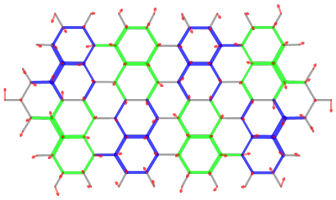

A_{12} (B_{3g}, *874* cm^{-1})

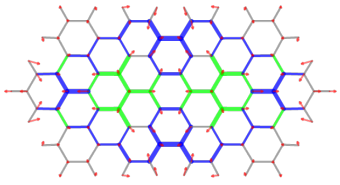

A_{13} (A_g, *911* cm^{-1})

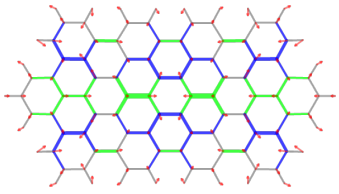

A_{14} (A_g, *966* cm^{-1})

Figure 3.4: *Sketch of the nuclear displacements of the normal modes of* ***C78*** *found at low wavenumber (from DFT calculations). Red segments represent displacement vectors; CC bonds are represented as green (blue) lines of different thickness according to their relative stretching (shrinking). Reported wavenumbers from DFT are unscaled.*

Weak Raman features: M and B regions The availability of good signal-to-noise ratio Raman spectra has allowed to detect also some weak Raman signals which went previously unnoticed.[13] These have been labeled M (middle modes) and

B (breathing modes) and have been respectively detected in the middle between the G and D bands and at lower wavenumber than the D band. They are very weak features, but they can be observed with green laser excitation (514.5 nm) with good reliability and also it is possible to find a match in DFT calculations, which allows to assign them. In Figures 3.5 and 3.6 a comparison between DFT calculations and experimental Raman spectra is offered for both the M and B signals. From the sketch of nuclear displacements it is possible to see that

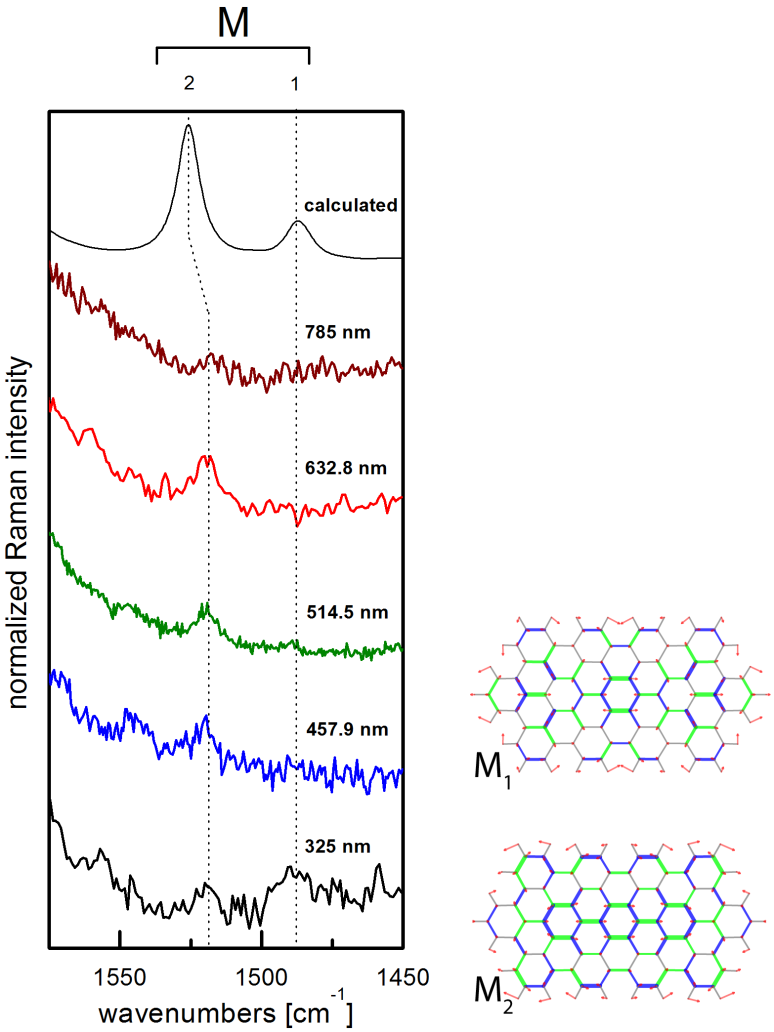

Figure 3.5: *Comparison between the calculated and experimental Raman spectra of* ***C78*** *in the 1450 - 1575 cm^{-1} spectral range (M region). The representation of the nuclear displacements of the M_1 and M_2 modes (respectively computed at 1519 and 1558 cm^{-1}) is based on DFT calculations. See the caption of Figure 3.4 for details on the representation of the modes.*

among the B features one finds breathing vibrations of a few selected rings in the core of **C78** (see for instance B_1 and B_2). As for the M-modes, they are reminiscent of the typical displacements of the G-modes (*i.e.*, ring stretching).

D region The experimental Raman spectra of **C78** recorded with several laser lines are reported in Fig 3.1. It is clear that the Raman spectra in this region are

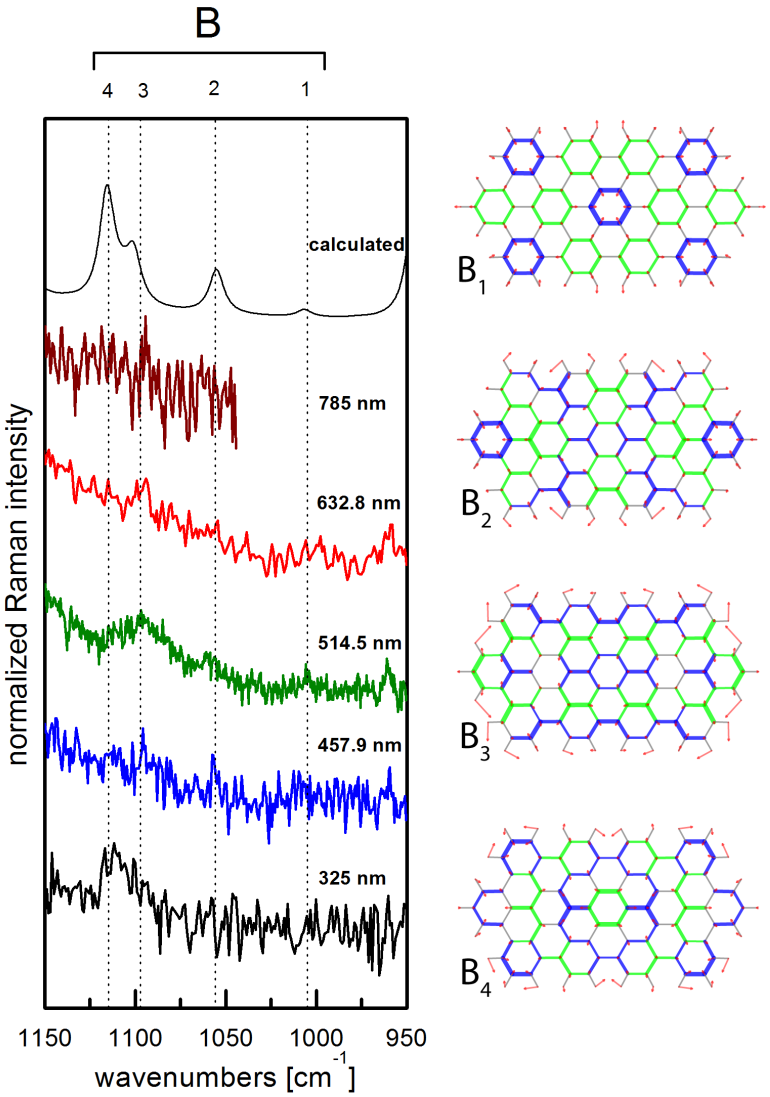

Figure 3.6: *Comparison between the calculated and experimental Raman spectra of* ***C78*** *in the 950 - 1150 cm^{-1} spectral range (B region). The representation of the nuclear displacements of the B_1, B_2, B_3 and B_4 modes (respectively computed at 1028, 1077, 1124 and 1139 cm^{-1}) is based on DFT calculations. See the caption of Figure 3.4 for details on the representation of the modes.*

remarkably sensitive to the variation of the excitation energy. At least eleven D peaks can be observed over the 1150-1450 cm^{-1}. Their wavenumbers have been determined through careful band deconvolution, as displayed in a series of panels in Figure 3.7 Table 3.2 collects all the observed positions of the D components as a function of the excitation wavelength. The position of these components is expected to be independent on laser excitation (within experimental error and band deconvolution uncertainty). This expectation is fulfilled by the data reported in Table 3.2 and it is due to the fact that each one of the D components is assigned to a specific molecular normal mode.

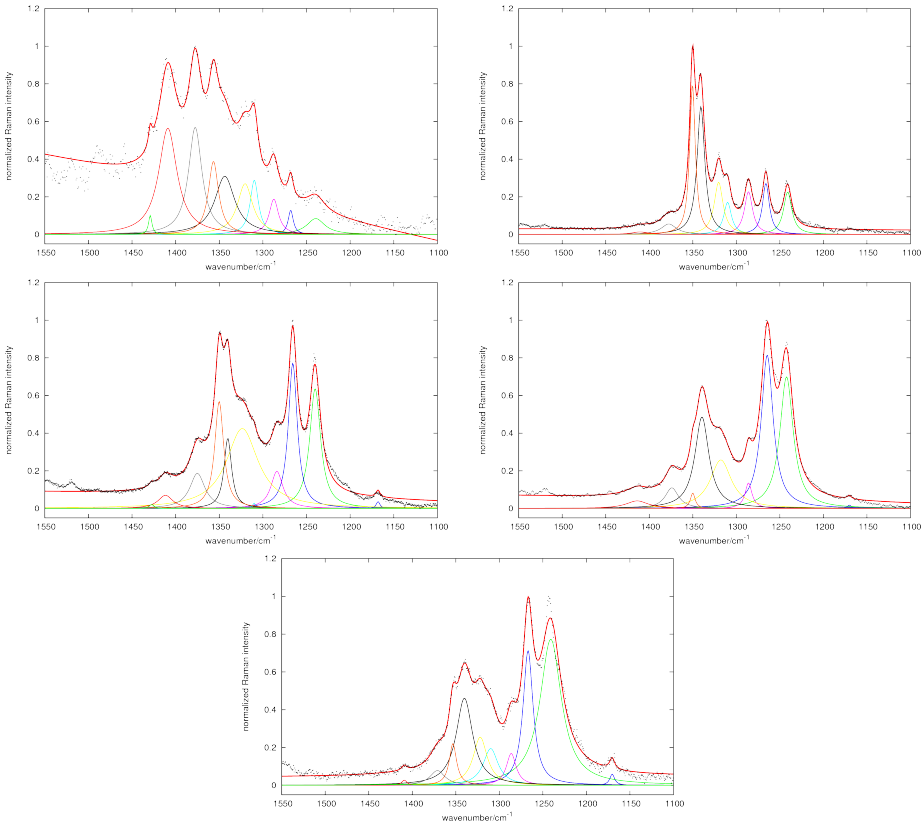

Figure 3.7: *Deconvolution of the Raman lines of **C78** over the D region as a function of the excitation wavelength (325, 458, 514, 633, 785 nm). Lorentzian lineshapes have been considered for the deconvolution.*

	325 nm	**457.9 nm**	**514.5 nm**	**632.8 nm**	**785 nm**
D_1	-	-	1168	1170	1170
D_2	1239	1241	1240	1242	1241
D_3	1268	1266	1266	1264	1267
D_4	1287	1286	1284	1286	1286
D_5	1310	1310	1310	-	1310
D_6	1320	1320	1324	1318	1322
D_7	1344	1341	1340	1339	1340
D_8	1357	1350	1350	1350	1350
D_9	1378	1378	1375	1374	1371
D_{10}	1409	1411	1412	1414	1409
D_{11}	1429	-	1428	-	1427

Table 3.2: *Wavenumber of the peaks obtained from band deconvolution in the D region of the multi-wavelength Raman spectrum of **C78**.*

G region Similar to the analysis which has been carried out for the D region, band deconvolution with Lorentzian lineshape has been also considered over the G region. The results are summarized in Figure 3.8 below. Compared to the D-band, the shape of the G-band is less sensitive to the laser excitation energy. Nevertheless the experimental Raman spectra show a structured G-band. The

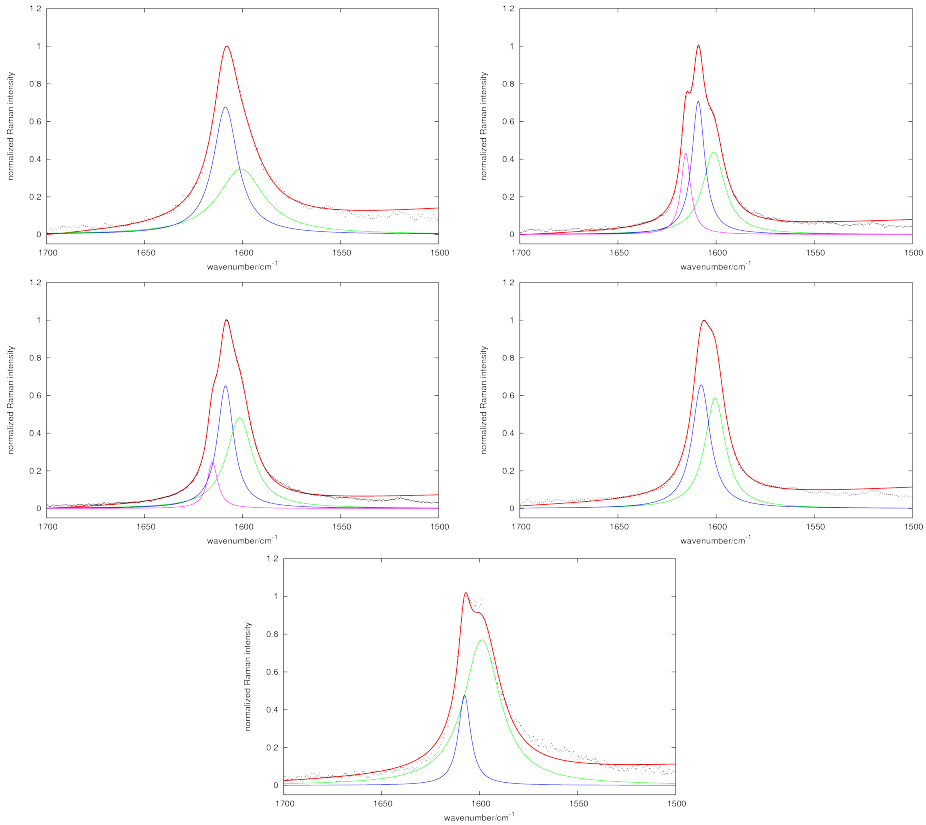

Figure 3.8: *Deconvolution of the lines in the G region of the Raman spectrum of **C78** as a function of the excitation wavelength (325, 458, 514, 633, 785 nm). Lorentzian lineshapes have been considered for the deconvolution.*

spectra recorded with 457.9 nm and 514.5 nm excitations display a good signal to noise ratio in the G region as reported in Figure 3.1. It is clear that the G signal is made by overlapping of at least three peaks centered at 1601, 1609 and 1615 cm^{-1}. The position of these components is expected to be independent on laser excitation (within experimental error and band deconvolution uncertainty, see similar discussion on the D components). Indeed, the data reported in Table 3.3 show the stability of the wavenumber of each component with respect to the laser excitation. DFT calculations (see Table 3.4) demonstrate five modes with

	325 nm	**457.9 nm**	**514.5 nm**	**632.8 nm**	**785 nm**
G_1	1601	1601	1601	1601	1599
G_2	1609	1609	1609	1608	1608
G_3	-	1615	1615	-	-

Table 3.3: *Wavenumber of the peaks obtained from band deconvolution in the G region of the multi-wavelength Raman spectrum of **C78**.*

sizable Raman activity, but they cluster into three groups with close wavenumbers which explains the experimentally observed number of components. For selected laser excitations (325, 632.8 and 785 nm) only two components out of three have been considered because the third component is too weak to allow a reliable peak

deconvolution.

wavenumber (cm^{-1})	I_{Raman} (A^4/amu)	irrep	Assignment
1635	21847	A_g	$\mathbf{G}_1$
1643	124	B_{3g}	$\mathbf{G}_2$
1646	2489	A_g	
1653	8988	A_g	$\mathbf{G}_3$
1656	117	A_g	

Table 3.4: *The components of the G band determined by DFT calculations on **C78**.*

Temperature dependence of the G peak The Raman spectra of **C78** have been recorded with 632.8 nm laser excitation at different temperatures from 25 to 200 $°C$. By increasing temperature, the position of G peak shifts to lower wavenumber. This shift has been related to thermal expansion phenomena,[12] which in molecular materials are expected to affect intermolecular distances and interaction strengths, thus possibly inducing spectral changes in Raman. By deconvolution of the G peak (see paragraph above), one determines that the position of the three G components markedly red shifts by increasing the temperature, as reported in Figure 3.9. The average slope of the linear dependence of their wavenumber versus temperature is -0.016 $cm^{-1}/°C$. Atashbar *et al.* have measured similar behavior for graphite but with a different slope (-0.031 $cm^{-1}/°C$).[97] The larger slope value of graphite may be due to the additional contribution from phonon-phonon scattering[97] (which is not expected to play a major role in a molecular material such as **C78**). On the other hand the contributions from $\pi - \pi$ interactions are expected to be similar in graphite and **C78**.

3.3 C84

The work by Schwab *et al.*[17] reports the details on the synthesis of **C84** (a large PAH formed by 84 sp^2 carbon atoms in the aromatic core) and the structurally related graphene nanoribbon **GNR 1**, which is characterized by an unprecedented "necklace-like" structure featuring an armchair edge configuration (see Figure 3.10).

DFT calculations[17] carried out on both the monomer **C84** and the polymer **GNR 1** have been carried out to investigate the energy of the frontier orbitals. In **C84** the HOMO is computed at -4.58 eV and the LUMO at -2.41 eV, leading to an energy gap of 2.17 eV. In **GNR 1**, the top of the valence band is located at -4.38 eV and the bottom of the conducting band is located at -2.98 eV, which leads to a bandgap of 1.40 eV (see Figure 3.11). Interestingly, this bandgap is relatively large compared other GNRs of similar width.[98]

The FT-IR spectrum of **C84** (see Figure 3.13) displays characteristic fingerprint peaks which are in agreement with DFT calculation. The DFT molecular model consider C6 alkyl chains instead of C12 (the size of the alkyl chains in the synthesized compound). This choice was made in order to keep the computational cost under control. Furthermore, a model with trans-planar chains – model (a) – has been compared with a model with slightly distorted chains – model (b),

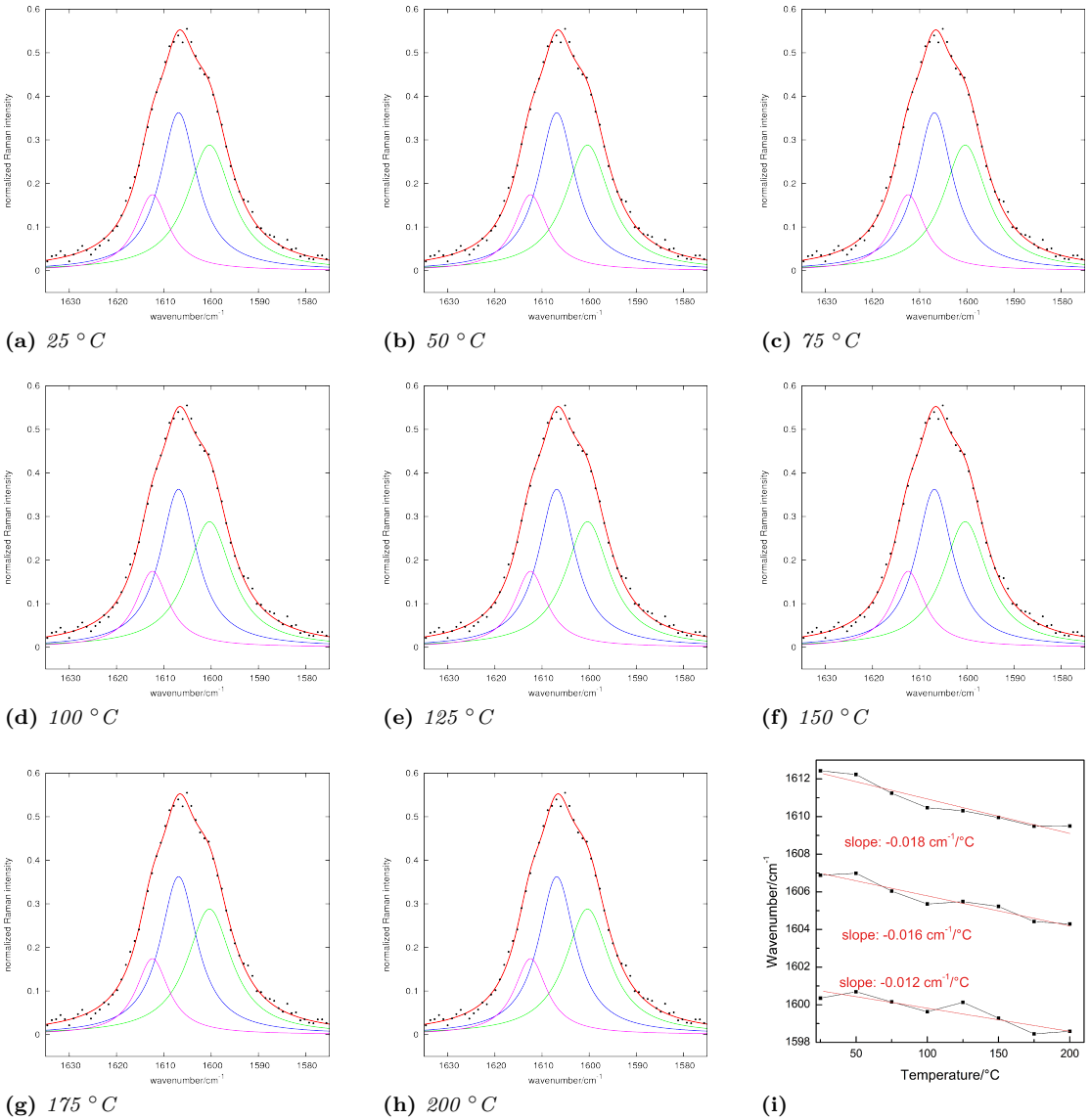

(a) *25 °C* **(b)** *50 °C* **(c)** *75 °C*

(d) *100 °C* **(e)** *125 °C* **(f)** *150 °C*

(g) *175 °C* **(h)** *200 °C* **(i)**

Figure 3.9: *Deconvolution of the Raman spectra of **C78** in the G region as a function of sample temperature. The spectra have been recorded with 632.8 nm laser excitation and have been analyzed with three Lorentzian peaks. In the rightmost bottom panel the linear trend of the position of the three G components is plotted vs. temperature.*

see Figure 3.12. In this way, it is possible to assign the main CH out-of-plane (*opla*) fingerprints[99] and assess the possible change in the IR spectrum induced by adding a little amount of gauche conformations in the alkyl chains.

By comparing the experimental and calculated spectra (see Figure 3.13), it is possible to find out that the peak observed at 856 cm^{-1} is sensitive to conformational changes of the alkyl chains and broadens in model (b). This band is assigned to the collective in-phase CH-*opla* vibration along the edge of **C84** (see the mode computed at 868 cm^{-1} – unscaled – reported in Figure 3.14). The structured peak observed at 819 cm^{-1} is assigned to a doublet in the simulated spectra, namely:

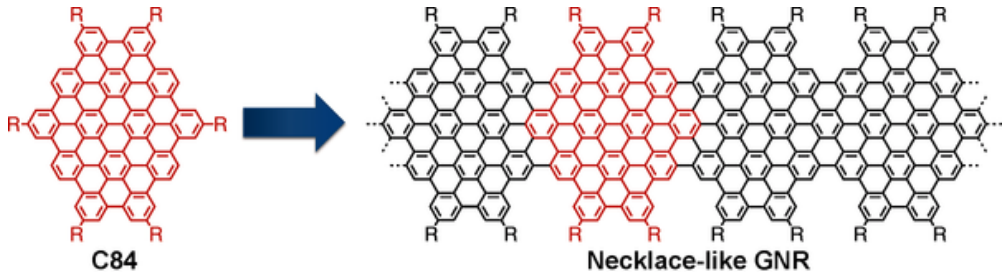

Figure 3.10: *Structure of the model molecular graphene **C84** and the related necklace-like **GNR 1**. R: dodecyl*

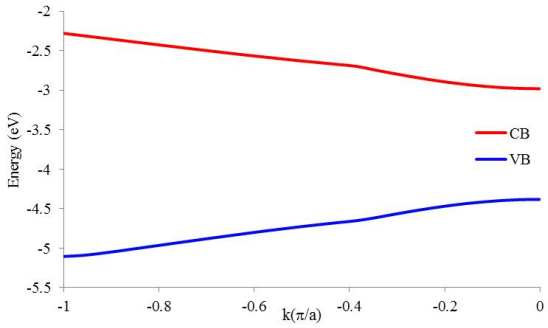

Figure 3.11: *Calculated band structure of **GNR 1**.*

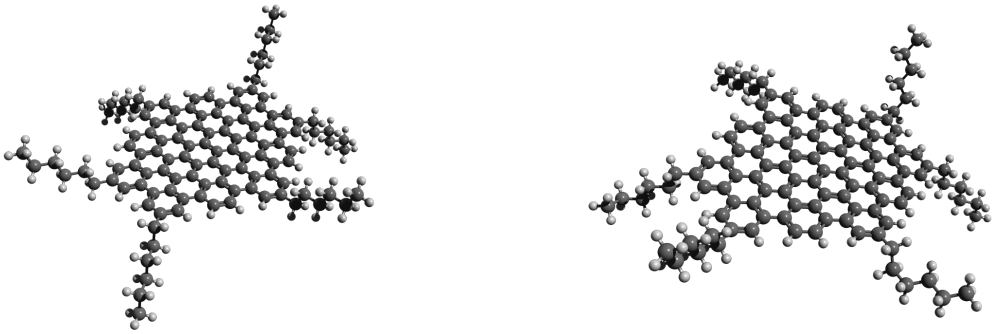

(a) ***C84*** *with trans-planar chains*

(b) ***C84*** *with slightly distorted chains*

Figure 3.12: *DFT models of **C84** with C6 alkyl chains instead of C12.*

(i) the CH-*opla* bending of the inner CH bonds along the four longer edges of **C84** (mode computed at 812 cm^{-1}, Figure 3.14) and (ii) a collective in-plane deformation of the honeycomb structure of the core of the **C84** (mode computed at 831 cm^{-1}, Figure 3.14). The relative intensity of the two components (i, ii) changes dramatically in the gas-phase calculations compared to the experimental FT-IR spectrum recorded in solid state. The peak observed at 719 cm^{-1} is assigned to the rocking modes of the alkyl chains (mode computed at 735 cm^{-1}, Figure 3.14). The structured features observed at lower wavenumber are calculated by DFT with poor relative intensities based on the simplifications required by the models (see above). The good correspondence between the measured and the simulated

IR spectra of **C84** provide support for the successful synthesis of this molecule. Furthermore the assignment of the peaks in the CH-out-of-plane bending region, fostered by DFT calculations, provide markers of the edge topology of the PAH which may prove useful for the molecular characterization of advanced functional materials containing **C84** as an active component.

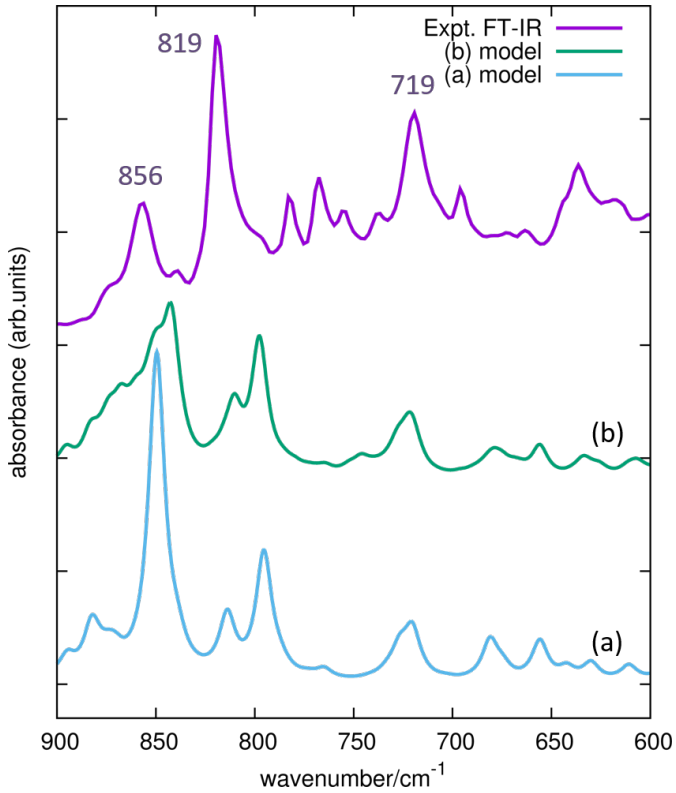

Figure 3.13: *Comparison between the experimental and the simulated IR spectra of **C84** obtained from DFT calculations on simplified models. Theoretical wavenumbers are scaled by 0.979.*

The Raman spectrum of **GNR 1** is shown in Figure 3.15. It is possible to observe the characteristic D and G peaks, together with their associated second order lines, which are typical of structurally well-defined GNRs, as already reported in the literature.[57,100,101] Furthermore, based on the UV-Vis absorption spectrum of **GNR 1**,[17] the observation of overtones and combinations in the Raman spectrum is consistent with resonance conditions reached with the 514.5 nm laser excitation used in the Raman experiment. Similarly to the case of **C78** (see Figure 3.1), the relative intensities and bandshapes observed over the overtone and combination region, approximately match the corresponding fundamentals. For instance, the 2D feature is more structured than 2G, consistently with the fact that in the first order spectrum the D feature is more structured than G.

3.4 tetra-zigzag-HBC

In the search for zigzag-edged extended PAHs, a novel HBC derivative, named **tetra-zigzag-HBC**, has been very recently obtained in Prof. Müllen group.[43] It

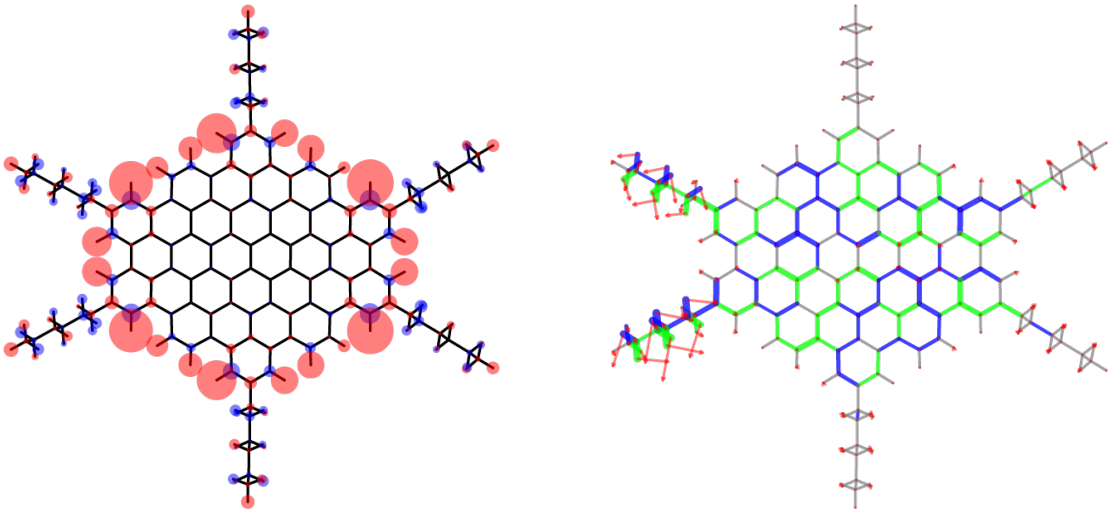

(a) *868 cm^{-1}*

(b) *735 cm^{-1}*

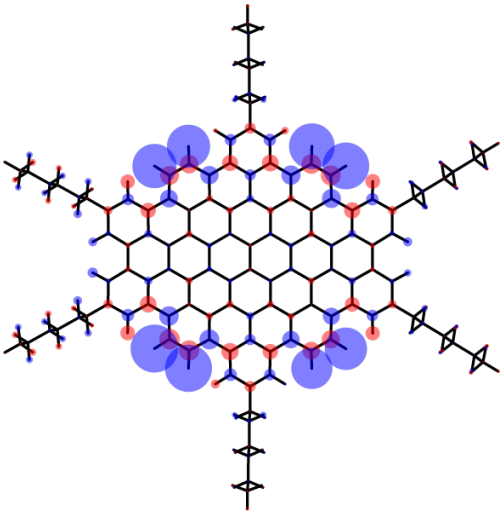

(c) *812 cm^{-1}*

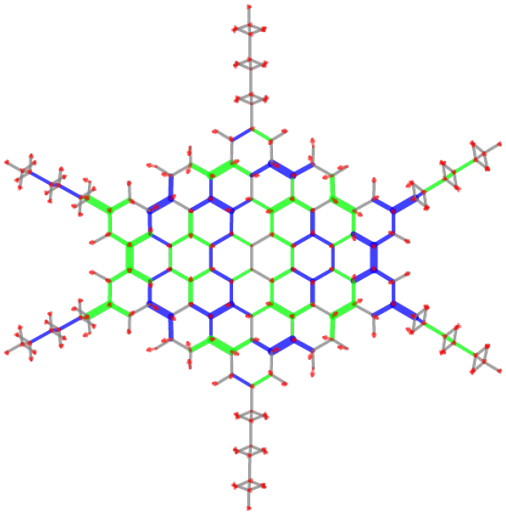

(d) *831 cm^{-1}*

Figure 3.14: *Nuclear displacements of characteristic IR modes of **C84** determined with DFT calculations. Red segments represent displacement vectors; CC bonds are represented as green (blue) lines of different thickness according to their relative stretching (shrinking). For out-of-plane modes the size of blue/red circles of the molecular sketch is proportional to nuclear displacements in the out-of-plane direction (z); red indicates displacements directed along $+z$ and blue indicates displacements directed along $-z$.*

has four K regions, *i.e.*, zig-zag peripheries, which can be seen as a cutout of an $N = 6$ zigzag GNR (see Figure 3.16). The procedure for its chemical synthesis is reported in details by Dumslaff *et al.*.[43] **tetra-zigzag-HBC** can also be considered as a slightly more extended analogue of teranthene;[50] it demonstrates good stability, which enables its spectroscopic characterization under ambient conditions. The structure of **tetra-zigzag-HBC** has been validated by IR, Raman and UV-Vis absorption spectroscopy. In particular, the computed IR and Raman spectra show remarkable agreement with their experimental counterparts

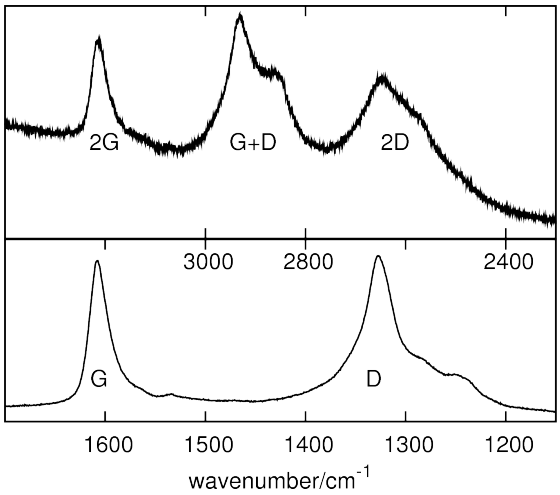

Figure 3.15: *Experimental Raman spectrum of **GNR 1** over the first and second order regions.*

and specific peaks originating from the armchair and zigzag peripheries can be assigned. Furthermore, the analysis of the UV-Vis absorption of **tetra-zigzag-HBC**, carried out within Clar's annellation theory,[2,16] exhibits a systematic red shift of the absorption compared to the related HBC derivatives with one to three K-regions.[40,42,102]

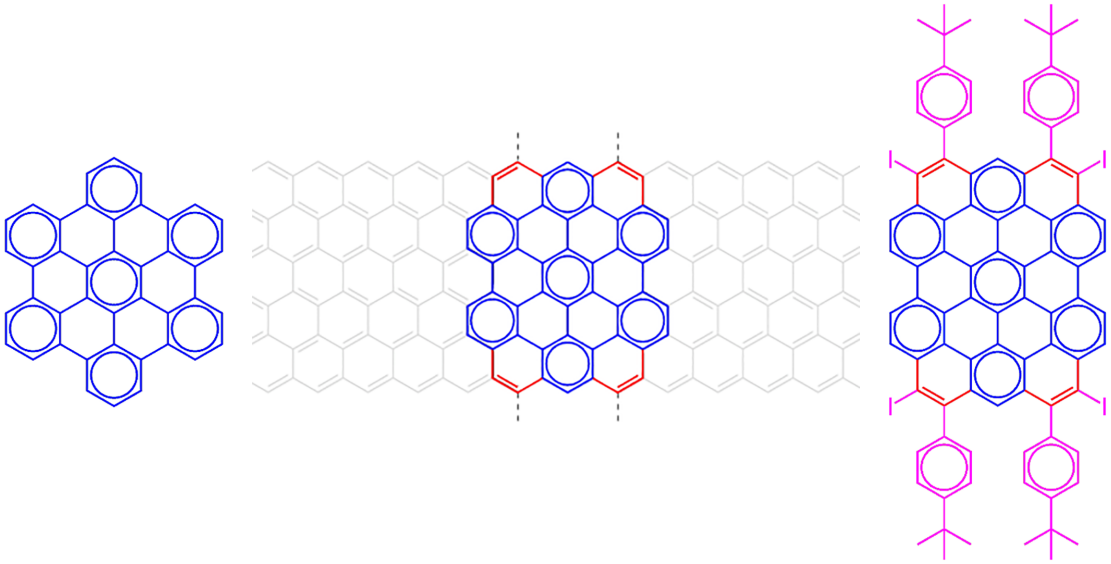

(a) *HBC*

(b) *Structure of unsubstituted-**tetra-zigzag-HBC** with four extra K regions as a cutout of N = 6 zigzag GNRs.*

(c) *synthesized **tetra-zigzag-HBC***

Figure 3.16: *Chemical structure of **HBC** (a), **tetra-zigzag-HBC** with four extra K regions as a cutout of N = 6 zigzag GNRs (b), and synthesized sample (c).*

3.4.1 UV/Vis absorption spectroscopy

Based on the fundamental work on the UV-Vis absorption of PAHs carried out by Clar,[2,16] there are three main transitions in the UV-Vis absorption spectra of

PAHs:

- $\alpha : HOMO - 1 \rightarrow LUMO$ (highest wavelength)
- $p : HOMO \rightarrow LUMO$ (intermediate wavelength)
- $\beta : HOMO + 1 \rightarrow LUMO + 1$ (lowest wavelength)

Clar has shown that the p band is significantly red shifted and the β band is weakly red shifted by adding one π bond to the structure of a given PAH. This explains how π-conjugation works in PAHs and molecular graphene. For instance, as it is shown in Figure 3.17, by adding two π bonds to the parent structure (A), the p band is red shifted by about 70 nm and the β band is red shifted by about 20 nm.[2,16] From the point of view of Clar's annellation theory, **tetra-zigzag-HBC**

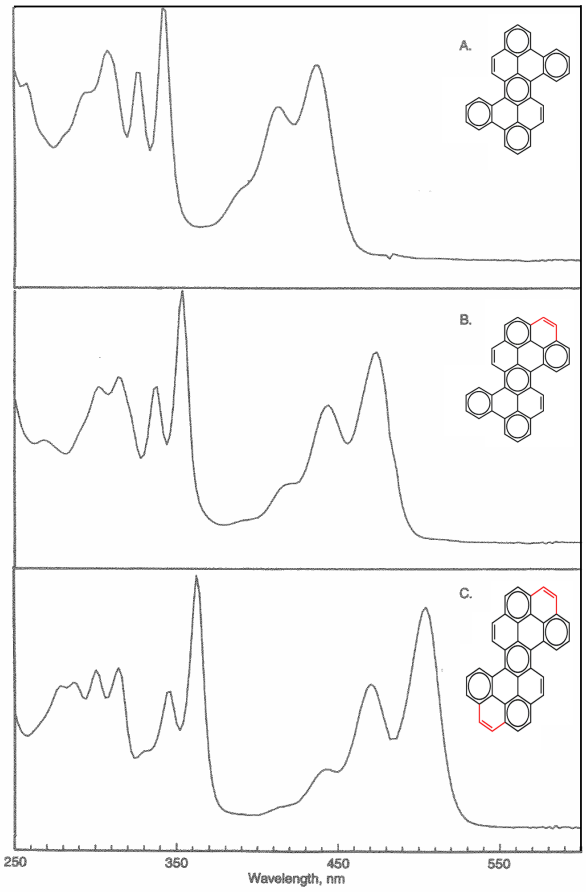

Figure 3.17: *The systematic large red shift of the p band and the weak red shift of the β band in the UV-Vis absorption spectra of a representative PAH (tetrabenzo[a,cd,j,lm]perylene, named structure A). These red shifts are observed as the result of adding one and two π-bonds to structure A. This kind of analysis is a practical example of the application of Clar's annellation theory (this figure has been adapted from ref.[16]).*

represents the analogue of HBC with the remarkable addition of four π-bonds (see Figure 3.16). This is expected to significantly enhance π-conjugation compared to HBC and thus red-shift the absorption maximum.

The optical properties of **tetra-zigzag-HBC** were investigated with UV/Vis absorption spectroscopy and the resulting absorption spectrum is reported in Figure 3.18. Time-dependent density functional theory (TDDFT) calculations were also carried out to determine the position of the vertical optical transitions and their oscillator strengths; these are displayed with violet vertical sticks in Figure 3.18. Additional calculations were carried out on unsubstituted-**tetra-zigzag-HBC** (see Figure 3.16) for assessing the effects of the adopted chemical substitutions on the position of the electronic transitions. Finally, a reference TDDFT calculation on HBC was considered for evaluating the effects of the increase of π-conjugation within Clar's annellation theory. The results of the latter TDDFT calculations are displayed in Figure 3.18as red and blue vertical sticks (respectively).

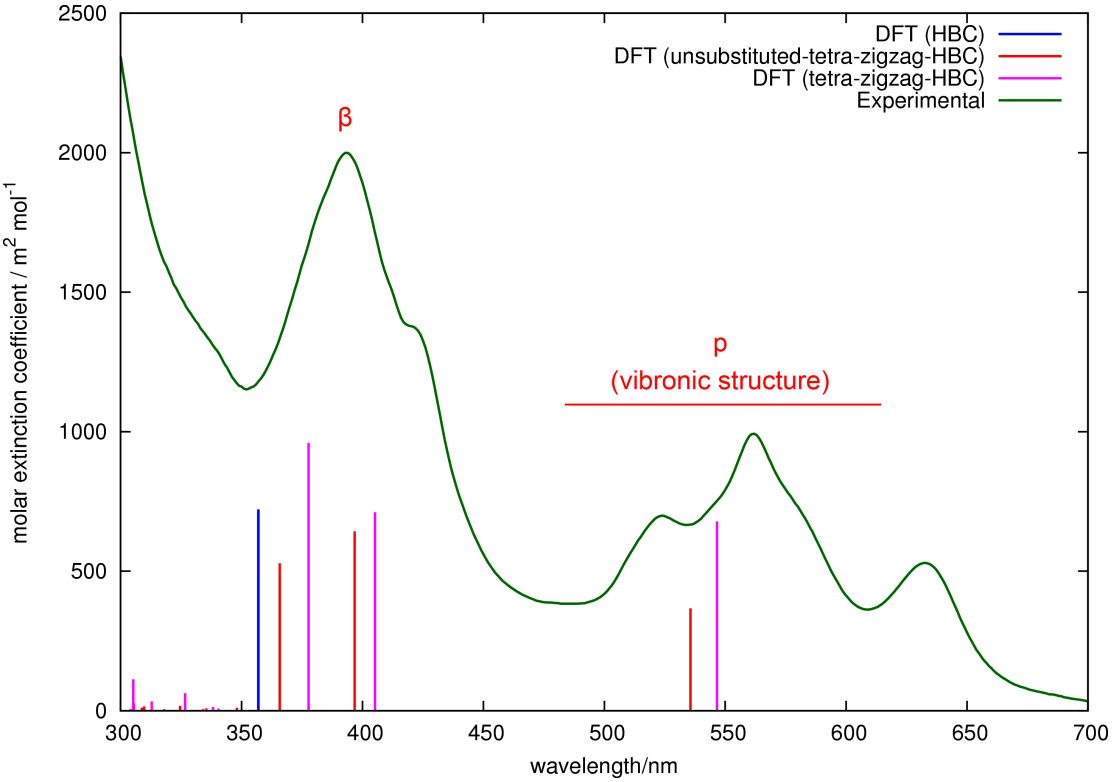

Figure 3.18: *Experimental UV-Vis absorption spectrum of* ***tetra-zigzag-HBC****. The position and oscillator strengths computed by TD-DFT of the vertical transitions of* ***HBC****, unsubstituted-****tetra-zigzag-HBC*** *and* ***tetra-zigzag-HBC*** *are shown by vertical sticks.*

By comparing the results from the calculations on **HBC** and unsubstituted-**tetra-zigzag-HBC** one finds a marked red shift (179 nm) of the bright transition with largest $HOMO \rightarrow LUMO$ character (compare 357 nm in **HBC** with 536 nm in unsubstituted-**tetra-zigzag-HBC**). This is expected based on Clar's annellation theory as described above,[2,16] since the structure of unsubstituted-**tetra-zigzag-HBC** is obtained from that of **HBC** by the addition of 4 C=C bonds, which leads to a substantial increase in π-conjugation. This finding matches the expected behavior of the p band in Clar's notation.

TDDFT calculations on **tetra-zigzag-HBC** reveal three optically-allowed vertical transitions characterized by a sizable oscillator strength (f). These fairly match the observed absorptions over the range displayed in Figure 3.18:

$$\text{I} : 546 \text{ nm: } HOMO \rightarrow LUMO (f = 0.68)$$

$$\text{II} : 405 \text{ nm: } HOMO \rightarrow LUMO + 1; \& HOMO - 1 \rightarrow LUMO (f = 0.71)$$

$$\text{III} : 378 \text{ nm: } HOMO - 1 \rightarrow LUMO + 1 (f = 0.96)$$

Based on this description of the transitions offered by TDDFT, the p band is located at 546 nm. Comparing this result with the results from unsubstituted-**tetra-zigzag-HBC**, the p band in substituted-**tetra-zigzag-HBC** red shifts by 10 nm as a result of the interaction of the aromatic core with the aryl and iodine substituents. The experimental UV/Vis spectrum of **tetra-zigzag-HBC** shows that the p band is located at 562 nm and, in contrast to **HBC**,[103] it is structured into 3 features due to vibronic coupling. Based on these data, the experimental red shift of the p band from HBC to **tetra-zigzag-HBC** reaches the considerable value of 170 nm.

The experimental absorption at 393 nm, characterized by the highest intensity, corresponds to the β band. TDDFT calculations show that it originates from a couplet of ($HOMO \rightarrow LUMO + 1, HOMO - 1 \rightarrow LUMO$) and ($HOMO - 1 \rightarrow LUMO + 1$) transitions. The molar extinction coefficient of this band (1800 m^2/mol^{-1}) and the corresponding wavelength is in the same range as was reported in the literature for mono-, and di-zigzag-HBCs.[6]

3.4.2 Raman spectroscopy

Off-resonance FT-Raman spectroscopy has been carried out on a powder sample of **tetra-zigzag-HBC** with laser excitation at 1064 nm (see Figure 3.19). The experimental FT-Raman spectrum agrees with the one simulated based on results from DFT calculations, which shows the successful formation of **tetra-zigzag-HBC**. As expected for the class of PAH molecules, the Raman spectrum of **tetra-zigzag-HBC** reveals the characteristic D and G lines (see Figure 3.19). It is interesting to compare in Figure 3.20 the simulated Raman spectra of **tetra-zigzag-HBC** and **HBC**. In particular, the most intense D-peak (D_3) found for **tetra-zigzag-HBC** shows a displacement pattern which closely match the one found in the parent **HBC** molecule (see for instance the displacements in correspondence of the starred rings reported in Figure 3.21). Consistently with the results from UV/Vis spectroscopy and Clar annellation theory, the results from the DFT calculations of the Raman spectra (Figure 3.20) show that, because of larger π-conjugation, the D-peak of **tetra-zigzag-HBC** is red shifted and shows a higher Raman activity compared to that of the parent **HBC** (see also Table 3.5).

The Raman spectra of **tetra-zigzag-HBC** excited with 458 and 514 nm laser lines are reported in Figure 3.22. Since these laser excitations are close enough to electronic transitions pre-resonance condition are reached (see the UV/Vis spectrum showing the position of the selected laser lines reported in Figure 3.23). This allows observing with good relative intensity not only the typical G and D

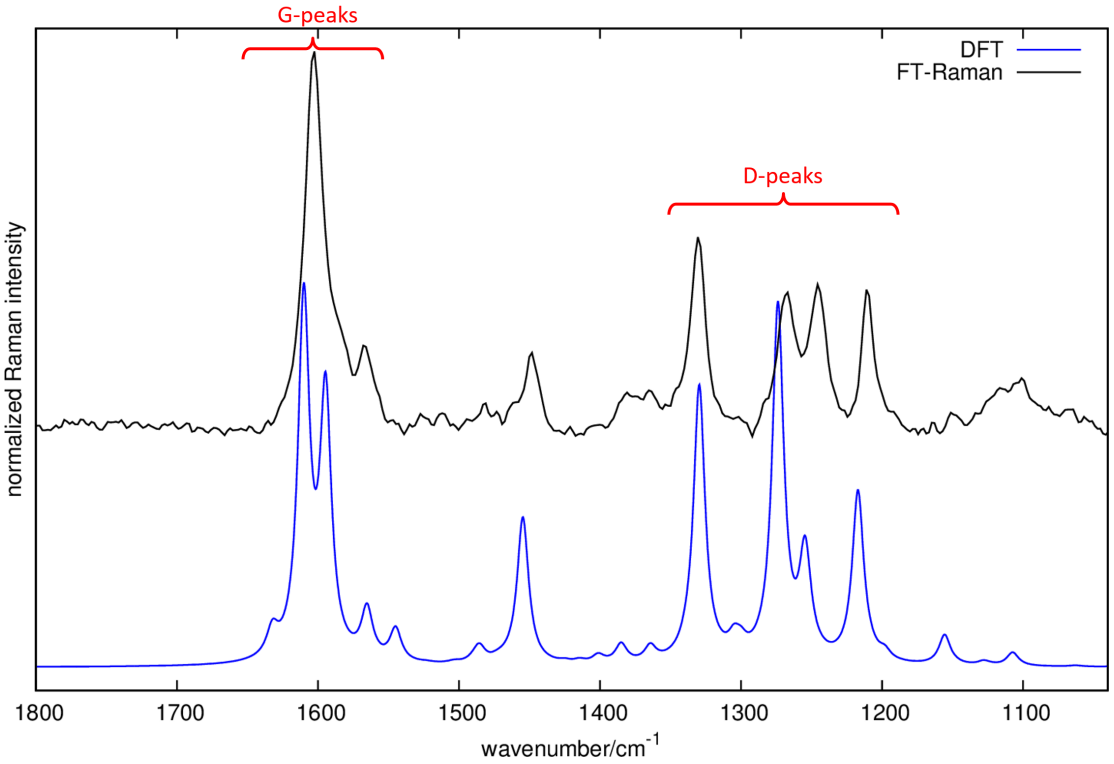

Figure 3.19: *FT-Raman spectrum (1064 nm excitation) of the powder sample of* ***tetra-zigzag-HBC*** *compared with the simulated spectrum obtained from DFT calculations.*

	HBC (experimental)	**HBC** (DFT)	**tetra-zigzag-HBC** (experimental)	**tetra-zigzag-HBC** (DFT)
D_3	1304	1325 (4020 A^4/amu)	1269	1300 (12720 A^4/amu)
D_4	1363	1384 (1188 A^4/amu)	1332	1357 (10360 A^4/amu)

Table 3.5: *Comparison between the experimental and calculated wavenumber of D_3 and D_4 in* ***HBC*** *and* ***tetra-zigzag-HBC*** *(cm^{-1}). Off-resonance Raman intensities computed by DFT are also reported (A^4/amu).*

features but also their overtones and combinations. Furthermore, due to better resonance condition (Figure 3.23), it is possible to observe a stronger second order with the 514 nm laser excitation. Such second-order peaks are otherwise too weak and could not be observed with the 1064 nm laser excitation, due to off-resonance conditions.[1,11]

The intensity pattern of the 2D and 2G signals displayed in Figure 3.22, rather closely follows that of their corresponding D and G fundamentals (respectively). The theoretical explanation for this behavior is the same as the one reported in Section 3.1, where it was observed for **C78** investigated with multi-wavelength Raman spectroscopy.

On the other hand, by comparing the Raman spectra excited with different laser lines, it is possible to observe different intensity patterns in the D region, due to changes in resonance conditions. The change of excitation energy drives a redistribution of the Raman intensity among the modes over the D region as

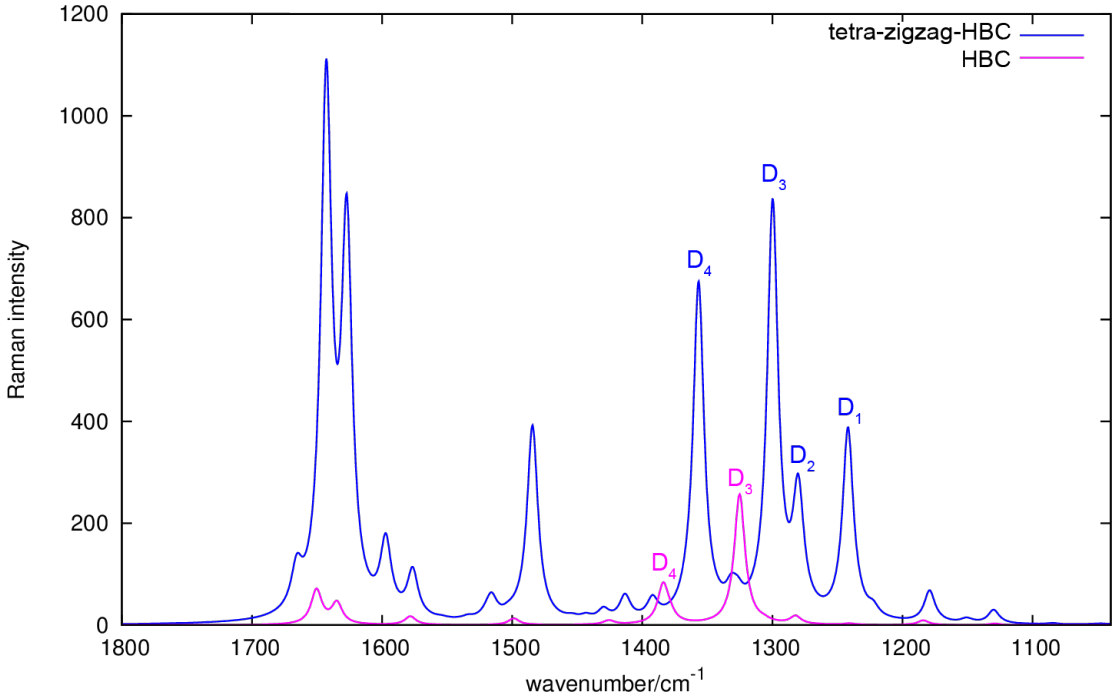

Figure 3.20: *DFT-calculated Raman spectra of* ***tetra-zigzag-HBC*** *and of the parent* ***HBC****. The D-peak of* ***tetra-zigzag-HBC*** *is red shifted and shows higher Raman activity compared to that of* ***HBC****.*

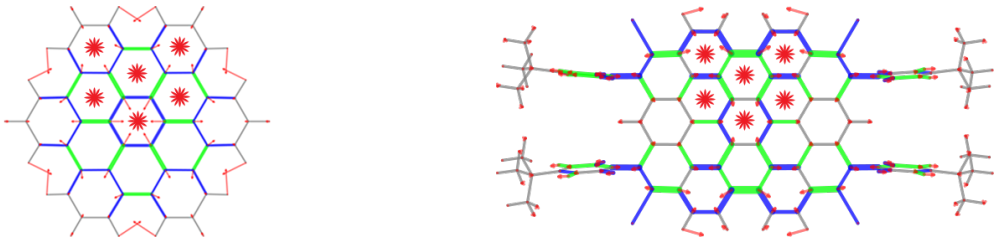

(a) ***HBC****,* D_3 *mode computed at 1325* cm^{-1}*, 4020* A^4/amu

(b) ***tetra-zigzag-HBC****,* D_3 *mode computed at 1300* cm^{-1}*, 12720* A^4/amu

Figure 3.21: *Nuclear displacement of the* D_3 *modes computed for* ***HBC*** *and* ***tetra-zigzag-HBC*** *(DFT). The displacements in correspondence of the starred rings display very similar patterns in the two molecules. Red segments represent displacement vectors; CC bonds are represented as green (blue) lines of different thickness according to their relative stretching (shrinking).*

it has been shown in Figure 3.24. While with 1064 nm excitation the four peaks in the D region have comparable relative intensities, with 458 nm excitation the most intense D peak is found at higher wavenumber and with 514 nm excitation the most intense D peak is found at lower wavenumber. A similar behavior has been observed and theoretically rationalized in **C78**.

The experimental multi-wavelength Raman spectra also display a structured G-band (see Figure 3.24). The results from DFT calculations reveal the presence of five modes with sizable Raman activity in the G peak region. The higher wavenumber mode (1666 cm^{-1}) is due to the phenyl substituents; it is so weak in

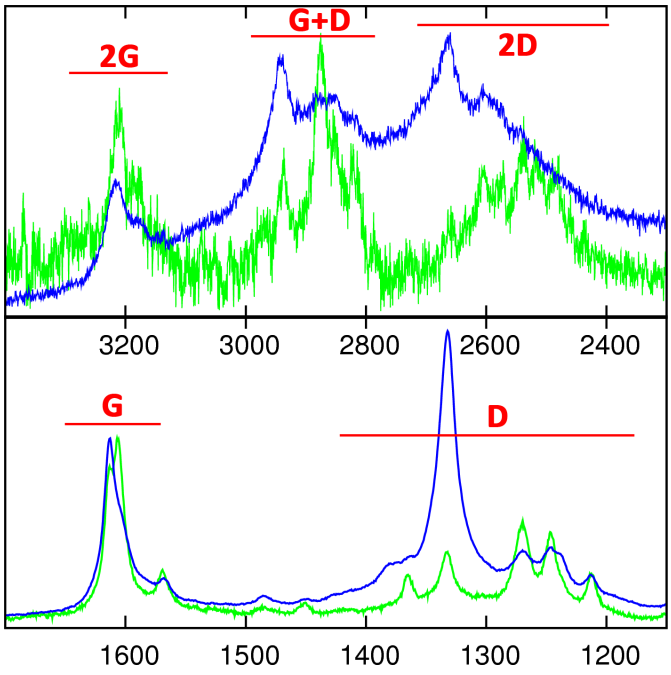

Figure 3.22: *First- and second-order experimental Raman spectra of* ***tetra-zigzag-HBC*** *excited with 458 and 514 nm laser lines. Green and blue lines respectively represent the 514 nm and the 458 nm excitation line.*

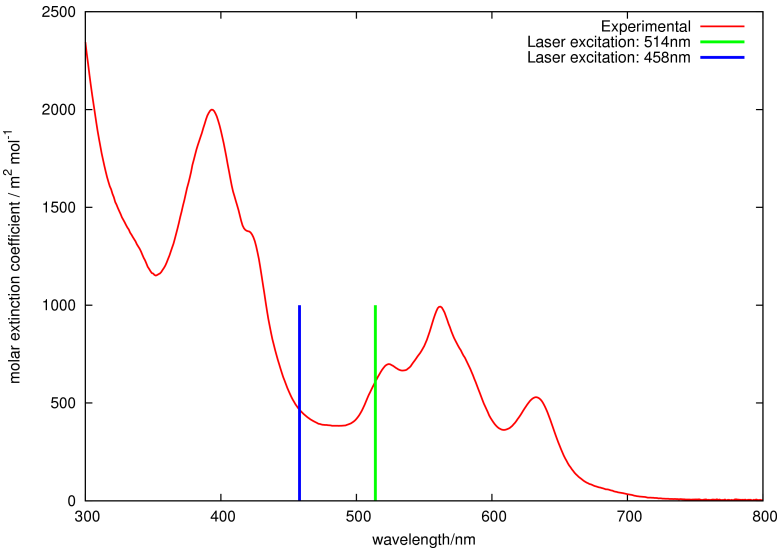

Figure 3.23: *Experimental UV/Vis spectrum of* ***tetra-zigzag-HBC*** *compared with the position of the laser excitations employed in the Raman experiments reported in Figure 3.22.*

the experiments that it is not observed. The next three modes (1643, 1627, and 1597 cm^{-1}) exhibit the typical displacements patterns of G modes. The last mode predicted by DFT in this region (1576 cm^{-1}) has some similarity with the typical G modes displacements in the center of the aryl core, but it is characterized by a different displacement pattern at the armchair edge of **tetra-zigzag-HBC**. Since it is almost not seen in experimental Raman spectra it has not been considered

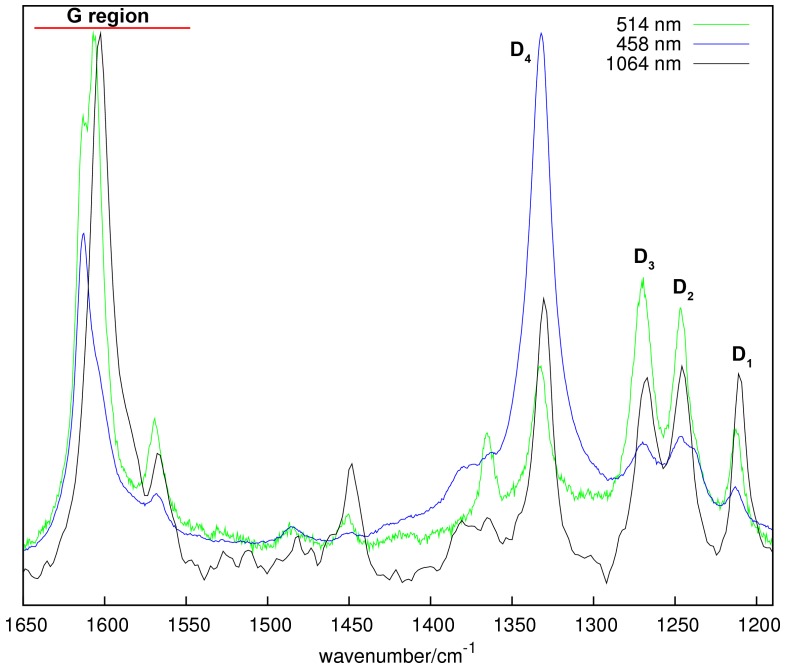

Figure 3.24: *D and G regions of the experimental Raman spectrum of* ***tetra-zigzag-HBC*** *excited with different laser lines.*

in the band deconvolution analysis reported in Figure 3.25.

As shown in Figure 3.25, based on peak deconvolution the spectra recorded with 457, 514, and 1064 nm laser excitations clearly reveal that the G band consists of four overlapped peaks centered at 1613, 1603, 1586, and 1568 cm^{-1}. Due to resonance effects, these lines also exhibit a systematic redistribution of the Raman intensities by changing the laser excitation energy. DFT calculations help rationalizing the presence of these peaks and foster their assignment after qualitatively considering the effects of anharmonicity. Considering a proper wavenumber scaling (which follows the popular scheme described by Merrick *et al.*[104]), the predicted position of the G_2 mode fits properly in between the two peaks observed at 1603 and 1586 cm^{-1}. On the other hand the scaled harmonic approximation based on DFT results accounts for the position of the observed G_1 and G_3 modes. Hence anharmonic effects suggest a resonance between the harmonically computed G_2 and a combination of modes (candidate observed lines could be $468 + 1128 cm^{-1}$). This explains the observed splitting of the G_2 harmonic feature. Within experimental error and band convolution uncertainty, the position of the G peak components is expected to be independent with respect to the laser excitation. Indeed, this is observed and it is due to the assignment of each G component to a specific molecular normal mode (whose wavenumber is not sensible to resonance effects). The assignment of the observed G features is shown in Figure 3.25 and Table 3.6. The computed nuclear displacement of the G_1, G_2 and G_3 modes have been reported in Figure 3.25.

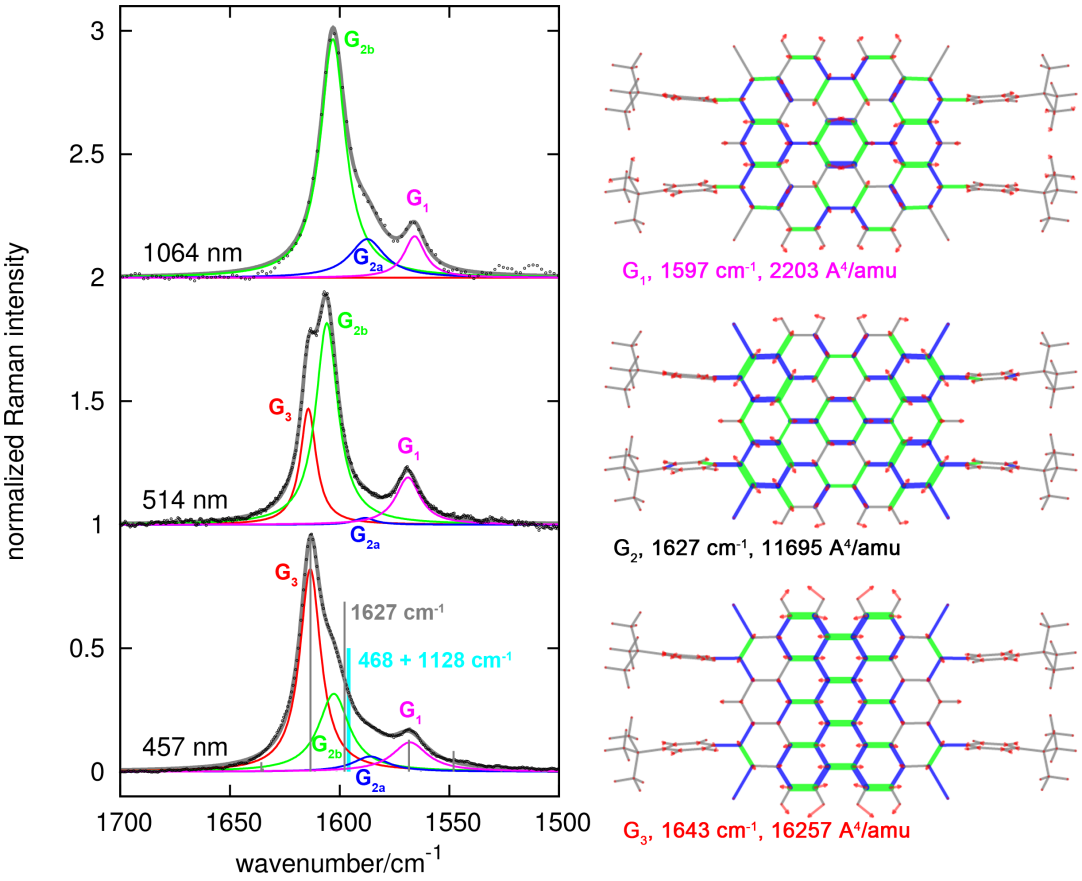

Figure 3.25: *Deconvolution of the G band in the Raman spectra of* ***tetra-zigzag-HBC*** *recorded with 457, 514, and 1064 nm laser excitations. The nuclear displacements of the related G modes computed by DFT are also displayed. The computed wavenumbers are reported unscaled. Red segments represent displacement vectors; CC bonds are represented as green (blue) lines of different thickness according to their relative stretching (shrinking).*

	DFT (unscaled, cm^{-1})	458 nm	514 nm	1064 nm
G_1	1597	1568	1568	1566
G_{2a}	1627	1586	1588	1587
G_{2b}		1603	1605	1603
G_3	1643	1613	1614	-

Table 3.6: *Deconvolution of the G band of* ***tetra-zigzag-HBC*** *recorded with 457, 514, and 1064 nm laser excitations; comparison with results from DFT calculations.*

3.4.3 IR spectroscopy

The FT-IR spectrum of a powder sample of **tetra-zigzag-HBC** was measured in a diamond anvil cell. This is compared with the simulation based on DFT calculations in Figure 3.26. With respect to Raman spectroscopy, which is mainly sensitive to the π-conjugated core of PAHs, it is easier to find markers of the edge structures by means of IR spectroscopy, since the mostly apolar core of PAHs usually provides weak IR signals.

The experimental IR spectrum nicely agrees with the simulated IR spectrum, which further supports the successful synthesis of the **tetra-zigzag-HBC** through

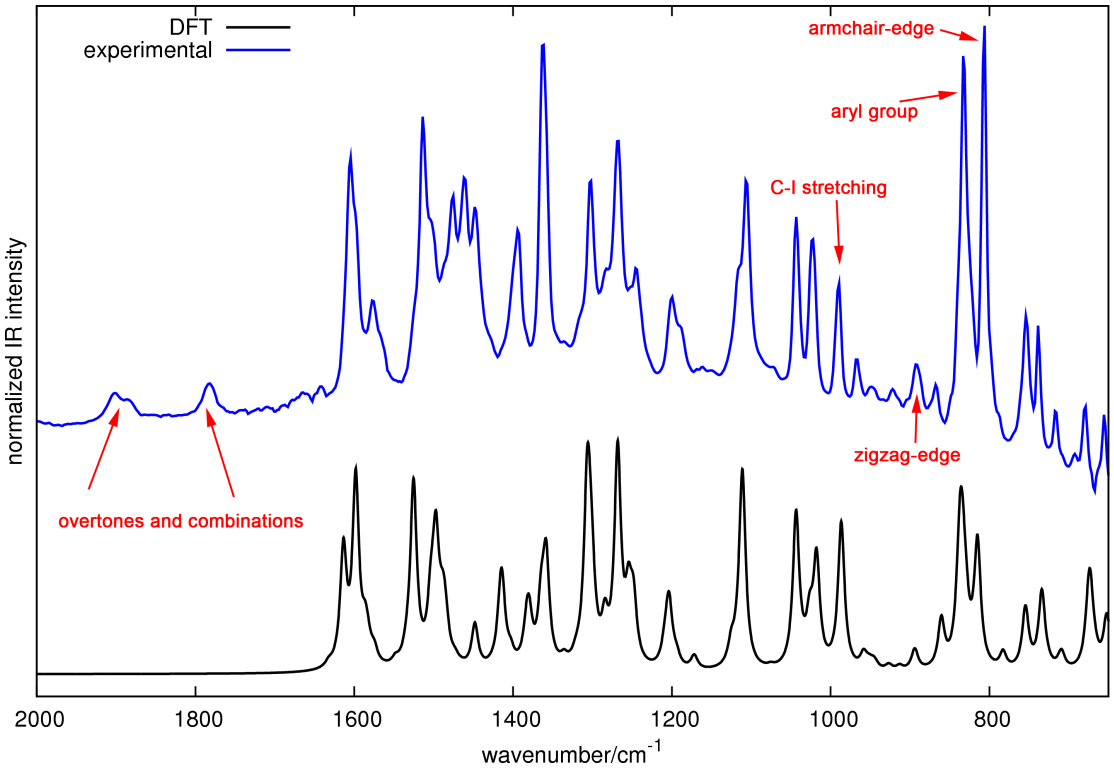

Figure 3.26: *Experimental FT-IR spectrum of* ***tetra-zigzag-HBC*** *compared with the simulation of the spectrum from DFT calculations. Several markers can be identified (see text).*

a series of characteristic edge-markers. In particular, the armchair-edge modes can be seen at a 807 cm^{-1} (unscaled DFT 832 cm^{-1}), while a peak with low intensity at 892 cm^{-1} (unscaled DFT 912 cm^{-1}) can be assigned to the characteristic zigzag-edge modes. The four aryl groups that functionalize two opposite sides of **tetra-zigzag-HBC** bring a CH-out-of-plane bending band at 832 cm^{-1}. Based on DFT calculations, five similar closely-spaced transitions should be attributed to this band; the most intense one is computed at 853 cm^{-1} (unscaled wavenumber). The C-I stretchings associated to the presence of the four iodine atoms are coupled to a collective CC stretching of the aromatic core, which produces a medium IR absorption band observed at 990 cm^{-1} (unscaled DFT 1007 cm^{-1}). In this normal mode the C-I stretching is obtained through the displacement of the carbon atoms while the much heavier iodine atoms are practically immobile. The iodine atoms are effectively displaced in correspondence of two very weak IR-active C-I stretching modes, which are computed at fairly low wavenumbers (unscaled DFT 142 cm^{-1} and 179 cm^{-1}). These modes fall outside the wavenumber range of the micro FT-IR instrumentation which has been used to carry out the experiments reported in this work. The nuclear displacement of all the IR modes described above can be examined in Figure 3.27. Finally, it is possible to observe some weak features in the experimental IR spectra around 1800 and 1900 cm^{-1}. These are absent in the simulated spectrum, which is based on the harmonic approximation. IR features of this sort are known to occur in several PAHs[105–108] and have been assigned to a manifold of overtones and combinations, thanks to recent quantum

chemical calculations beyond the harmonic approximation.[109]

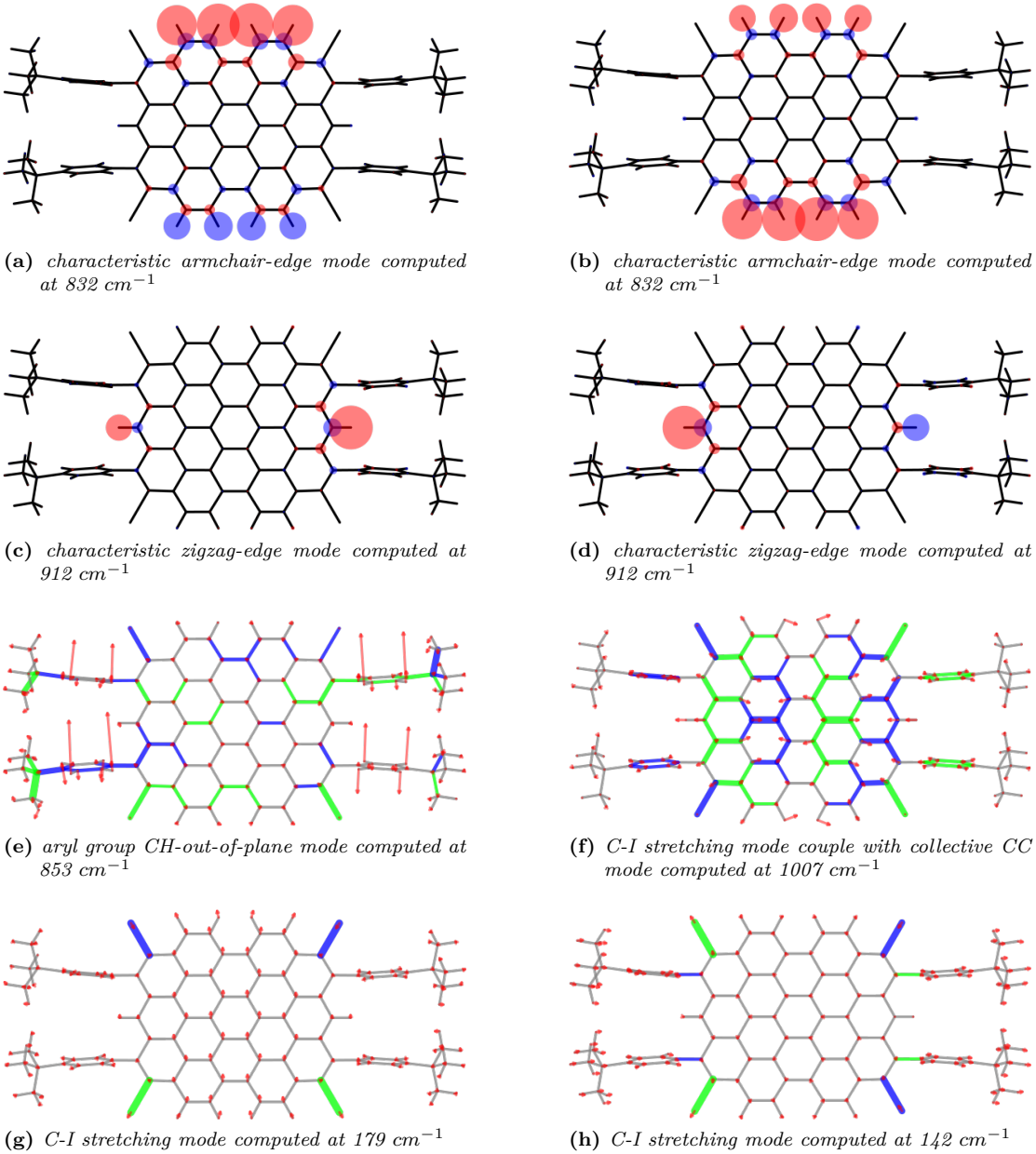

(a) *characteristic armchair-edge mode computed at 832 cm^{-1}*

(b) *characteristic armchair-edge mode computed at 832 cm^{-1}*

(c) *characteristic zigzag-edge mode computed at 912 cm^{-1}*

(d) *characteristic zigzag-edge mode computed at 912 cm^{-1}*

(e) *aryl group CH-out-of-plane mode computed at 853 cm^{-1}*

(f) *C-I stretching mode couple with collective CC mode computed at 1007 cm^{-1}*

(g) *C-I stretching mode computed at 179 cm^{-1}*

(h) *C-I stretching mode computed at 142 cm^{-1}*

Figure 3.27: *Nuclear displacement of characteristic IR modes of **tetra-zigzag-HBC** computed by DFT. Red segments represent displacement vectors; CC and C-I bonds are represented as green (blue) lines of different thickness according to their relative stretching (shrinking). For out-of-plane modes the size of blue/red circles of the molecular sketch is proportional to nuclear displacements in the out-of-plane direction (z); red indicates displacements directed along $+z$ and blue indicates displacements directed along $-z$.*

3.5 Graphene nanoribbons with partially zigzag edge structures

In this section, we report the results of the Raman and IR characterization of a new kind of graphene nanoribbon M_P with a hybrid edge structure formed by zigzag and gulf sections (see Figure 3.28). The chemical synthesis and further characterization of this graphene nanoribbon are described by Yang *et al.*[110] M_P can serve as the first step toward the fabrication of fully zigzag GNRs, which are expected to display an appealing electronic structure characterized by unpaired spin at the zigzag edge.[111–113] The M_P samples have been obtained with an estimated average length larger than 100 nm. DFT calculations have shown the presence of a band gap of the order of 1.5 eV for this narrow (1 nm) partially zigzag edged GNR, which makes it a semi-conducting system useful for photovoltaics.[98] Two model PAHs related to M_P have been investigated as well by IR and Raman spectroscopy, namely M_0 and M_1 (Figure 3.28). They correspond to short segments of M_P; the details about their chemical synthesis are given by Yang *et al.*[110] These model compounds are also relevant because they extend the field of available PAHs possessing zigzag edge structures. Their Raman and IR investigation, fostered by DFT modeling, revealed specific vibrational transitions attributable to their specific chemical structures, with useful edge markers available in their IR spectra.

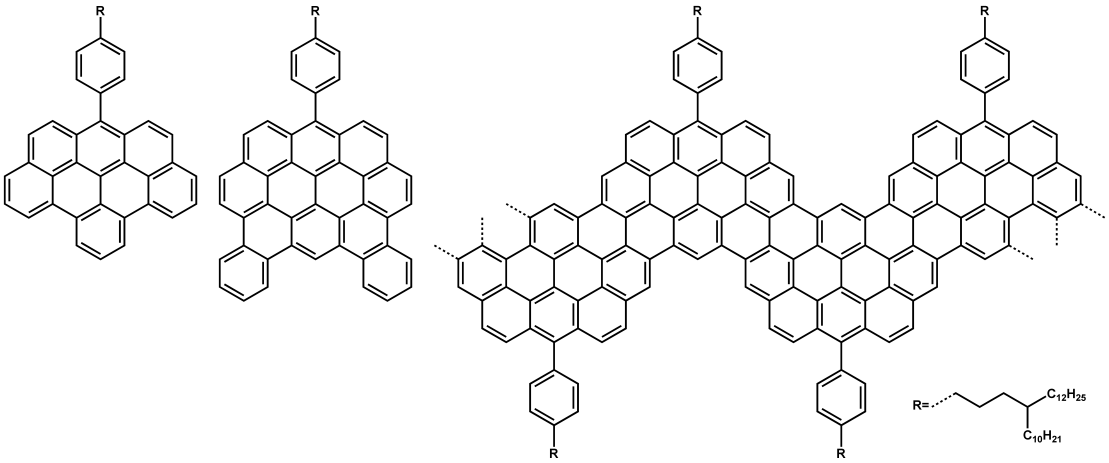

(a) M_0 **(b)** M_1 **(c)** M_P

Figure 3.28: *Chemical structure of the graphene molecules M_0, M_1 and of the related GNR M_P.*

3.5.1 Raman spectroscopy

As already mentioned elsewhere in this work, the Raman spectra of PAHs and GNRs are dominated by characteristic features associated to collective CC stretching vibrations of the honeycomb structure (G, D lines).[1,11,12] As expected (Figure 3.29), the Raman spectra of M_0 and M_1 are characterized by these characteristic signals. As reported in Figures 3.29,3.30 and 3.31 DFT calculations allow the identification of all minor features, which involve different normal modes re-

lated with collective breathing modes (D features) and ring stretching modes (G features). As it has been observed for other PAHs,[1,11] the multiplicity of D and G signals is a typical feature caused by the coupling of the characteristic collective CC stretching coordinates with the in-plane CH bending vibrations at the edge of the molecule.[62] Even if it is difficult to identify specific edge markers (at difference with IR spectroscopy, see Section 3.4.3 and 3.5.2), it is clear from the comparison of the Raman spectra of M_0 and M_1 that the manifold of peaks in the G and D region, as a whole, is a reliable fingerprint of the molecular structure. DFT calculations provide simulated Raman spectra of M_0 and M_1 which nicely correlate with observation (Figure 3.29). Inspection of the normal modes associated with the intense Raman peaks shows the expected nuclear displacements for G and D modes (see Figures 3.30 and 3.31).

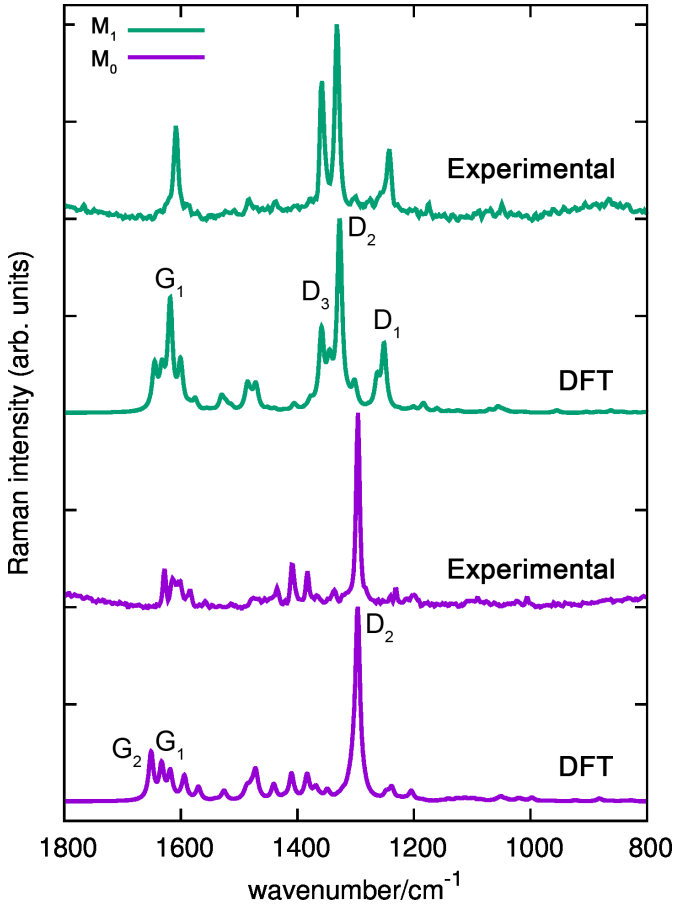

Figure 3.29: *Simulated and experimental FT-Raman spectra of M_0 and M_1 (1064 nm excitation).*

The experimental Raman spectrum of the M_P is reported in Figure 3.32. It displays the expected G and D features, in addition to their overtones and combinations (2D, G+D, 2G). As it is possible to observe obviously in Figure 3.32, the intensity pattern of the 2D and 2G signals rather closely follows that of their corresponding fundamentals, D and G signals, respectively. The theoretical explanation for this behavior is same as the one that reported in the Section 3.2, where

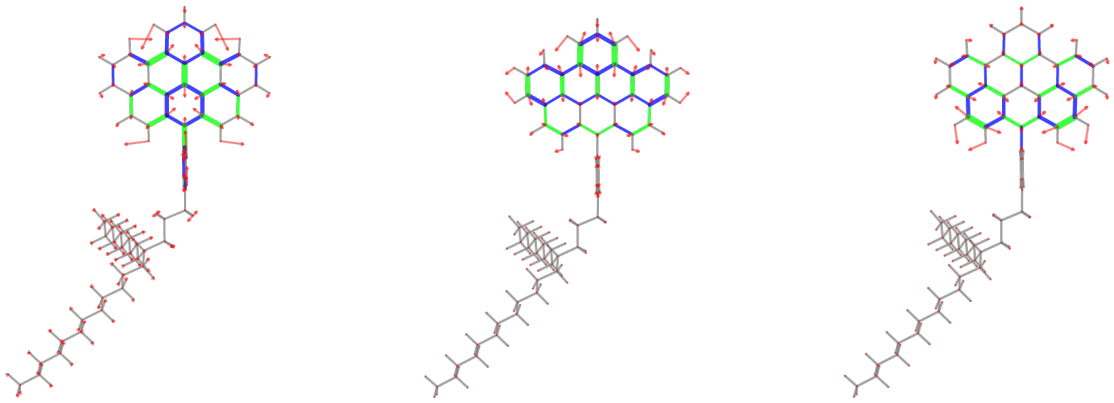

(a) *D_2, 1323 cm^{-1}, 1800 A^4/amu*

(b) *G_1, 1651 cm^{-1}, 286 A^4/amu*

(c) *G_2, 1685 cm^{-1}, 505 A^4/amu*

Figure 3.30: *Nuclear displacement of selected G and D modes of M_0 based on DFT calculations (see also Figure 3.29). Red segments represent displacement vectors; CC bonds are represented as green (blue) lines of different thickness according to their relative stretching (shrinking).*

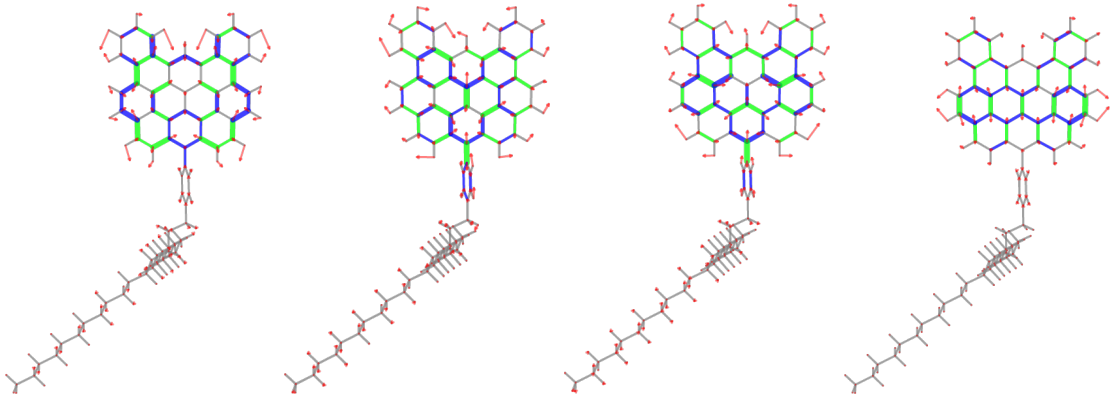

(a) *D_1, 1277 cm^{-1}, 1245 A^4/amu*

(b) *D_2, 1354 cm^{-1}, 3384 A^4/amu*

(c) *D_3, 1387 cm^{-1}, 977 A^4/amu*

(d) *G_1, 1651 cm^{-1}, 2048 A^4/amu*

Figure 3.31: *Nuclear displacement of selected G and D modes of M_1 based on DFT calculations (see also Figure 3.29). Red segments represent displacement vectors; CC bonds are represented as green (blue) lines of different thickness according to their relative stretching (shrinking).*

it was observed for **C78** investigated with multi-wavelength Raman spectroscopy.

3.5.2 IR spectroscopy

The IR signals of PAHs in the CH out-of-plane (opla) bending region (980 – 650 cm^{-1} range) are informative of the molecular structure and edge topology.[99] It is therefore interesting to examine the IR spectra of these compounds and assign the observed spectral features to collective CH-opla vibrations with the help of DFT calculations. The results are reported in Figure 3.33 and compared with the experimental IR spectra recorded on powder samples. The comparison

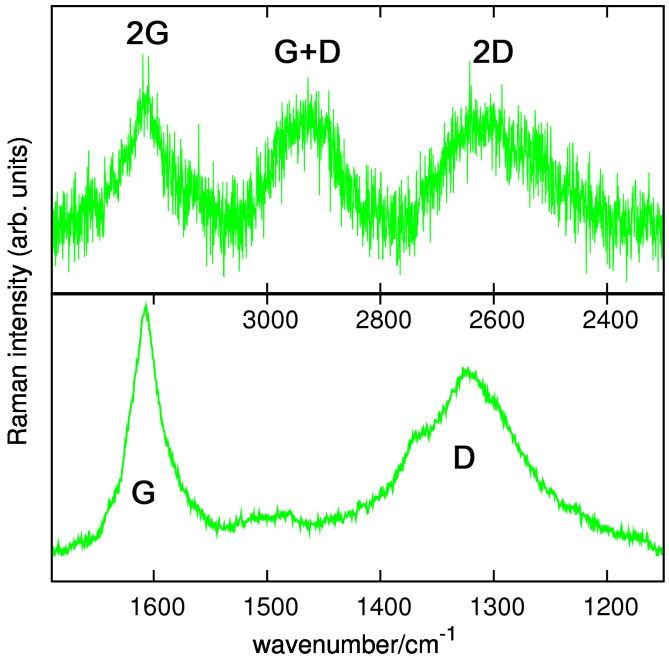

Figure 3.32: *First- and second-order experimental Raman spectrum of M_P excited with the 514 nm laser line.*

between theory and experiment is fair, with a better agreement shown by the calculations on monomers (M_0, M_1). Deviations between theory and experiment are presumably due to the isolated molecule approximation adopted and to the role of intermolecular interactions in the solid state. Moreover, the presence of alkyl substituents could play a role through contributions arising from the vast manifold of possible conformers that have not been included in our analysis. In fact, to focus on the CH-opla markers and limit the computational cost, the models just consider fully trans-planar conformations of the substituents (see Figure 3.34 for their graphical representation).

The a_1 IR feature of M_0 is assigned to the rocking modes of the alkyl chains; b_1 is the rocking mode in M_1. The theoretical counterpart of the c_2 feature of the polymer is the result of the overlap of rocking modes and in-plane CCC deformation modes. This is due to the short alkyl chains adopted in the polymer model that lead to weak simulated intensities of the rocking modes. Interestingly, the c_1 feature of the polymer is associated to another collective in-plane CCC deformation mode with a rather complex pattern. The c_3 IR band of the polymer provides the most characteristic fingerprint signal of its cove topology.

The remaining features labeled in the IR spectra of Figure 3.33 are all due to opla vibrations of CH bonds. With the exception of the weak a_5 feature, assigned to the lateral phenyl substitution, these IR signals (i.e., a_2, a'_3, $a"_3$, a_4, a_6 in M_0 and b_2, b_3 in M_1) are characteristic of the topology of the molecular edges.

Adopting the mode naming also described in,[99] based on the pattern of the normal modes, the b_2 signal in M_1 can be described as QUATRO and b_3 as DUO. The a_2 and a'_3 features of M_0 can be described as TRIO and a_4 as DUO. The remaining two modes ($a"_3$, a_6) have a more complex pattern of in-phase/out-of-phase

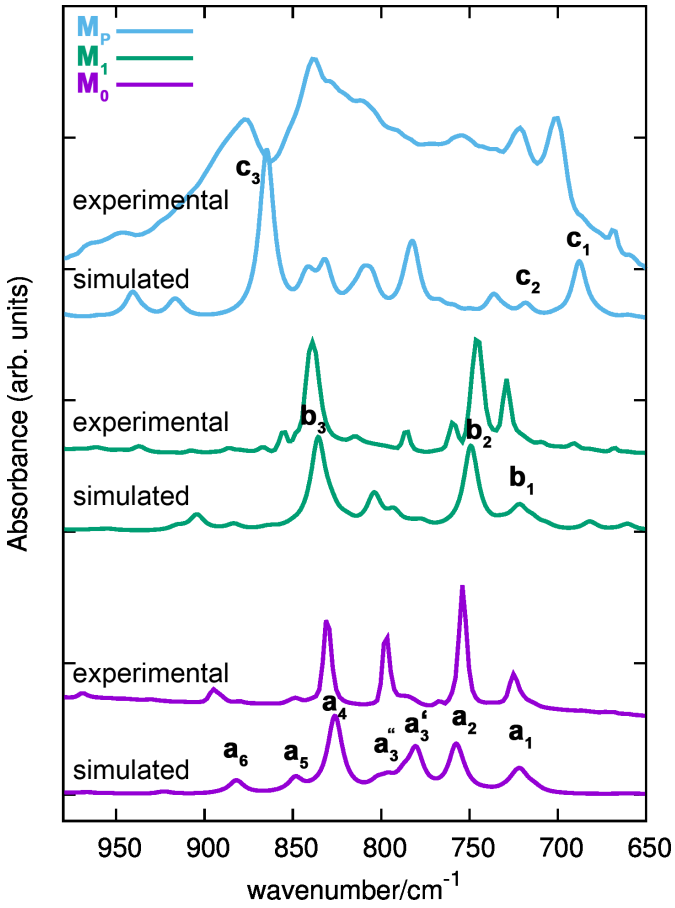

Figure 3.33: *Simulated and experimental IR spectra of M_0, M_1 and M_P in the CH out-of-plane bending fingerprint region.*

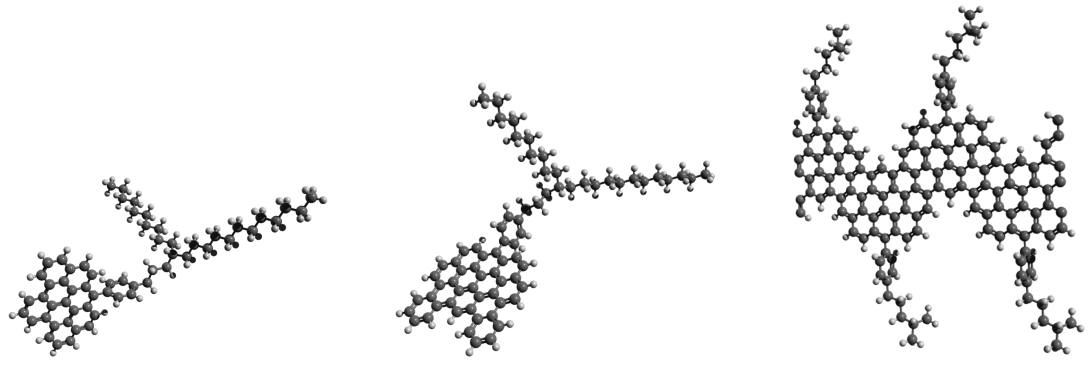

(a) M_0 **(b)** M_1 **(c)** M_P

Figure 3.34: *The molecular models of M_0, M_1 and M_P which have been adopted for the DFT calculations of IR and Raman data. The models just consider fully trans-planar conformations of the substituents.*

CH-opla contributions. See Figures 3.35, 3.36 and 3.37 for nuclear displacement of selected IR modes.

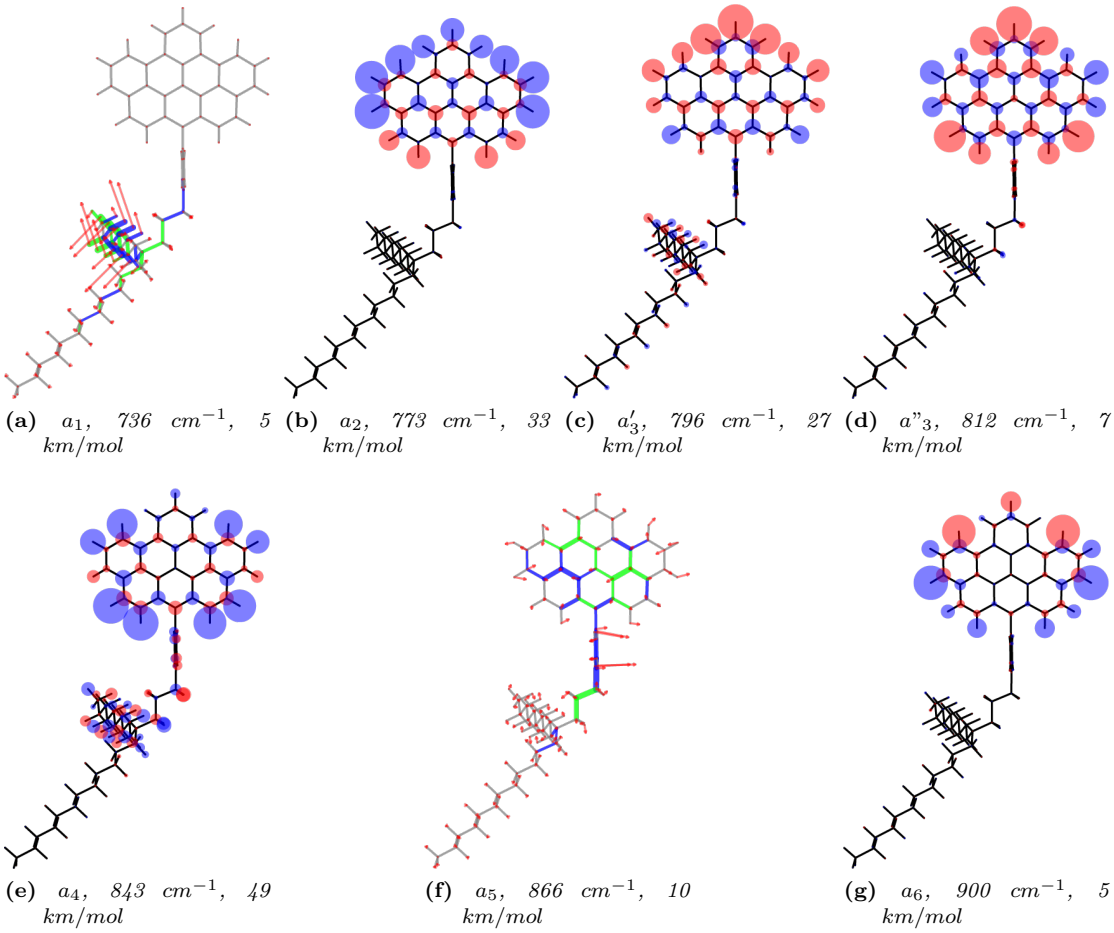

(a) a_1, *736* cm^{-1}, *5* km/mol **(b)** a_2, *773* cm^{-1}, *33* km/mol **(c)** a'_3, *796* cm^{-1}, *27* km/mol **(d)** $a"_3$, *812* cm^{-1}, *7* km/mol

(e) a_4, *843* cm^{-1}, *49* km/mol **(f)** a_5, *866* cm^{-1}, *10* km/mol **(g)** a_6, *900* cm^{-1}, *5* km/mol

Figure 3.35: *Nuclear displacement of selected IR modes of M_0 based on DFT calculations (see also Figure 3.33). Red segments represent displacement vectors; CC bonds are represented as green (blue) lines of different thickness according to their relative stretching (shrinking). For out-of-plane modes the size of blue/red circles of the molecular sketch is proportional to nuclear displacements in the out-of-plane direction (z); red indicates displacements directed along $+z$ and blue indicates displacements directed along $-z$.*

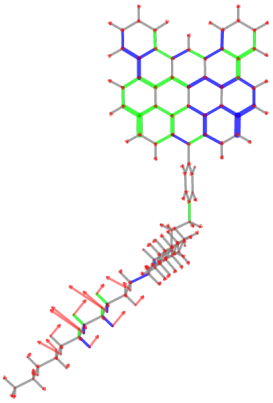

(a) b_1, *736* cm^{-1}, *6* km/mol

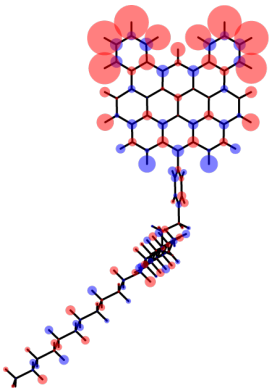

(b) b_2, *765* cm^{-1}, *55* km/mol

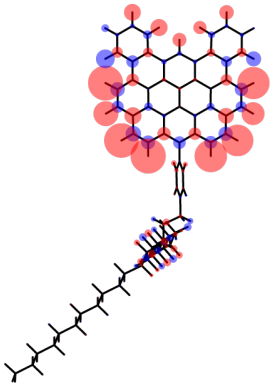

(c) b_3, *853* cm^{-1}, *68* km/mol

Figure 3.36: *Nuclear displacement of selected IR modes of* M_1 *based on DFT calculations (see also Figure 3.33). Red segments represent displacement vectors; CC bonds are represented as green (blue) lines of different thickness according to their relative stretching (shrinking). For out-of-plane modes the size of blue/red circles of the molecular sketch is proportional to nuclear displacements in the out-of-plane direction (z); red indicates displacements directed along* $+z$ *and blue indicates displacements directed along* $-z$.

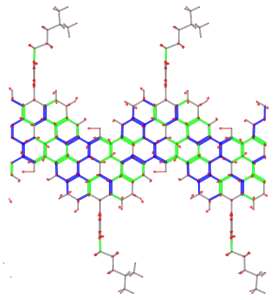

(a) c_1, *702* cm^{-1}, *34* km/mol

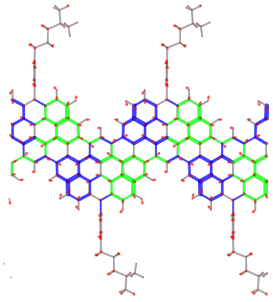

(b) c_2, *733* cm^{-1}, *8* km/mol

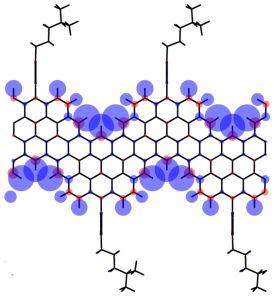

(c) c_3, *882* cm^{-1}, *98* km/mol

Figure 3.37: *Nuclear displacement of selected IR modes of* M_P *based on DFT calculations (see also Figure 3.33). Red segments represent displacement vectors; CC bonds are represented as green (blue) lines of different thickness according to their relative stretching (shrinking). For out-of-plane modes the size of blue/red circles of the molecular sketch is proportional to nuclear displacements in the out-of-plane direction (z); red indicates displacements directed along* $+z$ *and blue indicates displacements directed along* $-z$.

CHAPTER 4

Chlorinated graphene molecules

In this chapter the molecular structure and vibrational properties of perchlorinated hexa-*peri*-hexabenzocoronene (**HBC-Cl**) will be investigated by Density Functional Theory (DFT) calculations, IR and Raman spectroscopy. The results will be compared with those obtained for the parent molecule hexabenzocoronene (**HBC**) one of the most promising graphene molecules suitable for molecular electronics, since it is known to form by π-stacking self-assembled columnar arrays, characterized by useful electron-transport properties.[114] The molecular structure and vibrational properties of another pair of large graphene molecules with D_{3h} symmetry are also reported in this Chapter, namely $C_{96}H_{30}$ (**C96**), and the chlorinated analogue $C_{96}H_3Cl_{27}$ (**C96-Cl**) – see Figure 4.1 for the representation of their chemical structures. The assignment of several IR and Raman transition was made robust by the very good agreement observed between the experimental vibrational spectra and the associated DFT simulations. Compared with the

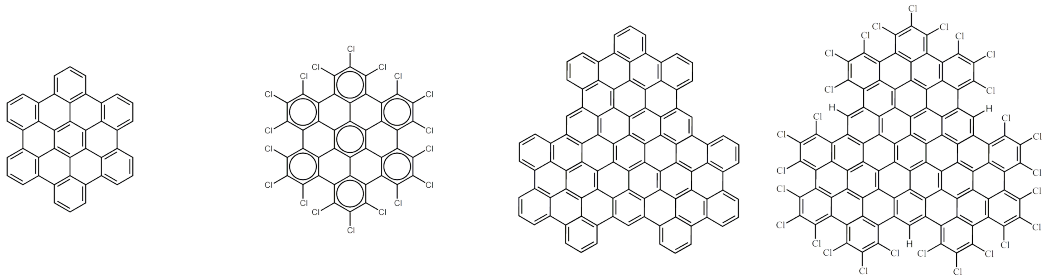

(a) ***HBC*** **(b)** ***HBC-Cl*** **(c)** ***C96*** **(d)** ***C96-Cl***

Figure 4.1: *Representation of the chemical structures of* ***HBC***, ***HBC-Cl***, ***C96*** *and* ***C96-Cl****.*

parent **HBC** or **C96**, the edge chlorination significantly alters the planarity of the molecules. Nevertheless, as discussed below based on DFT calculations and Raman observations, this structural distortion does not significantly impair the inherent π-conjugation of these graphene molecules.

Perchlorination of graphene molecules (that are effective models of finite graphene domains[44,45]) has been recently developed as a convenient way not only to modulate the optical properties, but also to improve the solubility of such disk-shaped molecules.[23] Solubility is a technology-enabling key concept in view of the use of such π-conjugated molecules in real devices. The mechanism responsible for the enhancement of the solubility in perchlorinated graphene molecules was identified as an evident structural distortion of the molecules driven by steric hindrance of the chlorine atoms at the molecular edges.[23] This structural effect was shown to interfere with the well-known π-stacking propensity of such large PAHs, hence boosting their solubility.[23]

HBC is one of the prototypical PAHs that are able to form columnar arrays in discotic liquid crystals,,[115] which constitute relevant supramolecular architectures appealing for applications in molecular electronics.[31,114]

The packing of **HBC-Cl** in its crystalline form clearly reveals the presence of cofacial dimers,[23] with properly interlocked orientation due to the accommodation of the out-of-plane deviations of the aromatic core of the molecule. This kind of interaction geometry is not merely the result of packing effects in the crystalline phase. DFT calculations on the isolated dimer of **HBC-Cl** straightforwardly account for this kind of molecular arrangement as shown in Figure 4.2. Hence the cofacial self-assembly of **HBC-Cl** is essentially driven by interactions at the intermolecular level. The dimer shown in Figure 4.2 can be also used as a model to evaluate the transfer integral (electronic coupling t),[116] which is one of relevant physical parameters at the basis of the appealing charge transport properties of graphene molecules, and determines their suitability for molecular electronics.[114]

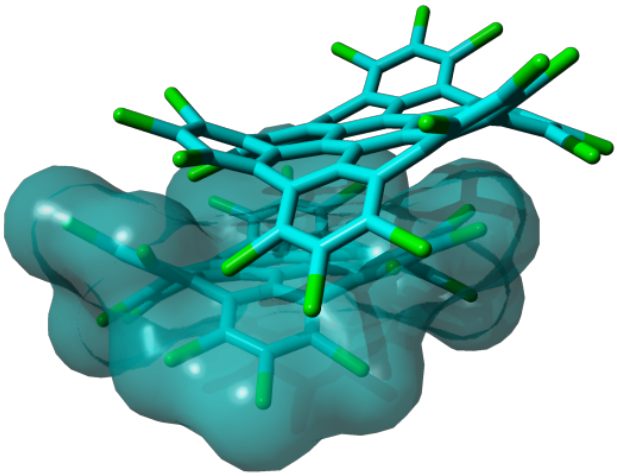

Figure 4.2: *Representation of a π stacked dimer of **HBC-Cl** obtained from geometry optimization with DFT methods including Grimme's dispersion (B3LYP/6-31G(d,p) GD3BJ).[22] This structure matches the one determined by X-ray diffraction.[23]*

An approximate t value can be easily obtained in the framework of the so called Energy-Splitting-in Dimer Method.[116] It considers how the doubly degenerate HOMO and LUMO levels of isolated **HBC-Cl** split and spread into the four occupied and four unoccupied frontier orbitals of the dimer. By evaluating half the energy bandwidth over which the four occupied (unoccupied) levels of the dimer spread out one gets $t = 0.04$ eV for holes ($t = 0.03$ eV for electrons). Interestingly, these values fall in lower limit of the expected range found in other graphene molecules with planar molecular shapes.[114] This shows that perchlorination and the non-planarity of the molecule are not spoiling the charge transport properties: by proper tuning of the relative molecular disposition and design of the chlorination pattern one could possibly enhance the value of t, which is known to dramatically depend on even small changes of the relative orientation angle and relative sliding of the aromatic cores.[114,116]

4.1 Assessment of the molecular structure of HBC-Cl and C96-Cl by DFT

The annotated chemical structure of **HBC-Cl** is shown in Figure 4.3. While the parent HBC is a planar π-conjugated system,[117] substitution with chlorine atoms at the edge introduces significant steric hindrance at the bay positions such as 1-18 (see Figure 4.3). For this reason the equilibrium structure of **HBC-Cl** significantly deviates from planarity in order to increase the Cl-Cl distances at 1-18 and other bay positions (*e.g.*, 3-4). On the other hand, because of the larger Cl-Cl distances involving the substitutions at positions 1, 2 and 3, we may practically consider co-planarization of the three chlorine atoms (1, 2, 3) together with the carbon atoms to which they are bonded. This is a first approximation useful to simplify the notation for describing the possible out-of-plane conformations.

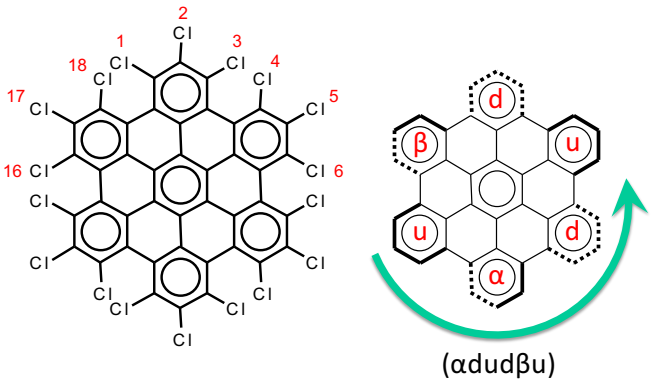

Figure 4.3: *Left panel: the molecular structure of HBC-Cl. Right panel: the notation scheme for the possible out-of-plane conformations at the chlorinated edge (see text for details).*

Depending on the position of a given edge aryl moiety with respect to the average molecular plane, we may have four possible conditions, which are exemplified in Figure 4.3:

- up (or down) if the aryl moiety lies above (or below) the plane;
- α (or β) if the aryl moiety lies in a propeller blade fashion, with α being related with P-helicity.

Because of steric hindrance (see Figure 4.3) the conformation sequences can not contain pairs such uu, dd, $\alpha\beta$, $\beta\alpha$, $u\beta$, $d\alpha$, αu, and βd. The exhaustive enumeration of all possible combinations satisfying this prescription, considering the equivalence between enantiomeric pairs, leads to the eight conformers listed in Table 4.1. These conformers have been considered for geometry optimization with DFT method in order to obtain information on their relative energies, which are also reported in Table 4.1.

#	**description**	**short form**	S **energy**	**group**	
1	$(ududud)$	$(ud)_3$	12	0.0	D_{3d}
2	$(u\alpha du\alpha d)$	$(u\alpha d)_2$	8	4.6	D_2
3	$(udu\alpha d\beta)$	–	8	6.5	C_s
4	$(\alpha dudu\alpha)$	$\alpha_2(du)_2$	8	8.9	C_2
5	$(\alpha\alpha\alpha\alpha du)$	$(\alpha_4 du)$	4	17.3	C_2
6	$(\alpha\alpha\alpha d\beta u)$	$(\alpha_3 d\beta u)$	4	19.1	C_2
7	$(\alpha\alpha d\beta\beta u)$	$(\alpha_2 d\beta_2 u)$	4	22.8	C_{2h}
8	$(\alpha\alpha\alpha\alpha\alpha\alpha)$	(α_6)	0	28.2	D_6

Table 4.1: *The description of the eight conformers of HBC-Cl and their relative energies (kcal/mol) as determined by DFT calculations.*

When α or β symbols are present in the structure, it is possible to have enantiomeric pairs. For the sake of compactness, for each enantiomeric pair in Table 4.1 we report the representative with a number of α symbols greater than the number of β symbols (this does not apply to conformers #3 and #7 which have the same number of α and β symbols). Obviously the conformation symbols can be cyclically permuted without changing the nature of the conformation. They can be also subjected to mirror symmetry with respect to the average molecular plane, *i.e.* $\alpha \to \beta$, $u \to d$, and so on. This operation exchanges with one another the members of one enantiomeric pair, which of course possess the same relative energy. Hence the conformation shown in Figure 4.3, namely $(\alpha dud\beta u)$, by cyclic permutation can be transformed to $(dud\beta u\alpha)$ and by mirror symmetry is transformed to $(udu\alpha d\beta)$, which corresponds to conformer #3 in Table 4.1.

Interestingly, the most stable conformation of **HBC-Cl** corresponds to the only one non-chiral conformation. This is $(ududud) \equiv (ud)_3$, which belongs to point group symmetry D_{3d} (see Figure 4.4 and 4.5). On the contrary (α_6), the conformation with more extensive chirality (point group symmetry D_6), is predicted to be the one with highest relative energy.

Inspection of the relative energies of **HBC-Cl** conformations reported in Table 4.1 reveals an approximate correlation of their stability with the molecular structure at the edge, as described by the conformation symbol. We can introduce a score number S defined as follows:

$$S = s_1 N_1 + s_2 N_2 + s_3 N_3 \tag{4.1}$$

where N_1 represents the number of ud (or du) sequences along the conformation string, considered in a cyclic manner, so that $N_1 = 6$ for $(ud)_3$. Similarly, N_2 represents the total number of $u\alpha$, αd, $d\beta$, βu sequences along the string and N_3 is the total number of $\alpha\alpha$, $\beta\beta$ sequences along the string. s_1, s_2, s_3 are suitable

numerical coefficients which weight the different stability of the possible local edge conformation. The choice made in Table 4.1 simply assumes $s_1 = 2$, $s_2 = 1$ and $s_3 = 0$, so that higher scores are associated to higher molecular stabilities. This effectively allows highlighting in Table 4.1 clusters of conformations characterized by similar energies and the same score number S.

After the evaluation of the stable conformations of **HBC-Cl** by means of the analysis of the DFT results, we can conclude that the most stable structure is fully consistent with experimental observation by X-ray diffraction, which clearly reveals $(ud)_3$ as the unique structure of **HBC-Cl** in crystal phase.[23] This is expected based on the relatively large energy separation (4.6 $kcal/mol$) of $(ud)_3$ with the second most stable conformer, $(u\alpha d)_2$.

We can conclude on this basis that the packing motif observed in the crystal simultaneously minimizes the intramolecular (conformational) energy and allows an effective intermolecular packing in the dimer.

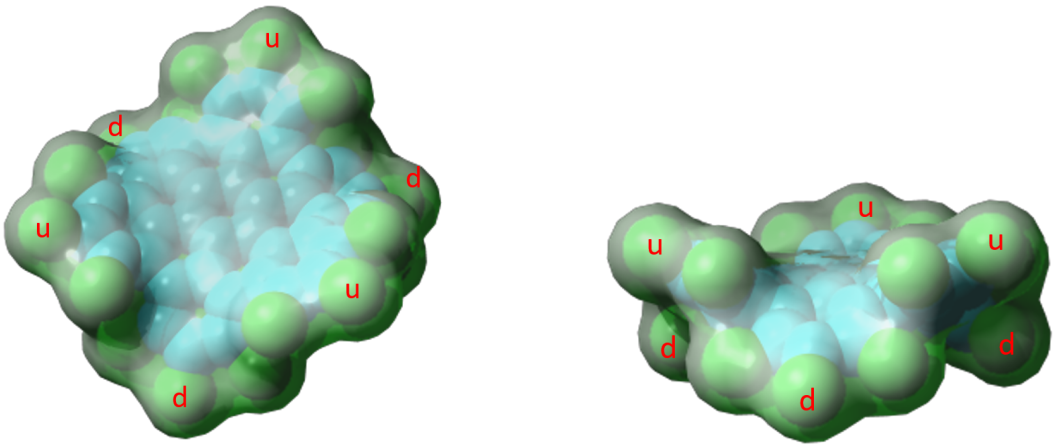

(a) *top view* **(b)** *side view*

Figure 4.4: *Three-dimensional representation of* $(ud)_3$*, the most stable conformer of HBC-Cl. The model represents the equilibrium structure obtained from DFT calculations.*

Functionalisation of **HBC** with Cl at the molecular edge drives the molecule out of planarity, with a rich possibility of conformations, even though $(ud)_3$ is markedly more stable than all the others (see Table 4.1). In principle out-of-plane distortions could negatively affect π-conjugation. Notably this is observed in π-conjugated polymers possessing torsional degrees of freedom able to affect the nearest neighbor π-interactions.[118]

Hence, to dwell more into the effects of distortion out of planarity, we have considered a molecular model with the same conformation of the aromatic core as in $(ud)_3$, but with a hydrogen-terminated molecular edge (the hydrogen positions have been fully optimized while keeping the position of the carbon atoms frozen at the positions they have in perchlorinated $(ud)_3$). For simplicity we name this model **HBC***. In addition to this model, we consider also **HBC**†, which is obtained starting from the structure of **HBC*** and fully optimizing all internal coordinates except dihedral angles. This effectively allows to maintain the char-

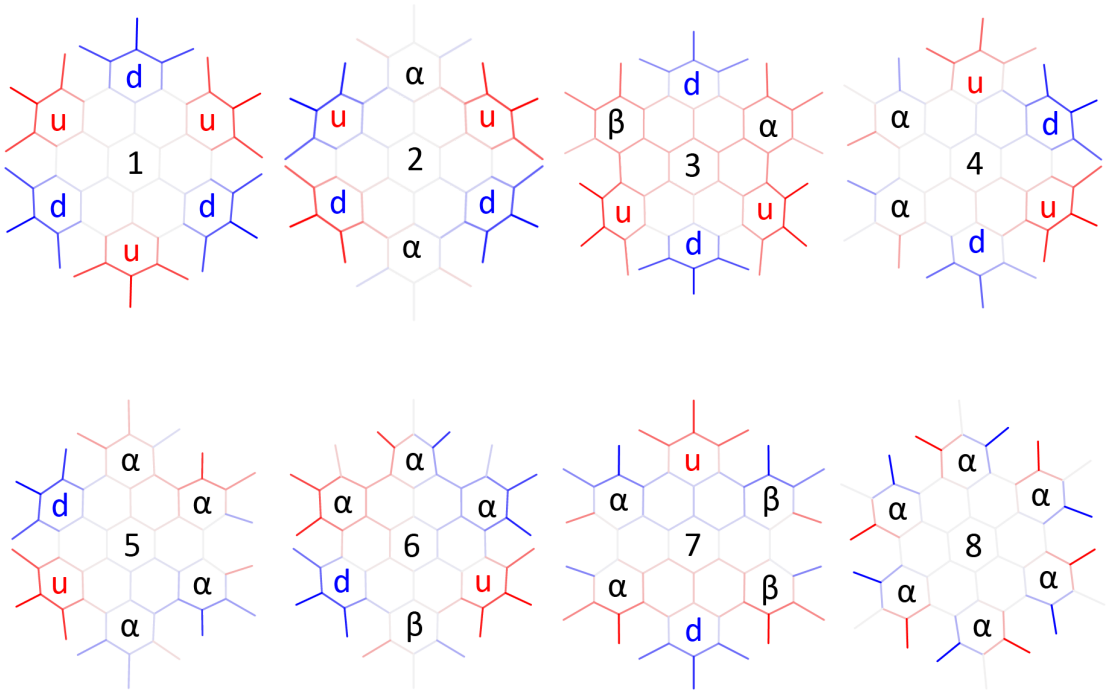

Figure 4.5: *Orthogonal projection of the eight conformations of HBC-Cl where the out-of-plane z-coordinate of the middle point of each bond is coded in shades of red ($z > 0$) and blue ($z < 0$). In-plane bonds are coded with light gray shade.*

acteristic curved shape found in $(ud)_3$, while fully relaxing the bond lengths and valence angles. The energy difference ΔE between the total energy of **HBC***, **HBC**† and **HBC** (see Table 4.2) is a measure of the energy cost associated to the distorsion of the aromatic core out of planarity. By considering the number of π-conjugated carbon atoms in the **HBC** analogues (42) this results in about 1.3 $kcal/mol$ per carbon, a rather limited value which explains the good stability of the compound despite its seeming dramatic distortion out of planarity.

	HBC	**HBC**†	**HBC***	**HBC-Cl** $(ud)_3$
$\Delta E(kcal/mol)$	0	53	54	–
HOMO (hartree)	-0.1929	-0.1898	-0.1897	-0.2316
LUMO (hartree)	-0.061	-0.0618	-0.0626	-0.115
Δ_{HL} **(hartree)**	0.132	0.128	0.127	0.117
λ_{max} **(nm)**	357	372	375	415
$\Delta\lambda$ **(nm)**	0	15	18	58

Table 4.2: *Comparison of the relative positions of frontier orbitals (HOMO, LUMO) and of the lowest lying bright excited state (absorption maximum λ_{max}) in planar **HBC**, distorted **HBC***, **HBC**† and **HBC-Cl** in its more stable conformation. ΔE is the energy difference between the non-planar models **HBC*** and **HBC**† and planar **HBC**.*

Turning now to the electronic properties, we observe in Table 4.2 that along the sequence **HBC**, **HBC***, **HBC**† the position of the frontier orbitals does not change dramatically, which enforces the idea that π-conjugation is not seriously

affected by the distortion of **HBC** out of planarity. On the other hand perchlorination causes the decrease of the position of the frontier orbitals, as expected from an electron-withdrawing substitution. We notice that, compared to **HBC***, in **HBC-Cl** the position of the HOMO (decrease by 0.04 ha) is relatively less affected than the position of the LUMO (decrease by 0.05 ha), which explains the slight decrease of the HOMO-LUMO gap in **HBC-Cl**. Following the trend of the position and spacing between the frontier orbitals, according to TDDFT calculations the low-lying doubly degenerate bright state red shifts from 3.47 eV (357 nm) in **HBC** to 2.98 eV (415 nm) in **HBC-Cl**, while the total oscillator strength of the doublet slightly increases from $f = 1.44$ to $f = 1.54$, respectively.

Interestingly, as shown in Figure 4.6, perchlorination slightly affects the CC bond lengths, without altering the basic pattern based on the Clar structure formed by seven aromatic sextets.[35,119] In particular, by referring to the label scheme proposed in Figure 4.6 we notice that upon perchlorination the inner bonds d, e, f becomes shorted, while the outer bonds a, b, c become longer.

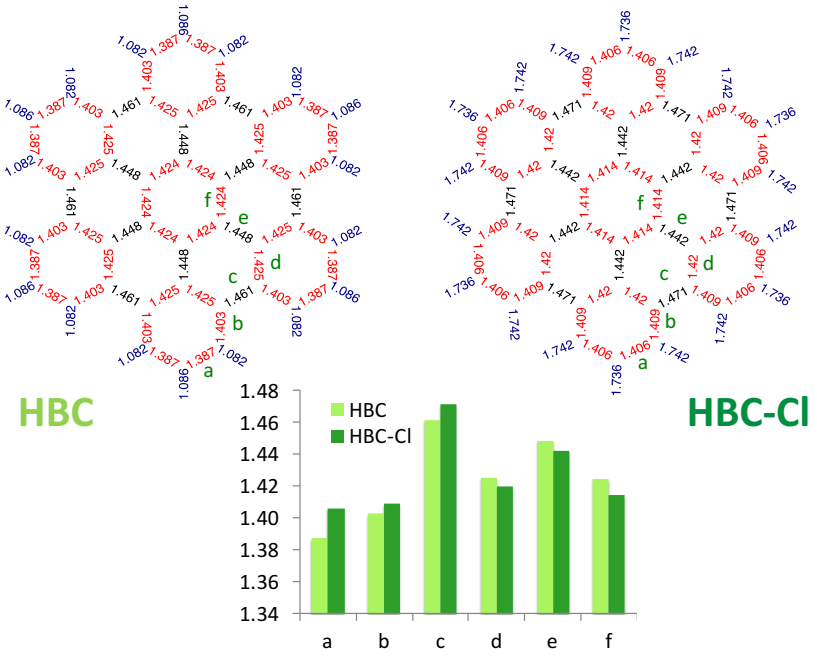

Figure 4.6: *Comparison of the equilibrium bond lengths in **HBC** and **HBC-Cl** ($(ud)_3$ conformer) computed with DFT.*

Finally, it is worth mentioning that interesting non-planar structures have been reported for fluorinated PAHs based on a coronene core.[120] These structures are distorted to a degree similar to the case of **HBC-Cl** here investigated.

4.1.1 C96-Cl

With respect to **HBC-Cl**, the case of **C96-Cl** potentially offers a richer conformational landscape. This is due to the larger number of chlorinated aryl moieties, namely 9 *vs.* 6 (see Figure 4.7). Hence the potential number of conformers in **C96-Cl** is $4^9 = 262144$ *vs.* $4^6 = 4096$ in **HBC-Cl**. However, by taking into

account steric hindrance restrictions and equivalence between enantiomeric pairs, these figures drop to 52 in **C96-Cl** (Table 4.3) and 8 in **HBC-Cl** (Table 4.1).

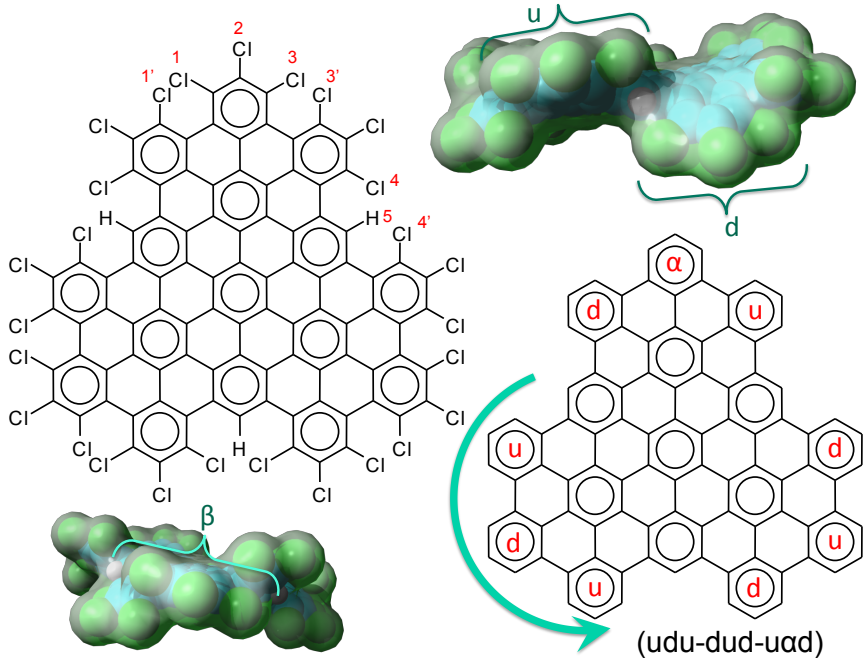

Figure 4.7: *Left panel: the molecular structure of **C96-Cl**. Right panel: the notation scheme for the possible out-of-plane conformations at the chlorinated edge. The reported three dimensional models are meant to help clarify the steric hindrance at the molecular edge through selected u, d and β local conformations.*

Furthermore the odd number of "blades" of **C96-Cl** (*i.e.*, its threefold structure) hinders the possibility of establishing the theoretically minimum energy conformation, which is expected to contain just alternated u,d symbols: for instance, the conformation with symbol ($udududududu$) establishes a contact between two u symbols (head and tail), leading to large steric hindrance. For this reason at least one α (or β) term is needed in the conformation string, which leads to the top two conformations with largest score reported in Table 4.3 (see Figure 4.8). Interestingly, because of the frustration of the conformation composed by just u and d, the minimum energy conformer of **C96-Cl** is chiral, at difference from the case of **HBC-Cl**.

4.2 IR spectroscopy of HBC-Cl and HBC

IR spectra of both **HBC** and **HBC-Cl** have been measured in solid state and compared with results from DFT calculations carried out on the lowest energy conformation $(ud)_3$ reported in Table 4.1. Figure 4.9 shows the outcomes of the IR analysis. The principal IR features found in the range between 650 and 2000 cm^{-1} have been labeled from 1 to 9 and assigned to the corresponding IR transitions predicted by DFT calculations (see Table 4.4). Overall we observe a good agreement between theory and experiments, which allows to propose the following assignment of the IR signals, based on the analysis of the nuclear displacements

conformer #	description	score	energy (kcal/mol)
1	dudududua	16	0.0
2	udududuad	16	2.5
3	duaduadua	12	3.8
4	duaduaadu	12	4.6
5	uduaduadb	12	5.3
6	duadbuadu	12	6.6
7	duaduadbu	12	6.9
8	udududuaadb	12	7.0
9	duaadudbu	12	8.0
10	duduaadua	12	8.4
11	duduadbua	12	8.6
12	dududbuaa	12	8.8
13	dudbuduaa	12	9.5
14	dudududuaaa	12	9.6
15	ududbuaad	12	9.6
16	udududuaaad	12	9.6
17	udbuaduad	12	9.7
18	duduaduaa	12	11.5
19	uaduaduad	12	12.7
(...)			
52	aaaaaaaaa	0	33.6

Table 4.3: *The lowest energy conformers of **C96-Cl** and their relative energies computed with DFT method.*

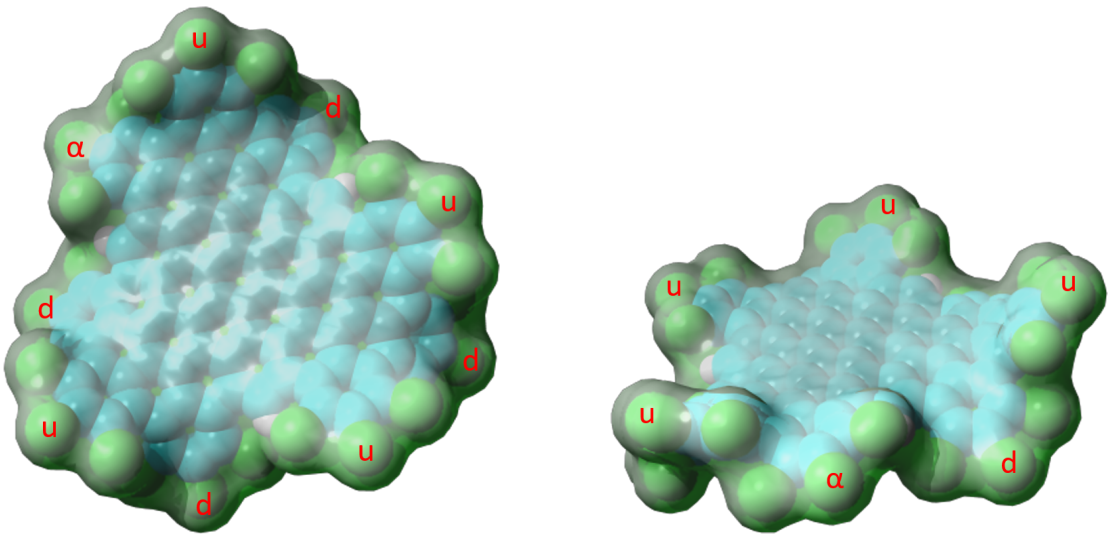

(a) *top view* **(b)** *side view*

Figure 4.8: *Three-dimensional representation of ududududα, the most stable conformer of **C96-Cl**. The model represents the equilibrium structure obtained from DFT calculations.*

computed for each normal mode. We begin by discussing the normal modes of **HBC-Cl**, assigned to the features identified with numbers in Figure 4.9.

- 1 is assigned to a degenerate pair of collective out-of-plane bending modes of the aromatic core; considering a given ring of the core, these modes involve the six carbon atoms with an alternated pattern of up/down displacements.

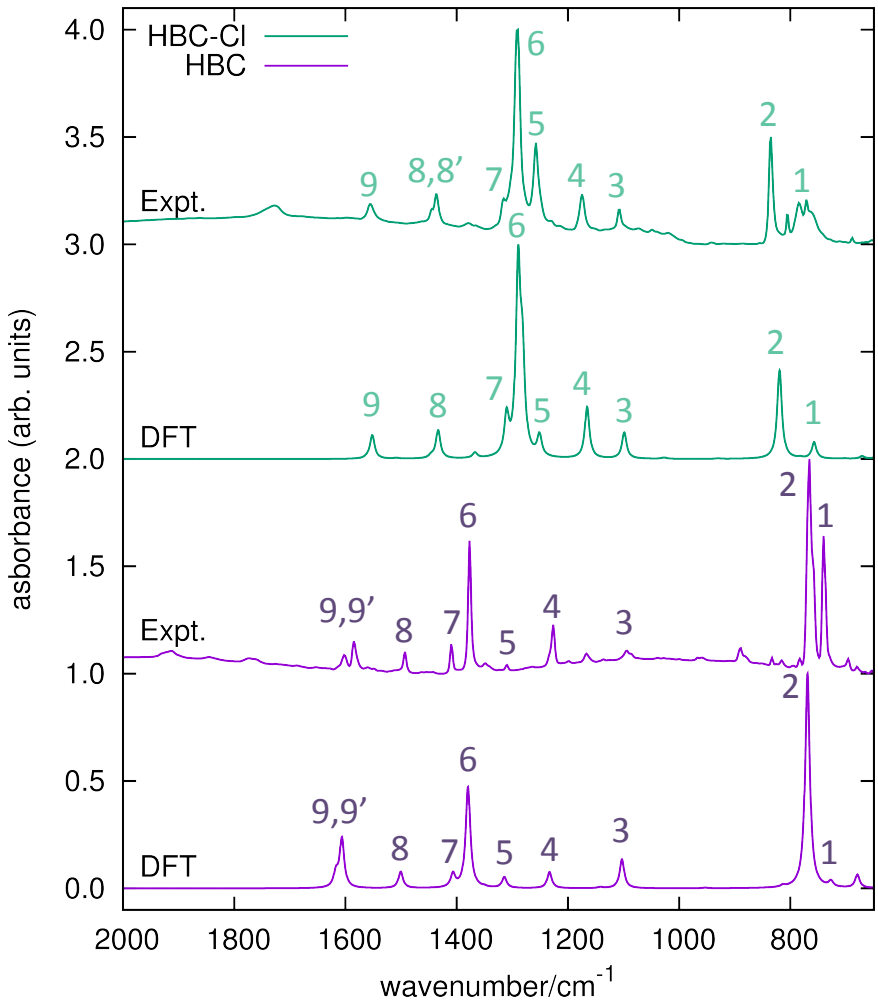

Figure 4.9: *IR absorption spectra of* ***HBC*** *and* ***HBC-Cl****.*

- 2 is assigned to a doubly degenerate mode involving the out-of-phase C-Cl stretching of the bonds at 1 and 3 (see Figure 4.3) of the chlorinated aryl moieties.
- 3 is assigned to a collective ring-breathing mode of the aromatic core; this occurs with an alternated pattern and mainly involves the six outer Clar rings of **HBC-Cl**.
- 4 is assigned to a doubly degenerate mode which mainly involves the in-phase C-Cl stretching of the bonds at 1 and 3 (see Figure 4.3) of the chlorinated aryl moieties.
- 5 is assigned to a doubly degenerate mode which mainly involves the CC stretching of the bonds which could be thought to form the edge of a coronene moiety inscribed in **HBC-Cl** aromatic core (*i.e.* bonds of kind c and d in Figure 4.6).
- 6 is assigned to two closely located degenerate modes, computed at 1308

cm^{-1} and 1316 cm^{-1}. In both cases the pattern of nuclear displacements is complex and mainly involves the CC bonds of the aromatic core.

- 7 is assigned to the in-phase stretching of the three C-Cl bonds of each chlorinated aryl moiety; the pattern of the mode is alternated along **HBC-Cl** edge (*i.e.*, three aryl moieties have shrinking C-Cl bonds while the other three have stretching C-Cl bonds).

- 8 is assigned to two closely located modes (1463 cm^{-1}, E_u and 1475 cm^{-1}, A_{2u}). The two peaks are not well resolved and appear as a structured feature both in the experimental and simulated spectrum. The E_u normal modes collectively involve CC bonds of the aromatic core; the A_{2u} mode displays a more recognizable pattern, with bonds of kind e (see Figure 4.6) which alternatively stretch in an out-of-phase fashion.

- 9 is assigned to a collective doubly degenerate ring stretching vibration (computed at 1583 cm^{-1}), whose pattern is close to that found in discussing the G line in Raman spectroscopy of PAHs.[1]

feature #	**HBC-Cl**		**HBC**	
	wavenumber (DFT)	wavenumber (expt.)	wavenumber (DFT)	wavenumber (expt.)
	D_{3d}, $(ud)_3$		D_{6h}	
1	773 (E_u)	771	742 (A_{2u})	740
2	836 (E_u)	836	784 (A_{2u})	766
3	1121 (A_{2u})	1108	1125 (E_{1u})	1094
4	1189 (E_u)	1175	1259 (E_{1u})	1227
5	1277 (E_u)	1258	1341 (E_{1u})	1310
6	1308 (E_u), 1316 (E_u)	1291	1408 (E_{1u})	1377
7	1337 (A_{2u})	1315	1435 (E_{1u})	1409
8	1463 (E_u), 1475 (A_{2u})	1437, 1444	1531 (E_{1u})	1493
9	1583 (E_u)	1555	1639 (E_{1u}), 1650 (E_{1u})	1585, 1602

Table 4.4: *List of observed and computed (unscaled) IR features in **HBC** and **HBC-Cl**.*

In comparison, the case of **HBC** presents a similar number of IR signatures, with a good correspondence between experiments and DFT calculations (see Figure 4.9).

- 1 is assigned to an alternated out-of-plane bending vibration of the carbon atoms in the aromatic core, coupled with the in-phase out-of-plane bending of the CH bonds at 1,3 (see Figure 4.3).

- 2 is assigned to the collective out-of-plane bending of all CH bonds and correlates with the characteristic TRIO features of PAHs.[99,121,122]

- 3 is a degenerate doublet involving a collective ring-breathing of the six outer Clar rings of **HBC**, with half the molecule vibrating out-of-phase with respect to the other half.

- 4,5,6,7,8 are assigned to degenerate modes involving CC stretching of the aromatic core, coupled with in-plane CH bending.

- 9 is assigned to collective doubly degenerate ring stretching vibrations, whose pattern is close to that found in discussing the G line in Raman spectroscopy of PAHs.[1]

4.3 IR spectroscopy of C96-Cl

The IR spectrum of **C96-Cl** has been recorded with the diamond anvil cell technique in solid state (see Chapter 9) and compared with the results from DFT calculations carried out on the two lowest energy conformers reported in Table 4.3. Figure 4.10 shows the outcome of the IR analysis. The principal IR features found

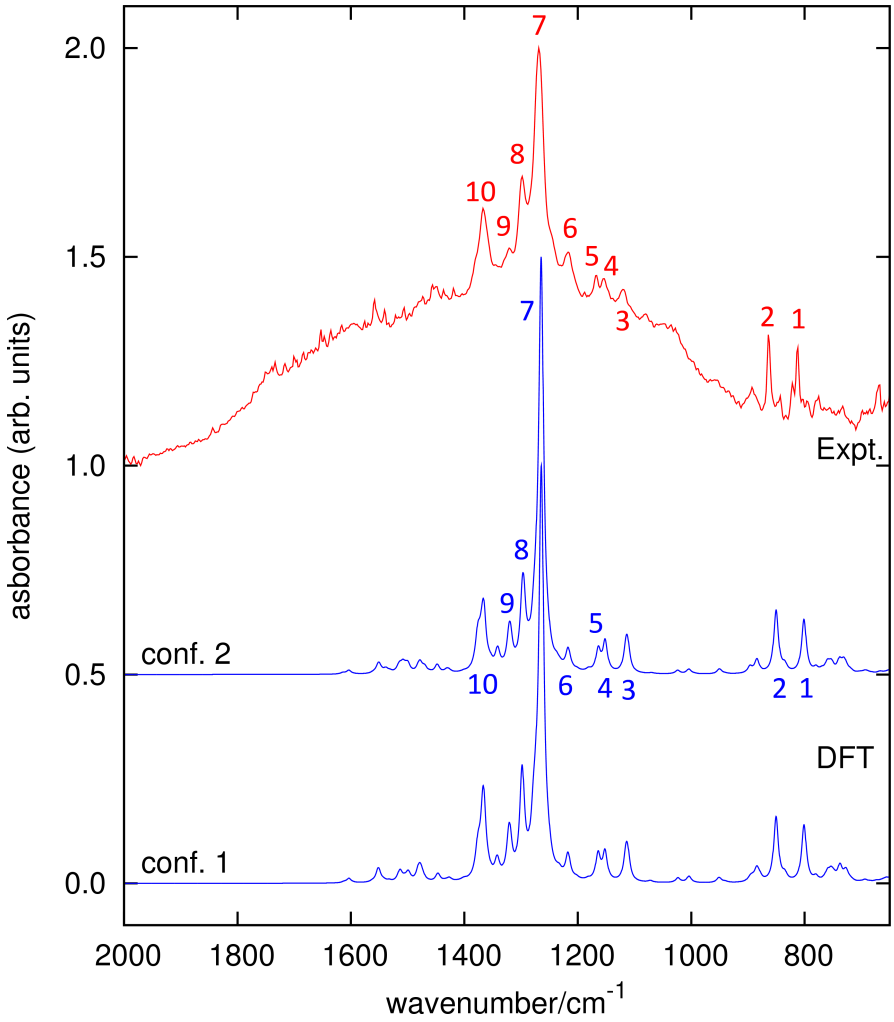

Figure 4.10: *IR absorption spectrum of **C96-Cl**. The simulated spectra are based on DFT calculations of the lowest two energy conformers (see Table 4.3).*

in the range between 650 and 2000 cm^{-1} have been labeled from 1 to 10 and assigned to the corresponding IR transitions predicted by DFT calculations (see Table 4.5). Overall, we observe a good agreement between theory and experimental data, which allows to assign the IR signals based on the analysis of the nuclear displacements computed for each normal mode. The nuclear displacements of selected IR features are reported in Figure 4.11. One can observe rather complex

feature #	wavenumber (DFT)	wavenumber (expt.)
1	818	813
2	868	863
3	1136	1120
4	1175	1154
5	1188	1168
6	1242	1217
7	1290	1269
8	1325	1298
9	1348	1321
10	1394	1367

Table 4.5: *List of observed and computed (unscaled) IR features in **C96-Cl**. Computed numbers are reported based on conformation 1 in the Figure 4.10 and Table 4.3.*

and collective nuclear displacement patterns, among which some normal modes stand out for their relative intensity. Modes 1 and 2 display a sizable content of C-Cl stretching, while mode 10 couples C-Cl stretching more significantly with collective CC stretching of the aromatic core. Mode 7 displays CH bending contributions coupled with collective π-conjugated CC stretching. As a whole, the observed IR transitions can be considered a robust fingerprint of the molecular structure of **C96-Cl** molecule. Hence, their observation strongly supports the successful synthesis of this chlorinated graphene molecule.

4.4 Raman spectroscopy of HBC and HBC-Cl

The Raman spectra of **HBC** and **HBC-Cl** are reported in Figure 4.12. The two molecules display a similar spectral pattern, dominated by features which have been attributed to G and D modes in **HBC**.[1,29] In fact, the analysis of the nuclear displacements computed by DFT for the G and D Raman lines displays typical and recognizable patterns which can be put in correspondence between **HBC** and **HBC-Cl** (see Table 4.6).

Following the labeling scheme adopted in Figure 4.12, we show in Figures 4.13, 4.14, 4.15 and 4.16, the nuclear displacements of selected modes characterized by intense experimental Raman relative intensities.

In both **HBC** and **HBC-Cl** the mode A_1 is assigned to the in-phase collective breathing of the molecule along a radial direction. In **HBC** it rather uniformly involves the whole molecule while in **HBC-Cl** this mode is more delocalized at the outer edge of the molecule and it involves the C-Cl moieties. The collective breathing of **HBC** (feature A_1, observed at 355 cm^{-1}) is significantly red shifted in **HBC-Cl** (feature A_1, observed at 292 cm^{-1} – see Figure 4.12). This is due to the mass effect of the heavy chlorine atoms at the molecular edge. In fact, compared with the breathing in **HBC** which involves the displacement of the hydrogen atoms at the periphery (Figure 4.13), the breathing of **HBC-Cl** requires displacing chlorine atoms, which are significantly heavier than hydrogen. Interestingly, the A_0 feature observed in **HBC** (assigned to a doubly degenerate mode which involve mainly the CC stretching of aromatic core) is characteristic of **HBC**: no similar mode is computed or observed in **HBC-Cl**.

feature #	**HBC-Cl**		**HBC**	
	wavenumber (DFT)	wavenumber (expt.)	wavenumber (DFT)	wavenumber (expt.)
	D_{3d}, $(ud)_3$		D_{6h}	
A_0	-	-	279 (E_{2g})	279
A_1	276 (A_{1g})	292	352 (A_{1g})	355
A_2	415 (A_{1g}, E_g)	412	-	-
B_1	1095 (A_{1g})	1086	1022 (A_{1g})	1007
B_2	1173 (E_g)	1157	-	-
D_1	1259 (E_g)	1235	1282 (E_{2g})	1255
D_2	1280 (A_{1g})	1259	1184 (A_{1g})	1150
D_3	1336 (A_{1g})	1321	1325 (A_{1g})	1304
D_4	1399 (A_{1g})	1376	1426 (A_{1g})	1402
D_5	-	-	1384 (A_{1g})	1363
G_1	1500 (E_g)	1470	1499 (E_{2g})	1476
G_2	1544 (A_{1g})	1514	1647 (A_{1g})	-
G_3	1567 (E_g)	1536	1650 (E_{2g})	1606
G_{4a}	1621 (E_g)	1589	1635 (E_{2g})	-
G_{4b}			1578 (E_{2g})	1533

Table 4.6: *List of observed and computed (unscaled) Raman features in **HBC-Cl** and **HBC**. The G and D features of **HBC** have been also discussed previously.[29] The G_2 feature is unresolved in the experimental spectrum because it is very close to the strong G_3 feature, while feature G_{4a} is too weak to be observed.*

In the low wavenumber region we find in the experimental spectrum of **HBC-Cl** a strong Raman line at 412 cm^{-1} (A_2). Based on DFT calculations, this corresponds to three very close Raman active modes computed at 415 cm^{-1} (see Figure 4.14) which arise from the accidental degeneracy of an A_{1g} mode with a doublet of E_g species. The three modes computed at 415 cm^{-1} are characterized by vibrational displacements which have a sizable contribution both along the z-axis and within the (x, y) plane. For this reason we report in Figure 4.14 different kinds of representations for these particular normal modes. DFT calculations predict a significantly stronger intensity for the A_{1g} mode than the degenerate E_g doublet. For instance with 514 nm excitation one obtains 2946 Å$^4/amu$ *vs.* 110 Å$^4/amu$ and in off-resonance conditions one gets 119 Å$^4/amu$ *vs.* 1 Å$^4/amu$. Hence it is a reasonable approximation to associate the experimental A_2 feature mainly to the totally symmetric mode represented in Figure 4.14; looking at the (x, y) representation of this A_{1g} mode, one recognizes the breathing pattern of the 7 inner rings (which could be associated to a coronene moiety) in the center of **HBC-Cl**. During this vibration the outer part of the molecule breathes out-of-phase with respect to the center. As for the E_g degenerate doublet, the associated nuclear displacements shown in Figure 4.14 display a collective pattern characterized by alternated out-of-plane displacements along the z-direction accompanied by displacements in the (x, y) plane which are mostly localized at the molecular periphery. The modes associated to the A_2 feature are observed only in **HBC-Cl** and do not find a counterpart in **HBC**.

At higher wavenumber, in the region located between the A-modes and the D-band modes we find Raman active modes which are described as collective breathing vibrations of the Clar rings which can be identified in the molecular

structure and which have been also identified in a previous chapter on the graphene molecule C78.[11] Peak B_1 is assigned to the ring-breathing mode of the central Clar ring of **HBC** and **HBC-Cl** which vibrates out-of-phase with respect to the six outer Clar rings. In **HBC-Cl** mode B_1 is coupled with the collective C-Cl stretching of the chlorinated aryl moieties. In particular C-Cl stretching at (1, 3) (see Figure 4.3) are both out-of-phase with respect to C-Cl stretching at 2 (see Figure 4.3). Compared to **HBC**, this mode is remarkably blue-shifted in **HBC-Cl** (experimentally by 79 cm−1, while according to DFT by 73 cm^{-1}). Mode B_2 is only found in **HBC-Cl** molecule and it is assigned to a doubly degenerate mode which involves the CC stretching of the outer part of the molecule (mainly bonds of kind c and d, see Figure 4.6) coupled with the C-Cl stretching of the chlorinated aryl moieties.

At progressively higher wavenumbers one finds modes which can be related to the pattern expected for D-modes.[1] The weak Raman active doubly degenerate mode D_1 is assigned to a vibration which involves the breathing of four Clar rings in both **HBC** and **HBC-Cl**. In **HBC-Cl** the D_1 mode is coupled with the in-phase C-Cl stretching of the chlorinated aryl moieties. In **HBC** the D_1 mode is coupled with in-plane CH bending.

The strong Raman active mode D_2 is assigned to the ring breathing of the central Clar ring, out of phase with respect to the stretching of the radial CC bonds which emanate from the central Clar ring. It partially displays the canonical D-mode pattern,[1] the notable exception being the wrong phase of the stretching of the bonds of kind d (see Figure 4.6). In **HBC-Cl** the D_2 mode is coupled with the in-phase C-Cl stretching of the chlorinated aryl moieties. In **HBC** the D_2 mode is coupled with the collective in-plane bending of the CH bonds at positions (1,3) (see Figure 4.3). Similarly to the case of the B_1 feature, also D_2 is notably blue-shifted in **HBC-Cl** compared to **HBC** (experimentally by 109 cm^{-1}, while according to DFT calculations by 96 cm^{-1}).

Mode D_3 is assigned to the in-phase ring breathing of all the seven Clar rings coupled with the CC shrinking of the bonds of kind c and e (see Figure 4.6). This is the mode which fully displays the expected D-mode pattern.[1] In **HBC** the D_3 mode is coupled with the collective in-plane bending of the CH bonds at positions (1,3) (see Figure 4.3). Interestingly, comparing modes D_2 and D_3 in **HBC**, one finds that the relative phase between the inner Clar ring breathing and the outer CH-bending inverts. Hence the modes D_2 and D_3 of **HBC** can be approximately described as the doublet arising from the vibrational coupling between the collective breathing coordinate of the seven Clar rings and the collective CH bending of the CH bonds at positions (1,3).

Mode D_4 is assigned to the breathing of the central Clar ring, out-of-phase with respect to the approximate breathing of the outer six Clar rings. In **HBC** the D_4 mode is coupled with the collective in-plane bending of the CH bonds at (1,3) (see Figure 4.3) while in **HBC-Cl** the D_4 mode is coupled with the collective stretching of the C-Cl bonds at 2 (see Figure 4.3). Finally, feature D_5 is found just in **HBC** and it is assigned to the collective CC stretching at the edge of the molecule, mainly at bonds of kind c and d (Figure 4.6) coupled with the collective in-plane CH bending at positions (1,3) (see Figure 4.3).

The G-modes are found in the next wavenumber region, above the D-modes. In graphene molecules the G-modes display collective displacement patterns[1] which can be associated to that of the ν_{16} E_{2g} ring-stretching mode of benzene.[123]

The experimental G_1 feature of **HBC** and **HBC-Cl** (see Figure 4.12) is assigned to doubly degenerate modes of E species which mainly involve the CC stretching of bonds in the center of the molecule. In **HBC** the mode G_1 is coupled with collective in-plane CH bending.

Feature G_2 is assigned to a totally symmetric mode which involves CC stretching (*i.e.* ring stretching – see above) mainly at the outer rings of the molecule (bonds of kind b in Figure 4.6). In **HBC** mode G_2 is coupled with collective in-plane CH bending at positions (1,3) (see Figure 4.3). In **HBC-Cl** the G_2 mode involves the collective C-Cl stretching of bonds at 2 (see Figure 4.3) and it is significantly red shifted compared to **HBC** (according to DFT by 103 cm^{-1}; the experimental determination of the position of G_2 for **HBC** is not feasible because it is a weak mode overlapped with other G components).

The G_3 Raman feature of **HBC** is assigned to a doubly degenerate mode which involves CC stretching mainly in outer part of the molecule and it is coupled with collective in-plane CH bending at positions (1,3) (see Figure 4.3). The G_3 feature of **HBC-Cl** is assigned to a doubly degenerate mode with a similar pattern as **HBC** but, compared to **HBC**, it is remarkably red shifted (experimentally by 70 cm−1, while according to DFT by 83 cm^{-1}).

Finally, the G_4 feature of **HBC-Cl** is assigned to a doubly degenerate mode which involves the ring stretching of the three central rings next to each other along a row. In **HBC** there are two doubly degenerate modes with a similar nuclear displacement pattern which have been named G_{4a} and G_{4b}. They both involve ring stretching vibrations coupled with a collective in-plane CH bending.

4.5 Raman spectroscopy of C96-Cl

The experimental and simulated Raman spectra of **C96-Cl** over the (G, D) region are reported in Figure 4.17. DFT calculations has been carried out for the two lowest conformation based on Table 4.3. The experimental and simulated spectra are in good agreement and it is possible to observe the expected D and G features. The nuclear displacements of selected D and G modes have been reported in Figure 4.18. The proposed assignment of these modes to experimental Raman features is reported in Table 4.7. For the experimental G_1 peak, two modes computed by DFT should be considered since both these modes are intense and they are computed at very close wavenumbers. Also in the case of G_3, from DFT calculations one finds three close and intense modes. The nuclear displacements of these modes have been reported in Figure 4.18. The experimental and DFT calculated Raman spectra of **C96-Cl** over the low wavenumber region are shown in Figure 4.19. Also in this case DFT calculations of the Raman spectra have been carried out for the two lowest conformation based on the results summarized in Table 4.3. The experimental and simulated spectra are in good agreement and it is possible to observe many peaks in this region. All these modes display collective nuclear displacements with complex patterns and it is hard to find a

feature #	wavenumber (DFT) cm^{-1}, unscaled	Intensity (DFT) Å$^4/amu$	wavenumber (expt.) cm^{-1}
D_1	1309	19937	1295
D_2	1350	53824	1324
G_1	1618	5064	1590
	1619	5093	
G_2	1645	1897	1613
	1645	3626	
	1646	4333	

Table 4.7: *List of observed and computed (unscaled) IR features in **C96-Cl**. The data from DFT calculations are relative to the conformation 1 reported in Figure 4.10 and Table 4.3.*

simple descriptor to name them. However, as observed in discussing the case of IR of **C96-Cl**, they can be used as a reliable fingerprint of this molecule.

The second-order Raman spectrum of **C96-Cl** is shown in Figure 4.20, where it is compared with the corresponding first-order Raman spectrum. Herein, we observe the characteristic D and G peaks together with their associated second order lines which are typical of structurally well-defined PAHs. Furthermore, the observation of overtones and combinations in the Raman spectrum is consistent with resonance conditions reached with the 514.5 nm laser excitation used in the Raman experiment. In fact the UV-Vis spectrum of **C96-Cl** displays strong absorption in a region close to 500 nm.[23]

As described in Chapter 3, the Raman intensity of a combination (or overtone) is proportional to the product of the Raman intensities of the corresponding fundamentals. Hence, similarly to **C78** and other PAHs (see Chapter 3), the relative intensities and band shapes observed over the overtone and combination region approximately match the corresponding fundamentals. For instance, the 2D feature is more structured than 2G, consistently with the fact that in the first order spectrum the D feature is more structured than G.

In conclusion, the results presented in this Chapter show that out-of-plane distortions in chlorinated graphene molecules are not seriously impairing the π-conjugation. This is supported by DFT calculations on perchlorinated **HBC** which shows a markedly non-planar equilibrium structure due to the steric hindrance of Cl atoms at the molecular edge, which is in agreement with the structure by the single-crystal X-ray analysis. However, both the computed HOMO-LUMO gap and the vibrational properties observed with Raman and IR spectroscopies show that **HBC-Cl** possesses a π-conjugation similar to that of **HBC**. Interestingly, even in the non-planar case of **HBC-Cl**, the π-stacking, which is a very crucial property for charge transport in molecular electronics devices based on **HBC**,[31] is still possible due to specific steric interactions and interlocking of chlorine hindrances, as depicted in Figure 4.2. Vibrational spectroscopy complemented with DFT calculations proves to be informative about the chemical structure of **HBC** and **HBC-Cl**: distinct markers can be directly associated to specific moieties. For instance, the TRIO marker in the IR of HBC (766 cm^{-1}) is due to the symmetric hydrogen-terminated molecular edge, while the persistence of the strong D_3 peak in **HBC** (1304 cm^{-1}) and **HBC-Cl** (1321 cm^{-1}) proves

the similar π-conjugated nature of the two molecules, independently of planarity.

A thorough analysis of the different stable conformers of **HBC-Cl**, carried out by geometry optimization with DFT methods, revealed that a rich variety of structures, including chiral enantiomers, can be obtained by suitable chemical substitution at the edges of **HBC**. While, in the case under study, the lowest energy conformation with achiral $(ud)_3$ conformation is the structure found in the crystal,[23] we can infer that the introduction of selected edge substituents and/or synthetic pathways could give rise to novel structures, for instance based on propeller-shaped chiral units. These could exhibit appealing chiroptical properties, similar to the class of helicenes.[124]

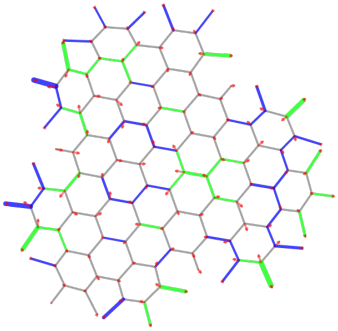

1: 818 cm^{-1}, 94 km/mol

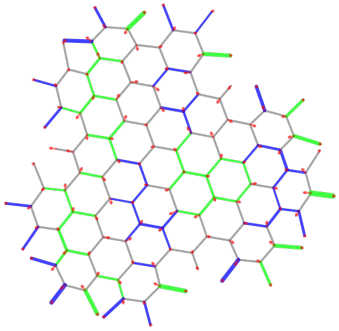

2: 868 cm^{-1}, 110 km/mol

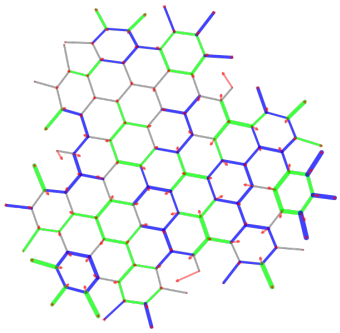

3: 1136 cm^{-1}, 40 km/mol

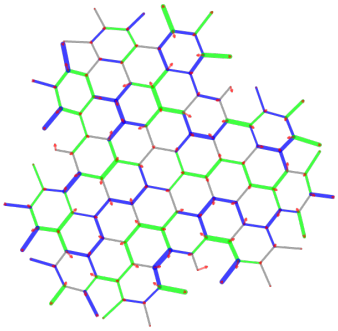

4: 1175 cm^{-1}, 52 km/mol

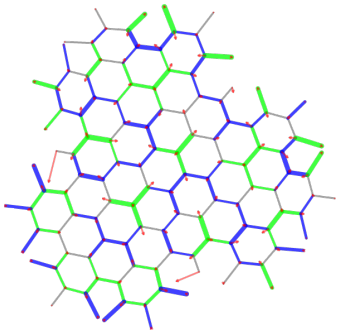

5: 1188 cm^{-1}, 47 km/mol

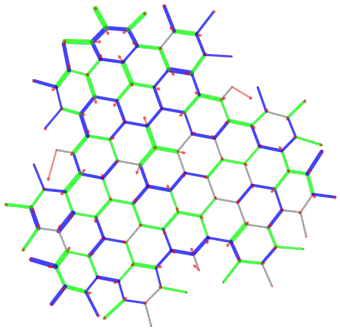

6: 1242 cm^{-1}, 43 km/mol

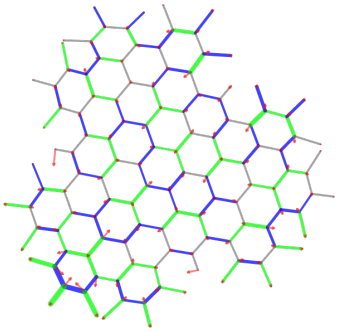

7: 1290 cm^{-1}, 426 km/mol

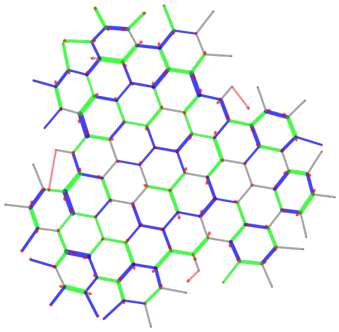

8: 1325 cm^{-1}, 173 km/mol

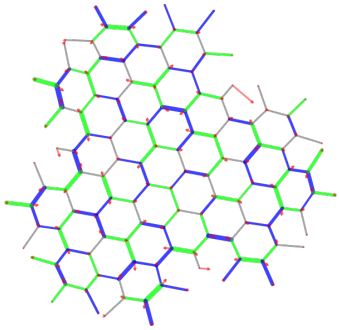

9: 1348 cm^{-1}, 51 km/mol

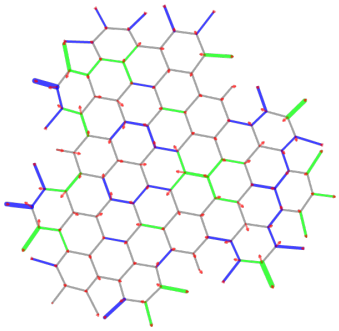

10: 1394 cm^{-1}, 141 km/mol

Figure 4.11: *Nuclear displacement of selected IR features of **C96-Cl**. These nuclear displacements are based on DFT calculation on conformation 1 (see Table 4.3). Red segments represent displacement vectors; CC bonds are represented as green (blue) lines of different thickness according to their relative stretching (shrinking).*

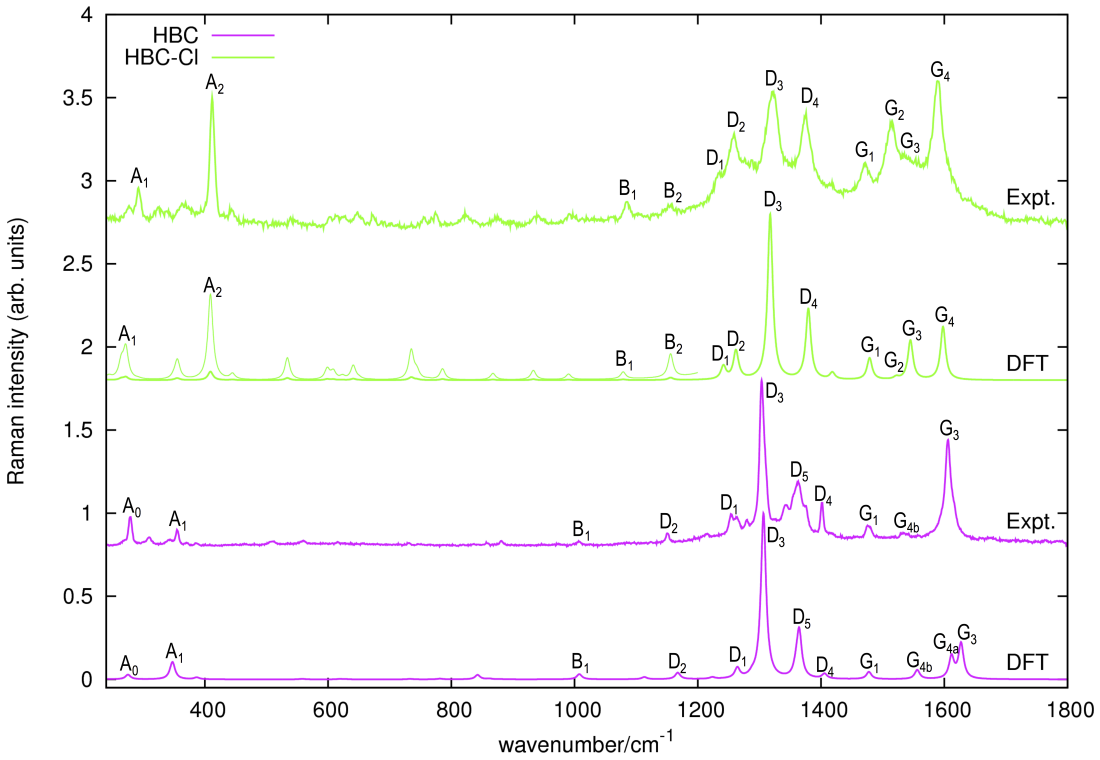

Figure 4.12: *Raman spectra of* ***HBC*** *and* ***HBC-Cl*** *excited with 458 nm and 325 nm laser lines, respectively. The simulated Raman spectra computed in off-resonance conditions with DFT method B3LYP/6-31G(d,p) are displayed below each experimental spectrum. For* ***HBC-Cl*** *just the* $(ud)_3$ *conformation has been considered in simulating the Raman spectrum. Wavenumbers computed by DFT have been scaled by 0.98. For* ***HBC-Cl*** *the lower wavenumber side of the simulated spectrum is also displayed with enhanced intensity (10×) to help the assignment of the experimental features. This intensity mismatch in the simulation is due to limitations in the treatment of resonance effects in the standard implementation of Raman scattering currently available in Gaussian09.*[24]

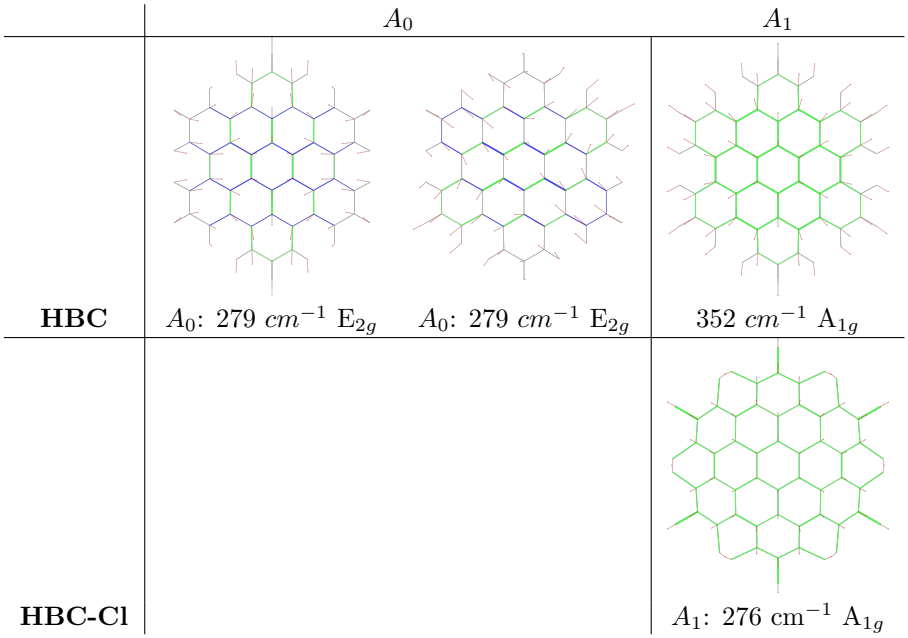

Figure 4.13: *Representation of the low wavenumber (A region) normal modes of **HBC** and **HBC-Cl** relevant for Raman spectroscopy according to DFT calculations: A_0: doubly degenerate mode of **HBC**; A_1: breathing modes of **HBC-Cl** and **HBC**. Red segments represent displacement vectors; CC bonds are represented as green (blue) lines of different thickness according to their relative stretching (shrinking).*

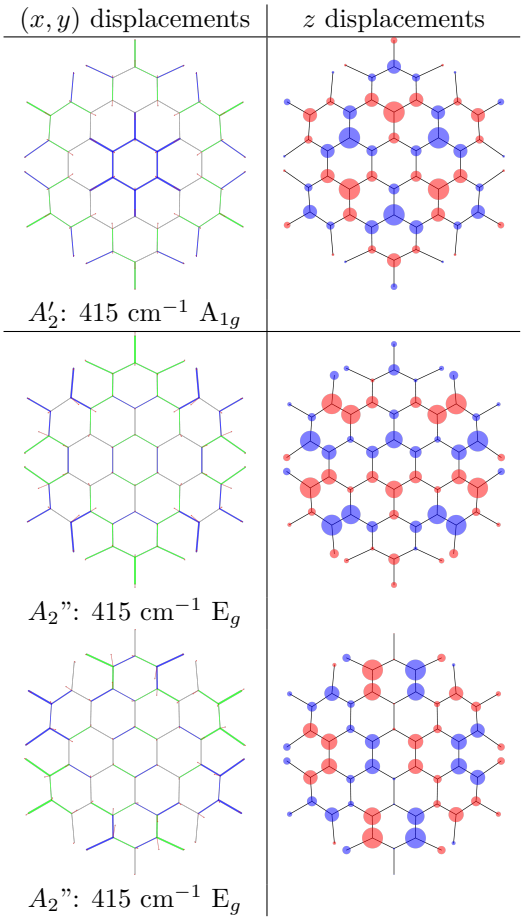

Figure 4.14: *Representation of the A_2 low wavenumber normal modes of **HBC-Cl** relevant for Raman spectroscopy according to DFT calculations: the accidentally degenerate A_{1g} and E_g modes computed at 415 cm^{-1}. Red segments represent displacement vectors; CC bonds are represented as green (blue) lines of different thickness according to their relative stretching (shrinking). For out-of-plane modes the size of blue/red circles of the molecular sketch is proportional to nuclear displacements in the out-of-plane direction (z); red indicates displacements directed along $+z$ and blue indicates displacements directed along $-z$.*

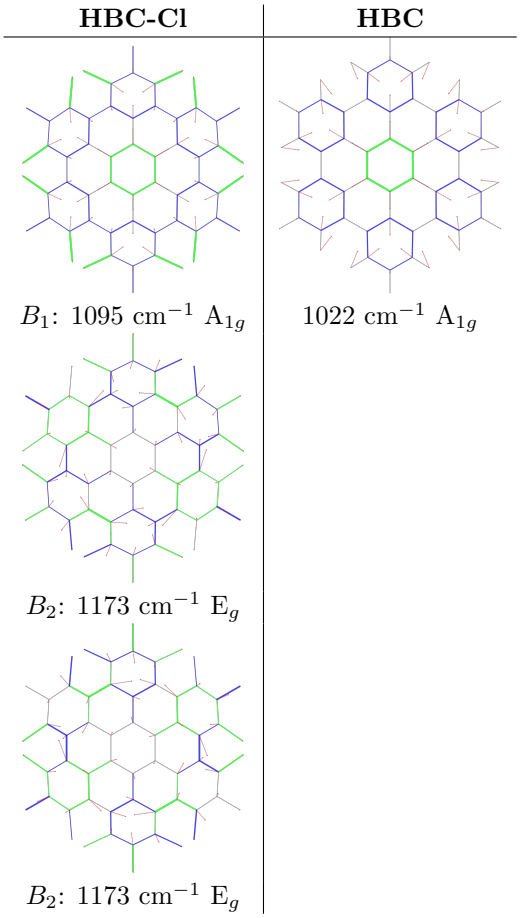

Figure 4.15: *Representation of the normal modes of **HBC-Cl** relevant for Raman spectroscopy in the B region according to DFT calculations. Red segments represent displacement vectors; CC bonds are represented as green (blue) lines of different thickness according to their relative stretching (shrinking).*

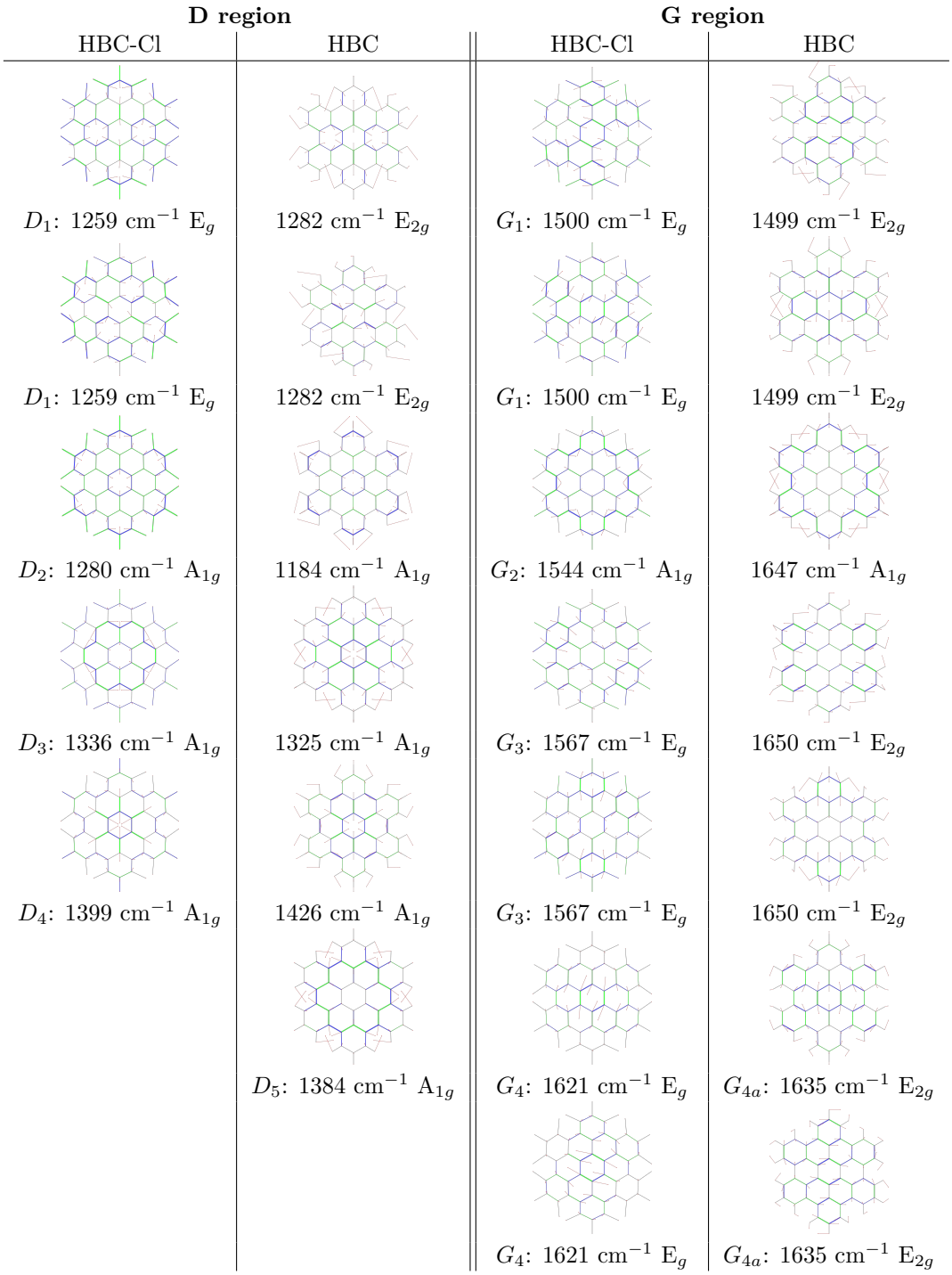

Figure 4.16: *Representation of the normal modes of **HBC-Cl** and **HBC** relevant for Raman spectroscopy in the D and G region according to DFT calculations. Red segments represent displacement vectors; CC bonds are represented as green (blue) lines of different thickness according to their relative stretching (shrinking).*

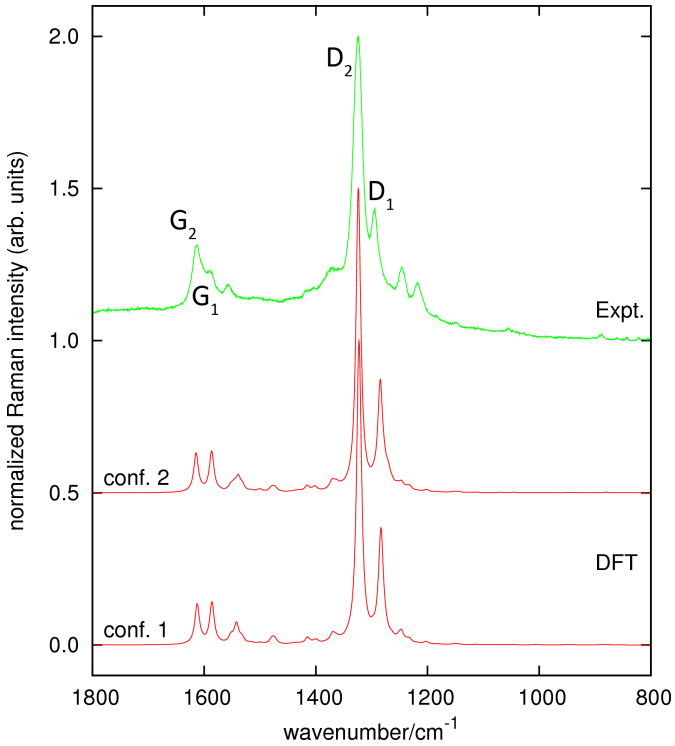

Figure 4.17: *Raman spectrum of **C96-Cl** over the D, G region. The simulated spectra are based on DFT calculations of the lowest two energy conformers (see Table 4.3*

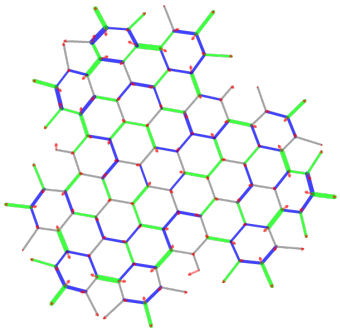

D_1: 1309 cm^{-1}, 19937 Å^4/amu

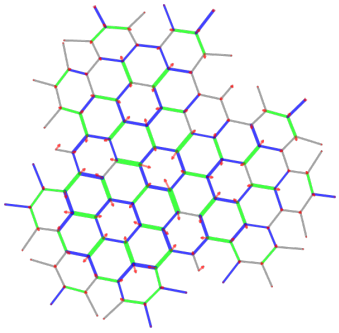

D_2: 1350 cm^{-1}, 53824 Å^4/amu

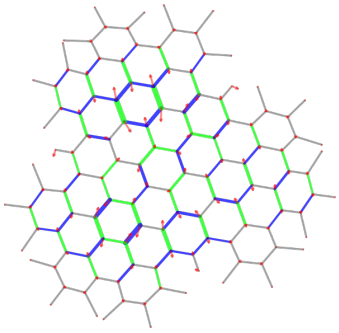

G_1: 1618 cm^{-1}, 5064 Å^4/amu

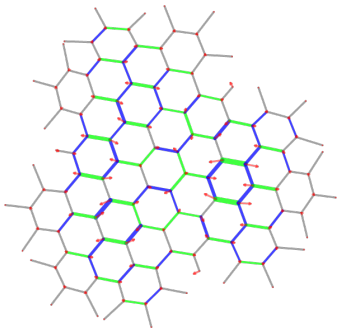

G_1: 1619 cm^{-1}, 5093 Å^4/amu

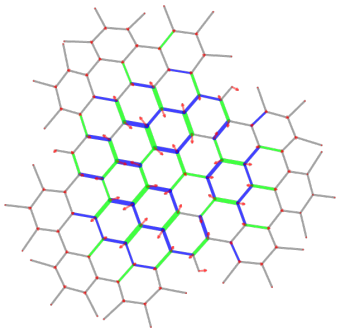

G_2: 1645 cm^{-1}, 1897 Å^4/amu

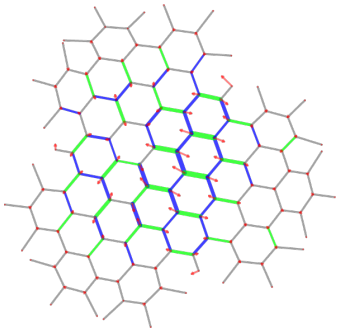

G_2: 1645 cm^{-1}, 3626 Å^4/amu

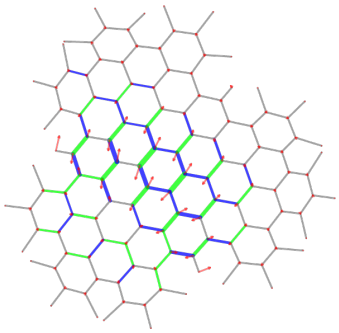

G_2: 1646 cm^{-1}, 4333 Å^4/amu

Figure 4.18: *Nuclear displacement of selected Raman features of* ***C96-Cl*** *in D, G region. These nuclear displacements are based on DFT calculation on conformation 1 (see Table 4.3). Red segments represent displacement vectors; CC bonds are represented as green (blue) lines of different thickness according to their relative stretching (shrinking).*

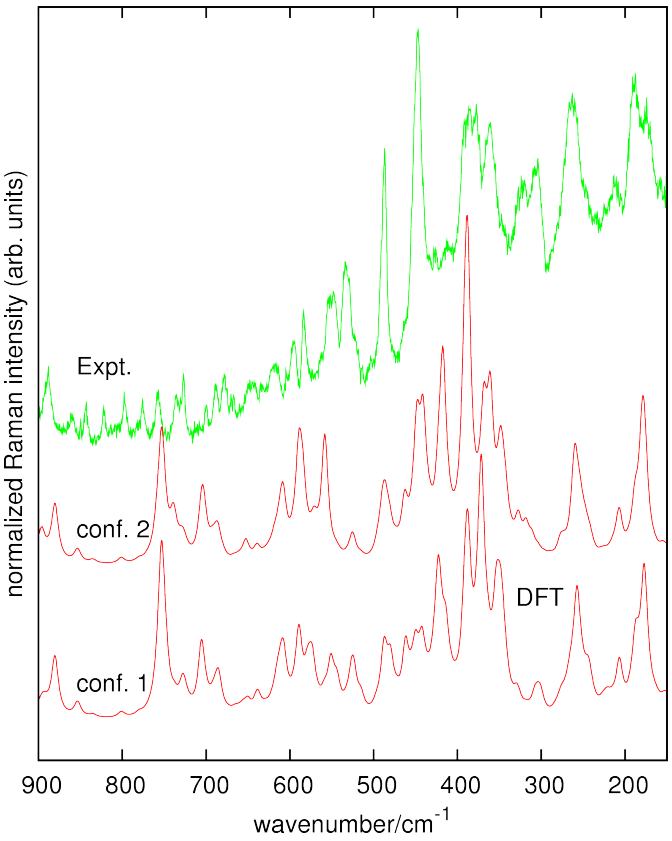

Figure 4.19: *Raman spectrum of* ***C96-Cl*** *over the low wavenumber region. The simulated spectra are based on DFT calculations of the lowest two energy conformers (see Table 4.3*

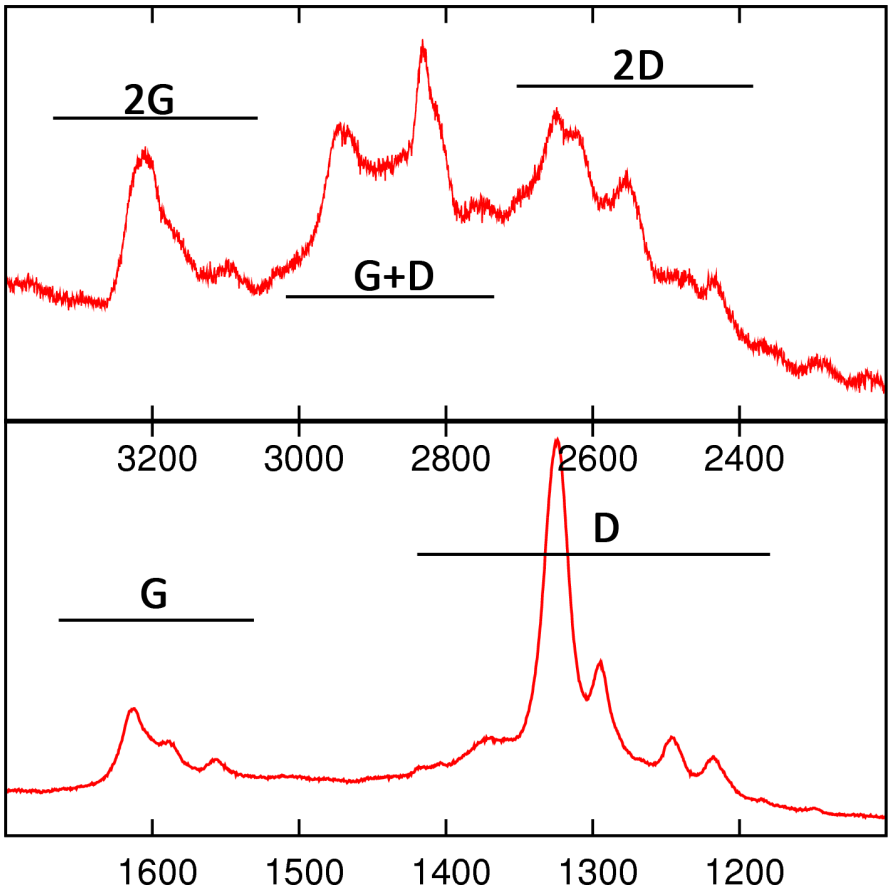

Figure 4.20: *Second order Raman spectrum of* ***C96-Cl****. The lower panel represents the first order spectrum plotted exactly over the range defined by half the limiting values of the top panel. This allows a straightforward comparison of the position and lineshape of the 2D and 2G overtones with respect to their first order counterpart.*

CHAPTER 5

Models of holes in molecular graphenes

This Chapter presents the investigation of the molecular structure of $C_{216}H_{48}$ (**C216**), the analogue of the $C_{222}H_{42}$ (**C222**) molecular graphene with the missing central ring (hole). It is shown how Vibrational Spectroscopy, complemented by DFT calculations, can be used as a very specific probe of molecular structure and can provide direct signatures of the presence of the "hole" in such a novel molecular graphene, which may serve as a model of holey graphene. It is shown that, compared with the parent molecular graphenes, this type of functionalization may alter the planarity of the molecule. While this out-of-plane distorsion does not significantly impair π-conjugation, the presence of a hole in **C216** alters the conjugation pattern and affects more significantly the HOMO-LUMO gap.

5.1 IR spectroscopy of C216

The interesting case of **C216** (see Figure 5.1) allows investigating theoretically and for the first time also experimentally the effects of a "hole" (*i.e.*, a missing ring in the honeycomb network) in the vibrational spectroscopy of a large PAH. This molecular structure was recently discussed[125] in the general context of kekulenes, a family of cyclic arenes. The hole structure of **C216** is capped with hydrogen atoms, which turn out to be rather close so to exert some steric hindrance. For instance the geometry optimization of a close analogue of **C216**, namely **C108** (Figure 5.2), as a planar structure provides an imaginary (negative in Gaussian[24] phrasing) frequency of $i120$ cm^{-1} with associated nuclear displacements described as alternated (ududud) out-of-plane CH bending at the hole edge.

By relaxing planarity in geometry optimization, the **C108** molecule escapes from this saddle point and reaches a minimum more stable by only 0.16 $kcal/mol$

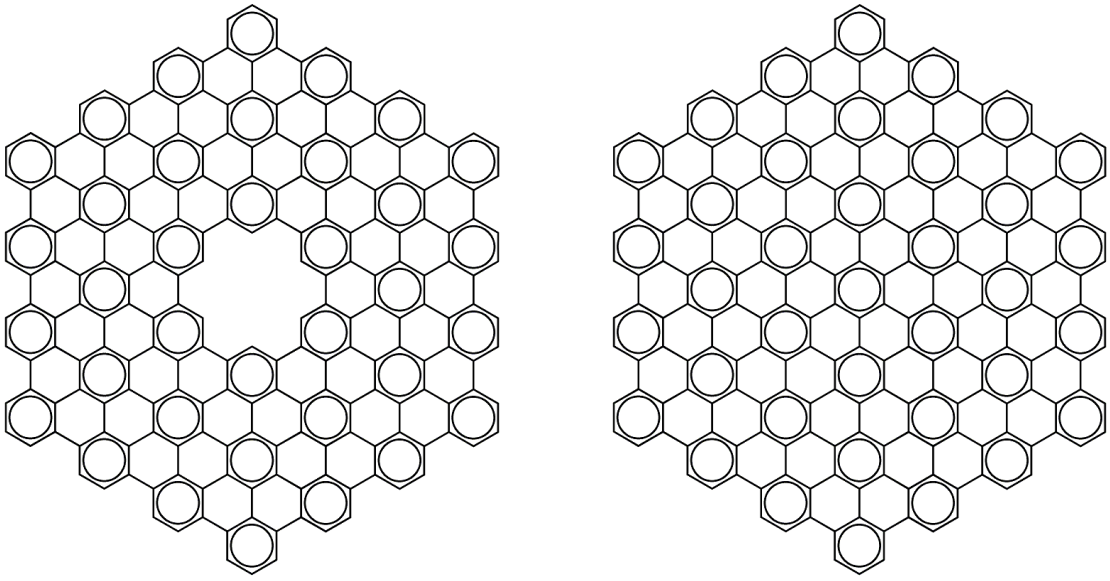

(a) *C216* (b) *C222*

Figure 5.1: *Representation of the molecular structure of* ***C216****, the analogue of the* ***C222*** *molecular graphene with the missing central ring (hole).*

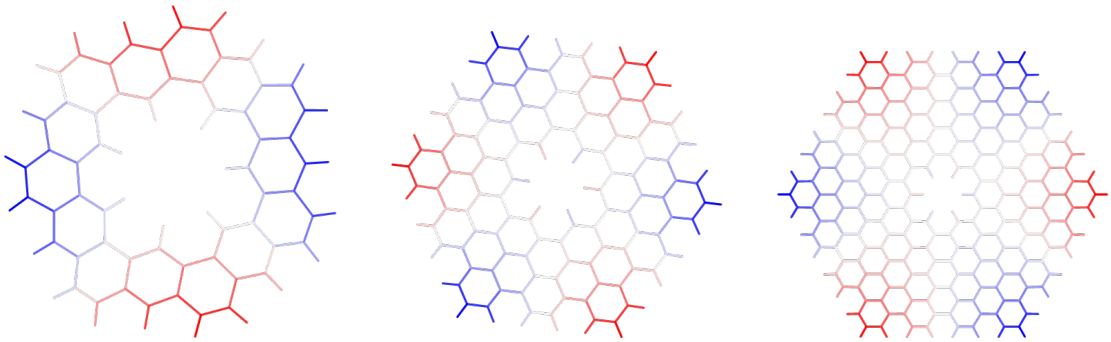

(a) *septulene: min:-1.6Å, max:1.6Å* (b) ***C108****: min:-0.5Å, max:0.5Å* (c) ***C216****: min:-0.8Å, max:0.8Å*

Figure 5.2: *The non planar structure of* ***C216*** *compared with that of septulene and that of* ***C108****, the smaller analogue of* ***C216*** *obtained from the giant PAH* ***C114*** *by subtraction of the inner ring. The molecules have been represented by means of an orthogonal projection where the out-of-plane z-coordinate of the middle point of each bond is coded in shades of red ($z > 0$) and blue ($z < 0$). In-plane bonds are coded with light gray shade. These structures have been obtained from geometry optimization with DFT method B3LYP/6-31G(d,p). The calculation of the Hessian does not produce any imaginary frequency, thus confirming that these are all stable structures. With respect to the average plane on which the molecule is lying, the six vertexes of* ***C216*** *adopt an alternated up-down conformation. This can be schematically labeled (ududud) by following a path along the periphery of the molecule. As shown in Chapter 4 this non planar conformation reminds the one adopted by the six vertexes of* ***HBC-Cl****.*

in correspondence of which no imaginary frequencies are found anymore. However little this strain energy is, the collective CH out-of-plane bending, a very characteristic IR marker of the hole (see Figure 5.3), is affected and it is computed at

873 cm^{-1} in the planar case, while it is computed at 886 cm^{-1} in the non planar case, *i.e.*, blue-shifted by 13 cm^{-1}.

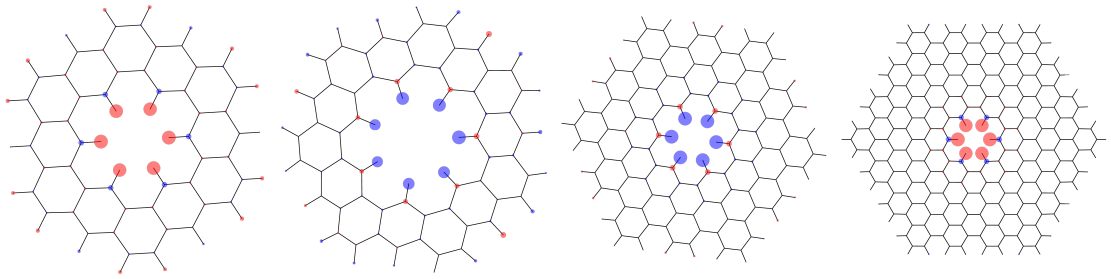

(a) *kekulene, 893 cm*$^{-1}$ **(b)** *septulene, 895 cm*$^{-1}$ **(c)** ***C108****, 886 cm*$^{-1}$ **(d)** ***C216****, 881 cm*$^{-1}$

Figure 5.3: *CH-out-of-plane nuclear displacements associated to the IR markers of the hole topology in annular PAHs according to DFT calculations.*

Similarly to **C108**, the steric hindrance at the hole drives also **C216** out-of-planarity with an overall (ududud) shape, as shown in Figure 5.2. Hence, even if steric hindrance is not as severe as in the perchlorinated case of **HBC-Cl** and **C96-Cl** (see Chapter 4), also **C216**, in the isolated molecule limit, adopts an overall non-planar and slightly bent structure.

We report in Figure 5.4 the IR spectrum of **C216** compared with the corresponding simulated spectrum from DFT calculations. Three clear hydrogenated edge markers are found in the low wavenumber region of the spectrum. Two of them are associated to the outer edge. The peak observed at 786 cm^{-1} corresponds to a collective CH-out-of-plane bending vibration which is more localized at the six outer vertexes of **C216** and it could be also named as TRIO marker.[99] The peak observed at 802 cm^{-1} is due to the collective CH out-of-plane vibration of the six armchair edges of **C216** and it could be named as DUO marker.[99] Finally, the third IR marker observed at 857 cm^{-1} is a characteristic feature of **C216** hole. Its position correlates well with results from DFT calculations (Figures 5.5, 5.4) and experimental data on PAHs with related structures, such as kekulene[126] and septulene.[127] We also observe at 887 cm^{-1} a weak peak (which finds a correspondence in DFT calculations at 902 cm^{-1}). Based on DFT, this is assigned to a degenerate E_u vibration which can be described as a collective in-plane motion of both hydrogen atoms at the hole and carbon atoms of the aromatic core.

5.2 Raman spectroscopy of C216

The Raman spectrum of **C216** excited with the 514 nm laser line is shown in Figure 5.6. It displays several features which are characteristic of graphene molecules, notably the G and D band in the first-order Raman. Furthermore, due to resonance conditions reached with the 514nm laser excitation, it is also possible to observe clear second-order Raman transitions which involve two quanta, leading to 2D, D+G and 2G signatures.[11] Remarkably we also observe three quanta Raman transitions assigned to 3D, 2D+G, 2G+D, 3G signals (see Figures 5.6 and 5.7).

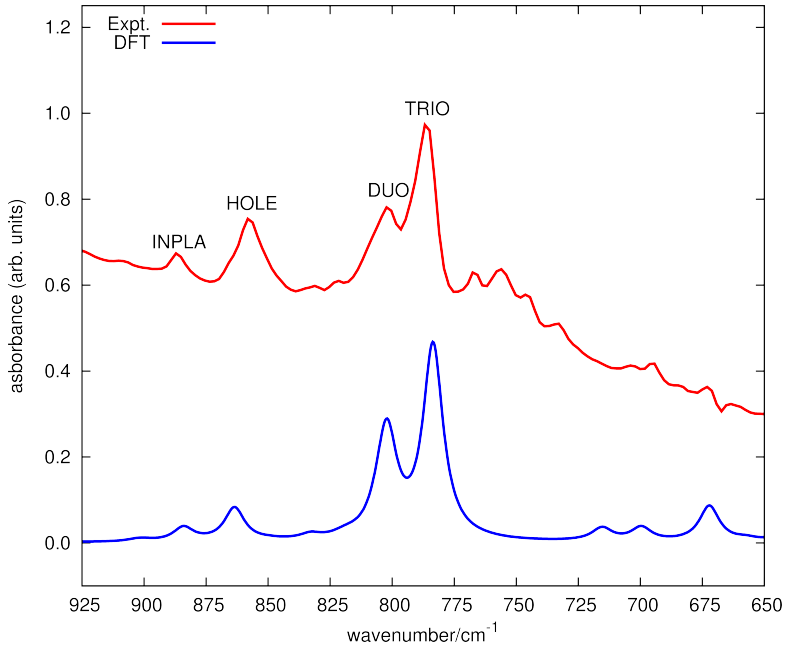

Figure 5.4: *DFT calculated and experimental IR spectrum of* ***C216****.*

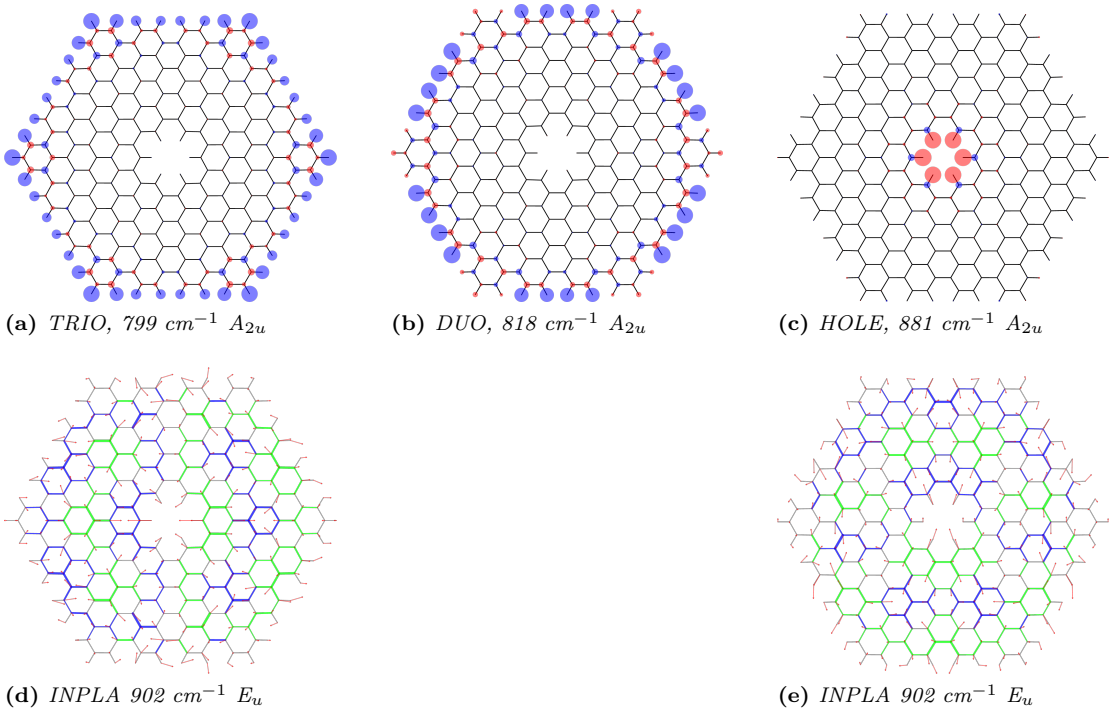

(a) *TRIO, 799 cm*$^{-1}$ A_{2u} **(b)** *DUO, 818 cm*$^{-1}$ A_{2u} **(c)** *HOLE, 881 cm*$^{-1}$ A_{2u}

(d) *INPLA 902 cm*$^{-1}$ E_u **(e)** *INPLA 902 cm*$^{-1}$ E_u

Figure 5.5: *Representation of the nuclear displacements associated to the IR markers which are characteristic of the hydrogenated edges of* ***C216****.*

Notably the Raman intensity profiles in the two- and three-quanta transitions are reminiscent of the intensity pattern found in the first-order Raman spectrum (see Figure 5.7). This has been observed previously in Chapter 3 and rationalized

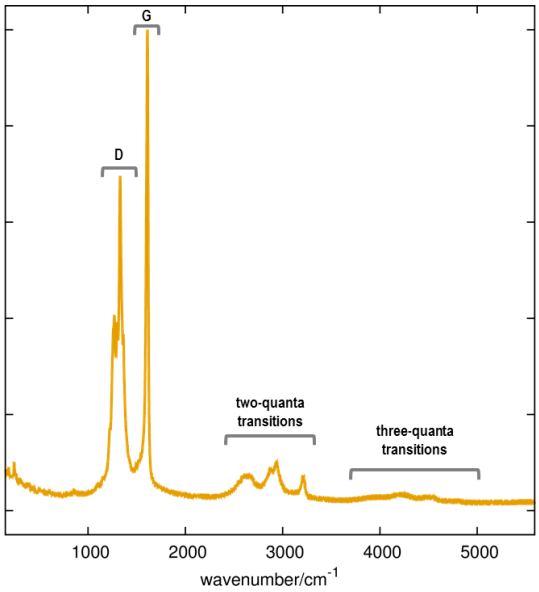

Figure 5.6: *Raman spectrum of* ***C216*** *displayed over the fundamental (150 – 1700 cm^{-1}) and overtones/combinations regions (2200 – 5000 cm^{-1}). Two-quanta Raman transitions assigned to (2D,G+D,2G) are easily observed between 2200 and 3500 cm^{-1} as well as weaker three-quanta Raman transitions assigned to (3D,2D+G,D+2G,3G) which are observed above 3600 cm^{-1}.*

based on an a theoretical description of the Raman cross section for overtones and combinations which, under resonance conditions, leads to the following approximate relation:[11]

$$I_{h+k} \approx I_h I_k \tag{5.1}$$

where I_h, I_k denote the Raman intensities of two first-order Raman transitions and I_{h+k} denotes the Raman intensity of the corresponding combination, with $h = k$ in the case of an overtone. Eq. (5.1) qualitatively explains the experimental results of Figure 5.7 and helps in assigning them straightforwardly. The position of the overtones of the G and D peaks is clearly close to the one expected based on harmonic approximation. The structured shape of the D band leads to 2D and 3D features which are progressively less structured. This is due to the increasing number of possible combination bands among the several D_i peaks which tend to fill the gaps existing among the $2D_i$ and $3D_i$ overtones. Given the same set of D_i peaks, due to the greater number of three quanta states with respect to the two quanta states, it is possible to realize that the 3D signal must be less structured than the 2D signal, as observed in Figure 5.7. With a similar approach, supported by Eq. (5.1), it is straightforward to justify the two features observed in the G+D band, which are due to the relatively sharp G peaks combining with the structured features observed in the D band.

Before dwelling more into the details of the Raman signals of **C216** over the different regions of the spectrum, it is worth mentioning that the comparison of experimental data with simulations of the Raman spectrum based on DFT calculations reveals interesting details which can not be very accurately evaluated with the currently available pre-resonance implementation of the Raman cross section

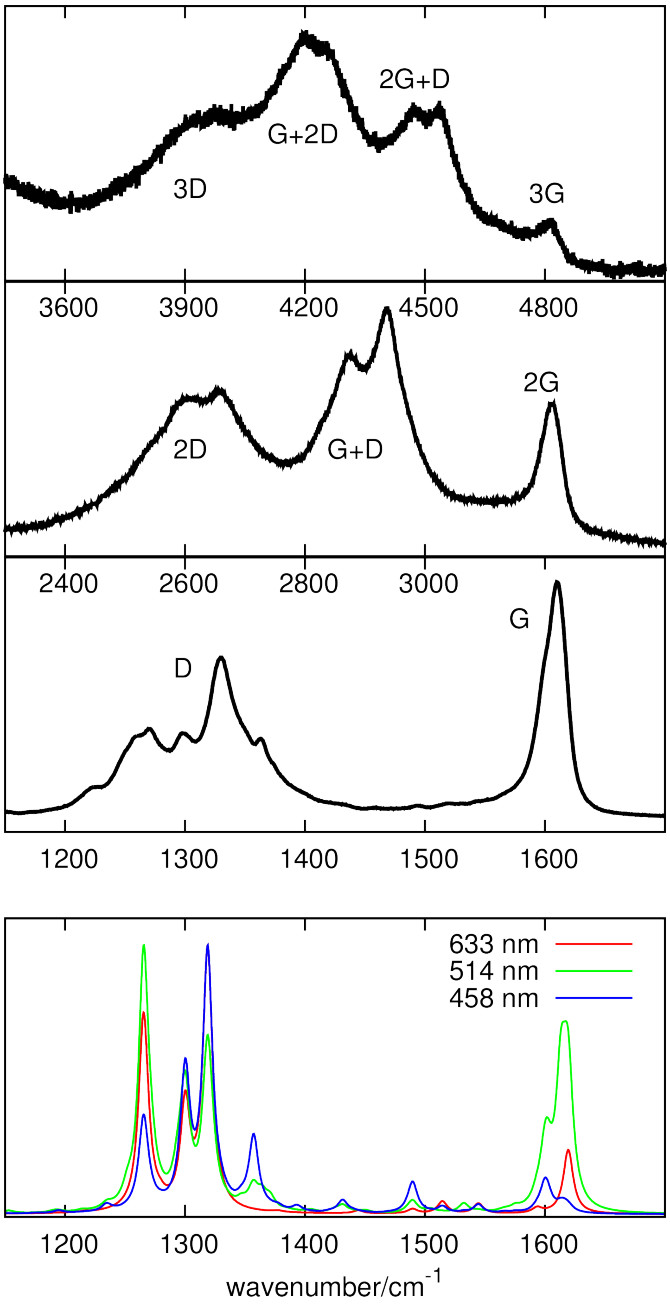

Figure 5.7: *Raman spectrum of* ***C216*** *in the overtones and combination regions involving two and three quanta processes (recorded with 514 nm excitation). The first order Raman spectrum is displayed in the bottom panel to help visually assigning overtones and combinations based on the associated fundamentals. The bottom panel shows the simulated first order Raman spectra based on DFT calculations of the Raman cross section carried out with pre-resonance theory for selected excitation wavelengths.*

available in Gaussian09 D.01,[24] due to the onset of resonance conditions. For instance, inspecting the simulated Raman spectrum obtained with several trial excitation wavelengths reveals a strong dependence of the D vs. G intensity as a function of the excitation wavelength, as displayed in Figure 5.7. The compar-

ison of these simulations against the experimental spectrum recorded with 514 nm excitation reveals that the spectrum computed with 514 nm excitation reasonably accounts for the relative intensity of the G features compared to the D features (see Figure 5.7). However, the relative intensities within the D region are not accounted for reliably, presumably due to the above mentioned limitations of the available theoretical approach. This is based on a far from resonance approach, which may include pre-resonance effects for a given laser excitation on molecular polarizability, but can not exactly cope with the vibronic details of the Raman excitation profile: to this challenging task more accurate quantum chemical treatments have been very recently introduced[128,129] which allow the accurate evaluation of the required Franck-Condon factors, also including the effects of Duschinsky rotation, and could be considered in the near future for further investigation of these interesting aspects.

The G band of **C216** is analyzed in details in Figure 5.8. While the G peak in PAHs with sixfold symmetry belongs to degenerate E species,[1] in the present case we observe for the first time a totally symmetric A_{1g} component in the G peak (named G_1), together with the expected doubly degenerate E_g vibrations (named G_2, G_{3a} and G_{3b}, see Figure 5.8). When focusing the attention on the external edge of **C216** in Figure 5.8 one easily recognizes that the nuclear displacements associated to G_1 match the expected pattern for G-line modes.[1] The totally-symmetric pattern of the G_1 mode is obtained by identically repeating the characteristic G-mode pattern along each one of the six external edges of **C216**. Hence G_1 could be named as the tangential (or perimetral) G-mode of **C216**. Being G_1 totally symmetric, and in a situation close to resonance conditions, this somehow unusual component acquires intensity and becomes comparable to the typical Raman modes usually found in the G band region of six-fold and three-fold symmetric PAHs, which belong to degenerate E_g species. In fact, the other two components of the G-band of **C216** which can be observed after the band deconvolution procedure reported in Figure 5.8, namely G_2 and G_3, are all assigned to E_g modes and display the characteristic vibrational pattern of G-modes.[1] In particular the nuclear displacements of the G_2 feature are localized in the region between the hole and a couple of nearby external vertexes of the **C216** molecule. On the other hand, the G_3 feature encompasses two very close modes computed by DFT with a sizeable intensity, named G_{3a} and G_{3b}, whose nuclear displacements are somehow delocalized over large areas of the **C216** disc. This is especially true for G_{3b}. See Figure 5.9 for representation of nuclear displacement of G modes.

The D band of **C216** is analyzed in details in Figure 5.10. After band deconvolution we can recognize several components and the most intense ones (D_1, D_2, D_3, D_4) find a good counterpart in DFT simulations carried out with the pre-resonance approach and 514 nm excitation, even though, similarly to the G-band case, there are some inaccuracies. Notably the relative intensity of D_3 vs. D_1 is not predicted correctly, as well as there are issues in reproducing the observed spectral pattern above D_4 and below D_1 since the relative intensities of the modes computed in these regions are not correct. The mode D_3 represented in Figure 5.11 displays the nuclear displacement pattern expected for D-modes in molecular graphenes[1] (blue breathing rings in Figure 5.11 are centered at the Clar

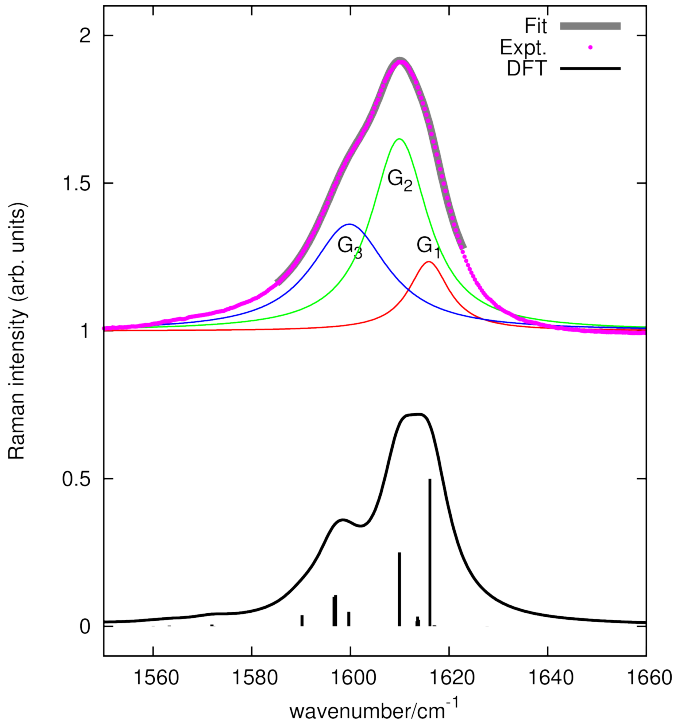

Figure 5.8: *Band deconvolution of the G band region in the Raman spectrum of* ***C216****.*

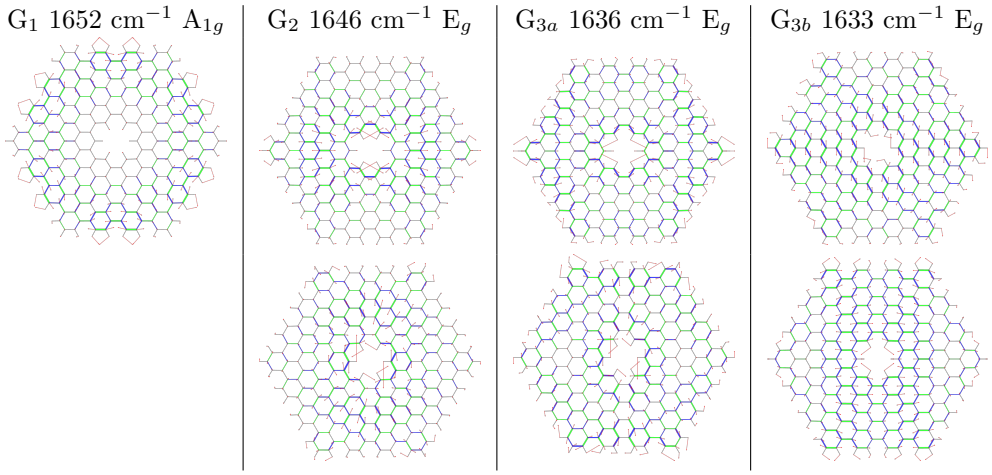

Figure 5.9: *Representation of the normal modes of* ***C216*** *associated with the main experimental G band features.*

rings of **C216** reported in Figure 5.1). Interestingly D_3 is more localized toward the hole of **216**. Mode D_1 nearly displays the expected D-mode displacement pattern (almost completely green breathing rings in Figure 5.11 are centered at the Clar rings of **C216**). Differently from D_3, mode D_1 has nuclear displacements which are larger at the outer edge of **C216**. In any case both D_1 and D_3 modes are truly collective and basically involve the whole π-conjugated disc of the molecule. Mode D_4 displays the expected D-mode pattern at the vicinity of the hole (almost completely blue rings in Figure 5.11) but the other blue breathing

rings are not corresponding to the remaining Clar rings of **C216**. With reference to the discussion of the D-mode of graphitic systems within a periodic boundary conditions approach,[19] the situation found for mode D_4 would correspond to the linear combination of degenerate phonons picked up in the vicinity of the **K** point at the 1st Brillouin edge of graphene (the D-mode of whole graphene would be taken exactly at the **K** mode). Finally, the D_2 mode presents a rather intricate pattern of collective CC stretching vibrations over the whole **C216** disc and it is not straightforward to recognize the typical D-mode pattern.

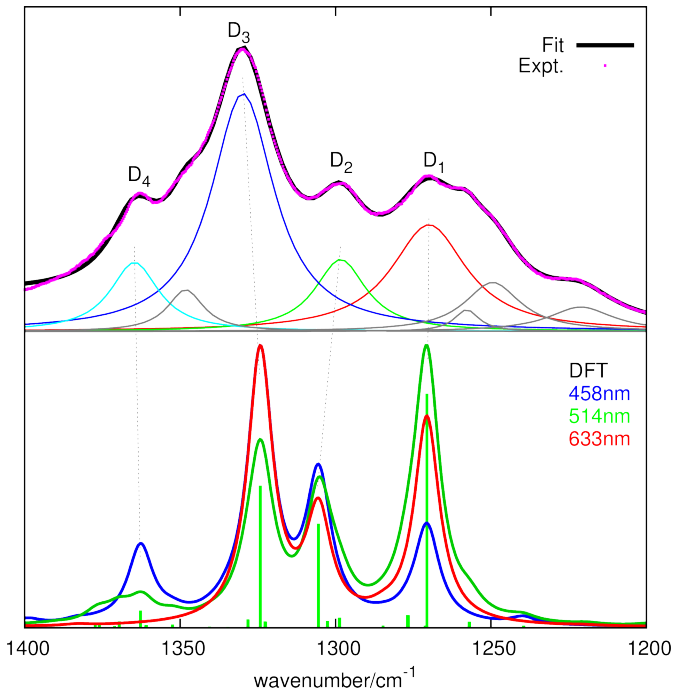

Figure 5.10: *Band deconvolution of the D band region in the Raman spectrum of* ***C216****.*

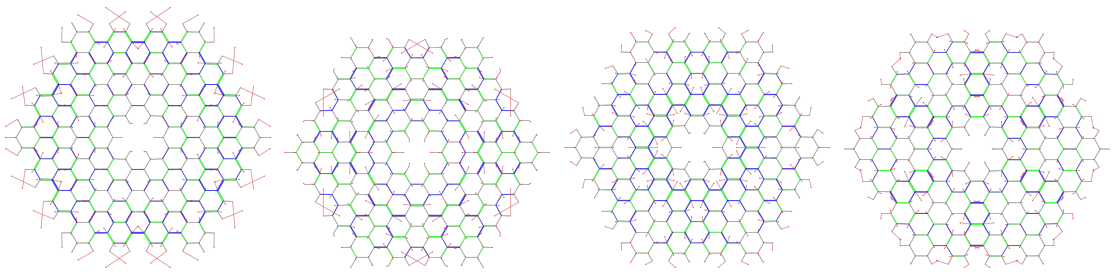

(a) D_1 *1291* cm^{-1} A_{1g} **(b)** D_2 *1327* cm^{-1} A_{1g} **(c)** D_3 *1346* cm^{-1} A_{1g} **(d)** D_4 *1385* cm^{-1} A_{1g}

Figure 5.11: *Representation of the normal modes of* ***C216*** *associated with the main experimental D band features.*

The low wavenumber region of the spectrum displays several characteristic collective deformations (A_1, A_2 and A_6 – see Figure 5.12). Features A_1 and A_2 are assigned to degenerate modes (by symmetry) which involve a shear-like deformation of the overall hexagonal shape of the **C216** molecule. On the other hand A_6 is assigned to a pair of close modes which can be described as the breathing vi-

bration of the hole. In fact, in correspondence of the experimental A_6 signal DFT calculations exhibit two normal modes with close wavenumber and a very similar displacement pattern involving the radial displacement of the carbon atoms from the center of the hole (see Figure 5.13). As observed for the G and D regions, subtle resonance effects are also found in the low wavenumber region of the Raman spectrum, where the experimental spectrum is rather rich of signals. Depending on the chosen excitation in the DFT calculation of the Raman cross section some of them can be evidenced (notably the A_1 peak with 458 nm excitation and the A_2 peak with 514 nm excitation). Overall, the simulation with 514 nm excitation appears as the best option currently available, in line with the fact that the experiments have been carried out with this excitation and considering also the fact that TDDFT calculations carried out on **C216** reveal vertical transitions which are close to experimental absorption features.[44] See Table 5.1 for observing the list of observed and computed Raman features of **C216** in the low wavenumber region.

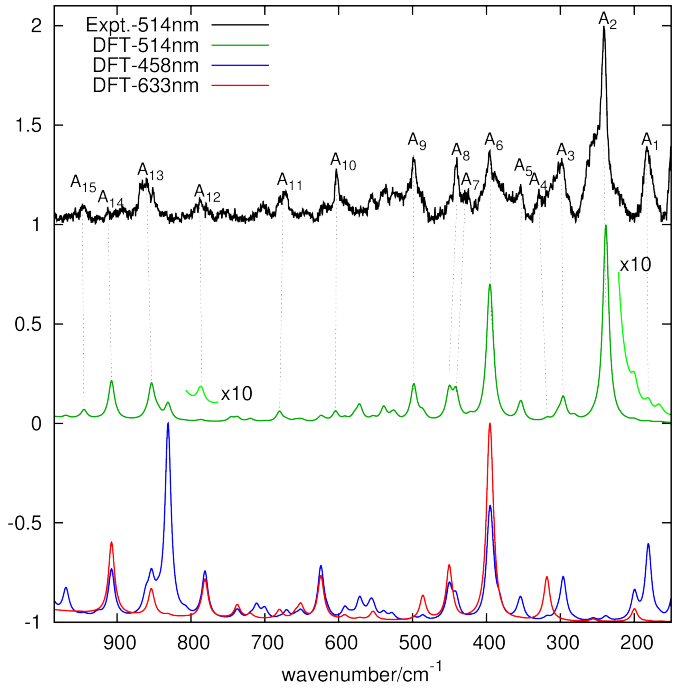

Figure 5.12: *Low wavenumber region of the Raman spectrum of **C216** recorded with 514 nm laser excitation.*

5.3 UV/Vis absorption spectroscopy

Despite the very poor solubility of C216, by using an integration sphere its UV/Vis absorption spectrum could be measured from a suspension in chlorobenzene (Figure 5.14). The obtained spectrum of **C216** displayed a broad absorption centered roughly at about 500 nm. A closer look at the spectrum by taking the second derivative displayed subtle changes in the slope at 620, 520, and 450 nm, which might correspond to different optical transitions (Figure 5.14). TD-DFT calcu-

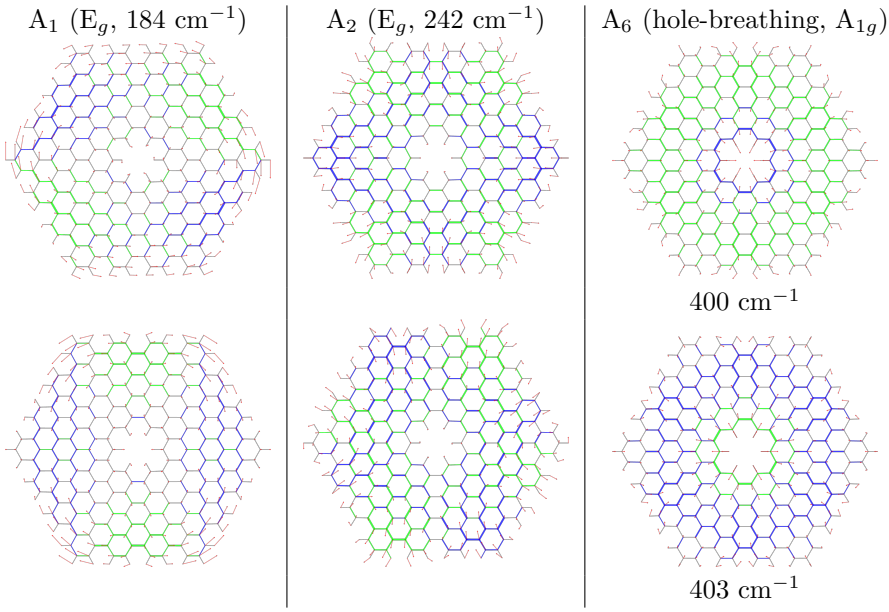

Figure 5.13: *Representation of the normal modes of **C216** associated with the main experimental A band features.*

feature #	wavenumber (DFT)	wavenumber (expt.)
A_1	184 (E_g)	183
A_2	242 (E_g)	241
A_3	301 (E_g)	298
A_4	323 (A_{1g})	329
A_5	359 (E_g)	353
A_6	400,403 (A_{1g}, A_{1g})	395
A_7	448 (E_g)	429
A_8	458 (A_{1g})	440
A_9	506 (E_g)	499
A_{10}	614 (E_g)	603
A_{11}	691 (A_{1g})	675
A_{12}	798 (E_g)	788
A_{13}	867 (A_{1g})	860
A_{14}	922 (A_{1g})	912
A_{15}	960 (E_g)	947

Table 5.1: *List of observed and computed (unscaled) Raman features of **C216** in the low wavenumber region.*

lations on **C216** indeed revealed doubly degenerate transitions at 613 and 519 as well as a cluster of transitions at 455, 439, 426, and 414 nm. This respectively corresponds to p-, β-, and β′-bands in Clar's notation, and are consistent with the positions estimated from the experimental spectrum. In contrast, the absorption spectrum of **C222** features a broad absorption roughly peaked at 750 nm.[130] TD-DFT calculation reveals that the p-band, which is generally the one most related to the HOMO-LUMO transition in PAHs, blue-shifts by about 100 nm (0.3 eV), when comparing **C222** (714 nm) with **C216** (613 nm). Furthermore, DFT calculations on coronoid **C216** and **C222** gave more insight into the

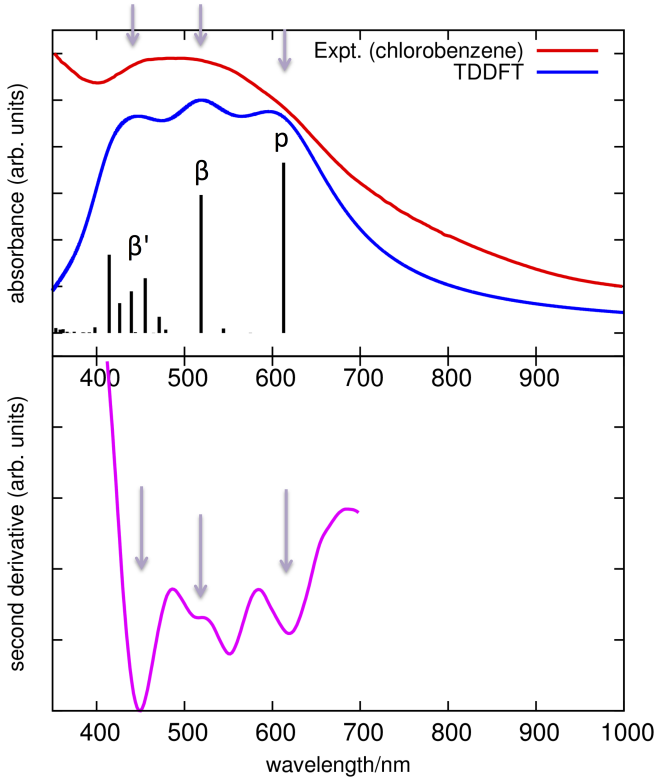

Figure 5.14: *UV-Vis absorption spectrum of **C216** in chlorobenzene suspension (top) with its second derivative (bottom). The arrows indicate the positions of the transitions determined by TD-DFT, which are also shown with black sticks whose length is proportional to the oscillator strength. The simulated absorption profile from TD-DFT transitions is also reported for comparison with experimental data.*

effect of the "hole". The HOMO and LUMO levels of **C216** are found at -4.7 and -2.5 eV, respectively, with a HOMO-LUMO gap of 2.2 eV while the HOMO and LUMO levels of **C222** are found to be at -4.5 and -2.7 eV, respectively, with a HOMO-LUMO gap of 1.8 eV.[131]

This result shows that the introduction of the hole in the **C222** disk increases the HOMO-LUMO gap by 0.4 eV (see Figure 5.15: decrease of the HOMO and increase of the LUMO by 0.2 eV). This is in agreement with the blue shift of the maximum of the UV-Vis absorption of **C216** compared with that of **C222**.

In conclusion, the presence of a "hole" in the structure of an extended molecular graphene as **C216** is a source of non-planarity. This concept may be exploited as well as chlorination to modulate the three dimensional structure of molecular graphenes out of the usual two dimensions of the plane. However, this modification of the structure is able to change to a greater extent the HOMO-LUMO gap of the molecule compared to chlorination since the presence of the hole can partially break π-conjugation pathways.

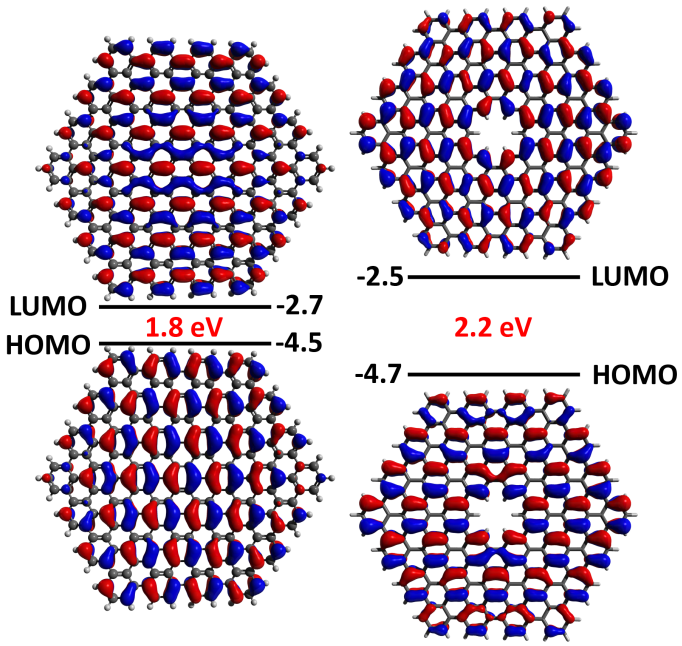

Figure 5.15: *HOMO and LUMO levels and HOMO-LUMO gap of* ***C222*** *and* ***C216*** *calculated by TD-DFT at the B3LYP/6-31G(d,p) level.*

CHAPTER 6

Thiophene-based heterophenoquinones

This Chapter deals with the characterization by vibrational spectroscopy of two members[1] of the bithiophene family substituted with cyclohexadienones, namely **QDTT** and **QBT** (see Figure 6.1). In the paper by Tampieri *et al.*[83] one can find the synthesis procedure for both molecules and the results of characterization techniques other than vibrational spectroscopy (namely, electron paramagnetic spectroscopy (EPR), NMR and XRD). In QDTT the central units of QBT are replaced by fused rings in order to investigate the influence of the QBT cis-trans isomerization together with the stiffening of the central conjugated thienilenic core. Hence the Dithieno[3,2-b:2',3'-d] thiophene unit was chosen since it is characterized by the same number of π-electrons as bithiophene. One thus expects in the Dithieno[3,2-b:2',3'-d] thiophene unit similar π-conjugation to that of cis bithiopene. A minor influence of the trans vs. cis form of bithiophene could play a role when comparing QDTT with QBT since QBT exhibits both *cis* (*i.e.*, *syn*) or *trans* (*i.e.*, anti) conformations at the bond linking the two thiophene units.

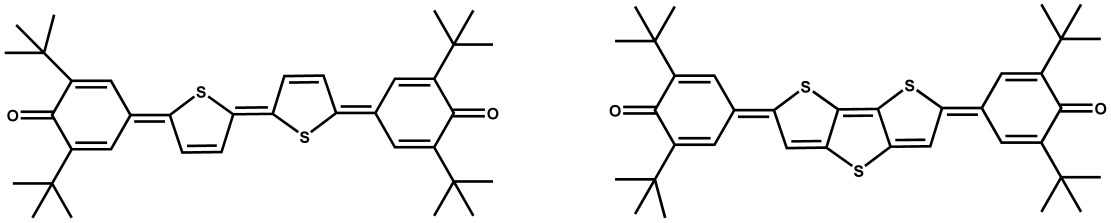

(a) *Molecular structure of* ***QBT*** **(b)** *Molecular structure of* ***QDTT***

Figure 6.1: *Molecular structures of* ***QBT*** *and* ***QDTT****.*

[1] Chemically named: 4,4'-(dithieno[3,2-b:2',3'-d]thiophene-2,6-di-yl)bis(2,6-ditert-butylcyclohexa-2,5-dienone)

6.1 Results and discussion

It has been shown that, due to the peculiar radicaloid electronic structure of thiophene-based heterophenoquinones, DFT is not able to fully cope with their molecular properties and structure.[75] However, as a practical way to partially overcome these limitations of current DFT methods, it has been demonstrated that by displacing the geometry of the molecule along the Effective Conjugation Coordinate (see below) it is possible to amend the most dramatic deviations of the simulated Raman spectra from experimental observation.[75] The computational cost of this procedure is very convenient, compared for instance with more satisfactory multi-configuration computational approaches (*e.g.*, Complete Active Space Self-Consistent Field – CASSCF). Navarrete *et al.*[132] reformulated the dynamical theory of polyconjugated molecules by defining an Effective Conjugation Coordinate (ECC, also labeled as Я). It describes the vibrational trajectory which best favors relative changes of C=C/C-C bond lengths, *i.e.*, which mostly involves π-electron delocalization along the conjugated polymer chain. In the case of polythiophene, the Я coordinate has been defined by Navarrete *et al.* as a linear combination of internal stretching coordinates in the following form:

$$Я = 1/N(R_1 - R_2 + R_3 - R_4 + R_5 - R_6 + R_7 - R_8) \tag{6.1}$$

where the internal coordinates R, can be identified with the specific CC stretching of the thiophene moieties in Figure 6.2; N is a normalization factor.

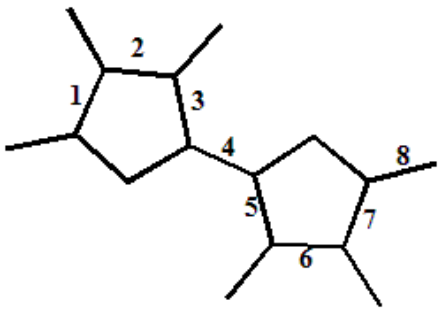

Figure 6.2: *Definition of the Я coordinate (also named ECC) in polythiophene.*

Hence, we have displaced by $\Delta Q = 0.15$ Å amu$^{1/2}$ the geometry optimized at B3LYP/6-31G(d,p) level of both **QBT** and **QDTT**. The mode with largest Raman intensity at the optimized geometry was selected for displacing the geometry, following the procedure described by Canesi et al.[75] This implies that the mode with largest electron-phonon coupling is selected: in fact, a characteristic feature of the ECC is the strong electron-phonon coupling (see for instance the work by Tommasini et al.*et al.*[10] and references therein). As can be seen in Figure 6.3 below, the mode computed at 1467 cm^{-1} (the strongest Raman mode of **QBT** at the optimized geometry) presents the alternated CC stretching pattern expected based on the definition of ECC described above (see Figure 6.2 and Equation 6.1).

After displacing the geometry of **QBT** as described above, the mode significantly changes its wavenumber, which improves the simulated Raman spectrum

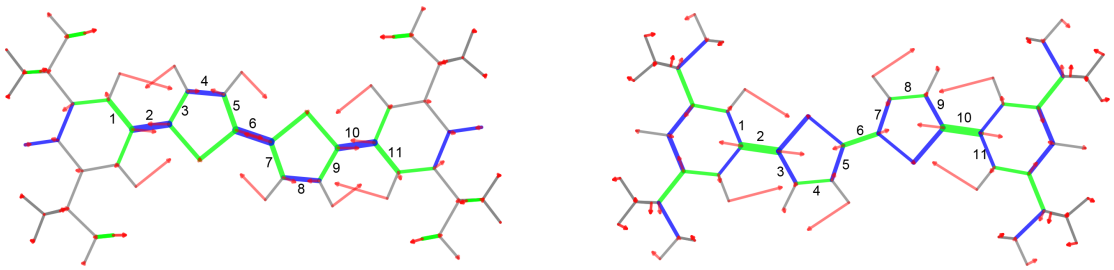

(a) *1467 cm^{-1}; 0 km/mol; 162052 A^4/amu; ECC mode, B3LYP/6-31G(d,p) optimized geometry*

(b) *1335 cm^{-1}; 0 km/mol; 81855 A^4/amu; ECC mode, displaced geometry*

Figure 6.3: *Representation of the ECC normal modes of **QBT** in the optimized and displaced geometries. The reported wavenumbers have not been scaled by the 0.98 factor. Red segments represent displacement vectors; CC bonds are represented as green (blue) lines of different thickness according to their relative stretching (shrinking).*

(see Figure 6.4). However the ECC character of the mode is maintained after in the displaced geometry, which can be taken as an indication of the soundness of this approach.

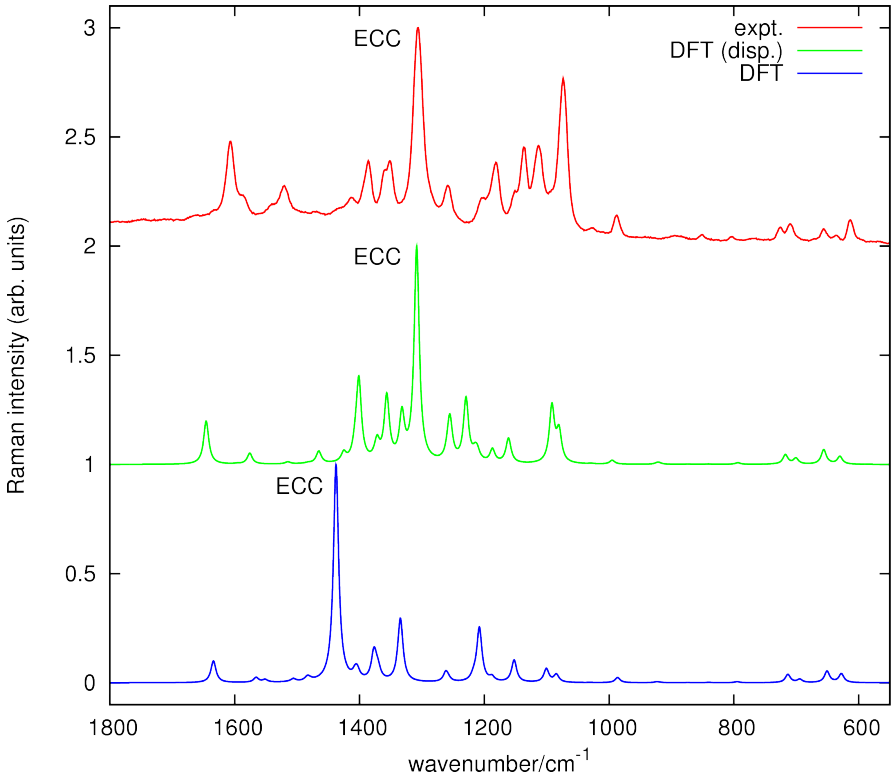

Figure 6.4: *Raman spectrum of **QBT** recorded with 632.8 nm excitation (red line). The Raman spectra simulated with DFT methods (B3LYP/6-31G(d,p), frequency scaled by 0.98) before and after displacing geometry are displayed with blue and green lines respectively.*

Compared with the standard DFT calculation carried out at equilibrium geometry, this peculiar geometry displacement significantly improves the simulation of the Raman spectra of **QDTT** as well, as reported in Figure 6.5. For both

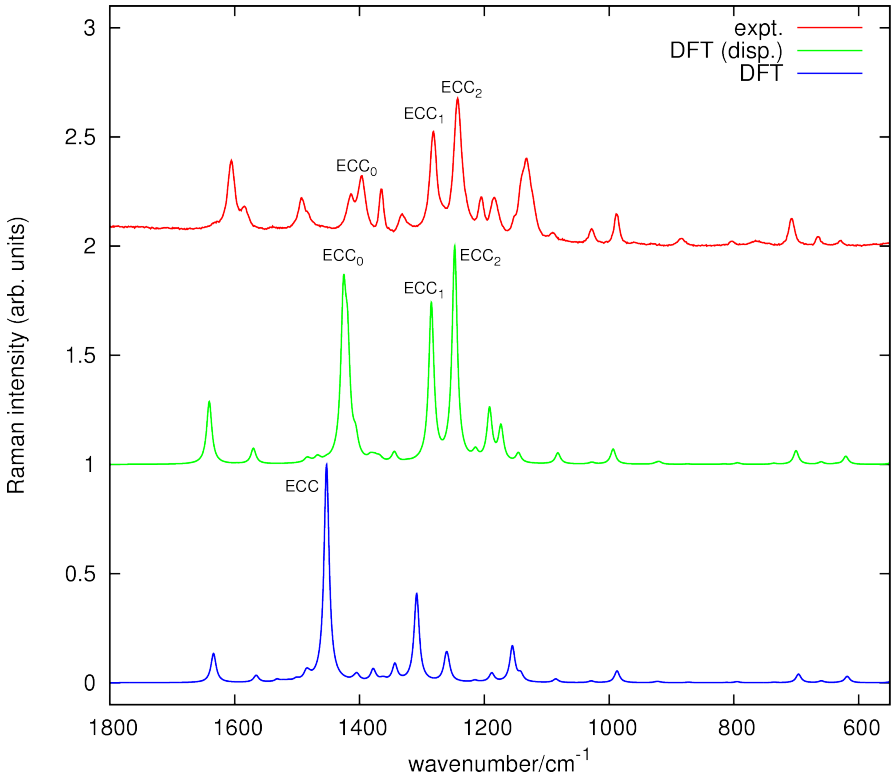

Figure 6.5: *Raman spectrum of **QDTT** recorded with 632.8 nm excitation (red line). The Raman spectra simulated with DFT methods (B3LYP/6-31G(d,p), frequency scaled by 0.98) before and after displacing geometry are displayed with blue and green lines respectively.*

molecules, the simulated Raman spectrum after geometry displacement is in a good agreement with the experimental one. In particular, the experimentally observed intense ECC features fall in the correct spectral range in the simulated spectra at displaced geometries. In order to further check the reliability of the geometry displacement method, it is also worth analyzing the normal modes relevant for Raman spectroscopy of **QDTT** before and after the displacement procedure. One expects that the pattern of the nuclear displacement relevant for assigning the Raman spectra does not substantially change upon geometry displacement, so that the description of vibrational structure is renormalized but qualitatively preserved. Figure 6.6 reports the graphical representation of the ECC modes in **QDTT** before and after geometry displacement. In **QDTT**, upon geometry displacement, it is possible to find three intense ECC modes. These have been labeled ECC_0, ECC_1 and ECC_2 and are shown in Figure 6.6. In **QDTT**, just ECC_2 strictly follows completely the ECC definition reported above. ECC_0 and ECC_1 follow this definition partially. For instance (see Figure 6.6), in the case of ECC_0, the bond at position 6 should stretch (while it shrinks) and for ECC_1, the bonds at positions 3 and 9 would have to stretch (while they shrink).

Further support to the displaced geometry approach is given by the analysis of the IR spectra reported in Figure 6.7. At the B3LYP/6-31G(d,p) equilibrium structure the simulated IR spectra do not capture correctly the experimental features in the vicinity of 1600 cm^{-1} (labeled *a* and *b* in Figure 6.7). However, for

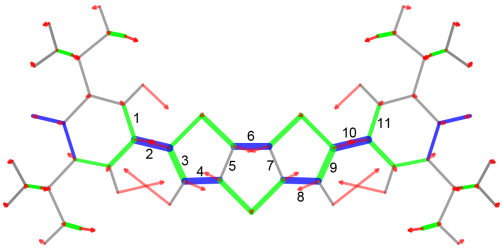

(a) *1482 cm^{-1}; 2 km/mol; 131755 A^4/amu; ECC mode, B3LYP/6-31G(d,p) optimized geometry*

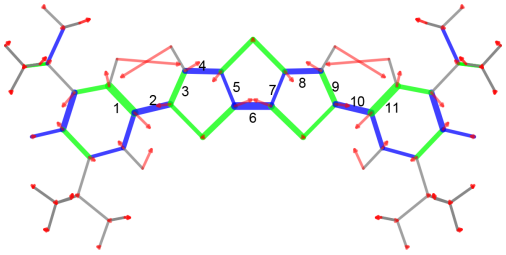

(b) *1455 cm^{-1}; 1 km/mol; 43930 A^4/amu; ECC_0 mode, displaced geometry*

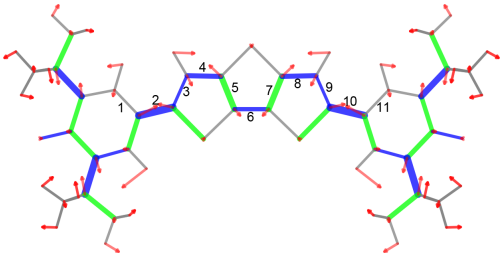

(c) *1311 cm^{-1}; 0 km/mol; 41204 A^4/amu; ECC_1 mode, displaced geometry*

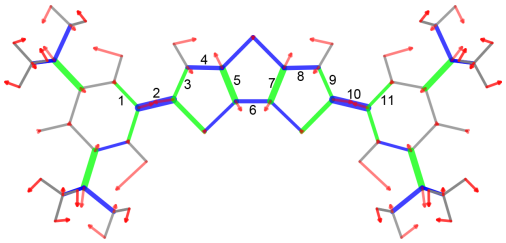

(d) *1273 cm^{-1}; 0 km/mol; 54400 A^4/amu; ECC_2 mode, displaced geometry*

Figure 6.6: *Representation of the ECC normal modes of **QDTT** in the optimized and displaced geometries. The reported wavenumbers have not been scaled by the 0.98 factor. Red segments represent displacement vectors; CC bonds are represented as green (blue) lines of different thickness according to their relative stretching (shrinking).*

both **QBT** and **QDTT**, the two features *a* and *b* nicely emerge in the simulated IR spectra at the displaced geometries. These are assigned to the anti-symmetric C=O stretching (band *a*) and to the anti-symmetric ring stretching (band *b*) of the quinoid end groups of each molecule. The normal modes of **QBT** and **QDTT** associated to bands *a* and *b* are sketched in Figure 6.8 and Figure 6.9, respectively.

Interestingly, DFT calculations on **QBT** and **QDTT** reveals that the IR intensity of the antisymmetric C=O stretching bands (computed at 1625 cm^{-1} – unscaled) are remarkably strong: the absorption intensity is 2448 km/mol in **QBT** and 2322 km/mol in **QDTT**. This intensity is a magnitude higher compared to the intensity of the C=O stretching in the molecule without a radicaloid character (see Figure 6.10). Because of this large absorption, and in agreement with the experimental spectra, the antisymmetric C=O stretching bands dominate the IR spectra over the whole fingerprint region (see Figure 6.7).

In conclusion, compared with the previously reported investigation on radicaloid thiophene-based heterophenoquinones,[75] the presented investigation shows the reliability of the "displaced geometry" approach not only for helping the analysis of experimental Raman data (as initially proposed) but also for supporting the assignment of IR spectra.

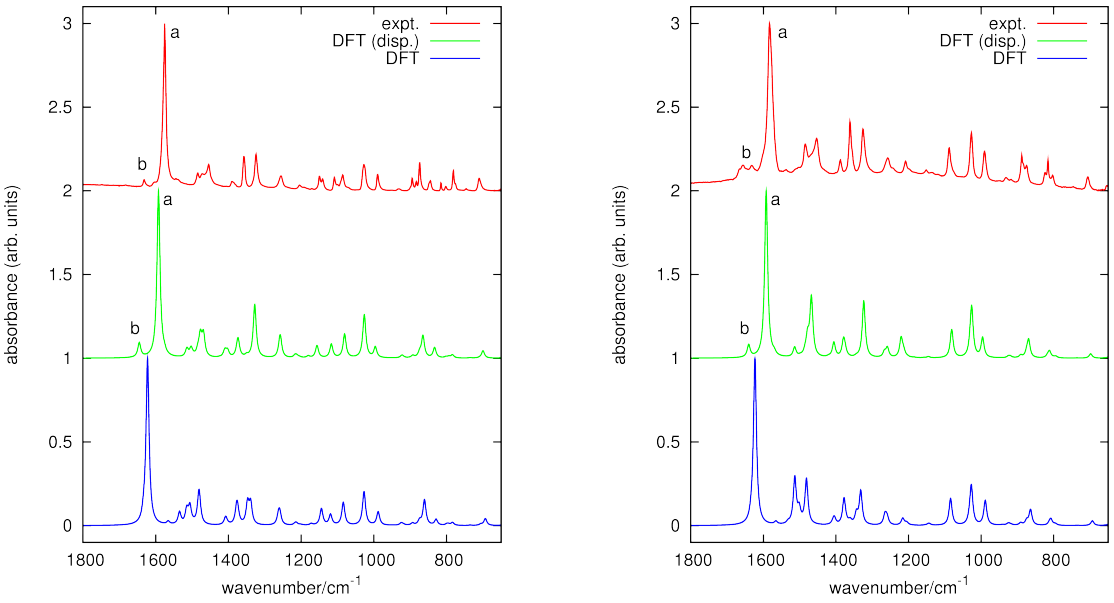

(a) ***QBT*** **(b)** ***QDTT***

Figure 6.7: *IR spectra of* ***QBT*** *and* ***QBT*** *recorded with micro-IR setup (red line). The IR spectra simulated with DFT methods (B3LYP/6-31G(d,p), frequency scaled by 0.98) before and after displacing geometry are displayed with blue and green lines respectively.*

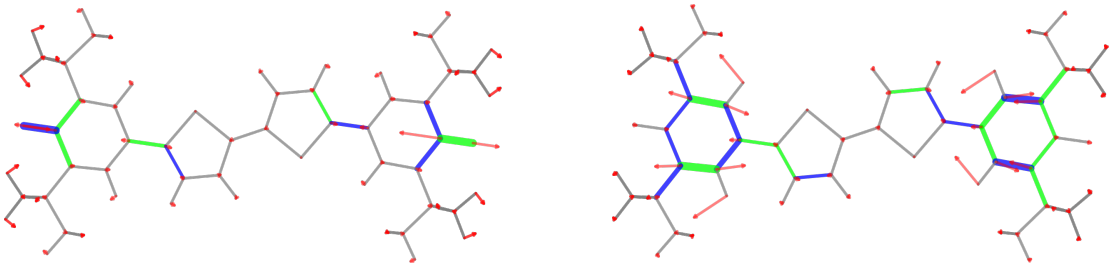

(a) *1625 cm^{-1}; 2448 km/mol; 0 A^4/amu; Mode a, antisymmetric C=O stretching*

(b) *1679 cm^{-1}; 211 km/mol; 0 A^4/amu; Mode b, antisymmetric ring stretching*

Figure 6.8: *Normal modes assigned to features a and b in the IR spectra of* ***QBT*** *(from DFT calculations on displaced geometries). The reported wavenumbers have not been scaled by the 0.98 factor. Red segments represent displacement vectors; CC bonds are represented as green (blue) lines of different thickness according to their relative stretching (shrinking).*

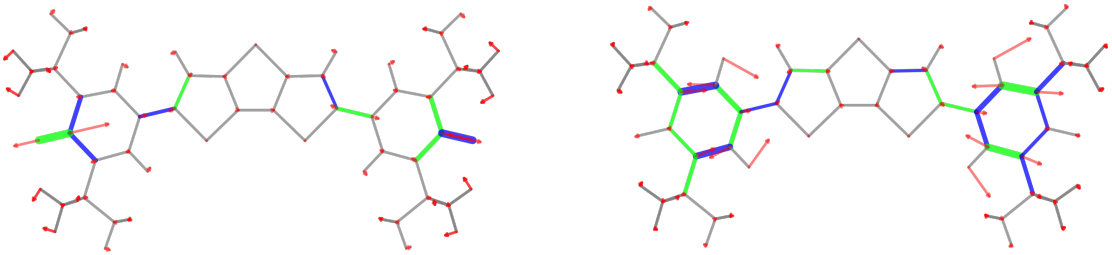

(a) *1625 cm^{-1}; 2322 km/mol; 6 A^4/amu; Mode a, antisymmetric C=O stretching*

(b) *1674 cm^{-1}; 171 km/mol; 194 A^4/amu; Mode b, antisymmetric ring stretching*

Figure 6.9: *Normal modes assigned to features a and b in the IR spectra of **QDTT** (from DFT calculations on displaced geometries). The reported wavenumbers have not been scaled by the 0.98 factor. Red segments represent displacement vectors; CC bonds are represented as green (blue) lines of different thickness according to their relative stretching (shrinking).*

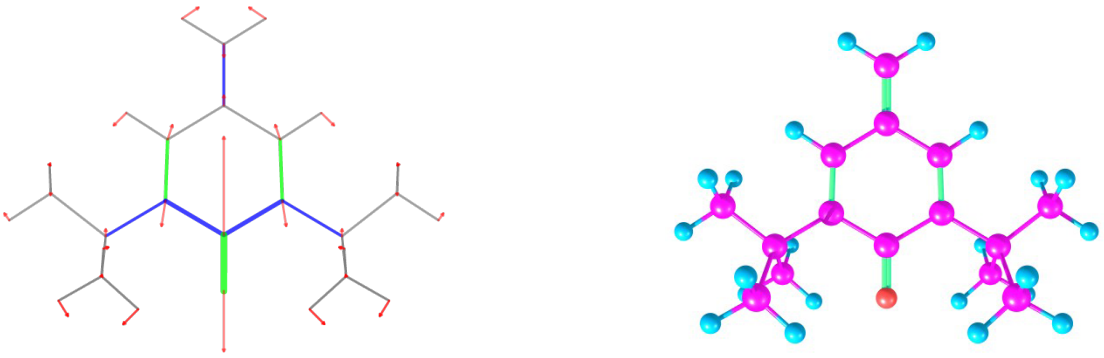

(a) *nuclear displacement*

(b) *structure*

Figure 6.10: *Nuclear displacement of the C=O stretching vibration of the end group of the thiophene derivatives considered in this work. This is a closed shell molecule with no radicaloid character. DFT calculations determine this mode at 1692 cm^{-1}, with absorption intensity of 227 km/mol. Red segments represent displacement vectors; CC bonds are represented as green (blue) lines of different thickness according to their relative stretching (shrinking).*

CHAPTER 7

Other applications of molecular spectroscopy: rubbers and π-stacking in Amphotericin B

In this chapter, vibrational spectroscopy has been used to investigate orientational and crystallization properties of rubbers and intermolecular interactions in Amphotericin B (**AmB**). In particular, in first section IR spectroscopy has been used to analyze strain induced crystallization and orientation in natural rubber (NR), polybutadiene rubber (BR) and their blend (NR/BR); and in second section Resonance Raman spectroscopy has been used for monitoring aggregation of **AmB** in solution state as a function of concentration.

7.1 Molecular spectroscopy of natural rubber, *cis*-polybutadiene and their blend

7.1.1 Introduction

Several methods are available for the analysis of the crystal structure of polymers. Among these X-ray diffraction is considered one of the most powerful tools available. However, since vibrational spectroscopys provides information at the molecular level, it is capable to support the analysis of polymers, also disclosing details on their crystal structure.[133] In particular, among non-destructive quantitative methods, vibrational spectroscopy provides valuable information on the molecular orientation and crystallization. These data can be used to correlate the physical and mechanical properties of polymers to their structure at the molecular level.[134] In our research, we have focused on the relation between the micro-structure and the mechanical properties of rubber, an important polymeric material with several applications in industry and engineering.

From the point of view of vibrational spectroscopy, upon crystallization of polymers, several bands in their spectra may remarkably increase their intensity. These are named crystallization-sensitive bands and can be used as markers of the degree of crystallinity of the polymeric material. Some polymers may crystallize into in different crystal structures associated to different molecular conformations. For example, poly(vinylidene fluoride) (PVDF) crystallizes into at least four crystal modifications depending on the preparation condition. The vibrational spectra of these crystal forms are different from each other and the bands characteristic of the associated conformers can be detected. Hence, by analysing conformation-sensitive bands, one can investigate the molecular structure existing in the crystalline phase of the polymer and detect changes in the crystal structure of samples depending on the preparation conditions.[133,135]

In the case of natural rubber (**NR**) it is possible to orient and crystallize it under tension, while it reverts to its original amorphous state by relaxation of the stress.[136] The mechanical properties of the crystallites (*e.g.*, the Young's modulus along the chain axis) are very sensitive to molecular conformation, even if the chemical structure of the different conformers is necessarily the same.[137] Such a dependence in the Young's modulus on the chain conformation can be investigated by understanding the deformation mechanism of the polymeric material at the molecular level, *i.e.*, by describing it in terms of the atomic displacement induced by the external force. Hence vibrational spectroscopy, being a molecular structure sensitive technique, can be profitably employed to sensitively detect even slight changes in structure and conformation of the polymer chains under mechanical stress.[133]

While almost complete data are present in the literature for **NR** and **BR**,[25–28] little is known for **NR/BR** blends. This motivates the experimental study reported in this chapter.

In this work FT-IR spectroscopy has been used to study the strain induced orientation and crystallization of **NR**, Polybutadiene rubber (**BR**) and their blend (**NR/BR**). The vibrational frequencies of characteristic spectral features of the samples have been shown to be sensitive to the structure of the molecules of interest and to changes in their environment induced by mechanical stress.

For selected FT-IR experiments a polarizer was used to help distinguishing between orientation and crystallization effects. Finally, FT-IR results were compared with the outcomes from X-Ray diffraction (XRD) experiments.

Finally, it has been shown that it is possible to find the onset strain induced crystallization by FT-IR spectroscopy in **NR** and **BR**s. Also, it is possible to analyze orientation by polarized FT-IR spectroscopy. In the future, it is probable to analyze onset and propagation of cracks by polarized FT-IR spectroscopy in different types of rubbers.

7.1.2 Materials

Natural rubber (**NR**), different *cis*-1,4-polybutadiene rubbers (**BR**) and their 50/50 blends have been studied. The **BR**s have been selected with a different *cis*-unit content, molecular weight (Mw) and molecular weight distribution (MWD) of the uncured rubber. $\mathbf{BR}_{LL}$ means **BR** sample with low *cis*-unit content and

low molecular weight, and $\mathbf{BR}_{MM}$ means **BR** sample with medium *cis*-unit content and medium molecular weight (see Table 7.1). All materials were supplied by Versalis S.p.A (Ravenna, Italy), together with the structural characterization data reported in Table 7.1. The interested reader may find further information about the sample preparation and molecular weight characterization in the cited literature.[87]

Material	*cis*-content	Mw	MWD
$\mathbf{BR}_{LL}$	94	384000	2.5
$\mathbf{BR}_{MM}$	96.4	487000	4.1

Table 7.1: *Structural characteristics of the different **BR**s.*

7.1.3 Experimental methods

Preparation of the thin samples for FT-IR measurements

Sheets of 0.12 mm thickness were cured according to the method described by Mohammad Poor[87] by using two flat discs. Sample strips with dimensions 25 × 10 × 0.12 mm^3 were then cut and stretched at room temperature with nominal strain rate of 1.8 min^{-1} from $\varepsilon = 0$ to $\varepsilon = 8$.

FT-IR

Micro FT-IR measurements were carried out with Nicolet Nexus equipment coupled with a Thermo-Nicolet Continuμm infrared microscope using a 15× infrared objective and a cooled MCT detector (77 K) or DTGS detector. The spectra of the stretched samples were acquired with 4 cm^{-1} resolution in the 400 - 4000 cm^{-1} spectral range by accumulating at least 128 scans. The PIKE Technologies wire grid IR polarizer was used in some experiments to polarize the IR light parallel and perpendicular to the stretching direction of the samples.

XRD

Wide angle X-ray spectroscopy (WAXS) was carried out using a Bruker D8 advanced X-ray diffractometer. An X-ray radiation (λ = 1.5406 Å) with the incidence angle (2θ) from 15° to 40° was used. Scanning rate was $0.02°s^{-1}$. The specimens were stretched in a controlled way and fixed onto a rigid holder. After about 30 minutes, WAXS patterns were obtained at room temperature.

7.1.4 Results and discussion

The representative FT-IR spectra of **NR** and **BR** samples are reported in Figure 7.1. Comparing these spectra with literature data,[25–28] it is possible to straightforwardly assign all the relevant bands. Figure 7.1 is given as a reference helpful for listing the spectral markers which will be later considered for the characterization of the rubber samples. In particular CH out-of-plane bending (840 cm^{-1}), C-CH_3 stretching (980 cm^{-1}), C-C stretching (1126 cm^{-1}), CH_2 twisting (1240 cm^{-1}) and CH_2 wagging (1361 cm^{-1}) bands for **NR**, and CH_2 twisting (1240 cm^{-1}) and CH_2 in-plane asymmetrical bending (1404 cm^{-1}) bands

for **BR**, will be shown to be dependent on strain and sensitive to strain-induced crystallization.

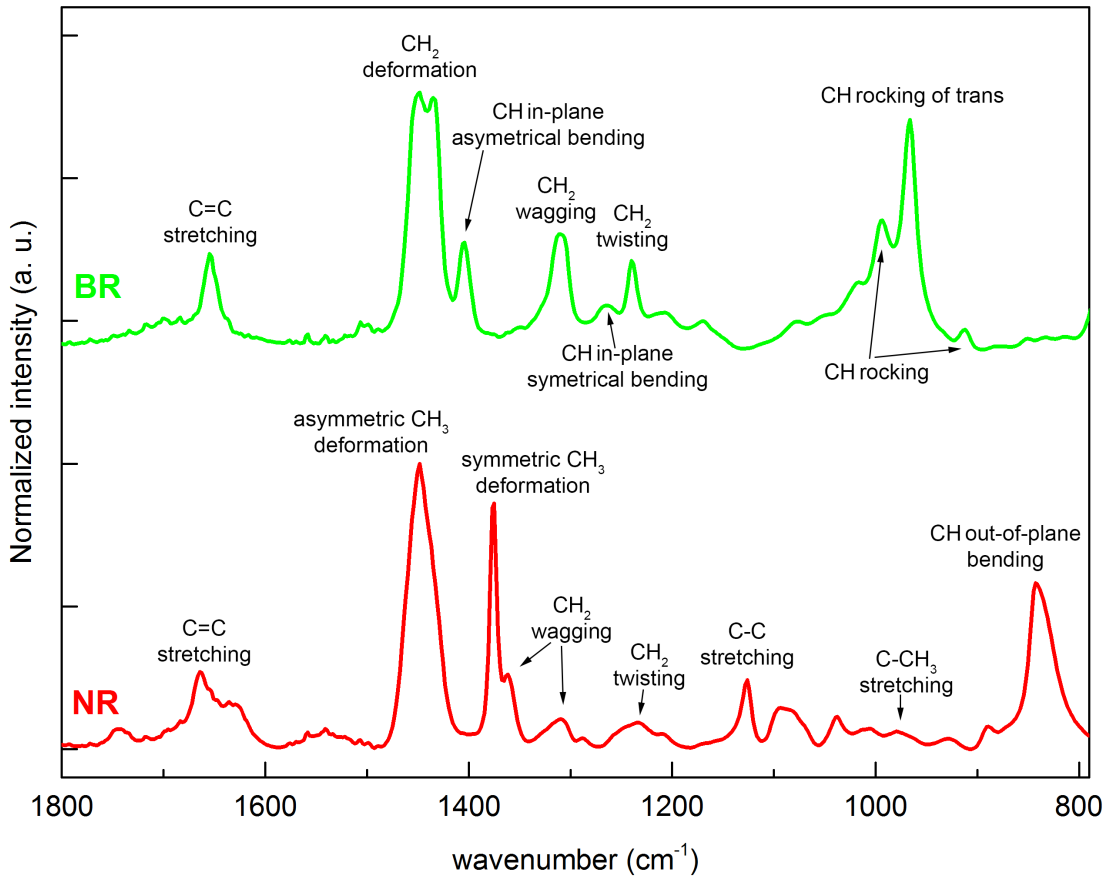

Figure 7.1: *FT-IR spectra of **NR** and **BR** samples recorded at imposed strain ε=5 with the relevant band assignments deduced from literature.*[25–28]

Since the applied strain causes molecular orientation phenomena which are also leading to crystallization for higher strain values, it is of interest to record polarization dependent FT-IR spectra.[136] In particular, it is useful to record the IR spectra as a function of the angle θ formed by the stretching direction and the direction of the electric field associated to the IR light (which is controlled by a polarizer). Both directions lie within the plane defined by the thin rubber sheet which constitutes the sample; in the FT-IR experiments this plane is perpendicular to the propagation of the IR light beam.

The experiments have been planned as follows:
(1) FT-IR spectroscopy of **NR** samples over a range of strains (ε=0 to ε=5).
(2) FT-IR spectroscopy of $\mathbf{BR}_{MM}$ samples over a range of strains (ε=0 to ε=5).
(3) FT-IR spectroscopy of $\mathbf{NR/BR}_{MM}$ samples over a range of strains (ε=0 to ε=8).
(4) Polarized FT-IR spectroscopy of $\mathbf{NR/BR}_{MM}$ and $\mathbf{NR/BR}_{LL}$ samples over a range of strains (ε=0 to ε=8).

NR samples

Strips of **NR** samples have been stretched over a range of strains, *i.e.*, from ε=0 to ε=5. The IR spectra of unstretched and stretched samples are compared in Figure 7.2. Due to the thickness of the sample (of the order of 10 to 100 μm depending on the applied strain) the IR spectra are saturated in the wavenumber range extending from 1370 cm^{-1} to 1500 cm^{-1}, where two IR transitions are present, namely the symmetric CH_3 deformation (1376 cm^{-1}) and the asymmetric CH_3 deformation (1450 cm^{-1}).[138]

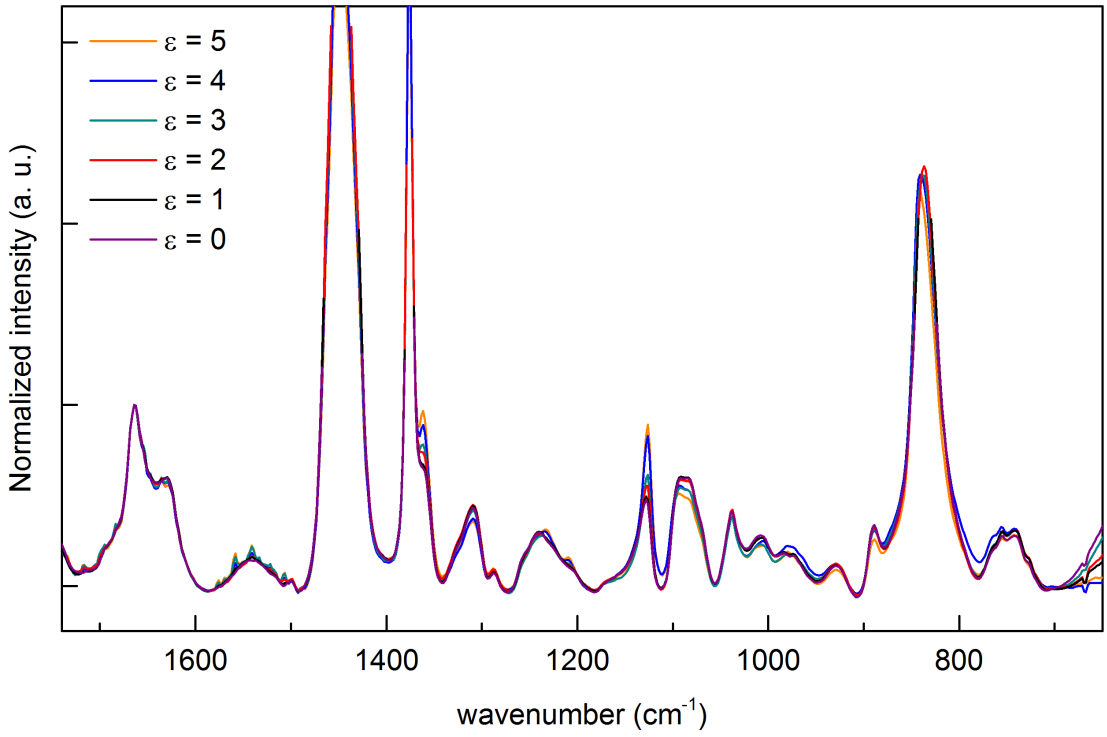

Figure 7.2: *Infrared spectra of **NR** samples recorded on specimens stretched at different strain (ε=0-5) in the 650 – 1750 cm^{-1} wavenumber range. The two bands at 1376 cm^{-1} and 1450 cm^{-1} are saturated.*

The intensities of the reported spectra have been normalized with respect to the C=C stretching band at 1663 cm^{-1}.[139] The intensity of the C=C stretching band have been used for normalization because it does not depend on the strain (refer to Siesler *et al.*[140]) This was proved during a series of experiments on $\mathbf{NR/BR}_{LL}$ samples, which have been stretched over a range of strains (from $\epsilon = 0$ to $\epsilon = 7$). At each strain, the thickness of the samples was measured and the FT-IR spectra were recorded. The intensity of the C=C stretching band divided by the thickness of the sample has been plotted in Figure 7.3. As it is possible to observe in this figure, the C=C stretching intensity is stable and it does not depend on strain. Hence it can be used reliably for normalization purposes.

In the FT-IR spectra of **NR** samples reported in Figure 7.2 it is clearly possible to observe systematic changes induced by stretching. Some of these changes are related to strain-induced crystallization of **NR** and will be further discussed below.

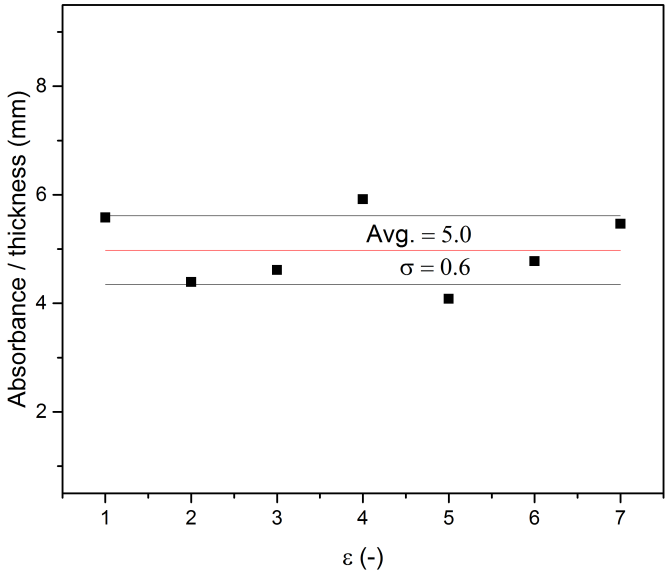

Figure 7.3: *IR intensity of the C=C stretching band versus strain for the* $\boldsymbol{NR/BR}_{LL}$ *sample. The reported data are proportional to the measured IR intensity (absorbance) divided by the sample thickness.*

The FT-IR spectra reported in Figure 7.2 reveal that by increasing ε the out-of-plane CH bending vibration blue shifts from 836 cm^{-1} (observed in amorphous **NR** at ε=0) to 842 cm^{-1} (observed in partially crystallized **NR** at ε=5). Healey *et al.*[26] determined that this blue shift is due to the existence of a crystalline phase in the sample. To analyze the behavior of the out-of-plane CH bending band, its position is plotted as a function of the strain values in Figure 7.4. The large part of the blue-shift occurs in correspondence of the onset of the strain-induced crystallization, which XRD measurements locate for ε values between 3 and 4. This nicely shows the potential of FT-IR analysis for precisely following this phenomenon. XRD data of **NR** samples which have been stretched over a range of strains, have been depicted in Figure 7.5 which made in collaboration with Prof. Marano (Dipartimento di Chimica, Materiali e Ingegneria Chimica – Politecnico di Milano, Italy) group.[87] Peak at $2\theta = 21.9 \pm 0.4°$ is ascribed to the diffraction angle of the (120) plane of the orthorhombic cell of crystalline **NR**.[141] As shown in the Figure 7.5, we can clearly see that this peak appears after ε=3 indicating the crystallinity of **NR**.

A behavior opposite to that of the out-of-plane CH bending band can be observed for the band located at about 1240 cm^{-1}, which is assigned to CH_2 twisting.[26] By increasing ε, this band red shifts from 1240 cm^{-1} (amorphous **NR**, ε=0) to 1233 cm^{-1} (partially crystallized **NR**, ε=5). However, similarly to the case of the out-of-plane CH bending band, the major changes of the position of the CH_2 twisting band occurs in the range $3<\varepsilon<4$ (Figure 7.6), which is close to the onset of strain induced crystallization of natural rubber obtained from XRD experiments.

For increasing strain values ($\varepsilon> 3$, see Figure 7.7), it is also possible to observe two new bands showing up around 980 cm^{-1} and 1210 cm^{-1}. The peak at 980 cm^{-1}

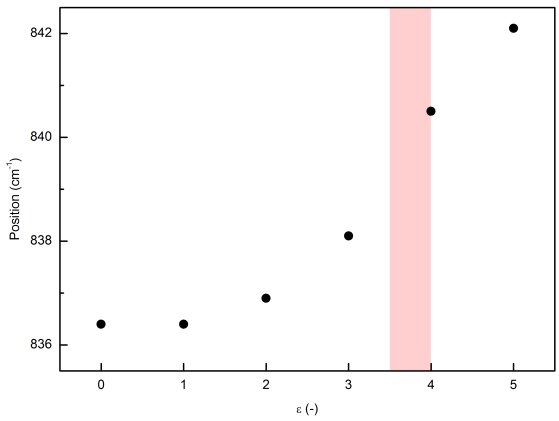

Figure 7.4: *Position of CH out-of-plane bending band vs. applied strain for* ***NR*** *samples. The red region shows the onset of crystallization determined by XRD.*

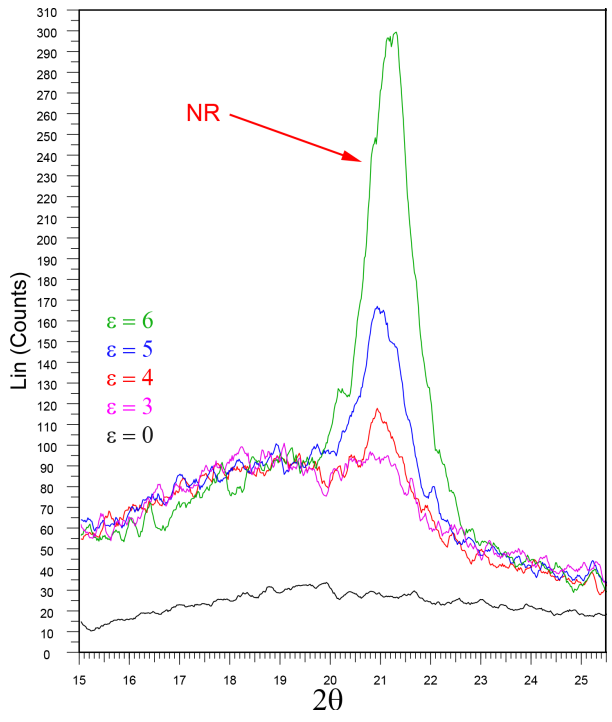

Figure 7.5: *XRD diffraction recorded on* ***NR*** *samples as a function of strain.*

is assigned to C-CH_3 stretching.[26] These peaks appear at ε>3, hence, consistently with present XRD data and literature data,[26] they can be ascribed to the onset of strain induced crystallization of natural rubber.

In addition to the spectral changes discussed above, strain-dependent FT-IR data recorded on **NR** also display evident changes in the intensity of the bands at 1126 cm^{-1} (*cis* C-C stretching), and 1361 cm^{-1} (CH_2 wagging).[26,138] Consistently with the observed onset of crystallization in **NR** (see above), one can note in Figure 7.8 a rather sharp stepwise increase of the intensity of the C-C stretching band at the expected strain value close to ε= 3.

Finally, the CH_2 wagging band at 1361 cm^{-1}, appears as a shoulder of the

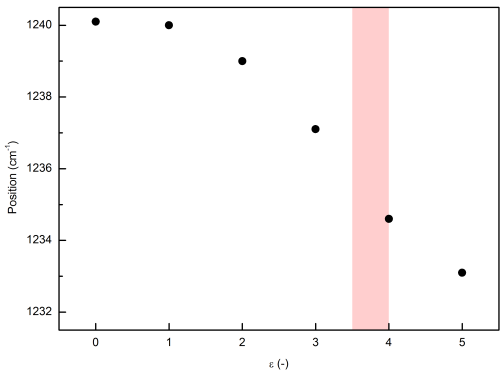

Figure 7.6: *Position of the CH_2 twisting band as a function of the applied strain for a representative **NR** sample. The region shaded in red shows the onset of crystallization determined by XRD.*

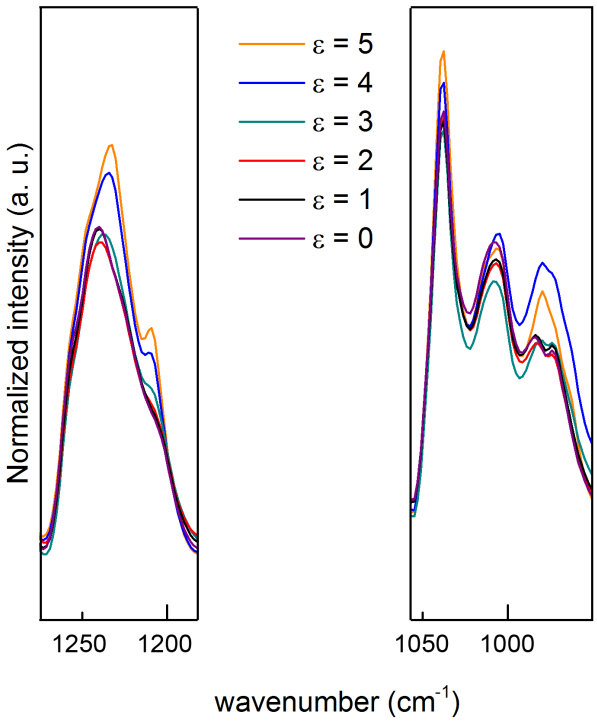

Figure 7.7: *New peaks appear for ε>3 in the IR spectra of **NR**. The spectra have been magnified for a better visualization of the trends.*

CH_3 deformation band (1376 cm^{-1}). In this case, the diagram of intensity *vs.* ε has not been plotted due to the inaccurate intensity determination of the CH_2 wagging band. The reason for this inaccuracy is the saturation of the nearby CH_3 deformation band. However, from a qualitative point of view, it is possible to note in Figure 7.2 the increasing intensity induced by higher strain values.

BR and NR/BR samples

Similarly to the case of **NR**, strips of $\mathbf{BR}_{MM}$ samples have been stretched with different strains in the range from ε=0 to ε=5. The FT-IR spectra of unstretched

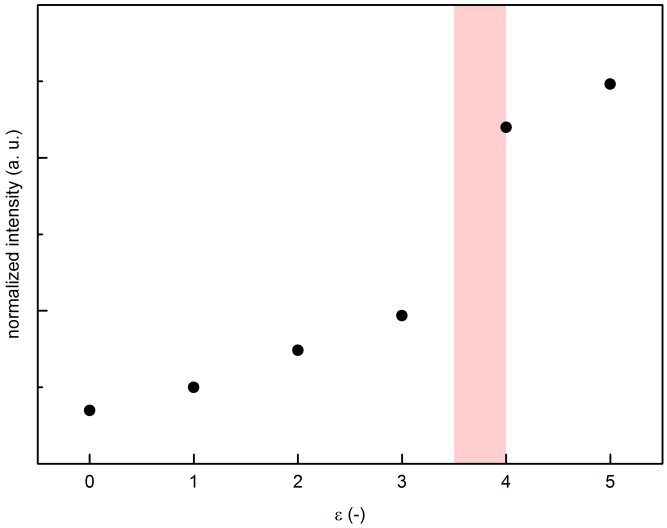

Figure 7.8: *Intensity change of the C-C stretching band vs. strain for the **NR** sample. The red region shows the onset of crystallization as determined by XRD.*

and stretched samples are shown in Figure 7.9, where they have been normalized by the intensity of the C=C stretching band observed at 1650 cm^{-1}. As we discussed above, the intensity of the C=C stretching band does not depend on the strain.

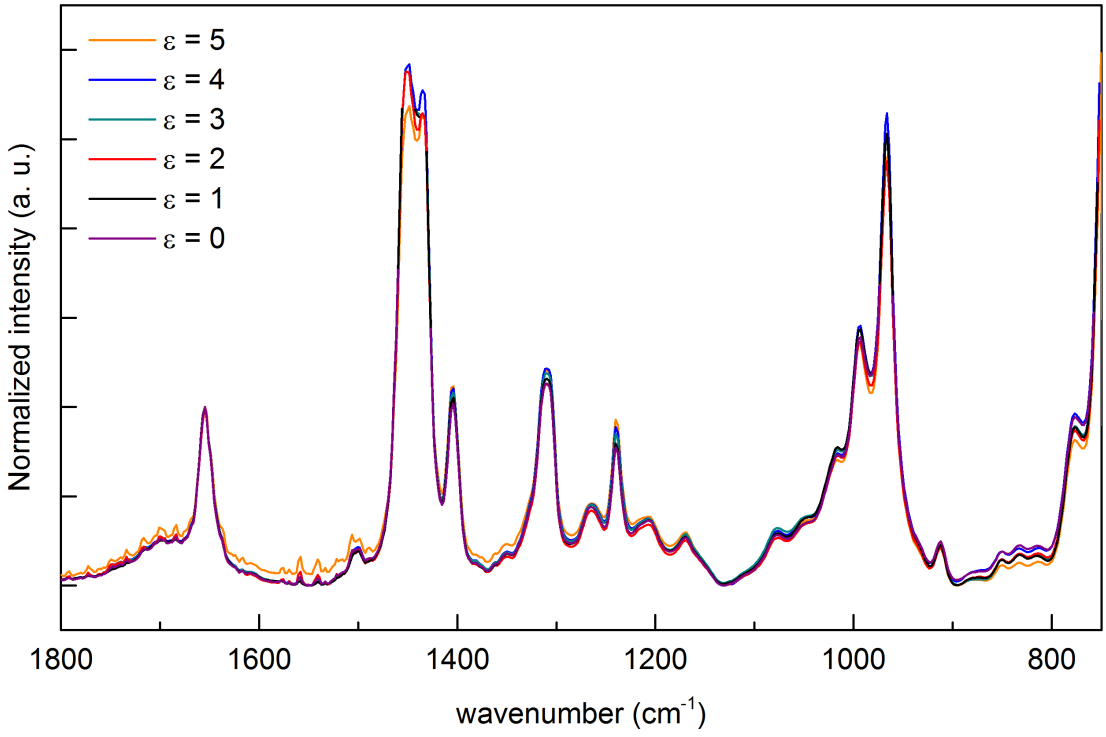

Figure 7.9: *IR spectra of $\boldsymbol{BR}_{MM}$ recorded on specimens stretched at different strain values in the range 0<ε<5.*

$\mathbf{BR}_{MM}$ samples were breaking by applying strain values larger than ε= 5.

Based on the reported Mooney-Rivlin plot discussed by Mohammad Poor[87] this strain is lower than the one needed for the onset of crystallization (ε=5.5). Accordingly, the changes observed in spectra are negligible and are not related to crystallization.

It is however possible to stretch samples up to ε=8 by preparing blends of **NR** and $\mathbf{BR}_{MM}$, and then analyze the onset of $\mathbf{BR}_{MM}$ crystallization. **NR** and **BR** crystallizes separately in the blend based on XRD data (see Figure 7.10), and based on this fact it is possible to analyze the onset crystallization of them in the blend separately by FT-IR spectroscopy. The XRD data of $\mathbf{NR/BR}_{MM}$ samples during stretching have been shown in Figure 7.10. **NR** part has been crystallized at $\epsilon > 4$ (peak at $2\theta = 21.9 \pm 0.4°$ is ascribed to the diffraction angle of the (120) plane of the orthorhombic cell of crystalline **NR**[141]) and then **BR** part has been crystallized at $\epsilon > 5$ (peak at $2\theta = 19°$ is ascribed to the diffraction angle of the (020) plane of the equator cell of crystalline **BR**[87]).

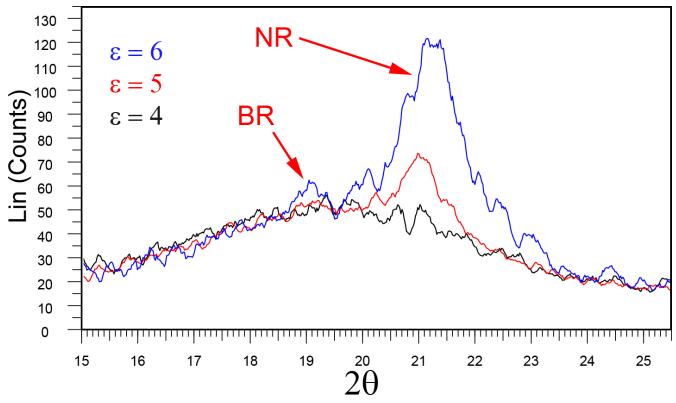

Figure 7.10: *XRD diffraction recorded on* $\mathbf{NR/BR}_{MM}$ *samples as a function of strain.*

Strips of $\mathbf{NR/BR}_{MM}$ samples have been stretched with different strain values, ranging from ε=0 to ε=7. The corresponding FT-IR spectra of the stretched and unstretched samples are shown in Figure 7.11 where they have been normalized by the intensity of C=C stretching band at 1650 cm^{-1}.

The analysis of the spectra reported in Figure 7.11 is helped by the comparison among the FT-IR spectra of **NR**, $\mathbf{BR}_{MM}$ and $\mathbf{NR/BR}_{MM}$ samples. This is offered in Figure 7.12), where one can observe some isolated bands which are related to the **NR** component or to the $\mathbf{BR}_{MM}$ component of the blend. Hence, for investigating the onset of crystallization of $\mathbf{BR}_{MM}$, the band located around 1240 cm^{-1} has been considered. This band is assigned to the CH_2 twisting vibration of $\mathbf{BR}_{MM}$.[25] As it is shown in Figure 7.13, a sharp change in intensity of this band appears at a strain value close to the expected onset of crystallization of $\mathbf{BR}_{MM}$.

7.1.5 Polarization-dependent FT-IR measurements

The results discussed in the paragraphs above show that, in general, it is possible to apply IR spectroscopy as a method for assigning the onset of crystallization in **NR** and **NR/BR** blends. It was also shown that the onset of strain induced

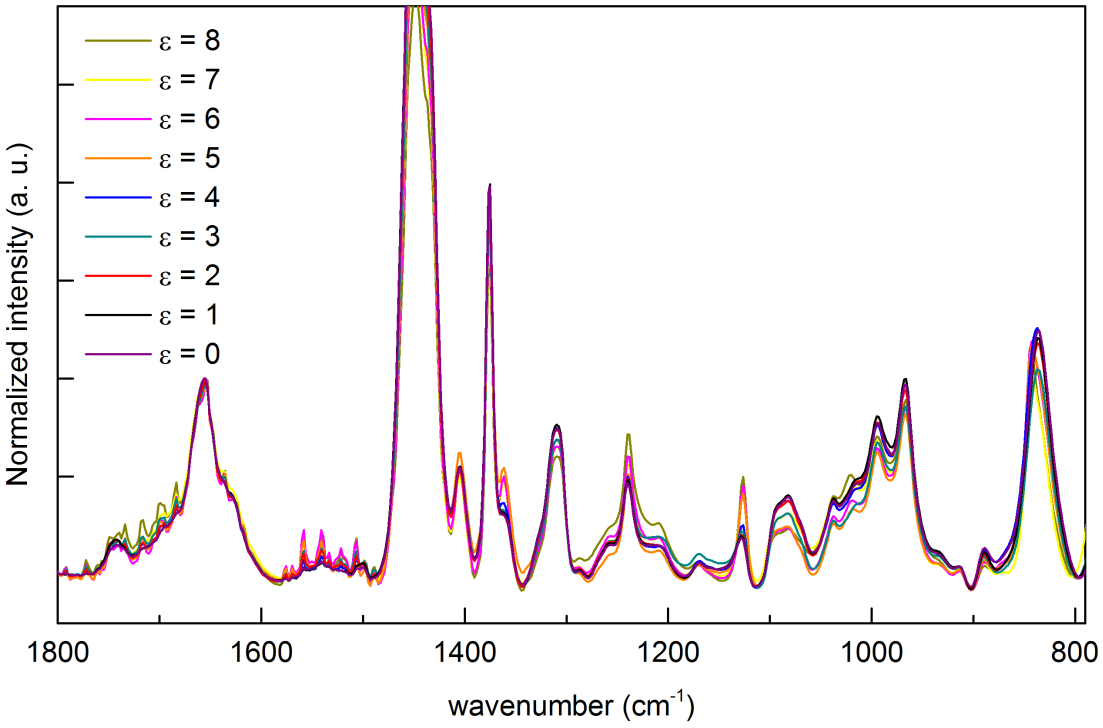

Figure 7.11: *Infrared spectra of* ***NR/BR***$_{MM}$ *recorded on specimens stretched at different strain (ε=0-8). The band around 1400 cm*$^{-1}$ *saturates. The spectra have been normalized by the C=C stretching band at around 1650 cm*$^{-1}$.

crystallization happens at lower strain in **NR** ($3 < \epsilon < 4$) compared to **NR/BR** ($\epsilon > 5$). However, the maximum degree of crystallinity reached in **NR** is higher than that found in **BR** (respectively 20% and 11%, see Mohammad Poor[87]).

Since molecular orientation can also affect the mechanical behavior, it is important to investigate the use of FT-IR to assess strain induced molecular orientation in the samples. This can be done by using polarized light in the FT-IR experiment, i.e., by placing a polarizer after the IR light source. The blends of **NR/BR**$_{LL}$ and **NR/BR**$_{MM}$ have been analyzed by polarized FT-IR spectroscopy to study the effect of microstructure on the orientability of rubber.

In the experiments IR light was polarized either parallel ($\theta = 0°$) or perpendicular ($\theta = 90°$) to the stretching direction of the sample. The orientation effects on a particular band in the spectrum can be assessed by the dichroic ratio (R):[140]

$$R = \frac{I_{\parallel}}{I_{\perp}} \tag{7.1}$$

where $I_{\parallel}$ and $I_{\perp}$ denote the IR absorbance of a given band measured with polarized IR light either parallel ($\theta = 0°$) or perpendicular ($\theta = 90°$) to the stretching direction (respectively). Through the dichroic ratio R the orientation function (f) f can be calculated by Equation 7.2:[140]

$$f = \frac{R-1}{R+2} \tag{7.2}$$

The dichroic ratio and the orientation function of two selected bands (CH_2

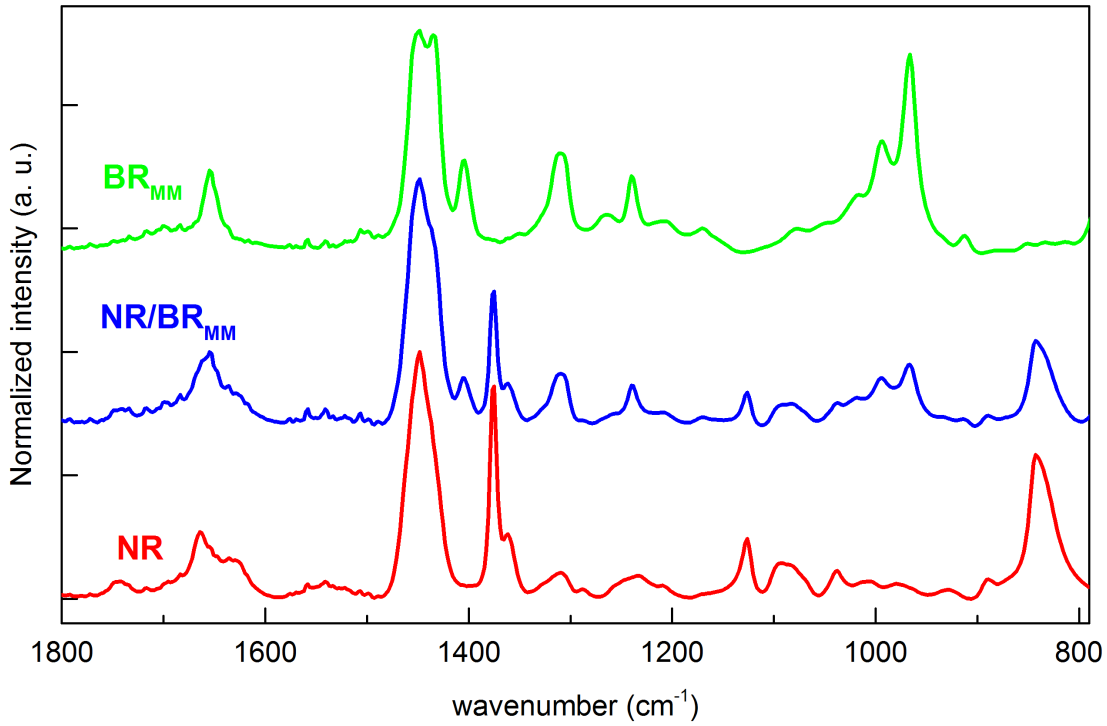

Figure 7.12: *Comparison among the FT-IR spectra of* ***NR***, $\boldsymbol{BR}_{MM}$ *and their blend. The three spectra have been recorded at* ε*=5.*

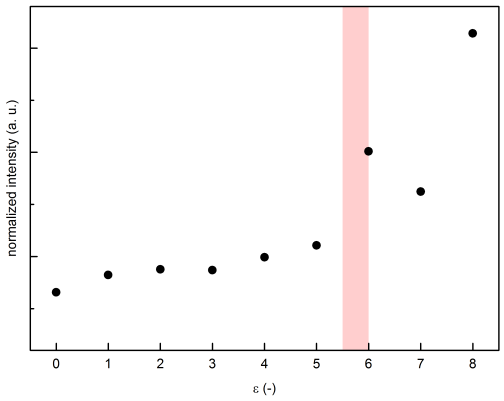

Figure 7.13: *Changes in the intensity of the* CH_2 *twisting band of* $\boldsymbol{BR}_{MM}$ *vs. strain in* $\boldsymbol{NR/BR}_{MM}$*. The region shaded in red shows the onset of crystallization as determined by XRD.*

twisting at 1240 cm^{-1} and CH in-plane asymmetrical bending at 1404 cm^{-1}[25]) have been calculated and plotted versus the applied strain in Figures 7.14 and 7.15 (respectively). R and f have been calculated using the intensities of the two selected bands mentioned above.

As it is possible to see in Figure 7.14, the dichroic ratio is close to unity for applied strain values less than 3. By increasing the strain above 3, the dichroic ratio increases sharply, which marks the starting point of molecular orientation phenomena. Consistently with XRD results, for both $\mathbf{NR/BR}_{MM}$ and $\mathbf{NR/BR}_{LL}$

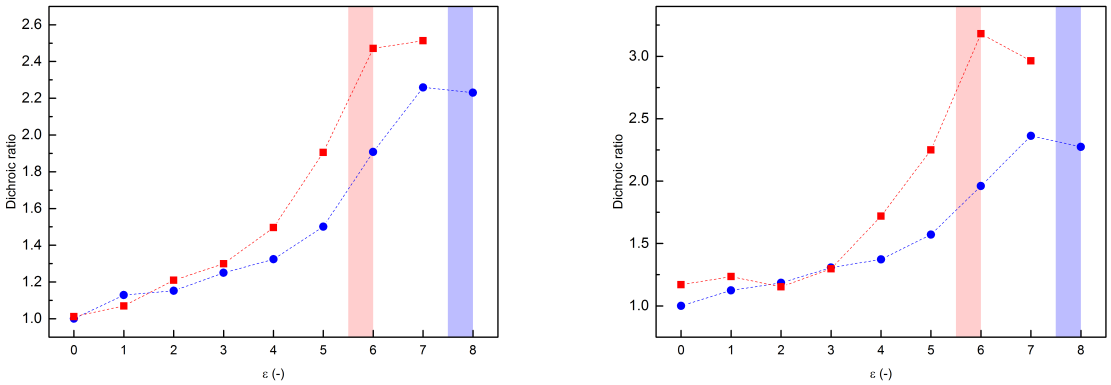

(a) *CH_2 twisting (1240 cm^{-1})*

(b) *CH in-plane asymmetrical bending (1404 cm^{-1})*

Figure 7.14: *Dichroic ratio vs. applied strain calculated for two different bands. Blue: **NR/BR**$_{LL}$; Red: **NR/BR**$_{MM}$. Red and blue regions show then onset of crystallization determined by XRD for **NR/BR**$_{MM}$ and **NR/BR**$_{LL}$, respectively.*

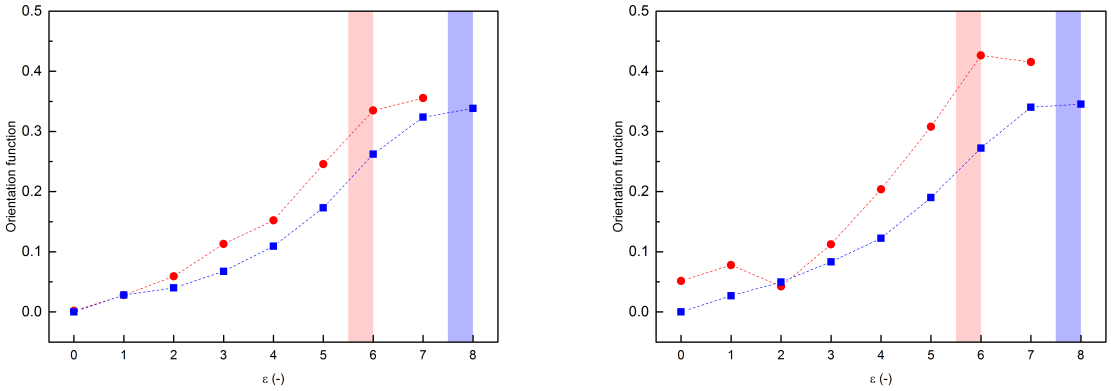

(a) *CH_2 twisting (1240 cm^{-1})*

(b) *CH in-plane asymmetrical bending (1404 cm^{-1})*

Figure 7.15: *Orientation function vs. applied strain calculated for two selected bands. Blue: **NR/BR**$_{LL}$; Red: **NR/BR**$_{MM}$. Red and blue regions show the onset of crystallization determined by XRD for **NR/BR**$_{MM}$ and **NR/BR**$_{LL}$, respectively.*

samples (and for both analyzed IR bands), a sudden change in the dichroic ratio is seen for strain values close to the onset of crystallization. This shows that also polarized IR spectroscopy, through the use of the dichroic ratio, is sensitive to crystallization phenomena in rubber systems.

On the other hand, by analyzing the orientation function (Figure 7.15), it is possible to note that orientation significantly occurs for ε>3. For the **NR/BR**$_{MM}$ sample it is possible to observe a step in the orientation function around the onset of crystallization determined by XRD. For the **NR/BR**$_{LL}$ sample, at least one more point is needed to determine exactly the onset crystallization by the use of the orientation function, but it is not possible to stretch sample more than $\epsilon > 8$ related to the rupture of the sample.

For both selected bands the orientation function is higher in the **NR/BR**$_{MM}$

sample compared to the $\mathbf{NR/BR}_{LL}$ sample. This means that higher molecular orientation is reached under strain in the $\mathbf{NR/BR}_{MM}$ sample. This observation may justify the onset and propagation of sideways cracks occurred in $\mathbf{NR/BR}_{MM}$ (for more information on crack propagation in different samples refer to Mohammad Poor[87]). However, in order to correlate satisfactorily the behavior of the orientation function and the crack propagation, further analysis and statistics on different samples would be required. This constitutes the natural follow up of the research activity described in this chapter.

7.2 Raman investigation of the aggregation of Amphotericin B in methanol

Probing molecular aggregation is important in several fields such as drug delivery and materials science (*e.g.* producing homogeneous films with dispersed active molecules). Amphotericin B (**AmB**) is a well known polyene antibiotic macrolide with 7 π-conjugated C=C bonds (see Figure 7.16). **AmB** can be used as a prototype of a bent oligoene and its electronic absorption falls in the blue-violet region. It is widely used in the treatment of systemic fungal infections.[142] The poor water solubility of **AmB** is one of the important factors limiting its application, but the main disadvantage is related to its toxic effects, which depend on its aggregation state in vitro as well as in vivo.[143] Several efforts have been devoted to the investigation of **AmB** aggregation process in different solvents, employing a variety of electronic spectroscopy techniques (UV-Vis absorption, fluorescence and circular dichroism).[144–147]

As far as the author is aware of, Raman spectroscopy has been considered for characterizing aggregation of **AmB** just by monitoring the position[148] of the Я mode (*i.e.*, the effective conjugation coordinate mode of the π-system[1]). However, the Raman intensity of the Я line was not considered. Compared to electronic spectroscopy, Raman spectroscopy (as well as other vibrational spectroscopy techniques) offers a better sensitivity to molecular structure. This may help addressing signal assignment concerns which have been pointed out in the literature for the interpretation of the fluorescence spectrum of **AmB** dimers.[149]

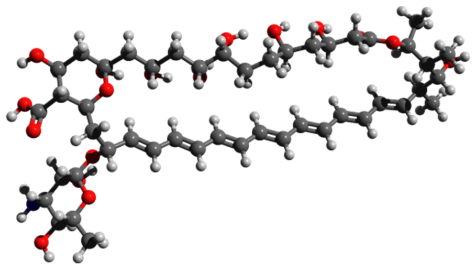

Figure 7.16: *Molecular structure of **AmB** calculated by DFT at the B3LYP/6-311G(d,p) level.*

AmB has been dissolved in methanol (MeOH) at different concentrations, in the 0.3×10^{-3} – 1.5×10^{-7} M range. Resonance Raman spectra have been recorded on these solutions with 325 nm laser excitation (see Figure 7.17). In Figure 7.18, the experimental Raman spectrum of **AmB** is compared with a simulated spectrum obtained from DFT calculations. The characteristic Я mode of **AmB** (1560

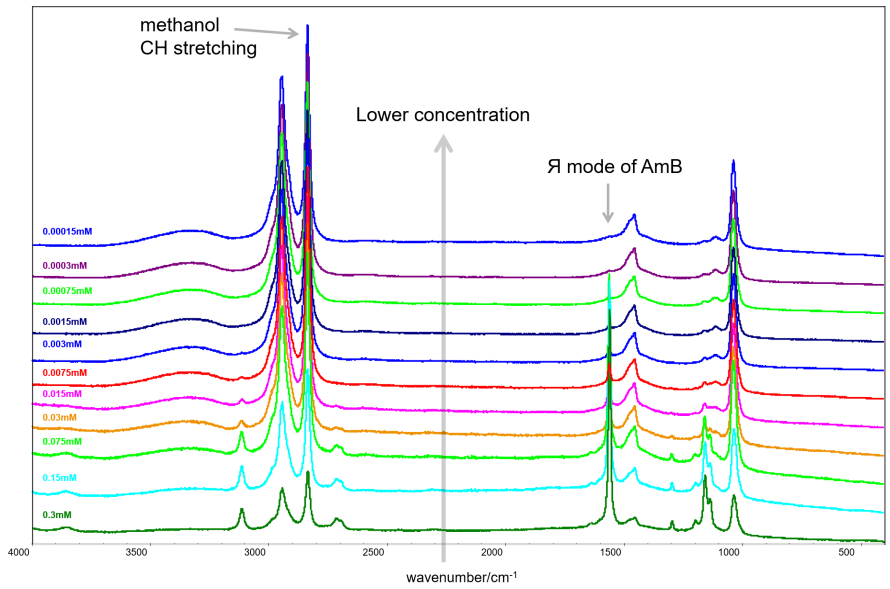

Figure 7.17: *Experimental Raman spectra of **AmB** dissolved in methanol at different concentrations (325 nm excitation).*

cm^{-1}) can be clearly identified and reliably assigned. The characteristic Я mode

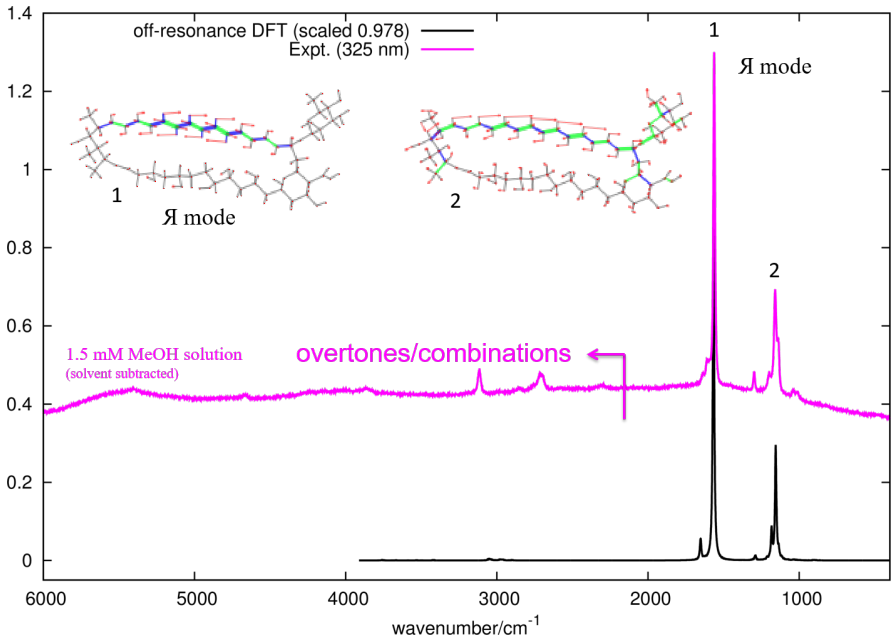

Figure 7.18: *Experimental Raman spectrum of **AmB** dissolved in methanol (1.5 mM, 325 nm excitation) compared with results from DFT calculations (B3LYP/6-311G(d,p) level, frequency scaled by 0.98).*

of **AmB** (1560 cm^{-1}) and the CH stretching mode of MeOH (2835 cm^{-1}) have been used for determining the relative Raman intensity ($I_Я/I_{CH}$), thus obtaining

the Raman cross section of **AmB** through Equation 7.3:

$$\left.\begin{aligned} I_{AmB} &\propto C_{AmB} \times \sigma_{AmB} \times I_{laser} \\ I_{MeOH} &\propto C_{MeOH} \times \sigma_{MeOH} \times I_{laser} \end{aligned}\right\} \qquad (\frac{\sigma_{AmB}}{\sigma_{MeOH}}) = \frac{I_{AmB}}{I_{MeOH}} \times \frac{C_{MeOH}}{C_{AmB}} \tag{7.3}$$

where I denotes the Raman (or laser) intensity, C denotes concentration and σ is the Raman cross section.

By plotting $\sigma_{AmB}/\sigma_{MeOH}$ *vs.* **AmB** concentration (see Figure 7.19), it is possible to distinguish three regions: the free state of **AmB** in MeOH, a transition state and the formation of aggregates at high concentrations of **AmB**. The Raman cross section of **AmB** turns out to be a sensitive probe of the aggregation state of **AmB** as a function of concentration, and by resonance Raman spectroscopy, it is possible to monitor aggregation in solution state as a function of **AmB** concentration.

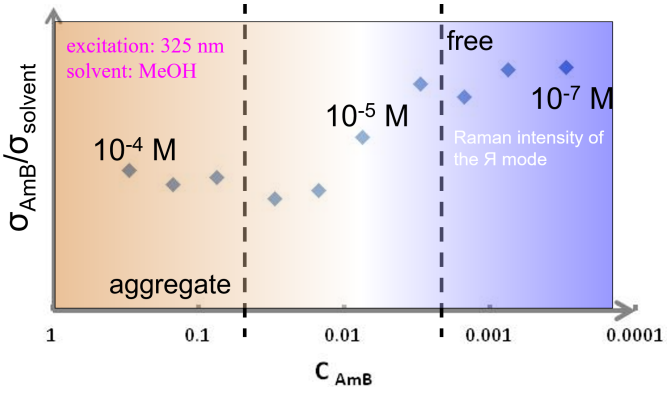

Figure 7.19: *Relative Raman cross section of **AmB** vs. concentration. It is possible to distinguish three different regions in this plot (see text).*

By plotting the UV/Vis absorption spectra of **AmB** at different concentrations, the same behavior can be observed for the molecular absorbivity (ϵ, see Figure 7.20).

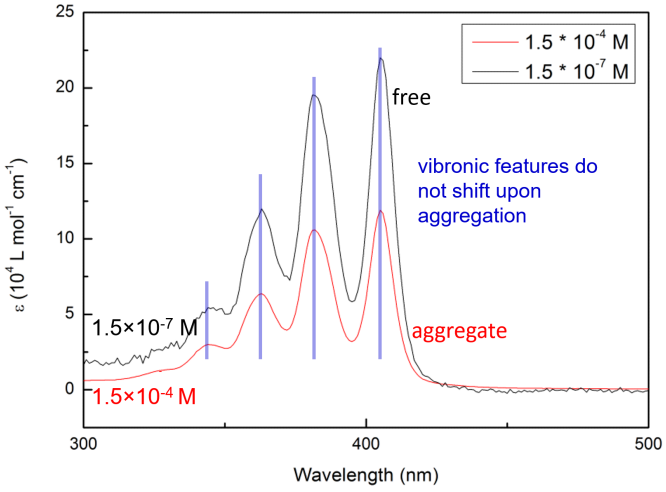

Figure 7.20: *UV/Vis absorption spectra of **AmB** at different concentrations.*

It is found that π-stacking consistently reduces by about a factor of two both the Raman cross section and molar absorptivity. The Raman cross section of **AmB** follows the behavior of molecular absorptivity in UV-Vis absorption, but offers improved molecular specificity. In general, the π-stacking of **AmB** is alike that of π-conjugated materials used in molecular electronics. Hence the method proposed here may be useful to probe aggregation phenomena in π-conjugated materials. Controlled aggregation (self assembly) is known to be a key-ingredient affecting the transport properties of films produced with π-conjugated materials. The method proposed here for **AmB** may then find useful applications in materials science.

CHAPTER 8

Conclusion

The analysis and discussion of the results presented in this thesis highlight the role of vibrational spectroscopy as a reliable probe of molecular structure in several systems of current interest in materials science. Molecular graphenes, thiophene derivatives, rubber blends have been successfully characterized revealing interesting aspects related to their molecular structure. IR and Raman spectroscopy of molecular graphenes allowed establishing a true spectroscopic fingerprint of molecular shapes, size and chemical functionalization (*e.g.*, chlorination). Through different markers, Raman and IR spectroscopy have shown a great sensitivity to the peculiar radicaloid character of novel phenoquinone thiophene derivatives. Vibrational spectroscopy was also found useful in investigating intermolecular interactions: IR spectroscopy revealed the onset of strain induced crystallization in rubber blends, while Raman intensity was found to be sensitive to π-stacking aggregation phenomena in solution state, through the analysis of the representative case of Amphotericin B (AmB).

Current standard DFT methods (B3LYP/6-31G(d,p)) were found to provide a computationally very convenient first approach for assigning the observed transitions in IR and off-resonance/pre-resonance Raman of the advanced materials examined in this thesis. In specific cases (thiophene derivatives with radicaloid character) *ad-hoc* treatments helped to partially overcome the shortcoming of DFT.

It has been possible to rationalize the resonance Raman behavior of several graphene molecules in terms of Nafie-Stein-Peticolas theory complemented by the use of DFT calculations. This allowed to carry out quantitative calculations of resonance Raman of one selected graphene molecule (**C78**) which provided a very good simulation of the observed resonance Raman spectra. Interestingly, even

in its qualitative form, Nafie-Stein-Peticolas also allowed to justify the observed relative intensities of overtones and combinations in a representative series of molecular graphenes with different size and shape.

The analysis of chlorinated graphene molecules led to the rationalization of their non-planar molecular structure based on DFT calculations. DFT also provided sound simulations of the observed IR and Raman spectra which fostered the assignment of the main features. DFT models supported the concept that in chlorinated graphene molecules π-conjugation is not impaired by the significant out-of-plane distorsion of the molecules.

An unprecedented model of holey graphene was experimentally investigated by IR, Raman and UV/Vis spectroscopy. A specific IR marker of the hydrogenated hole structure was found. Compared with the parent graphene molecule not possessing the central hole, UV/Vis spectroscopy and TDDFT calculations revealed a significant blue shift of the electronic transition with largest HOMO-LUMO character. Furthermore resonant Raman spectroscopy revealed well-resolved third order transitions, which have not been observed previously in other graphene molecules.

Finally Clar annellation theory and TDDFT calculations were successful in rationalizing the observed marked red-shift of the UV/Vis absorption of a novel molecular graphene with partial zig-zag edge. Raman and IR spectra were also found to provide several useful markers of its molecular structure.

CHAPTER 9

Experimental and Theoretical Methods

This Chapter briefly presents the methods used to carry out the experimental and theoretical works presented in this Ph.D. Thesis.

Raman spectroscopy

All reported Raman spectra in this Ph.D thesis have been recorded with a Jobin-Yvon Labram HR800UV spectrometer equipped with different laser lines, namely 325 nm excitation of a He-Cd laser, 457.9 and 514.5 nm excitations of a Ar^+ laser, 632.8 nm excitation of a He-Ne laser and 785 nm excitation of a high power diode laser. The laser power at the sample was always of the order of a few mW to prevent (or reduce as possible) laser-induced effects on the samples and care has been adopted to verify the reproducibility of the spectra. Samples were analyzed by using the microscope with the 50× objective for all laser lines except the one at 325 nm for which an UV-grade 15× objective was used, in a back-scattering geometry on glass slides. The intensity of the all presented Raman spectra (325 nm excitation excluded) have been corrected with white light calibration.

FT-Raman spectra have been recorded with a Nicolet NXR 9650 FT-Raman spectrometer collecting 4096 scans with a resolution of 4 cm^{-1} on powder samples gently placed on a metallic sample holder. Laser excitation at 1064 nm has been kept focused on the sample (50 μm beam diameter) with a power of 50 mW.

Temperature dependent Raman

For recording temperature dependent Raman spectra, the Linkam THMS600 stage was used. Increasing temperature has been started from room temperature (RT) and increased stepwise by 25°C up to 200°C. In correspondence of each tempera-

ture step, the Raman spectra have been recorded, allowing the sample to reach a stable equilibrium temperature.

IR spectroscopy

The micro FT-IR measurements reported in this Thesis were carried out with a Nicolet Nexus equipment coupled with a Thermo-Nicolet Continuμm infrared microscope and a cooled MCT detector (77 K). The spectra of the samples (as powders) were acquired by using the diamond anvil cell technique with a 15× infrared objective in 650 – 4000 cm^{-1} spectral range.

In preparing the samples for the diamond anvil cell, care was taken to minimize their thickness while keeping a good signal to noise ratio. This was mandatory to avoid saturation of the IR spectra. In particular the very strong C=O stretching band of both **QBT** and **QDTT** samples (see Chapter 6) proved to be more challenging than the other samples investigated in this Thesis. Compared with the KBr pellet technique, the micro FT-IR setup allows recording spectra with a minimal sample amount, which is a very appealing experimental advantage when sample availability is scarce or multiple experiments on a given sample are planned.

UV/Vis spectroscopy

The UV/Vis spectra reported in this Thesis have been recorded on a Jasco UV/Vis/NIR V-570 spectrometer. The integrating sphere equipment was used in order to reliably detect the absorption spectrum in presence of scattering contributions due to the formation of dispersed aggregates.

Quantum chemical calculations

Quantum chemical calculations in this chapter have been carried out within Density Functional Theory. The selected method, B3LYP/6-31G(d,p), is a good compromise between accuracy and computational costs when simulating the vibrational properties of sizable π-conjugated compounds such as those examined in the Chapters dealing with graphene molecules (3, 4, 5) and thiophene-based heterophenoquinones (6). Gaussian09 rev. D.01[24] was employed to carry out all calculations here reported on molecular species.

Simulated Raman and IR spectra were obtained from the corresponding peak intensities and wavenumber determined by DFT methods. A sum of lorentzian lineshapes with FWHM = 10 cm^{-1} was used to determine the final simulated spectrum. When comparing against experimental data, the computed wavenumber were uniformly scaled by values equal to 0.98 (or very close).

The calculation of the IR spectrum of the M_P sample (see Chapter 3) has been carried out within 1D periodic boundary conditions with the CRYSTAL14 code[150] (B3LYP/6-31G(d,p) level) in collaboration with Alberto Milani (Dipartimento di Chimica, Materiali e Ingegneria Chimica "Giulio Natta" – Politecnico di Milano). Furthermore, in order to limit the computational cost the DFT molecular model of this polymer was built considering shorter alkyl substituents.

To foster the interpretation of UV/Vis absorption data, Time-Dependent (TD) DFT has been employed, at the same level considered for the description of vibrational spectroscopy (*i.e.*, B3LYP/6-31G(d,p)). The calculation of the lowest fifty excited states provided a converged description of the observed UV/Vis absorption spectra.

Custom computer codes (developed by Matteo Tommasini, Dipartimento di Chimica, Materiali e Ingegneria Chimica "Giulio Natta" – Politecnico di Milano) have been used to post-process the output from Gaussian09 and CRYSTAL14 calculations and provide a graphical representation of normal modes.

Bibliography

[1] C. Castiglioni, M. Tommasini, and G. Zerbi, "Raman spectroscopy of polyconjugated molecules and materials: confinement effect in one and two dimensions," *Philosophical Transactions of the Royal Society A: Mathematical, Physical and Engineering Sciences*, vol. 362, pp. 2425–2459, nov 2004.

[2] E. Clar, *Aromatic Sextet*. John Wiley and Sons Ltd, 1972.

[3] S. Ito, M. Wehmeier, J. D. Brand, C. Kübel, R. Epsch, J. P. Rabe, and K. Müllen, "Synthesis and self-assembly of functionalized hexa-peri-hexabenzocoronenes," *Chem. Eur. J.*, vol. 6, pp. 4327–4342, dec 2000.

[4] J. Liu, Z. Liu, C. J. Barrow, and W. Yang, "Molecularly engineered graphene surfaces for sensing applications: A review," *Analytica Chimica Acta*, vol. 859, pp. 1–19, feb 2015.

[5] L. A. Ponomarenko, F. Schedin, M. I. Katsnelson, R. Yang, E. W. Hill, K. S. Novoselov, and A. K. Geim, "Chaotic dirac billiard in graphene quantum dots," *Science*, vol. 320, pp. 356–358, apr 2008.

[6] A. Gharib, L. V. Fard, N. N. Pesyan, and M. Roshani, "A new application of nano-graphene oxide (ngo) as a heterogeneous catalyst in oxidation of alcohols types," *Chemistry Journal*, vol. 1, no. 4, pp. 151–158, 215.

[7] R. Rieger and K. Müllen, "Forever young: polycyclic aromatic hydrocarbons as model cases for structural and optical studies," *Journal of Physical Organic Chemistry*, pp. n/a–n/a, 2010.

[8] S. Laschat, A. Baro, N. Steinke, F. Giesselmann, C. Hägele, G. Scalia, R. Judele, E. Kapatsina, S. Sauer, A. Schreivogel, and M. Tosoni, "Discotic liquid crystals: From tailor-made synthesis to plastic electronics," *Angewandte Chemie International Edition*, vol. 46, pp. 4832–4887, jun 2007.

[9] M. Tommasini, C. Castiglioni, and G. Zerbi, "Raman scattering of molecular graphenes," *Phys. Chem. Chem. Phys.*, vol. 11, no. 43, pp. 10185–10194, 2009.

[10] M. Tommasini, G. Longhi, S. Abbate, and G. Zerbi, "Theoretical investigation and computational evaluation of overtone and combination features in resonance raman spectra of polyenes and carotenoids," *J. Raman Spectrosc.*, vol. 45, pp. 89–96, jan 2014.

[11] A. Maghsoumi, L. Brambilla, C. Castiglioni, K. Müllen, and M. Tommasini, "Overtone and combination features of g and d peaks in resonance raman spectroscopy of the c78h26 polycyclic aromatic hydrocarbon," *J. Raman Spectrosc.*, vol. 46, pp. 757–764, jun 2015.

[12] A. C. Ferrari and D. M. Basko, "Raman spectroscopy as a versatile tool for studying the properties of graphene," *Nature Nanotech*, vol. 8, pp. 235–246, apr 2013.

[13] E. D. Donato, M. Tommasini, G. Fustella, L. Brambilla, C. Castiglioni, G. Zerbi, C. D. Simpson, K. Müllen, and F. Negri, "Wavelength-dependent raman activity of d2h symmetry polycyclic aromatic hydrocarbons in the d-band and acoustic phonon regions," *Chemical Physics*, vol. 301, pp. 81–93, may 2004.

[14] D.-E. Jiang and Z. Chen, eds., *Graphene Chemistry*. Wiley-Blackwell, aug 2013.

[15] L. F. Dössel, V. Kamm, I. A. Howard, F. Laquai, W. Pisula, X. Feng, C. Li, M. Takase, T. Kudernac, S. D. Feyter, and K. Müllen, "Synthesis and controlled self-assembly of covalently linked hexa- peri -hexabenzocoronene/perylene diimide dyads as models to study fundamental energy and electron transfer processes," *J. Am. Chem. Soc.*, vol. 134, pp. 5876–5886, apr 2012.

[16] W. John C. Fetzer, Fetzer, *Large (C = 24) Polycyclic Aromatic Hydrocarbons: Chemistry and Analysis*. JOHN WILEY & SONS INC, 2000.

[17] M. G. Schwab, A. Narita, S. Osella, Y. Hu, A. Maghsoumi, A. Mavrinsky, W. Pisula, C. Castiglioni, M. Tommasini, D. Beljonne, X. Feng, and K. Müllen, "Bottom-up synthesis of necklace-like graphene nanoribbons," *Chem. Asian J.*, vol. 10, pp. 2134–2138, jul 2015.

[18] J. T. Bauman, *Fatigue, Stress, and Strain of Rubber Components: A Guide for Design Engineers*. HANSER GARDNER PUBL, 2009.

[19] C. Mapelli, C. Castiglioni, G. Zerbi, and K. Müllen, "Common force field for graphite and polycyclic aromatic hydrocarbons," *Phys. Rev. B*, vol. 60, pp. 12710–12725, nov 1999.

[20] J. Maultzsch, S. Reich, C. Thomsen, H. Requardt, and P. Ordejón, "Phonon dispersion in graphite," *Phys. Rev. Lett.*, vol. 92, feb 2004.

[21] A. Ferrugiari, M. Tommasini, and G. Zerbi, "Raman spectroscopy of carbonaceous particles of environmental interest," *J. Raman Spectrosc.*, vol. 46, pp. 1215–1224, jul 2015.

[22] S. Grimme, S. Ehrlich, and L. Goerigk, "Effect of the damping function in dispersion corrected density functional theory," *J. Comput. Chem.*, vol. 32, pp. 1456–1465, Maggio 2011.

[23] Y.-Z. Tan, B. Yang, K. Parvez, A. Narita, S. Osella, D. Beljonne, X. Feng, and K. Muellen, "Atomically precise edge chlorination of nanographenes and its application in graphene nanoribbons," *Nat. Commun.*, vol. 4, p. 2646, Novembre 2013.

[24] M. J. Frisch, G. W. Trucks, H. B. Schlegel, G. E. Scuseria, M. A. Robb, J. R. Cheeseman, G. Scalmani, V. Barone, B. Mennucci, G. A. Petersson, H. Nakatsuji, M. Caricato, X. Li, H. P. Hratchian, A. F. Izmaylov, J. Bloino, G. Zheng, J. L. Sonnenberg, M. Hada, M. Ehara, K. Toyota, R. Fukuda, J. Hasegawa, M. Ishida, T. Nakajima, Y. Honda, O. Kitao, H. Nakai, T. Vreven, J. A. Montgomery, Jr., J. E. Peralta, F. Ogliaro, M. Bearpark, J. J. Heyd, E. Brothers, K. N. Kudin, V. N. Staroverov, R. Kobayashi, J. Normand, K. Raghavachari, A. Rendell, J. C. Burant, S. S. Iyengar, J. Tomasi, M. Cossi, N. Rega, J. M. Millam, M. Klene, J. E. Knox, J. B. Cross, V. Bakken, C. Adamo, J. Jaramillo, R. Gomperts, R. E. Stratmann, O. Yazyev, A. J. Austin, R. Cammi, C. Pomelli, J. W. Ochterski, R. L. Martin, K. Morokuma, V. G. Zakrzewski, G. A. Voth, P. Salvador, J. J. Dannenberg, S. Dapprich, A. D. Daniels, Ö. Farkas, J. B. Foresman, J. V. Ortiz, J. Cioslowski, and D. J. Fox, "Gaussian 09, revision D.01." Gaussian Inc. Wallingford CT 2009.

[25] B. Amram, L. Bokobza, L. Monnerie, and J. Queslel, "Fourier-transform infra-red dichroism study of molecular orientation in high cis-1,4-polybutadiene," *Polymer*, vol. 29, pp. 1155–1160, jul 1988.

[26] A. M. Healey, P. J. Hendra, Y. D. West, "A fourier-transform raman study of the strain-induced crystallization and cold crystallization of natural rubber," *Polymer*, vol. 37, no. 18, pp. 4009–4024, 1996.

[27] X. Liu, T. Zhou, Y. Liu, A. Zhang, C. Yuan, and W. Zhang, "Cross-linking process of cis-polybutadiene rubber with peroxides studied by two-dimensional infrared correlation spectroscopy: a detailed tracking," *RSC Adv.*, 2015.

[28] S. M. P. NALLASAMY, P.M. ANBARASAN, "Vibrational spectra and assignments of cis- and trans-1,4-polybutadiene," *TURKISH JOURNAL OF CHEMISTRY*, vol. 26, no. 1, pp. 105–112, 2002.

[29] F. Negri, E. di Donato, M. Tommasini, C. Castiglioni, G. Zerbi, and K. Mullen, "Resonance raman contribution to the d band of carbon materials: Modeling defects with quantum chemistry," *Journal of Chemical Physics*, vol. 120, pp. 11889–11900, 2004.

[30] N. Bachar, L. Liberman, F. Muallem, X. Feng, K. Müllen, and H. Haick, "Sensor arrays based on polycyclic aromatic hydrocarbons: Chemiresistors versus quartz-crystal microbalance," *ACS Appl. Mater. Interfaces*, vol. 5, pp. 11641–11653, nov 2013.

[31] J. Wu, W. Pisula, and K. Müllen, "Graphenes as potential material for electronics," *Chemical Reviews*, vol. 107, pp. 718–747, mar 2007.

[32] B. F. Machado and P. Serp, "Graphene-based materials for catalysis," *Catal. Sci. Technol.*, vol. 2, no. 1, pp. 54–75, 2012.

[33] W. M. Baird, L. A. Hooven, and B. Mahadevan, "Carcinogenic polycyclic aromatic hydrocarbon-DNA adducts and mechanism of action," *Environmental and Molecular Mutagenesis*, vol. 45, no. 2-3, pp. 106–114, 2005.

[34] B. T. Draine and A. Li, "Infrared emission from interstellar dust. IV. the silicate-graphite-PAH model in the post- spitzer era," *ApJ*, vol. 657, pp. 810–837, mar 2007.

[35] M. Solà, "Forty years of clar's aromatic π-sextet rule," *Front. Chem.*, vol. 1, 2013.

[36] R. Yamaguchi, S. Ito, B. S. Lee, S. Hiroto, D. Kim, and H. Shinokubo, "Functionalization of hexa-peri -hexabenzocoronenes: Investigation of the substituent effects on a superbenzene," *Chem. Asian J.*, vol. 8, pp. 178–190, oct 2012.

[37] T. Wassmann, A. P. Seitsonen, A. M. Saitta, M. Lazzeri, and F. Mauri, "Clar's theory, π-sextet-electron distribution, and geometry of graphene nanoribbons," *J. Am. Chem. Soc.*, vol. 132, pp. 3440–3451, mar 2010.

[38] Z. Sun, Z. Zeng, and J. Wu, "Benzenoid polycyclic hydrocarbons with an open-shell biradical ground state," *Chem. Asian J.*, vol. 8, pp. 2894–2904, jul 2013.

[39] T. Kubo, "Recent progress in quinoidal singlet biradical molecules," *Chem. Lett.*, vol. 44, no. 2, pp. 111–122, 2015.

[40] M. Kastler, J. Schmidt, W. Pisula, D. Sebastiani, and K. Müllen, "From armchair to zigzag peripheries in nanographenes," *J. Am. Chem. Soc.*, vol. 128, pp. 9526–9534, jul 2006.

[41] X. Feng, J. Wu, M. Ai, W. Pisula, L. Zhi, J. P. Rabe, and K. Müllen, "Triangle-shaped polycyclic aromatic hydrocarbons," *Angewandte Chemie International Edition*, vol. 46, pp. 3033–3036, apr 2007.

[42] Z. Wang, Ž. Tomović, M. Kastler, R. Pretsch, F. Negri, V. Enkelmann, and K. Müllen, "Graphitic molecules with partial "zig/zag" periphery," *J. Am. Chem. Soc.*, vol. 126, pp. 7794–7795, jun 2004.

[43] T. Dumslaff, A. Maghsoumi, K. Mali, S. D. Feyter, C. Castiglioni, and M. T. A. N. A. F. A. Müllen, "Synthesis and characterization of "tetrazigzag"-hexa-*peri*-hexabenzocoronene with four extra k-regions," *In preparation*, 2016.

[44] A. Narita, X.-Y. Wang, X. Feng, and K. Müllen, "New advances in nanographene chemistry," *Chem. Soc. Rev.*, vol. 44, no. 18, pp. 6616–6643, 2015.

[45] L. Chen, Y. Hernandez, X. Feng, and K. Müllen, "From nanographene and graphene nanoribbons to graphene sheets: Chemical synthesis," *Angewandte Chemie International Edition*, vol. 51, pp. 7640–7654, jul 2012.

[46] S. Dutta and S. K. Pati, "Novel properties of graphene nanoribbons: a review," *Journal of Materials Chemistry*, vol. 20, no. 38, p. 8207, 2010.

[47] O. V. Yazyev, "A guide to the design of electronic properties of graphene nanoribbons," *Accounts of Chemical Research*, vol. 46, pp. 2319–2328, oct 2013.

[48] O. V. Yazyev, "Emergence of magnetism in graphene materials and nanostructures," *Rep. Prog. Phys.*, vol. 73, p. 056501, apr 2010.

[49] Y.-W. Son, M. L. Cohen, and S. G. Louie, "Half-metallic graphene nanoribbons," *Nature*, vol. 446, pp. 342–342, mar 2007.

[50] A. Konishi, Y. Hirao, M. Nakano, A. Shimizu, E. Botek, B. Champagne, D. Shiomi, K. Sato, T. Takui, K. Matsumoto, H. Kurata, and T. Kubo, "Synthesis and characterization of teranthene: A singlet biradical polycyclic aromatic hydrocarbon having kekulé structures," *J. Am. Chem. Soc.*, vol. 132, pp. 11021–11023, aug 2010.

[51] A. Konishi, Y. Hirao, K. Matsumoto, H. Kurata, R. Kishi, Y. Shigeta, M. Nakano, K. Tokunaga, K. Kamada, and T. Kubo, "Synthesis and characterization of quarteranthene: Elucidating the characteristics of the edge state of graphene nanoribbons at the molecular level," *J. Am. Chem. Soc.*, vol. 135, pp. 1430–1437, jan 2013.

[52] A. Konishi, Y. Hirao, H. Kurata, T. Kubo, M. N. Y. Hirao, H. K. M. Nakano, and K. Kamada, "Anthenes: Model systems for understanding the edge state of graphene nanoribbons," *PURE AND APPLIED CHEMISTRY*, vol. 86, no. 4, p. 497, 2014.

[53] X. Li, X. Wang, L. Zhang, S. Lee, and H. Dai, "Chemically derived, ultrasmooth graphene nanoribbon semiconductors," *Science*, vol. 319, pp. 1229–1232, feb 2008.

[54] J. Bai and Y. Huang, "Fabrication and electrical properties of graphene nanoribbons," *Materials Science and Engineering: R: Reports*, vol. 70, pp. 341–353, nov 2010.

[55] A. N. Abbas, G. Liu, B. Liu, L. Zhang, H. Liu, D. Ohlberg, W. Wu, and C. Zhou, "Patterning, characterization, and chemical sensing applications of graphene nanoribbon arrays down to 5 nm using helium ion beam lithography," *ACS Nano*, vol. 8, pp. 1538–1546, feb 2014.

[56] L. Jiao, L. Zhang, X. Wang, G. Diankov, and H. Dai, "Narrow graphene nanoribbons from carbon nanotubes," *Nature*, vol. 458, pp. 877–880, apr 2009.

[57] A. Narita, X. Feng, Y. Hernandez, S. A. Jensen, M. Bonn, H. Yang, I. A. Verzhbitskiy, C. Casiraghi, M. R. Hansen, A. H. R. Koch, G. Fytas, O. Ivasenko, B. Li, K. S. Mali, T. Balandina, S. Mahesh, S. D. Feyter, and K. Müllen, "Synthesis of structurally well-defined and liquid-phase-processable graphene nanoribbons," *Nature Chemistry*, vol. 6, pp. 126–132, dec 2013.

[58] Y.-C. Chen, T. Cao, C. Chen, Z. Pedramrazi, D. Haberer, D. G. de Oteyza, F. R. Fischer, S. G. Louie, and M. F. Crommie, "Molecular bandgap engineering of bottom-up synthesized graphene nanoribbon heterojunctions," *Nature Nanotech*, vol. 10, pp. 156–160, jan 2015.

[59] J. Wang, R. Zhao, M. Yang, Z. Liu, and Z. Liu, "Inverse relationship between carrier mobility and bandgap in graphene," *The Journal of Chemical Physics*, vol. 138, no. 8, p. 084701, 2013.

[60] A. Narita, X. Feng, and K. Müllen, "Bottom-up synthesis of chemically precise graphene nanoribbons," *The Chemical Record*, vol. 15, pp. 295–309, nov 2014.

[61] U. Zschieschang, H. Klauk, I. B. Müeller, A. J. Strudwick, T. Hintermann, M. G. Schwab, A. Narita, X. Feng, K. Müellen, and R. T. Weitz, "Electrical characteristics of field-effect transistors based on chemically synthesized graphene nanoribbons," *Adv. Electron. Mater.*, vol. 1, pp. n/a–n/a, feb 2015.

[62] F. Negri, C. Castiglioni, M. Tommasini, and G. Zerbi, "A computational study of the raman spectra of large polycyclic aromatic hydrocarbons: toward molecularly defined subunits of graphite †," *J. Phys. Chem. A*, vol. 106, pp. 3306–3317, apr 2002.

[63] C. Castiglioni, F. Negri, M. Rigolio, and G. Zerbi, "Raman activation in disordered graphites of the $A_1^{'}$ symmetry forbidden k≠0 phonon: The origin of the d line," *The Journal of Chemical Physics*, vol. 115, no. 8, p. 3769, 2001.

[64] A. C. Ferrari and J. Robertson, "Interpretation of raman spectra of disordered and amorphous carbon," *Phys. Rev. B*, vol. 61, pp. 14095–14107, may 2000.

[65] R. Escribano, J. Sloan, N. Siddique, N. Sze, and T. Dudev, "Raman spectroscopy of carbon-containing particles," *Vibrational Spectroscopy*, vol. 26, pp. 179–186, nov 2001.

[66] K. Ohno, "Normal coordinate calculations of benzenoid hydrocarbons," *Journal of Molecular Spectroscopy*, vol. 72, pp. 238–251, aug 1978.

[67] K. Ohno, "A simple predictive model for planar vibrations of polycyclic benzenoid hydrocarbons," *The Journal of Chemical Physics*, vol. 95, no. 8, p. 5524, 1991.

[68] S. Piscanec, M. Lazzeri, F. Mauri, A. C. Ferrari, and J. Robertson, "Kohn anomalies and electron-phonon interactions in graphite," *Phys. Rev. Lett.*, vol. 93, oct 2004.

[69] A. K. Geim and K. S. Novoselov, "The rise of graphene," *Nature Materials*, vol. 6, pp. 183–191, mar 2007.

[70] A. K. Geim, "Graphene: Status and prospects," *Science*, vol. 324, pp. 1530–1534, jun 2009.

[71] J. C. Ribierre, S. Watanabe, M. Matsumoto, T. Muto, D. Hashizume, and T. Aoyama, "Thickness dependence of the ambipolar charge transport properties in organic field-effect transistors based on a quinoidal oligothiophene derivative," *J. Phys. Chem. C*, vol. 115, pp. 20703–20709, oct 2011.

[72] T. Agostinelli, M. Caironi, D. Natali, M. Sampietro, G. Dassa, E. V. Canesi, C. Bertarelli, G. Zerbi, J. Cabanillas-Gonzalez, S. D. Silvestri, and G. Lanzani, "A planar organic near infrared light detector based on bulk heterojunction of a heteroquaterphenoquinone and poly[2-methoxy-5-(2'-ethyl-hexyloxy)-1, 4-phenylene vinylene]," *J. Appl. Phys.*, vol. 104, no. 11, p. 114508, 2008.

[73] Z. Kan, L. Colella, E. V. Canesi, G. Lerario, R. S. S. Kumar, V. Bonometti, P. R. Mussini, G. Cavallo, G. Terraneo, P. Pattanasattayavong, T. D. Anthopoulos, C. Bertarelli, and P. E. Keivanidis, "Triple bulk heterojunctions as means for recovering the microstructure of photoactive layers in organic solar cell devices," *Solar Energy Materials and Solar Cells*, vol. 120, pp. 37–47, jan 2014.

[74] Y. Zhang, T. P. Basel, B. R. Gautam, X. Yang, D. J. Mascaro, F. Liu, and Z. V. Vardeny, "Spin-enhanced organic bulk heterojunction photovoltaic solar cells," *Nature Communications*, vol. 3, p. 1043, sep 2012.

[75] E. V. Canesi, D. Fazzi, L. Colella, C. Bertarelli, and C. Castiglioni, "Tuning the quinoid versus biradicaloid character of thiophene-based heteroquaterphenoquinones by means of functional groups," *J. Am. Chem. Soc.*, vol. 134, pp. 19070–19083, nov 2012.

[76] M. Abe, "Diradicals," *Chemical Reviews*, vol. 113, pp. 7011–7088, sep 2013.

[77] D. A. Dougherty, "Spin control in organic molecules," *Accounts of Chemical Research*, vol. 24, pp. 88–94, mar 1991.

[78] M. Ruitenbeek, A. Barbon, E. van Faassen, and J. Geus, "Evidence for a new type of vanadyl pairs in (vo)2p2o7: an esr and magnetisation study," *Catalysis Letters*, vol. 54, no. 3, pp. 101–104, 1998.

[79] N. D. M. Neil W. Ashcroft, *Solid State Physics*. Cengage Learning, Inc, 1976.

[80] Z. Sun, Z. Zeng, and J. Wu, "Zethrenes, extended p-quinodimethanes, and periacenes with a singlet biradical ground state," *Accounts of Chemical Research*, vol. 47, pp. 2582–2591, aug 2014.

[81] T. Takahashi, K. ichi Matsuoka, K. Takimiya, T. Otsubo, and Y. Aso, "Extensive quinoidal oligothiophenes with dicyanomethylene groups at terminal positions as highly amphoteric redox molecules," *J. Am. Chem. Soc.*, vol. 127, pp. 8928–8929, jun 2005.

[82] K. Takahashi and T. Suzuki, "p-diphenoquinone analogs extended by dihydrothiophenediylidene insertion. a novel amphoteric multistage redox system," *J. Am. Chem. Soc.*, vol. 111, pp. 5483–5485, jul 1989.

[83] F. Tampieri, L. Colella, A. Maghsoumi, J. Marti-Rujas, E. Parisini, M. Tommasini, C. Bertarelli, and A. Barbon, "Meeting the challenging magnetic and electronic structure of thiophene-based heterophenoquinones," *In preparation*, 2016.

[84] D. Fazzi, E. V. Canesi, F. Negri, C. Bertarelli, and C. Castiglioni, "Biradicaloid character of thiophene-based heterophenoquinones: The role of electron-phonon coupling," *Chem. Eur. J. of Chem. Phys.*, vol. 11, pp. 3685–3695, nov 2010.

[85] L. Colella, L. Brambilla, V. Nardone, E. Parisini, C. Castiglioni, and C. Bertarelli, "Outside rules inside: the role of electron-active substituents in thiophene-based heterophenoquinones," *Phys. Chem. Chem. Phys.*, vol. 17, no. 16, pp. 10426–10437, 2015.

[86] J. T. and P. Rojruthai, "Molecular structure of natural rubber and its characteristics based on recent evidence," in *Biotechnology - Molecular Studies and Novel Applications for Improved Quality of Human Life*, InTech, mar 2012.

[87] S. M. Poor, *Study of the mechanical behavior of high cis-polybutadiene rubber: structure to property correlation*. PhD thesis, POLITECNICO DI MILANO, DEPARTMENT DI CHIMICA, MATERIALI E INGENERIA CHIMICA ''GIULIA NATTA", 2015.

[88] S. Toki, T. Fujimaki, and M. Okuyama, "Strain-induced crystallization of natural rubber as detected real-time by wide-angle x-ray diffraction technique," *Polymer*, vol. 41, pp. 5423–5429, jun 2000.

[89] M. Tosaka, "Strain-induced crystallization of crosslinked natural rubber as revealed by x-ray diffraction using synchrotron radiation," *Polym J*, vol. 39, pp. 1207–1220, oct 2007.

[90] S. Trabelsi, P.-A. Albouy, and J. Rault, "Crystallization and melting processes in vulcanized stretched natural rubber," *Macromolecules*, vol. 36, pp. 7624–7639, oct 2003.

[91] K. Saijo, Y.-P. Zhu, T. Hashimoto, A. Wasiak, and N. Brzostowski, "Oriented crystallization of crosslinkedcis-1,4-polybutadiene rubber," *Journal of Applied Polymer Science*, vol. 105, no. 1, pp. 137–157, 2007.

[92] J. Mark, *Science and Technology of Rubber*. Elsevier Science & Technology, 2013.

[93] F. BACCHELLI and S. COPPOLA, "Chain stretching and rheological behaviour of cis-br: Role of molecular architecture for tyre application," *Chem. Listy*, vol. 107, pp. S12–S14, 2013.

[94] W. W. H. Wong, J. Subbiah, S. R. Puniredd, B. Purushothaman, W. Pisula, N. Kirby, K. Müllen, D. J. Jones, and A. B. Holmes, "Liquid crystalline hexa-peri-hexabenzocoronene-diketopyrrolopyrrole organic dyes for photovoltaic applications," *Journal of Materials Chemistry*, vol. 22, no. 39, p. 21131, 2012.

[95] Y.-Z. Tan, S. Osella, Y. Liu, B. Yang, D. Beljonne, X. Feng, and K. Müllen, "Sulfur-annulated hexa- peri -hexabenzocoronene decorated with phenylthio groups at the periphery," *Angewandte Chemie International Edition*, vol. 54, pp. 2927–2931, jan 2015.

[96] I. Pócsik, M. Hundhausen, M. Koós, and L. Ley, "Origin of the d peak in the raman spectrum of microcrystalline graphite," *Journal of Non-Crystalline Solids*, vol. 227-230, pp. 1083–1086, may 1998.

[97] M. Z. Atashbar and S. Singamaneni, "Comparative studies of temperature dependence of g-band peak in single walled carbon nanotube and highly oriented pyrolytic graphite," *Appl. Phys. Lett.*, vol. 86, no. 12, p. 123112, 2005.

[98] S. Osella, A. Narita, M. G. Schwab, Y. Hernandez, X. Feng, K. Müllen, and D. Beljonne, "Graphene nanoribbons as low band gap donor materials for organic photovoltaics: Quantum chemical aided design," *ACS Nano*, vol. 6, pp. 5539–5548, jun 2012.

[99] M. Tommasini, A. Lucotti, M. Alfè, A. Ciajolo, and G. Zerbi, "Fingerprints of polycyclic aromatic hydrocarbons (pahs) in infrared absorption spectroscopy," *Spectrochimica Acta Part A: Molecular and Biomolecular Spectroscopy*, vol. 152, pp. 134–148, jan 2016.

[100] J. Cai, P. Ruffieux, R. Jaafar, M. Bieri, T. Braun, S. Blankenburg, M. Muoth, A. P. Seitsonen, M. Saleh, X. Feng, K. Müllen, and R. Fasel, "Atomically precise bottom-up fabrication of graphene nanoribbons," *Nature*, vol. 466, pp. 470–473, jul 2010.

[101] T. H. Vo, M. Shekhirev, D. A. Kunkel, M. D. Morton, E. Berglund, L. Kong, P. M. Wilson, P. A. Dowben, A. Enders, and A. Sinitskii, "Large-scale solution synthesis of narrow graphene nanoribbons," *Nature Communications*, vol. 5, feb 2014.

[102] Q. Zhang, H. Peng, G. Zhang, Q. Lu, J. Chang, Y. Dong, X. Shi, and J. Wei, "Facile bottom-up synthesis of coronene-based 3-Fold symmetrical and highly substituted nanographenes from simple aromatics," *J. Am. Chem. Soc.*, vol. 136, pp. 5057–5064, apr 2014.

[103] A. Cristadoro, H. J. Räder, and K. Müllen, "Clustering of polycyclic aromatic hydrocarbons in matrix-assisted laser desorption/ionization and laser desorption mass spectrometry," *Rapid Communications in Mass Spectrometry*, vol. 21, no. 16, pp. 2621–2628, 2007.

[104] J. P. Merrick, D. Moran, and L. Radom, "An evaluation of harmonic vibrational frequency scale factors," *J. Phys. Chem. A*, vol. 111, pp. 11683–11700, nov 2007.

[105] C. Cappelli, J. Bloino, F. Lipparini, and V. Barone, "Toward ab initio anharmonic vibrational circular dichroism spectra in the condensed phase," *J. Phys. Chem. Lett.*, vol. 3, pp. 1766–1773, jul 2012.

[106] F. Egidi, J. Bloino, C. Cappelli, and V. Barone, "Development of a virtual spectrometer for chiroptical spectroscopies: The case of nicotine," *Chirality*, vol. 25, pp. 701–708, jul 2013.

[107] C. Merten, J. Bloino, V. Barone, and Y. Xu, "Anharmonicity effects in the vibrational CD spectra of propylene oxide," *J. Phys. Chem. Lett.*, vol. 4, pp. 3424–3428, oct 2013.

[108] V. Barone, M. Biczysko, and J. Bloino, "Fully anharmonic IR and raman spectra of medium-size molecular systems: accuracy and interpretation," *Phys. Chem. Chem. Phys.*, vol. 16, no. 5, pp. 1759–1787, 2014.

[109] J. Bloino, "A VPT2 route to near-infrared spectroscopy: The role of mechanical and electrical anharmonicity," *J. Phys. Chem. A*, vol. 119, pp. 5269–5287, may 2015.

[110] B. Yang, A. Narita, K. Mali, A. Maghsoumi, L. A. Straasø, M. R. Hansen, P. Ruffieux, R. Fasel, C. Castiglioni, M. Tommasini, S. D. Feyter, X. Feng, and K. Müllen, "Bottom-up approach toward graphene nanoribbons with zigzag edge structures: Solution-mediated synthesis and characterizations," *In preparation*, 2016.

[111] Y.-W. Son, M. L. Cohen, and S. G. Louie, "Energy gaps in graphene nanoribbons," *Phys. Rev. Lett.*, vol. 97, nov 2006.

[112] K. Nakada, M. Fujita, G. Dresselhaus, and M. S. Dresselhaus, "Edge state in graphene ribbons: Nanometer size effect and edge shape dependence," *Phys. Rev. B*, vol. 54, pp. 17954–17961, dec 1996.

[113] Y. Morita, S. Suzuki, K. Sato, and T. Takui, "Synthetic organic spin chemistry for structurally well-defined open-shell graphene fragments," *Nature Chemistry*, vol. 3, pp. 197–204, mar 2011.

[114] X. Feng, V. Marcon, W. Pisula, M. R. Hansen, J. Kirkpatrick, F. Grozema, D. Andrienko, K. Kremer, and K. Muellen, "Towards high charge-carrier mobilities by rational design of the shape and periphery of discotics," *Nat. Mater.*, vol. 8, pp. 421–426, Maggio 2009.

[115] S. Sergeyev, W. Pisula, and Y. H. Geerts, "Discotic liquid crystals: A new generation of organic semiconductors," *Chem. Soc. Rev.*, vol. 36, no. 12, pp. 1902–1929, 2007.

[116] V. Coropceanu, J. Cornil, D. A. da Silva Filho, Y. Olivier, R. Silbey, and J.-L. Bredas, "Charge transport in organic semiconductors," *Chem. Rev.*, vol. 107, pp. 926–952, Aprile 2007.

[117] C. Kuebel, K. Eckhardt, V. Enkelmann, G. Wegner, and K. Mullen, "Synthesis and crystal packing of large polycyclic aromatic hydrocarbons: hexabenzo[bc,ef,hi,kl,no,qr]coronene and dibenzo[fg,ij]phenanthro[9,10,1,2,3-pqrst]pentaphene," *J. Mater. Chem.*, vol. 10, no. 4, pp. 879–886, 2000.

[118] L. Brambilla, M. Tommasini, I. Botiz, K. Rahimi, J. O. Agumba, N. Stingelin, and G. Zerbi, "Regio-regular oligo and poly(3-hexyl thiophene): Precise structural markers from the vibrational spectra of oligomer single crystals.," *Macromolecules*, vol. 47, pp. 6730–6739, Ottobre 2014.

[119] L. Gross, F. Mohn, N. Moll, B. Schuler, A. Criado, E. Guitián, D. Peña, A. Gourdon, and G. Meyer, "Bond-order discrimination by atomic force microscopy," *Science*, vol. 337, no. 6100, pp. 1326–1329, 2012.

[120] Y.-L. Loo, A. M. Hiszpanski, B. Kim, S. Wei, C.-Y. Chiu, M. L. Steigerwald, and C. Nuckolls, "Unusual molecular conformations in fluorinated, contorted hexabenzocoronenes," *Org. Lett.*, vol. 12, pp. 4840–4843, Novembre 2010.

[121] A. Centrone, L. Brambilla, T. Renouard, L. Gherghel, C. Mathis, K. Mullen, and G. Zerbi, "Structure of new carbonaceous materials: The role of vibrational spectroscopy," *Carbon*, vol. 43, pp. 1593–1609, 2005.

[122] M. Von Zander and B. G. Teubner, "Polycyclische aromaten (reihe: Teubner studienbücher chemie, stuttgart, 1995, isbn 3–519–03537–5)," *Angewandte Chemie*, vol. 108, no. 19, pp. 2411–2411, 1996.

[123] F. A. Miller, "Misassignment of the strong raman band near 1000 cm-1 in some substituted benzenes, and the herzberg versus wilson convention for numbering the vibrations of benzene," *J. Raman Spectrosc.*, vol. 19, pp. 219–221, Maggio 1988.

[124] S. Abbate, G. Longhi, F. Lebon, E. Castiglioni, S. Superchi, L. Pisani, F. Fontana, F. Torricelli, T. Caronna, C. Villani, R. Sabia, M. Tommasini, A. Lucotti, D. Mendola, A. Mele, and D. A. Lightner, "Helical sense-responsive and substituent-sensitive features in vibrational and electronic circular dichroism, in circularly polarized luminescence, and in raman spectra of some simple optically active hexahelicenes," *J. Phys. Chem. C*, vol. 118, pp. 1682–1695, jan 2014.

[125] H. Miyoshi, S. Nobusue, A. Shimizu, and Y. Tobe, "Non-alternant non-benzenoid kekulenes: the birth of a new kekulene family," *Chem. Soc. Rev.*, vol. 44, no. 18, pp. 6560–6577, 2015.

[126] S. P. Balm and H. W. Kroto, "Possible assignment of the 11.3-mu-m uir feature to emission from carbonaceous microparticles with internal hydrogens," *Mon. Not. Roy. Astron. Soc.*, vol. 245, pp. 193–197, Luglio 1990.

[127] B. Kumar, R. L. Viboh, M. C. Bonifacio, W. B. Thompson, J. C. Buttrick, B. C. Westlake, M.-S. Kim, R. W. Zoellner, S. A. Varganov, P. Moerschel, J. Teteruk, M. U. Schmidt, and B. T. King, "Septulene: The heptagonal homologue of kekulene," *Angew. Chem.-Int. Edit.*, vol. 51, no. 51, pp. 12795–12800, 2012.

[128] A. Baiardi, J. Bloino, and V. Barone, "A general time-dependent route to resonance-raman spectroscopy including franck-condon, herzberg-teller and duschinsky effects," *The Journal of Chemical Physics*, vol. 141, no. 11, p. 114108, 2014.

[129] A. Baiardi, J. Bloino, and V. Barone, "Accurate simulation of resonance-raman spectra of flexible molecules: An internal coordinates approach," *J. Chem. Theory Comput.*, vol. 11, pp. 3267–3280, Luglio 2015.

[130] C. D. Simpson, J. D. Brand, A. J. Berresheim, L. Przybilla, H. J. Räder, and K. Müllen, "Synthesis of a giant 222 Carbon graphite sheet," *Chemistry - A European Journal*, vol. 8, pp. 1424–1429, mar 2002.

[131] D. Moran, F. Stahl, H. F. Bettinger, H. F. Schaefer, and P. v. R. Schleyer, "Towards graphite: magnetic properties of large polybenzenoid hydrocarbons †," *J. Am. Chem. Soc.*, vol. 125, pp. 6746–6752, jun 2003.

[132] J. T. L. Navarrete and G. Zerbi, "Lattice dynamics and vibrational spectra of polythiophene. II. effective coordinate theory, doping induced, and photoexcited spectra," *The Journal of Chemical Physics*, vol. 94, no. 2, p. 965, 1991.

[133] J. C. Salamone, *Concise polymeric materials encyclopedia*. CRC Press LLC, 1999.

[134] B. Connolly, T. W. Patapoff, Y. J. Wang, J. M. Moore, T. J. Kamerzell, "Vibrational spectroscopy and chemometrics to characterize and quantitate trehalose crystallization," *Anal. Biochem.*, vol. 399, no. 1, pp. 48–57, 2010.

[135] K. Tashiro, M. Kobayashi, H. Tadokoro, "Vibrational spectra and disorder-order transition of poly(vinylidene fluoride) form iii," *Macromolecules*, vol. 14, no. 6, pp. 1757–1764, 1981.

[136] L. Mandelkern, *Crystallization of Polymers*. McGraw-Hill, 1964.

[137] K. Tashiro, "Molecular theory of mechanical properties of crystalline polymers," *Prog. Polym. Sci.*, vol. 18, no. 3, pp. 377–435, 1993.

[138] S. W. Cornell, J. L. Koenig, "Raman spectra of polyisoprene rubbers," *Macromolecules*, vol. 2, no. 5, pp. 546–549, 1969.

[139] R. A. Saunders and D. C. Smith, "Infra-red spectra and structure of hevea and gutta elastomers," *J. Appl. Phys.*, vol. 20, no. 10, p. 953, 1949.

[140] H. W. Siesler, "Rheo-optical Fourier-transform infrared (FTIR) spectroscopy of polymers," *Colloid & Polymer Sci*, vol. 262, pp. 223–229, mar 1984.

[141] R. Willemse, A. Speijer, A. Langeraar, and A. P. de Boer, "Tensile moduli of co-continuous polymer blends," *Polymer*, vol. 40, pp. 6645–6650, nov 1999.

[142] M. Baginski, P. Gariboldi, P. Bruni, and E. Borowski, "Conformational analysis of amphotericin b," *Biophysical Chemistry*, vol. 65, pp. 91–100, apr 1997.

[143] J. Mazerski and E. Borowski, "Molecular dynamics of amphotericin b. II. dimer in water," *Biophysical Chemistry*, vol. 57, pp. 205–217, jan 1996.

[144] P. Millié, J. Langlet, J. Bergès, J. Caillet, and J.-P. Demaret, "Self-association of amphotericin b in water. theoretical energy and spectroscopy studies," *The Journal of Physical Chemistry B*, vol. 103, pp. 10883–10891, dec 1999.

[145] J. Caillet, J. Bergès, and J. Langlet, "Theoretical study of the self-association of amphotericin b," *Biochimica et Biophysica Acta (BBA) - Biomembranes*, vol. 1240, pp. 179–195, dec 1995.

[146] W. I. Gruszecki, M. Gagoś, and M. Hereć, "Dimers of polyene antibiotic amphotericin b detected by means of fluorescence spectroscopy: molecular organization in solution and in lipid membranes," *Journal of Photochemistry and Photobiology B: Biology*, vol. 69, pp. 49–57, jan 2003.

[147] H. G. Brittain, "Circular dichroism studies of the self-association of amphotericin b," *Chirality*, vol. 6, no. 8, pp. 665–669, 1994.

[148] M. Gagosś, M. Arczewska, and W. I. Gruszecki, "Raman spectroscopic study of aggregation process of antibiotic amphotericin b induced by h^+ , na^+ , and k^+ ions," *The Journal of Physical Chemistry B*, vol. 115, pp. 5032–5036, may 2011.

[149] J. Bolard and M. Chéron, "Does fluorescence spectroscopy detect dimers of the polyene antibiotic amphotericin b?," *Journal of Photochemistry and Photobiology B: Biology*, vol. 72, pp. 101–102, dec 2003.

[150] R. Dovesi, R. Orlando, A. Erba, C. M. Zicovich-Wilson, B. Civalleri, S. Casassa, L. Maschio, M. Ferrabone, M. D. L. Pierre, P. D'Arco, Y. Noël, M. Causà, M. Rérat, and B. Kirtman, "C RYSTAL14 : A program for the ab initio investigation of crystalline solids," *Int. J. Quantum Chem.*, vol. 114, pp. 1287–1317, mar 2014.

Appendix

In this section are enclosed the copies of two published papers related with this Ph.D. thesis work.

1 Overtone and combination features of G and D peaks in resonance Raman spectroscopy of the $C_{78}H_{26}$ polycyclic aromatic hydrocarbon.

2 Bottom-Up Synthesis of Necklace-Like Graphene Nanoribbons.

It also attached the submitted manuscript by Tampieri et. al which describes the investigation on thiophene derivatives with radicaloid structure (Chapter 6): "Meeting the challenging magnetic and electronic structure of thiophene-based heterophenoquinones"

Other manuscripts related with the results presented in Chapters 3, 4 and 5 are currently in preparation:

1 Ali Maghsoumi, Akimitsu Narita, Renhao Dong, Xinliang Feng, Chiara Castiglioni, Klaus Müllen, and Matteo Tommasini; "Edge chlorination of hexa-peri-hexabenzocoronene investigated by density functional theory and vibrational spectroscopy"

2 Uliana Beser, Marcel Kastler, Ali Maghsoumi, Manfred Wagner, Chiara Castiglioni, Matteo Tommasini, Akimitsu Narita, Xinliang Feng, and Klaus Müllen; "A C216-Nanographene Molecule with Defined Cavity as Extended Coronoid"

3 Tim Dumslaff, Ali Maghsoumi, Kunal Mali, Steven De Feyter, Chiara Castiglioni, Matteo Tommasini, Akimitsu Narita, Xinliang Feng, and Klaus Müllen; "Synthesis and Characterization of Hexa-peri-hexabenzocoronene with Four Extra K-Regions"

4 Bo Yang, Akimitsu Narita, Kunal Mali, Ali Maghsoumi, Lasse Arnt Straasø, Michael Ryan Hansen, Pascal Ruffieux, Roman Fasel, Chiara Castiglioni, Matteo Tommasini, Steven De Feyter, Xinliang Feng, and Klaus Müllen; "Bottom-Up Approach Toward Graphene Nanoribbons with Zigzag Edge Structures: Solution-Mediated Synthesis and Characterizations"

Research article

Journal of RAMAN SPECTROSCOPY

Received: 30 January 2015 Revised: 27 April 2015 Accepted: 27 April 2015 Published online in Wiley Online Library

(wileyonlinelibrary.com) DOI 10.1002/jrs.4717

Overtone and combination features of G and D peaks in resonance Raman spectroscopy of the $C_{78}H_{26}$ polycyclic aromatic hydrocarbon

A. Maghsoumi,[a] L. Brambilla,[a] C. Castiglioni,[a] K. Müllen[b] and M. Tommasini[a]*

We have studied the Raman spectra of $C_{78}H_{26}$, a polycyclic aromatic hydrocarbon with D_{2h} symmetry point group resembling a longitudinally confined graphene ribbon (or a graphene island) with armchair edge. The experimental spectra recorded with several excitation laser lines have been compared with the results from a theoretical analysis of the resonant Raman response based on density functional theory calculations. Compared to previous investigation the spectra show better signal-to-noise ratio, which allows determining previously unresolved weak spectroscopic features. We have extended our analysis to the overtone and combination region (i.e. above 2000 cm^{-1}) demonstrating the presence of signals attributable to 2G, G + D, 2D, $D_j + D_k$ and G + acoustic-like modes. Moreover, we have measured the temperature dependence of the G peak position, which turns out to show a similar behavior with respect to that of graphene/graphite. Copyright © 2015 John Wiley & Sons, Ltd.

Additional supporting information may be found in the online version of this article at the publisher's website.

Keywords: Polycyclic Aromatic Hydrocarbon (PAH); Resonance Raman; DFT; graphene related materials

Introduction

Polycyclic aromatic hydrocarbons (PAHs) have inspired scientific research for several reasons. They have provided models to develop and test elementary π-bond theory.[1] The extended π-conjugation and self-organizing properties of PAHs are important properties for molecular electronics.[2] Their carcinogenic activity is of concern because PAHs occur as intermediate combustion products upon soot formation.[3] Furthermore, PAHs are organic molecular species present in interstellar space, and they represent an important research field in astrophysics.[4]

It is well-known that Raman spectroscopy is a convenient probe for analyzing PAHs[5–7] and graphenes[8] because, it is fast, is non-destructive, provides structural and electronic information, and can be adopted not only in academic laboratories but also, as a perspective, for the characterization of materials in industrial production frameworks.

The Raman spectroscopy of graphene, graphite and PAHs has been extensively investigated.[5–10] The first-order Raman spectra of these materials show a characteristic pattern constituted by two strong bands located at around 1600 cm^{-1} and 1300 cm^{-1}. For PAHs these Raman signals are also structured, i.e. they show several components. These signals are characteristic of sp^2 carbon materials and have been traditionally called G and D bands, respectively.

The D band (from 'disorder') appears in graphitic systems when some kind of disorder or discontinuity of the lattice occurs. Raman features in the D region are also observed in amorphous carbon systems with mixed sp^2/sp^3 content.[11] In PAHs the D peak is an intrinsic Raman signal that can be taken as signature of the confinement of π electrons and relaxation of the molecular structure with respect to the equalized CC bonds characteristic of graphene/graphite. It is worth considering that the Raman investigation of PAHs (as oligomers of graphene) can provide information that could be used for a better characterization of graphene itself. Obviously, since the advent of graphene,[12,13] this point may disclose important practical applications. For instance this kind of a situation occurred in the past, when the origin of the Raman D peak was debated[7,14,15] and the right early assignment of the phonon dispersion curves of graphene was the result of calculations originated from molecular models[10,16,17] later confirmed by first principles calculations.[18]

We may expect a similar situation here, because the D peak overtone in the Raman spectra of graphene and few layer graphenes is routinely used to characterize the quality of the materials produced.[8] However, even though a connection of the G and D peaks in graphene and PAHs does exist,[7] as far as the authors are aware of, the same cannot be said for the higher order Raman processes, such as 2D or 2G. This work is a first attempt to dwell more into this issue, by considering in details the Raman spectra of $C_{78}H_{26}$ (**C78**, for short—see Fig. 1) including overtones and combinations, and the dependence of the spectra with respect to the excitation wavelength.

On one side we have carried out a series of experiments in order to determine the Raman behavior of **C78** taken as representative model of D_{2h} PAHs. On the other side we have provided an interpretation of the experimental data by means of calculations of the Raman response, including overtones and combinations, which is based upon Density Functional Theory (DFT) and Nafie–Peticolas–Stein theory of resonant Raman.[19,20] Compared with

* *Correspondence to: Matteo Tommasini, Dip. Chimica, Materiali, Ing. Chimica, Politecnico di Milano, Italy.*
E-mail: matteo.tommasini@polimi.it

a *Dipartimento di Chimica, Materiali ed Ingegneria Chimica 'G. Natta', Politecnico di Milano, Italy*

b *Max Planck Institute for Polymer Research, Ackermannweg 10, D-55128, Mainz, Germany*

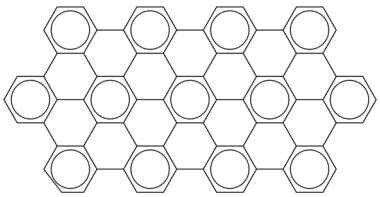

Figure 1. Molecular structure of **C78**, a PAH belonging to the D_{2h} point group. Clar's aromatic sextets are evidenced.

previous investigation of resonance Raman response of PAHs[6,7] the present method allows a substantial computational saving, because it does not require the optimization of the excited states. A resonance Raman approach has to be adopted because for **C78** with the excitations wavelengths adopted by us (785, 632.8, 514.5, 457.9 and 325 nm) we match electronic resonance conditions.[6,21]

Because **C78** represents a confined graphitic structure exhibiting peculiar G + D Raman combination signals, the results presented here could be useful to characterize with Raman spectroscopy other confined graphene systems such as graphene islands[22–25] or graphene ribbons.[26,27]

Experimental and theoretical methods

The powder of **C78**, already investigated in the past,[6] was synthesized as described by Watson *et al.*[21] To improve the quality of the Raman spectra, in this work we have repeatedly washed the sample with tetrahydrofuran (THF) in which **C78** is insoluble. This allowed reducing effectively the fluorescence background signal thus easing the collection of the weaker Raman features. The **C78** powder (about 2 mg) was dispersed in THF (about 3 ml) and sonicated for 15 min, hence centrifuged for 10 min at 5000 RPM. Then 2 ml of surnatant was removed and replaced with fresh THF. Thereafter the dispersion was sonicated again, and the whole procedure was repeated 3 times. The cleaned **C78** powder was recovered after complete evaporation of residual THF.

The Raman spectra presented here have been recorded with a Jobin-Yvon Labram HR800UV spectrometer. Different laser lines have been used, namely 325 nm (He–Cd laser), 457.9 and 514.5 nm (Ar^+ laser), 632.8 nm (He–Ne laser) and 785 nm (high power diode laser). The laser power at the sample was always of the order of a few mW to prevent (or reduce as possible) laser-induced effects on the samples; care has been adopted to verify the reproducibility of the spectra. Samples were analyzed in a back-scattering geometry on glass slides by using the microscope with the 50× objective for all laser lines except the one at 325 nm for which an UV-grade 15× objective was used. The intensity of all reported Raman spectra (325 nm excitation excluded) have been corrected with white light calibration.

The Linkam THMS600 stage was used for temperature-dependent Raman spectra starting from room temperature (RT) and increasing stepwise by 25 °C up to 200 °C. The Raman spectra were recorded in correspondence of each temperature step, allowing the sample to reach a stable equilibrium temperature.

We have modeled the Raman response of **C78** by means of DFT calculations carried out at the B3LYP/6-31G** level. At first, we have computed the off-resonance Raman spectra with the standard procedure available within the selected quantum chemistry code (Gaussian09 D.01[28]). When comparing experimental data with computed peak wavenumber we adopted a scaling factor of 0.9793 that has been adopted so to fit the position of the G peak in the simulated and experimental spectra. We have then evaluated the resonance Raman response of **C78** adopting the theoretical approach introduced by Nafie, Stein and Peticolas[19] which is discussed in details in[20] where it is applied to π conjugated systems (polyenes). It requires the calculation of the gradient at the Franck–Condon point on the potential energy surface of the excited state of interest. We adopted a Time-Dependent DFT (TDDFT) approach (B3LYP/6-31G**) to evaluate the gradient. From it, the electron–phonon coupling parameters of all normal modes can be determined, and the relative intensities of first-order Raman processes, overtones and combinations can be evaluated.[20][1] In the present treatment we have considered perfect resonance conditions with selected excited states of **C78** (namely S_1, S_4 and S_6). Based on our calculation we have analyzed the experimental spectra recorded with different excitations and rationalized the observed spectra in the low wavenumber, D, G, overtone and combination regions.

The chosen theoretical approach for the evaluation of resonance Raman has the benefit of requiring a limited computational effort, compared to more accurate treatments[29] of resonance Raman which can deal in more details with Raman excitation profiles and non-totally symmetric normal modes (see Section on Low Wavenumber Region). The consideration of the computational effort is particularly relevant in molecular graphenes, which are usually sizeable systems.

Discussion of the Raman spectra

Before addressing the experimental Raman spectra of **C78**, it is worth describing briefly the nature of the main Raman signals of PAHs, which are named G and D after their analogy with the corresponding Raman signals of graphene/graphite systems.

Graphite's G band (from 'graphite') is assigned to the degenerate $\mathbf{q} = \mathbf{0}$ (where **q** is the phonon wave vector) optical phonon of E_{2g} symmetry of the graphene lattice.[10] Because, compared with graphene, point group symmetry lowers in **C78** and becomes D_{2h} (see Fig. 1), the modes of the molecule which correspond to the degenerate G modes of graphene may formally belong to either A_g or B_{3g} irreducible representation. For A_g modes the nuclear displacements of the molecular core (i.e. the seven innermost condensed rings) occur along the long molecular axis, while for B_{3g} modes occur along the short molecular axis (see Fig. 2 and Table S1 (Supporting Information)). However, it is worth noticing that the totally symmetric modes are significantly stronger than the B_{3g} modes (this is expected in Raman spectroscopy, see also Table S1 (Supporting Information)). Hence the G peak of **C78** mainly features longitudinal modes.

The Raman intensity of the D peak is vanishing by symmetry in graphene, and it becomes sizeable only because of translational symmetry breaking (e.g. by the presence of defects/edges in the graphene flake, or by confinement of π electrons in finite size PAHs —see for instance[7,8,30]). The D peak is assigned to a specific vibrational mode that can be described as a cooperative breathing of alternated hexagonal rings in the core of the molecule[6,9] (see Fig. 3).

To simplify the discussion of the Raman spectra we divide the analysis in three sections, namely (a) the medium wavenumber region comprising the D, G signals (1000 – 1800 cm^{-1}), (b) the low

[1]The present approach does compute the Raman intensities of fundamentals, overtones and combinations within the harmonic approximation of the potential energy surface. Hence the assessment of the anharmonic effects of Fermi and Darling–Dennison resonances[33] in the simulated spectra is not straightforward within this theoretical framework.

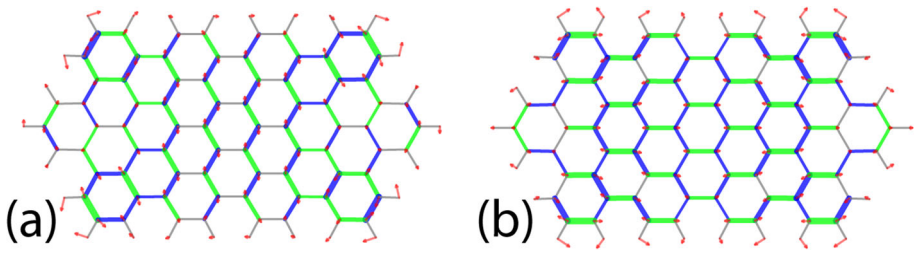

Figure 2. Representation of selected G-peak normal modes of **C78**: (a) transversal B_{3g} mode computed at 1643 cm^{-1}; (b) longitudinal A_g mode computed at 1635 cm^{-1}. Results from B3LYP/6-31G** calculations. Red arrows represent displacement vectors; CC bonds are represented as green (blue) lines of different thickness according to their relative stretching (shrinking).

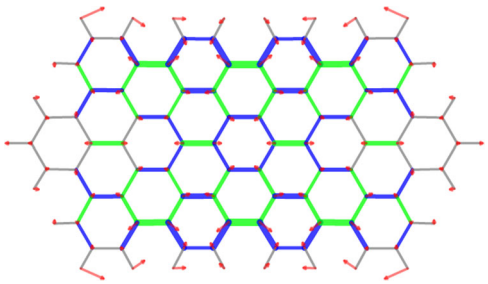

Figure 3. Representation of the D-peak normal mode of **C78** computed at 1294 cm^{-1} (B3LYP/6-31G** calculation). It is worth noticing that the rings corresponding to Clar's sextets in Fig. 1 are those involved in the collective breathing vibration, which is a characteristic feature of the modes in the D region. Red arrows represent displacement vectors; CC bonds are represented as green (blue) lines of different thickness according to their relative stretching (shrinking).

wavenumber region (<1000 cm^{-1}) and (c) the high wavenumber region (1800–3500 cm^{-1}) featuring overtone and combination lines. The temperature dependence of the G peak will be discussed in the ending paragraph of this section.

(a) **D, G region**. The experimental Raman spectra of **C78** excited with several laser lines are presented in Fig. 4. It is evident that the Raman spectra in this region are significantly sensitive to the variation of the excitation energy. Between 1150 cm^{-1} and 1450 cm^{-1} at least 11 D peaks (D_1–D_{11}) are observed, whose relative intensities are highly sensitive to the excitation wavelength. The positions of D_1–D_{11} are reported in Table 1 based on deconvolution of spectra (details are given in Fig. S1 (Supporting Information)). Within experimental error and band convolution uncertainty the position of these components is expected to be independent with respect to the laser excitation (as can be judged in Table 1). This is because of the assignment of each D component to a specific molecular normal mode. The relative intensity of the most distinguished peaks in the D region redistributes to the higher wavenumber transitions by increasing the laser excitation energy. In particular, the relative intensity of the D_2–D_3–D_4 triplet (collectively labeled D_{low}) compared with the quintuplet D_5–D_6–D_7–D_8–D_9 (collectively labeled D_{high}) decreases by increasing the laser excitation energy: the D_{low} dominates the D-region with the 632.8 nm excitation while the D_{high} dominates with 457.8 and 325 nm; excitations (see Fig. S2 (Supporting Information) for the quantitative D_{low}/D_{high} intensity ratio behavior as a function of excitation wavelength). The lowest wavenumber peak observed in the D region (D_1, 1170 cm^{-1}) is not particularly strong; however its relative intensity is significantly enhanced going form 325 nm to 785 nm laser excitation.

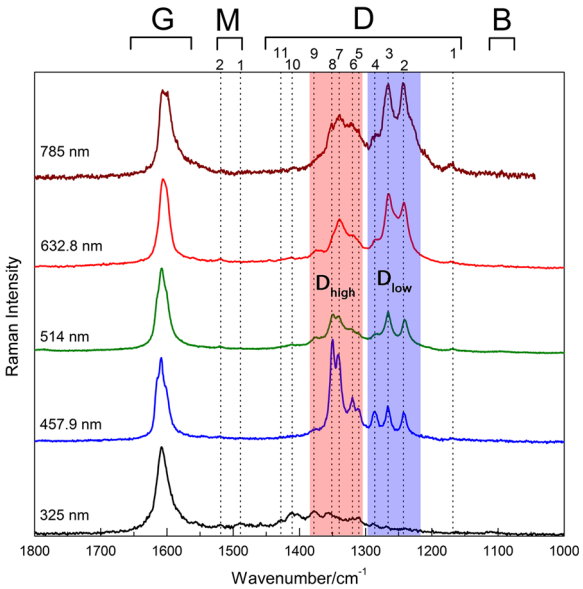

Figure 4. Comparison between experimental Raman spectra of **C78** recorded with different laser wavelengths.

Simulations of Raman spectra of **C78** in perfect resonance with the low lying bright exited states (S_1, S_4, S_6—see Table S2 (Supporting Information)), which are reported in Fig. 5, allow rationalizing the observed intensity redistribution within the D region. The lower wavenumber tail of the D region is comparatively stronger in S_1 than it is in S_6. To obtain a more quantitative agreement of theoretical data with experiments (i.e. a fine peak assignment going beyond the identification of the strongest features in the D region) one would require (i) a better determination of the vibrational structure of the molecule and (ii) a more accurate determination of the excited states to get more reliable relative intensities. We think that for the typical spectroscopic practice and the present case, issue (i) may be slightly more important than (ii). Issue (i) is important because, given the spectral congestion of the D peak region, small changes in the description of the normal modes (e.g. going from a lower to a higher level of calculation) may already affect the simulated Raman profile, even keeping the Raman polarizability tensors of the lower level calculation.[2] Of course, this point just considers the shape of the Raman spectrum, not the value of the absolute Raman intensities

[2]One can see this effect as a sort of mode mixing, i.e. the modes computed at a higher level can be expressed as a linear combination of the modes computed at the lower level.

Table 1. Position of the main components of the Raman signal in the D region as a function of the laser excitation (from band deconvolution)

	325 nm	457.9 nm	514.5 nm	632.8 nm	785 nm
D_1	—	—	1168	1170	1170
D_2	1239	1241	1240	1242	1241
D_3	1268	1266	1266	1264	1267
D_4	1287	1286	1284	1286	1286
D_5	1310	1310	1310	—	1310
D_6	1320	1320	1324	1318	1322
D_7	1344	1341	1340	1339	1340
D_8	1357	1350	1350	1350	1350
D_9	1378	1378	1375	1374	1371
D_{10}	1409	1411	1412	1414	1409
D_{11}	1429	—	1428	—	1427

or the excitation dependence of the Raman spectrum, which are known to depend on issue (ii). Unfortunately **C78** is too large to allow, with present technology, the straightforward use of more accurate basis sets and/or quantum chemistry methods.

The experimental Raman spectra show a structured G-band; however, the shape of the G-band is less sensitive to the laser excitation energy compared to the D-band. As it is shown in Fig. 4, the spectra recorded with 457.9 nm and 514.5 nm excitations have a good signal-to-noise ratio in the G region and clearly show that the G signal is contributed by at least three overlapped peaks centered at 1601, 1609 and 1615 cm^{-1}. Within experimental error and band convolution uncertainty the position of these components is expected to be independent with respect to the laser excitation (as can be judged in Table 2). This is because of the assignment of each G component to a specific molecular normal mode. The analysis of DFT calculations (Table S1 (Supporting Information)) shows the presence of five modes with sizeable Raman activity in the G peak region. However, their wavenumbers are such that they cluster into three groups, which explains the number of peaks experimentally observed. Based on this observation the G-band has been deconvoluted taking into account three components for the

Table 2. Position of the three main components of the Raman signal in the G region as a function of the laser excitation (from band deconvolution)

	325 nm	457.9 nm	514.5 nm	632.8 nm	785 nm
G_1	1601	1601	1601	1601	1599
G_2	1609	1609	1609	1608	1608
G_3	—	1615	1615	—	—

457.9 and 514.5 nm excitations. For the other laser excitations (325, 632.8 and 785 nm) we have just considered two components, because the third one is too weak to allow for a reliable peak deconvolution. The summary of the experimental G peak data is reported in Table 2 (Fig. S3 (Supporting Information) shows the result of the peak deconvolution).

The relative intensity of the G *versus* the D region does depend significantly upon the laser excitation energy, as it can be judged by inspecting Fig. 4. Because of the presence of several D (and G) signals, we have considered the integrated area under the G and D regions. The I_D/I_G ratio so evaluated (Fig. S2 (Supporting Information)) increases as the laser photon energy decreases (i.e. going from 325 nm; to 785 nm excitation). This behavior parallels a similar observation made by Pócsik *et al.* on microcrystalline graphite.[31]

In addition to the main G and D features, the 1000–1800 cm^{-1} spectral range shows other minor Raman signals, which have been labeled B (breathing modes) and M (middle modes). They are, respectively, found at lower wavenumbers than the D band and in the middle between the G and D bands. B and M signals are very weak, but they can be observed with good reliability with green laser excitation and also find a match in DFT calculations (see Fig. S4 (Supporting Information) and Fig. S5 (Supporting Information) for details about the B and M regions).

(b) **Low wavenumber region.** The Raman spectra of **C78** recorded with 514.5 and 632.8 nm laser excitations are presented in Fig. 6 over the 130–1000 cm^{-1} range. The inset plot of Fig. 6 allows judging the sizeable relative intensity

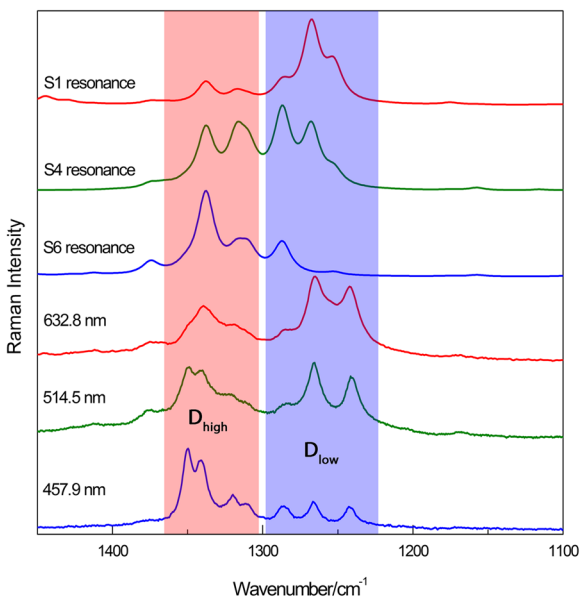

Figure 5. Comparison between calculated perfect resonances spectra and experimental spectra with different laser excitation in D region.

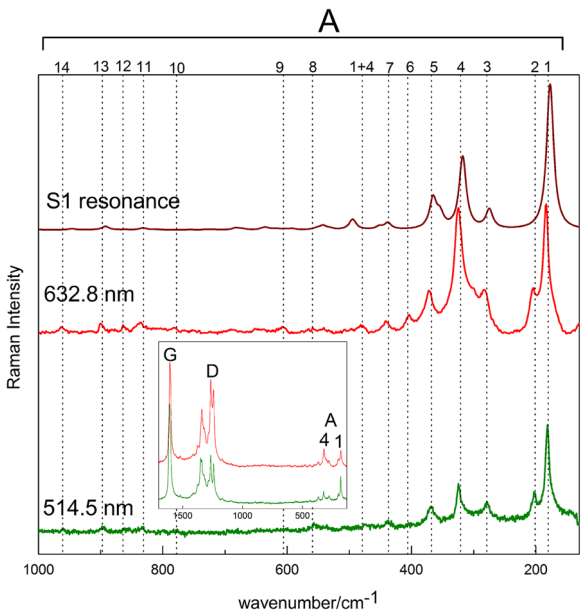

Figure 6. Raman spectra of **C78** in the low wavenumber range recorded with 514.5 nm and 632.8 nm laser excitation.

Table 3. Experimental Raman peaks in the low wavenumber region recorded with 514.5 nm and 632.8 nm laser excitations

		A_1	A_2	A_3	A_4	A_5	A_6	A_7	A_1+A_4	A_8	A_9	A_{10}	A_{11}	A_{12}	A_{13}	A_{14}
Computed wavenum.	A_g	181	—	281	324	373	—	447	505	565	616	790	849	—	911	966
	B_{3g}	—	202	284	—	—	414	—	—	—	—	—	—	874	—	—
Scaled wavenum.		177	198	275 278	317	365	405	438	494	553	603	774	831	856	892	946
Expt. (514.5 nm)		181	203	279	324	368	—	437	477	557	—	776	831	854	898	961
Expt. (632.8 nm)		180	201	281	321	369	401	438	479	556	606	779	833	864	897	960

of the low wavenumber region compared to the G–D region. We have named the Raman signals in this region A_k, after acoustic modes (see Table 3 for the full list). Their nature was already established in the past.[6] The signal-to-noise ratio is remarkably improved compared to previous results,[6] which allows detecting more features than before (mainly A_1 and A_4 were detected). In our analysis we have considered also the Raman signals of the region from 500 cm^{-1} to 1000 cm^{-1} obtained with 514.5 nm and 632.8 nm laser excitations. The use of two excitation wavelengths allows to reliably detecting also the weak features in this spectral region, totaling 15 Raman lines.

The nuclear displacements of the normal modes associated to these peaks can be related to those of in-plane acoustic phonons of a graphene sheet.[6] In particular, it has been shown that the position of A_1 is related to the longitudinal size of a series of PAHs with similar shape as **C78**.[6] The comparison between the experimental spectrum recorded with the 632.8 nm, and the spectrum calculated in perfect resonance with S_1 shows good agreement, which allows assigning the main peaks. The missing peaks in the simulation (A_2, A_6 and A_{12}) are related to non-totally symmetric modes belonging to the B_{3g} irreducible representation. Based on the theory that has been used for evaluating the resonance Raman response,[19,20] the diagonal matrix element of the electron–phonon coupling operator is responsible for Raman scattering (i.e. $< \alpha \mid \partial H/\partial Q_k \mid \alpha >$, with $\mid \alpha >$ being a given excited state electronic wavefunction and $\partial H/\partial Q_k$ the derivative of the electronic Hamiltonian with respect to the normal coordinate Q_k). It can be noticed straightforwardly that this integral vanishes when the normal coordinate Q_k belongs to any non-totally symmetric representation, as it is the case for A_2, A_6 and A_{12}. This implies that the strength of non-totally symmetric modes (e.g. B_{3g}) is zero when evaluating the resonance Raman response with this level of approximation of the theory. The calculation of the Raman intensity of fundamental transitions for non-totally symmetric modes would require the off-diagonal terms $< \alpha \mid \partial H/\partial Q_k \mid \beta >$, which, however, are not straightforwardly evaluated by available TDDFT codes.

Interestingly, it is also possible to observe a peak attributed to the $A_1 + A_4$ combination (see Fig. 6 and Table 3). Compared to the combinations and overtones of G and D peaks, the position of the sum of wavenumber of A_1 and A_4 is more significantly blue shifted with respect to the experimental observation. This may be because of stronger anharmonicity of this lower wavenumber region compared to the CC stretching modes (G, D).

The representation of the nuclear displacements of the first five peaks (A_1 to A_5, whose relative Raman intensity is stronger) is given in Fig. 7, and it is based on results from DFT calculations. Information about the other peaks in this region is available in Supporting Information (Fig. S6 (Supporting Information)).

(c) **Overtones and combinations.** Inspection of the Raman spectrum of **C78** over a wider wavenumber range (150–3500 cm^{-1}, see Fig. 8) reveals the presence of signals that in graphene/graphite systems are attributed to D and G overtones and combinations (i.e. 2D and 2G[8]). These Raman transitions are also predicted by the simulation of the resonance Raman spectrum obtained in perfect resonance condition with the S_1 state, which is compared in Fig. 8 with the spectrum recorded with red excitation at 632.8 nm. The overall agreement between theory and experiment in Fig. 8 is

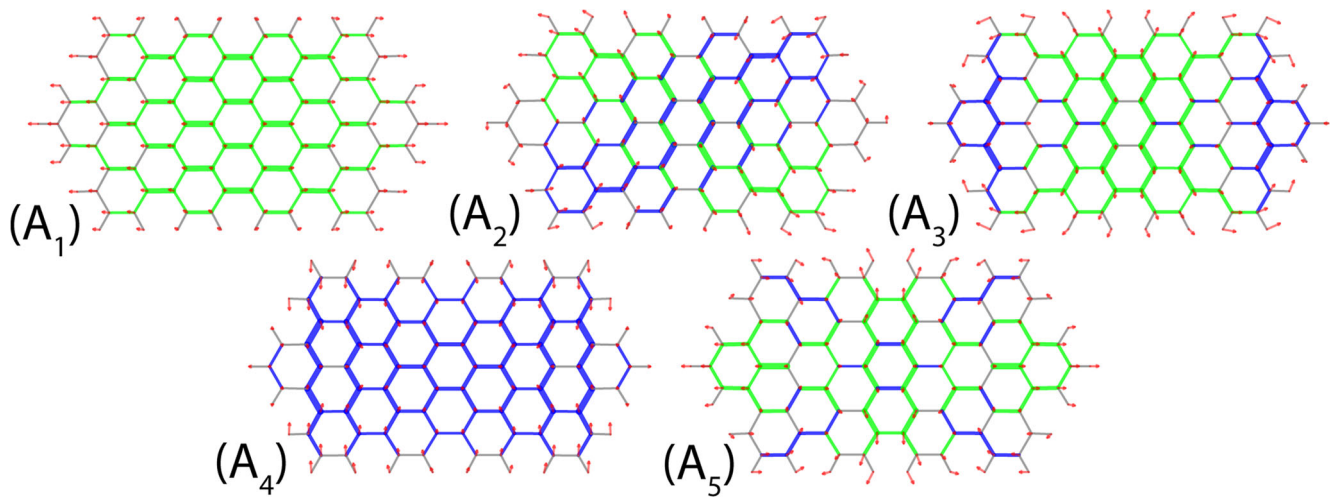

Figure 7. Representation of five most intense collective acoustic-like motion based on computed results from B3LYP/6-31G** calculation. A_1 longitudinal (A_g, 181 cm^{-1}); A_2 shear-like stretching (B_{3g}, 202 cm^{-1}, this mode is absent in the spectrum calculated in perfect resonance with S_1); A_3 collective bending (A_g, 281 cm^{-1}); A_4 transversal stretching (A_g, 324 cm^{-1}); A_5 collective bending (A_g, 373 cm^{-1}). Red arrows represent displacement vectors; CC bonds are represented as green (blue) lines of different thickness according to their relative stretching (shrinking).

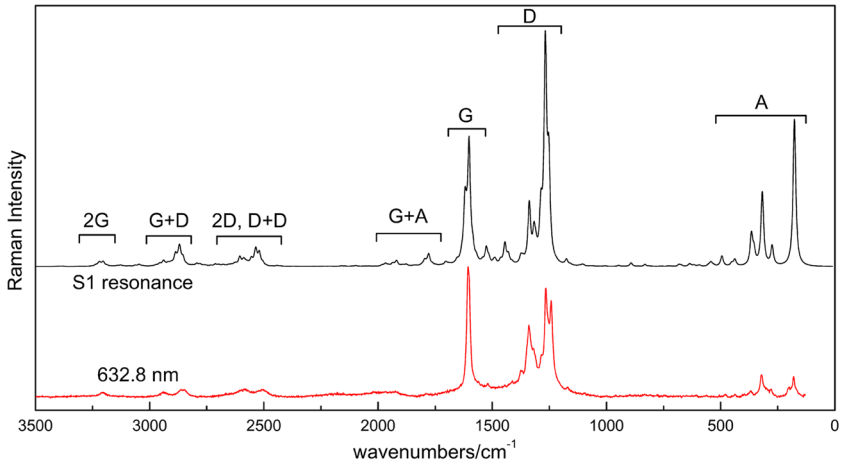

Figure 8. Comparison between calculated S_1 perfect resonance spectrum (black line) with experimental spectrum recorded with 632.8 nm laser excitation (red line).

good. Notably the relative intensity of the A region is overestimated compared to experiment. This is because of the assumption of the perfect resonance condition, which mostly affect the Raman intensities of the lower wavenumber normal modes. Interestingly, **C78** also provides signals which can be attributed to G + D and G + A combinations and which will be described later.

The Raman spectrum of **C78** in the overtone and combination region has been also recorded with excitation lines other than 632.8 nm. These spectra are plotted in Fig. 9. To ease the assessment of the relative intensity of overtones and combinations the G peak is also reported in the Fig. 9. Furthermore, overtones and combinations are also plotted with a 10× magnification factor to help capturing their secondary features. Overall we observe 15 peaks in this region that we label with letters 'a' to 'p' to make a distinction with the labeling scheme adopted for fundamentals. It is possible to distinguish five groups of Raman signals in this region. Based on their wavenumber range, they must be related to 2G overtones, G + D combinations, 2D overtones, $D_j + D_k$ combination and G + A combination. In fact, they match with results from calculations in perfect resonance with S_1 (see Fig. 8 above). In more details, peaks a, b, c, d are related to G + A, peaks e, g, h, j are related to $D_j + D_k$, peaks f, i are related to 2D, peaks k, l, m, n are related to D + G and peak p is related to 2G (see Table 4).

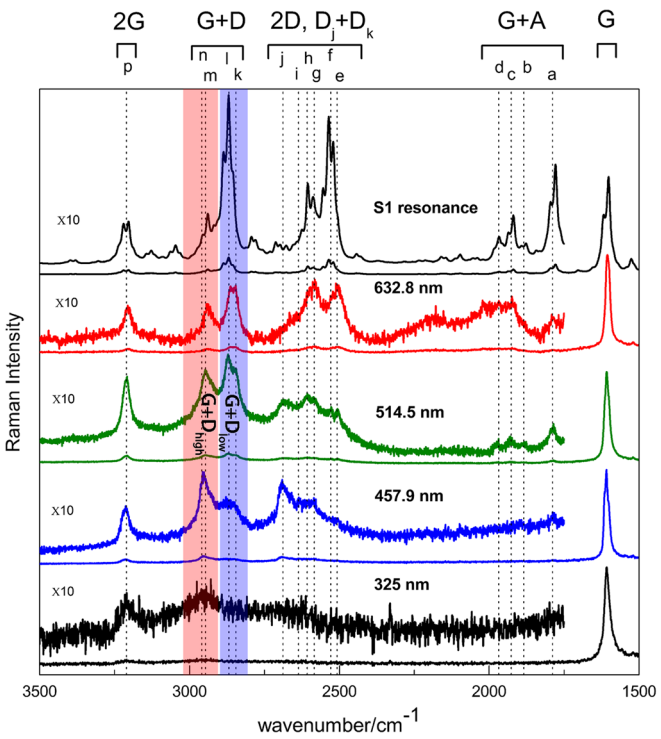

Figure 9. Raman spectra of **C78** in overtone and combination region compared with G peak, recorded with different laser wavelength excitation. For clarity the overtone and combination region has been also plotted overlaid by applying a 10× intensity magnification factor.

Interestingly, according to Ferrari[8] the G + D combination is normally absent in graphene, because of the selection rule based on phonon momentum: the phonon associated to the G peak is found at $\mathbf{q} = \mathbf{0}$, while the phonon associated to the D peak is found at $\mathbf{q} = \mathbf{K} \neq \mathbf{0}$. Hence, the transition associated to the G + D combination would require $\Delta\mathbf{q} \neq \mathbf{0}$. However, G + D combinations are observed in molecular graphenes because for them the phonon wave vector **q** may cease to be an effective quantum number, because of strong confinement over the molecular size. Hence, the intensity of the G + D combination could be used as an experimental measure of phonon confinement effects in graphitic materials. The G + D peak is expected to increase as a consequence of the fact that the **q** wave vector progressively loses its precise meaning as the density of defects increases in the graphitic lattice.

It is also possible to observe four peaks attributable to G + A combinations. In particular, from the analysis of their positions, it turns out that these peaks are related to the combination of the most intense peaks in the A region with the G peak (see Table 4). Interestingly, the G + A_2 combination is *not* observed. This is explained by the fact that A_2 is not totally symmetric (B_{3g}, see Table 3); hence, it cannot combine with any of the strongest components of the G signal, which belong to the totally symmetric representation.

Inspection of Fig. 9 also reveals that, in the overtone and combination region, the relative intensity changes with excitation match the observed behavior of the fundamentals (G, D—see Figs. 4 and 5). This is because of the fact that the Raman intensity of a combination is roughly proportional to the product of the Raman intensities of the corresponding fundamentals. The same holds for overtones too. This can be proved easily by recalling the equations for fundamental Raman transitions[20]

Table 4. Experimental peak position of overtones and combinations recorded with different laser excitations. The proposed assignments are based on the numerical data presented in Tables 1 and 2. When the G peak is involved in the assignment we do not try to identify any specific G component because the experimental signals are too broad to allow reliable peak analysis

	Assignment	325 nm	457.9 nm	514.5 nm	632.8 nm
a	$G + A_1$	—	1788	1786	1791
b	$G + A_3$	—	—	1884	—
c	$G + A_4$	—	—	1929	1924
d	$G + A_5$	—	—	1969	1968
e	$D_2 + D_3$	—	—	2507	2507
f	$2D_3$	—	—	2527	2530
g	$D_2 + D_7$	—	2585	2586	2582
h	$D_3 + D_7$	—	—	2607	2607
i	$2D_6$	—	2636	—	—
j	$D_7 + D_8$	—	2691	2686	—
k	$G + D_2$	—	—	2844	2845
l	$G + D_3$	—	2878	2872	2867
m	$G + D_7$	—	2951	2948	2942
n	$G + D_8$	2961	2957	—	—
p	2G	3210	3213	3209	3206

$$I_h \propto \left(\frac{1}{2\hbar\Omega_h}\right)\left|\frac{\hbar \boldsymbol{g}.\boldsymbol{L}_h}{i\Gamma(i\Gamma+\hbar\Omega_h)}\right|^2 \quad (1)$$

and combinations (the case of overtones is obtained considering the same normal mode index, i.e. $h = k$):

$$I_{h+k} \propto \left(\frac{1}{2\hbar\Omega_h}\right)\left(\frac{1}{2\hbar\Omega_k}\right)\times\left|\frac{(\hbar \boldsymbol{g}.\boldsymbol{L}_h)(\hbar \boldsymbol{g}.\boldsymbol{L}_k)}{i\Gamma(i\Gamma+\hbar\Omega_h)(i\Gamma+\hbar\Omega_h+\hbar\Omega_h)}\right. \quad (2)$$
$$\left.+\frac{(\hbar \boldsymbol{g}.\boldsymbol{L}_k)(\hbar \boldsymbol{g}.\boldsymbol{L}_h)}{i\Gamma(i\Gamma+\hbar\Omega_h)(i\Gamma+\hbar\Omega_h+\hbar\Omega_h)}\right|^2$$

where $\hbar\Omega_k$ represents the vibrational quantum of the k-th normal mode and the scalar product ($\hbar \boldsymbol{g}\cdot\boldsymbol{L}_h$) represents the electron–phonon coupling relative to mode h. The 3 N-components vector $\boldsymbol{g}$ (with N the number of atoms) represents the gradient on the excited state potential energy surface, evaluated with TDDFT methods at the Franck–Condon point. $\boldsymbol{L}_h$ is the 3 N-components vector describing the Cartesian nuclear displacements relative to mode h. Further details can be found in reference.[20] Provided that the resonance broadening parameter Γ is significantly larger than the typical vibrational quantum ($\Gamma \gg \hbar\Omega$), one easily gets from the comparison of Eqn (1) and (2) that $I_{h+k} \propto I_h \times I_k$.

Temperature dependence

We have recorded the Raman spectra of **C78** with 632.8 nm laser excitation over a temperature range extending from 25 °C to 200 °C. As one can see in Fig. 10, the position of G peak shifts to lower wavenumber with increasing temperature. These G peak shifts with temperature have been attributed to thermal expansion phenomena[8] that also affect intermolecular distances and interaction strengths. The position of the three G peak components (by Lorentzian deconvolution, see Fig. S7 (Supporting Information)) markedly red shifts for increasing temperature, as can be clearly observed in Fig. 11. The three components behave fairly similarly and

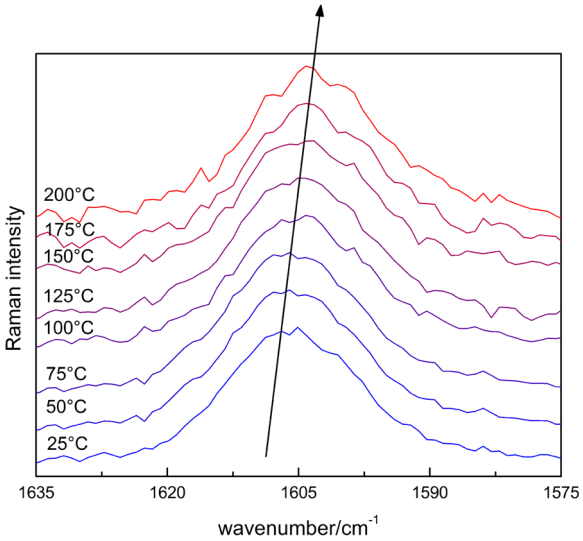

Figure 10. Raman spectra of **C78** over the G region as a function of temperature (632.8 nm excitation).

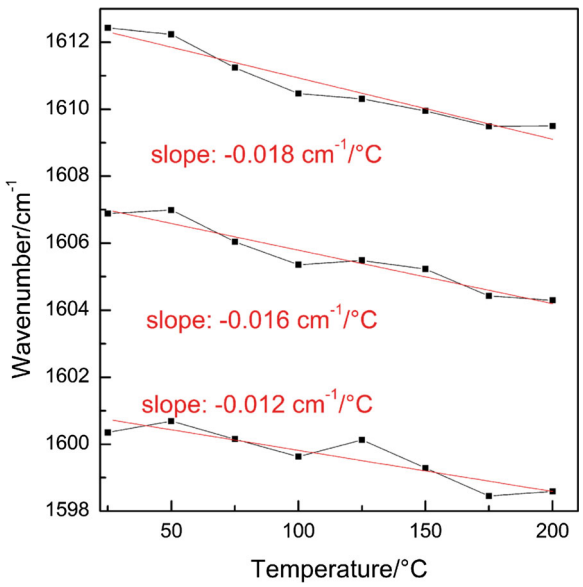

Figure 11. Position of the G peak deconvoluted by three Lorentzian peaks (from the data presented in Fig. 10).

the average slope of the linear dependence of their wavenumber *versus* temperature is $-0.016\ cm^{-1}/°C$.

A qualitatively similar behavior has been measured in graphite by Atashbar,[32] but a different slope was obtained ($-0.031\ cm^{-1}/°C$). Because π–π interactions are expected to be similar in graphite and **C78**, the larger value of graphite may be explained with the additional contribution from phonon-phonon scattering,[32] which is not expected to play a major role in a molecular material such as **C78**.

Conclusions

In this work we report the experimental and theoretical pre-resonance/resonance Raman spectra of **C78**. Compared with a previous investigation[6] the experimental data show better signal-to-noise ratio. More features can be distinguished in the lower wavenumber

region of the spectra, which is associated to in-plane acoustic like vibrations that depend on the molecular size.[6] Moreover, we have extended our analysis to the overtone and combination region (2000–3500 cm^{-1}), which were not explored in the past. We have observed that for selected wavelengths (514.5 and 457.9 nm, which better match resonance conditions) it is possible to observe Raman signals ascribed to 2D and 2G overtones. Furthermore, G + D combinations are also evident in the Raman spectra. This feature is a specific signature of confinement and is usually absent in graphene.[8] The intensity of the G + D combination could be used as an experimental measure of confinement in graphitic materials, and it is expected to increase as a consequence of the fact that the **q** wave vector progressively loses its precise meaning as the density of defects increases in the graphitic lattice.

Finally, we have measured the temperature dependence of the G peak in **C78**, and we have found a linear dependence of $-0.016\ cm^{-1}$/K, because of thermal expansion effects.[8]

References

[1] E. Clar, *The Aromatic Sextet*, Wiley, London, **1972**.
[2] S. Ito, M. Wehmeier, J. Diedrich Brand, C. Kübel, R. Epsch, J. P. Rabe, K. Müllen, *Chem. - Eur. J.* **2000**, *6*, 4327.
[3] W. M. Baird, L. A. Hooven, B. Mahadevan, *Environ. Mol. Mutagen.* **2005**, *45*, 106.
[4] B. T. Draine, A. Li, *Astrophys. J.* **2007**, *657*, 810.
[5] F. Negri, C. Castiglioni, M. Tommasini, G. Zerbi, *J. Phys. Chem. A* **2002**, *106*, 3306.
[6] E. Di Donato, M. Tommasini, G. Fustella, L. Brambilla, C. Castiglioni, G. Zerbi, C. D. Simpson, K. Müllen, F. Negri, *Chem. Phys.* **2004**, *301*, 81.
[7] C. Castiglioni, M. Tommasini, G. Zerbi, *Philos. Trans. R. Soc., A* **2004**, *362*, 2425.
[8] A. C. Ferrari, D. M. Basko, *Nat. Nanotechnol.* **2013**, *8*, 235.
[9] C. Castiglioni, F. Negri, M. Rigolio, G. Zerbi, *J. Chem. Phys.* **2001**, *115*, 3769.
[10] C. Mapelli, C. Castiglioni, G. Zerbi, K. Müllen, *Phys. Rev. B: Condens. Matter Mater. Phys.* **1999**, *60*, 12710.
[11] G. Gouadec, P. Colomban, *Prog. Cryst. Growth Charact. Mater.* **2007**, *53*, 1.
[12] A. K. Geim, K. S. Novoselov, *Nat. Mater.* **2007**, *6*, 183.
[13] A. K. Geim, *Science* **2009**, *324*, 1530.
[14] A. C. Ferrari, J. Robertson, *Phys. Rev. B: Condens. Matter Mater. Phys.* **2000**, *61*, 14095.
[15] R. Escribano, J. J. Sloan, N. Siddique, N. Sze, T. Dudev, *Vib. Spectrosc.* **2001**, *26*, 179.
[16] K. Ohno, *J. Mol. Spectrosc.* **1978**, *72*, 238.
[17] K. Ohno, *J. Chem. Phys.* **1991**, *95*, 5524.
[18] S. Piscanec, M. Lazzeri, F. Mauri, A. C. Ferrari, J. Robertson, *Phys. Rev. Lett.* **2004**, *93*, 185503.
[19] L. A. Nafie, P. Stein, W. L. Peticolas, *Chem. Phys. Lett.* **1971**, *12*, 131.
[20] M. Tommasini, G. Longhi, S. Abbate, G. Zerbi, *J. Raman Spectrosc.* **2014**, *45*, 89.
[21] M. D. Watson, A. Fechtenkötter, K. Müllen, *Chem. Rev. (Washington, DC, U. S.)* **2001**, *101*, 1267.
[22] G. M. Rutter, N. P. Guisinger, J. N. Crain, P. N. First, J. A. Stroscio, *Phys. Rev. B: Condens. Matter. Phys.* **2010**, *81*, 245408.
[23] P. Egberts, G. H. Han, X. Z. Liu, A. T. C. Johnson, R. W. Carpick, *ACS Nano* **2014**, *8*, 5010.
[24] J. M. Wofford, S. Nie, K. F. McCarty, N. C. Bartelt, O. D. Dubon, *Nano Lett.* **2010**, *10*, 4890.
[25] Z. Luo, S. Kim, N. Kawamoto, A. M. Rappe, A. T. C. Johnson, *ACS Nano* **2011**, *5*, 9154.
[26] Y. Son, M. L. Cohen, S. G. Louie, *Phys. Rev. Lett.* **2006**, *97*, 216803.
[27] K. A. Ritter, J. W. Lyding, *Nat. Mater.* **2009**, *8*, 235.
[28] M. J. Frisch, G. W. Trucks, H. B. Schlegel, G. E. Scuseria, M. A. Robb, J. R. Cheeseman, G. Scalmani, V. Barone, B. Mennucci, G. A. Petersson, H. Nakatsuji, M. Caricato, X. Li, H. P. Hratchian, A. F. Izmaylov, J. Bloino, G. Zheng, J. L. Sonnenberg, M. Hada, M. Ehara, K. Toyota, R. Fukuda, J. Hasegawa, M. Ishida, T. Nakajima, Y. Honda, O. Kitao, H. Nakai, T. Vreven, J. A. Montgomery Jr., J. E. Peralta, F. Ogliaro, M. Bearpark, J. J. Heyd, E. Brothers, K. N. Kudin, V. N. Staroverov, R. Kobayashi, J. Normand, K. Raghavachari, A. Rendell, J. C. Burant, S. S. Iyengar, J. Tomasi, M. Cossi, N. Rega, J. M. Millam, M. Klene, J. E. Knox, J. B. Cross, V. Bakken, C. Adamo, J. Jaramillo, R. Gomperts, R. E. Stratmann, O. Yazyev, A. J. Austin, R. Cammi, C. Pomelli, J. W. Ochterski, R. L. Martin, K. Morokuma, V. G. Zakrzewski, G. A. Voth, P. Salvador, J. J. Dannenberg, S. Dapprich, A. D. Daniels, Ö. Farkas, J. B. Foresman, J. V. Ortiz, J. Cioslowski, D. J. Fox, *Gaussian 09, Revision D.01*, Gaussian, Inc., Wallingford CT, **2009**.
[29] F. J. Avila Ferrer, V. Barone, C. Cappelli, F. Santoro, *J. Chem. Theory Comput.* **2013**, *9*, 3597.
[30] I. Childres, L. A. Jauregui, Y. P. Chen, *J. Appl. Phys. (Melville, NY, U. S.)* **2014**, *116*, 233101.
[31] I. Pócsik, M. Hundhausen, M. Koós, L. Ley, *J. Non-Cryst. Solids* **1998**, *227–230*, 1083.
[32] M. Z. Atashbar, S. Singamaneni, *Appl. Phys. Lett.* **2005**, *86*, 123112.
[33] M. Sun, Z. Zhang, L. Chen, H. Xu, *Adv. Opt. Mater.* **2013**, *25*, 449.

Supporting information

Additional supporting information may be found in the online version of this article at the publisher's website.

CHEMISTRY
AN ASIAN JOURNAL

Accepted Article

Title: Bottom-Up Synthesis of Beaded Graphene Nanoribbons

Authors: Matthias Georg Schwab; Akimitsu Narita; Silvio Osella; Yunbin Hu; Ali Maghsoumi; Alexey Mavrinsky; Wojciech Pisula; Chiara Castiglioni; Matteo Tommasini; David Beljonne; Xinliang Feng; Klaus Müllen

To be cited as: Chem. Asian J. 10.1002/asia.201500450

Link to VoR: http://dx.doi.org/10.1002/asia.201500450

Bottom-Up Synthesis of Necklace-Like Graphene Nanoribbons

Matthias Georg Schwab,[a,f] Akimitsu Narita,[a] Silvio Osella,[b] Yunbin Hu,[a] Ali Maghsoumi,[c] Alexey Mavrinsky,[a] Wojciech Pisula,[a,d] Chiara Castiglioni,[c] Matteo Tommasini,[c] David Beljonne,[b] Xinliang Feng,*[e] and Klaus Müllen*[a]

Dedication ((optional))

Abstract: Graphene nanoribbons (GNRs) with an unprecedented "necklace-like" structure were synthesized through a bottom-up chemical approach, based on the oxidative cyclodehydrogenation of tailor-made polyphenylene precursors. A polycyclic aromatic hydrocarbon consisting of 84 sp^2 carbons (**C84**) was also synthesized and characterized as a model compound. Characterizations by a combination of MALDI-TOF MS and FTIR, Raman, and UV–Vis absorption spectroscopy validated the formation of the necklace-like GNRs. The absorption spectrum and DFT calculations revealed a bandgap of approximately 1.4 eV for this novel GNR system, which has not been attained with other GNR structures, enabling further fine-tuning of GNR bandgaps by structural modulation.

Graphene nanoribbons (GNRs) are ribbon-shaped segments of graphene, which are attracting an increasing attention for their promising electronic properties.[1] With non-zero bandgaps induced by the lateral quantum confinement, GNRs are promising for future nano- and opto-electronic applications, in stark contrast to zero-bandgap graphene itself.[2] Whereas GNRs fabricated by top-down methods such as lithographic patterning of graphene[3] and unzipping of carbon nanotubes[4] lack the structural precision and reproducibility, bottom-up chemical synthesis based on solution-mediated[5] or surface-assisted[6] cyclodehydrogenation has enabled reproducible fabrication of GNRs with chemically defined and uniform structures.[7] Especially, the solution synthesis allows bulk-scale preparation of the GNRs, which can be processed from a liquid phase for fabrication of nanoelectronic devices.[8]

The width and the edge configuration of the GNRs have a critical effect on their optoelectronic properties, such as bandgaps, as theoretically[9] and experimentally[5d, 6c, 7] demonstrated. However, studies on the structure-property relationships of the GNRs have been mostly limited to those with specific edge structures, such as armchair, zigzag, and their hybrids, namely chiral, leaving the effect of the edge configurations still underexplored. Here, we report the synthesis of GNR **1** with an unprecedented "necklace-like" structure,[10] which features an armchair edge configuration (Figure 1). We further demonstrate the synthesis of a polycyclic aromatic hydrocarbon (PAH) **C84**, bearing 84 sp^2 carbon atoms in the aromatic core, as a model compound.

The electronic structures of **C84** and necklace-like GNR **1** has been investigated at the DFT level, with the HSE functional[11] and 6-31G* Pople basis set.[12] **C84** is thus predicted to have the highest occupied molecular orbital (HOMO) at –4.58 eV and the lowest unoccupied molecular orbital (LUMO) at –2.41 eV with an energy gap of 2.17 eV. Periodic boundary conditions applied to assess GNR **1** yield a band structure with the top of the valence band and the bottom of the conducting band located at –4.38 and –2.98 eV, respectively (see the SI). The corresponding bandgap of 1.40 eV is relatively larger as compared to other GNRs of similar width.[9c] Importantly, there has hitherto been no report on a synthesis of GNRs exhibiting a bandgap of around 1.4 eV.[5-7]

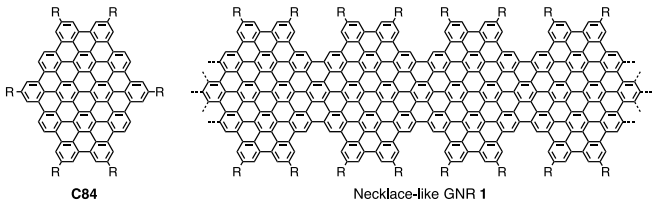

Figure 1. Structures of PAH **C84** and necklace-like GNR **1**. R: dodecyl.

Next, in order to investigate the feasibility of the fabrication of necklace-like GNR **1** through the oxidative

[a] Dr. M. G. Schwab, Dr. A. Narita, Dr. Y. Hu, Dr. A. Mavrinsky, Prof. Dr. W. Pisula, Prof. Dr. K. Müllen
Max Planck Institute for Polymer Research
Ackermannweg 10, D-55128 Mainz, Germany
E-mail: muellen@mpip-mainz.mpg.de
[b] Dr. S. Osella, Dr. D. Beljonne
Chemistry of Novel Materials, University of Mons
Place du Parc 20, B-7000 Mons, Belgium
[c] A. Maghsoumi, Prof. Dr. C. Castiglioni, Prof. Dr. M. Tommasini
Dipartimento di Chimica, Materiali ed Ingegneria Chimica "G. Natta", Politecnico di Milano
Piazza Leonardo da Vinci 32, 20133 Milano, Italy
[d] Prof. Dr. Wojciech Pisula
Department of Molecular Physics, Faculty of Chemistry
Lodz University of Technology
Zeromskiego 116, 90-924 Lodz, Poland
[e] Prof. Dr. X. Feng
Center for Advancing Electronics Dresden (cfaed)
& Department of Chemistry and Food Chemistry
Dresden University of Technology
Walther-Hempel-Bau Mommsenstrasse 4, 01062 Dresden, Germany
E-mail: xinliang.feng@tu-dresden.de
[f] Dr. M. G. Schwab
Present address:
BASF SE
Carl-Bosch-Straße 38, 67056 Ludwigshafen, Germany

Supporting information for this article is given via a link at the end of the document.

cyclodehydrogenation of polyphenylene precursor **10**, the synthesis of model compound **C84** was carried out as displayed in Scheme 1. 4,4'-Dibromo-2,2'-diiodo-1,1'-biphenyl (**2**)[13] was subjected to Sonogashira coupling with trimethylsilyl (TMS) acetylene at room temperature to selectively yield TMS-protected diethynylbiphenyl **3**, which was subsequently deprotected with potassium carbonate to form 4,4'-dibromo-2,2'-diethynyl-1,1'-biphenyl (**4**). Two-fold Diels–Alder cycloaddition of **4** with tetraphenylcyclopentadienone **5**[14] afforded oligophenylene **6**, which also serves as a monomer in the preparation of polyphenylene precursor **10** for necklace-like GNR **1** (Scheme 1).

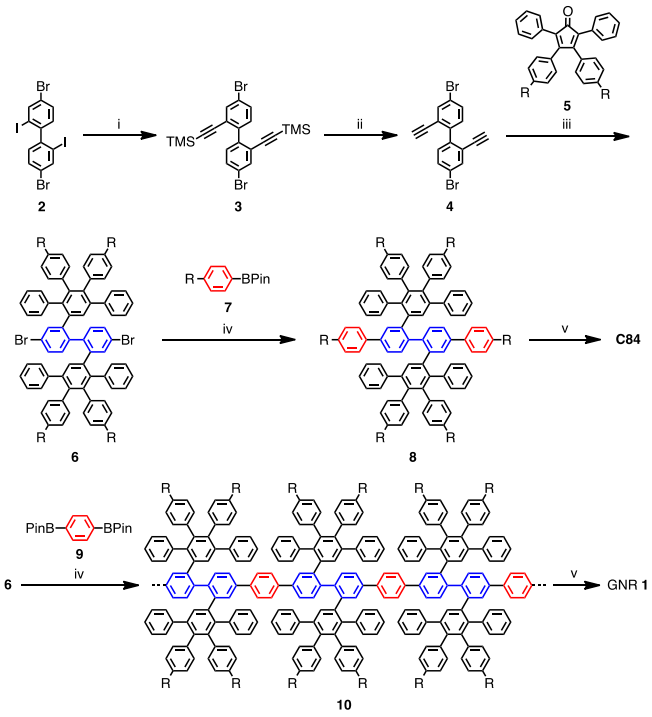

Scheme 1. Synthesis of **C84** and necklace-like GNR **1**. Reagents and conditions: (i) trimethylsilyl acetylene, $Pd(PPh_3)_2Cl_2$, CuI, NEt_3, rt, 62%; (ii) K_2CO_3, THF/MeOH, rt, 75%; (iii) *ortho*-xylene, 160 °C, μW, 300 W, 79%; (iv) $Pd(PPh_3)_4$, K_2CO_3, toluene, Aliquat 336, reflux, **8**: 76%; (v) $FeCl_3$, CH_2Cl_2/CH_3NO_2, rt, **C84**: 91%. R: dodecyl.

Suzuki coupling of oligophenylene **6** with 4-dodecylphenylboronic acid pinacol ester (**7**) provided corresponding oligophenylene precursor **8**. The cyclodehydrogenation of precursor **8** was successful with 7.5 equivalents of iron(III) chloride per hydrogen to be removed, providing **C84** in 91% isolated yield. Matrix-assisted laser desorption/ionization time-of-flight (MALDI-TOF) mass spectrometry (MS) analysis clearly demonstrated the elimination of 32 protons upon the cyclodehydrogenation and displayed the isotopic pattern of **C84** in perfect agreement with the simulation (Figure 2), proving the formation of **C84** without any partially fused species.[5a, 15] Signals from chlorinated products were also observed, but such peaks could be overestimated.[15] ^{1}H NMR analysis of **C84** was attempted in 1,1,2,2-tetrachloroethane-d_2, but peaks from aromatic protons could not be observed even at 140 °C, which was attributable to the strong aggregation in solution, similar to other large PAHs (Figure S4).[5a, 16] Nevertheless, the Fourier transform infrared (FTIR) spectrum of **C84** showed fingerprint peaks in agreement with DFT-based simulation, which provided further structural proof (Figure S16). Among the great variety of PAHs thus far synthesized,[17] **C84** reported here is the first PAH with 84 sp^2 carbons in the aromatic core.

C84 with six dodecyl chains shows in the differential scanning calorimetry (DSC) scan one phase transition at 74 °C, which is related to the reorganization of alkyl side chains (Figure S5), slightly affecting the supramolecular order. Two-dimensional wide-angle X-ray scattering (2D-WAXS) patterns of **C84** recorded at 30 and 90 °C indicate liquid crystallinity and the formation of columnar superstructures at both temperatures (Figure 3). Similar thermotropic properties have been observed for other core extended PAHs.[18] Equatorial small-angle reflections are assigned to a hexagonal unit cell of a_{hex} = 3.25 nm for the intercolumnar arrangement. In the stacks, the molecules are packed on top of each other due to π-stacking interactions with an intermolecular distance of 0.35 nm as derived from the wide-angle meridional reflections. The broad isotropic amorphous halo is attributed to side chains disordered in the columnar periphery, which is characteristic for a liquid crystalline phase. The LC organization remained unchanged for **C84** after cooling down the sample to 30 °C below the phase transition (Figure 3a). However, broadening of the meridional reflections suggests a slightly decreased intracolumnar order. This minor change can be explained in terms of increased steric demand of the alkyl substituents.

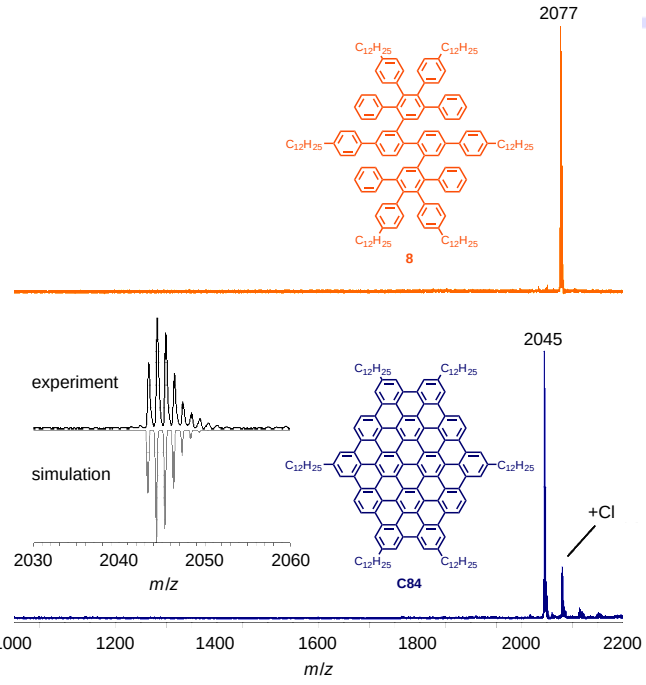

Figure 2. MALDI-TOF spectra of oligophenylene precursor **8** (top) and **C84** (bottom); the inset shows a comparison between experimental (black) and simulated (gray) isotopic pattern of **C84**.

Next, the synthesis of necklace-like GNR **1** was carried out starting from polyphenylene precursor **10** (Scheme 1). The repeating units of precursor **10** has the same arrangement of the aromatic rings as precursor **8**, which was demonstrated to undergo highly efficient cyclodehydrogenation, leading to the formation of **C84**. Hence, precursor **10** was prepared via a A_2B_2-type Suzuki polycondensation[8c, d, 19] of oligophenylene monomer **6** and 1,4-benzenediboronic acid bis(pinacol) ester (**9**). To circumvent the stoichiometry problem of the A_2B_2-type polymerization[7, 20] and achieve the highest possible polymerization efficiency, the monomers were thoroughly purified by using a recycling preparative size-exclusion chromatography (SEC) system before use and weighed with a great care (see the SI). After three days of refluxing, excess amounts of bromobenzene and then phenylboronic acid were added for the end-capping of the polymer. MALDI-TOF MS analysis of the resulting polymer precursor **10** showed a pattern of peaks, corresponding to the expected *m*/*z* values for **10**, extending over 17000 (Figure S9). Precursor **10** with molecular weight of ca. 17000 has ten repeating units and is expected to yield GNR **1** with a length of approximately 13 nm.

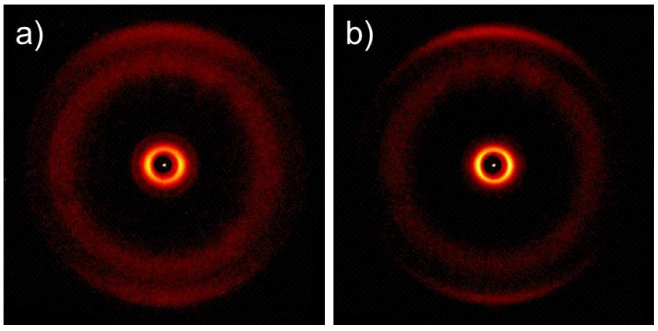

Figure 3. 2D-WAXS of **C84** at a) 30 °C and b) 90 °C.

SEC analysis of precursor **10** indicated its weight-average molecular weight (M_w) of 6900 g/mol and polydispersity index (PDI) of 1.7 against polystyrene (PS) standards. When poly(*p*-phenylene) (PPP) standards were applied M_w and PDI values were estimated to be 5100 g/mol and 1.5, respectively. Although these values based on the SEC analysis are only rough estimations according to the hydrodynamic volume of the solubilized polymer, they are useful for the comparison of different polyphenylene precursors of similar structures. The M_w of precursor **10** was smaller than that of a related polyphenylene prepared by AA-type Yamamoto polymerization,[5e] which is presumably because of the intrinsic stoichiometry problem of the A_2B_2-type Suzuki polymerization (see the SI)[7, 20] as well as the higher steric demand in this system.[8e]

The cyclodehydrogenation of precursor **10** was performed using the condition optimized for precursor **8** to afford necklace-like GNR **1** (Scheme 1). MALDI-TOF MS analysis of GNR **1** revealed a pattern of broadened peaks for up to octamers with intervals approximately corresponding to the molecular weight of one repeating unit (Figure S9). However, precise analysis was hindered by the limitation of the MALDI-TOF MS analysis for large aromatic molecules with broad molecular-weight distribution.[5e, 8e, 21]

Whereas elemental analysis is not reliable for such carbon-rich materials due to possible soot formation,[15] FTIR analysis provided more information about the efficiency of the cyclodehydrogenation (Figures 4a). Precursor **10** reveals a peak at 4050 cm^{-1}, a non-fundamental IR absorption associated to the presence of free-rotating benzene rings, as well as a group of signals at 3026, 3053, and 3084 cm^{-1} characteristic for C–H stretching vibrations of aromatic rings.[5a, d, e, 8e] These peaks are all starkly attenuated in the spectrum of GNR **1**. Moreover, out-of-plane (*opla*) C–H deformation bands at 699 and 764 cm^{-1} from mono-substituted benzene rings are strongly diminished and those at 815, 838, and 894 cm^{-1} from di-substituted benzene rings all disappeared after the cyclodehydrogenation.[5a, d, e, 8e] Considering the short length of GNR **1**, the remaining peaks at 693 and 758 cm^{-1} are probably from the phenyl groups introduced by the endcapping. Additionally, the peak at 719 cm^{-1} originates from the alkyl chains. Moreover, Raman spectrum of GNR **1** reveals characteristic D and G peaks as well as second-order peaks (Figure 4b), which are typical of other structurally well-defined GNRs in the literature.[5a, b, d, e, 6a] These observations underline the successful transformation of precursor **10** into GNR **1**.

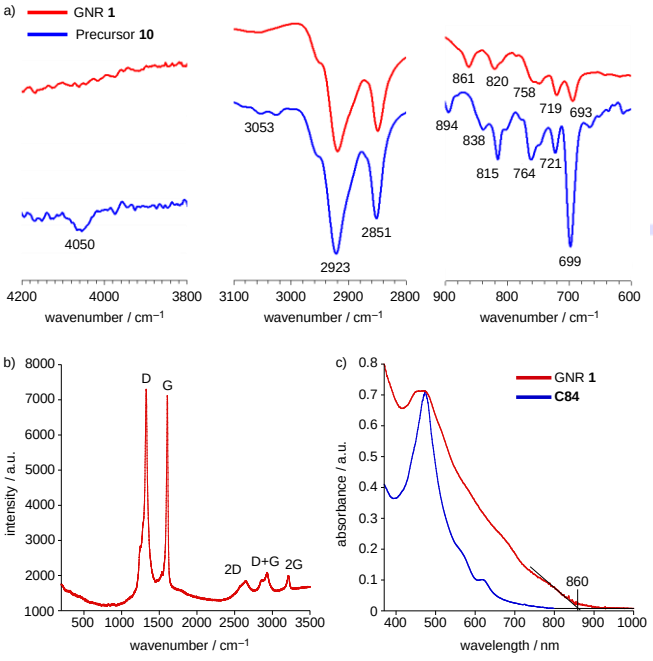

Figure 4. (a) Representative regions of the FTIR spectra of GNR **1** (red) and polyphenylene precursor **10** (blue). (b) Raman spectrum of GNR **1** at measured with 514.5 nm excitation. (c) Normalized UV–Vis absorption spectra of **C84** in THF and GNR **1** in NMP.

Thanks to the long alkyl chains placed at the peripheral positions, GNR **1** could be dispersed in *N*-methylpyrrolidone (NMP) by mild sonication.[5a, e] UV–Vis absorption spectrum of GNR **1** was thus measured in NMP and compared with that of **C84** in tetrahydrofuran (THF) (Figures 4c, S6, and S12). **C84**

was measured in THF, because it's solubility in NMP was limited. **C84** showed a prominent β-band at 473 nm with a molar extinction coefficient of 6864 m^2/mol, with smaller peaks at 564 and 620 nm, corresponding to the *p*- and α-bands, respectively. The HOMO-LUMO gaps of PAHs are related to the *p*-bands, and this experimental observation is in good accordance with the theoretical gap of 2.17 eV (571 nm). On the other hand, GNR **1** displayed broadened peaks with an absorption maximum at around 465 nm and shoulders approximately at 510, 680, and 780 nm. The broadening of the spectrum is most likely caused by the presence of shorter GNRs, possessing different bandgaps that are dependent on the length.[5a, e, 8e] Based on the absorption edge of 860 nm, the optical bandgap of longer GNRs contained in the obtained sample is estimated to be 1.44 eV, which again is well in line with the theoretically estimated bandgap of 1.40 eV. This result further validates the successful formation of GNR **1** and indicates that longer GNRs in the obtained sample are sufficiently elongated to possess the electronic band structure of the infinite GNR **1**.

In summary, we have synthesized an unprecedented PAH **C84** with 84 sp^2 carbons in the aromatic core and extended its synthesis to necklace-like GNR **1** applying A_2B_2-type Suzuki polymerization. Characterization by MALDI-TOF MS and FTIR, Raman, and UV–Vis absorption spectroscopy validated the successful formation of GNR **1** and demonstrated its optical bandgap of 1.44 eV in very good agreement with the theoretical value of 1.40 eV, which has not been attained with other GNR structures. Although the polymerization efficiency still needs to be improved to obtain longer necklace-like GNRs, this result contributes to the elucidation of structure-property relationships of GNRs and enables more precise tuning of their bandgap, which is of high importance for the future development of GNR-based nano- and opto-electronic devices.

Experimental Section

All the experimental and theoretical details are provided in the Supporting Information.

Acknowledgements

We are grateful for the financial support from the European Research Council grant on NANOGRAPH, DFG Priority Program SPP 1459, Graphene Flagship (No. CNECT-ICT-604391), and European Union Projects UPGRADE, GENIUS, and MoQuaS.

Keywords: Dehydrogenation • graphene • nanostructures • polycycles • vibrational spectroscopy

[1] X. Li, X. Wang, L. Zhang, S. Lee and H. Dai, *Science* **2008**, *319*, 1229-1232.

[2] a) J. Bai and Y. Huang, *Mater. Sci. Eng. R-Rep.* **2010**, *70*, 341-353; b) K. S. Novoselov, V. I. Falko, L. Colombo, P. R. Gellert, M. G. Schwab and K. Kim, *Nature* **2012**, *490*, 192-200.

[3] a) Z. Chen, Y. Lin, M. Rooks and P. Avouris, *Physica E* **2007**, *40*, 228-232; b) M. Han, B. Özyilmaz, Y. Zhang and P. Kim, *Phys. Rev. Lett.* **2007**, *98*, 206805; c) A. N. Abbas, G. Liu, B. Liu, L. Zhang, H. Liu, D. Ohlberg, W. Wu and C. Zhou, *ACS Nano* **2014**, *8*, 1538-1546.

[4] a) D. V. Kosynkin, A. L. Higginbotham, A. Sinitskii, J. R. Lomeda, A. Dimiev, B. K. Price and J. M. Tour, *Nature* **2009**, *458*, 872-876; b) L. Jiao, L. Zhang, X. Wang, G. Diankov and H. Dai, *Nature* **2009**, *458*, 877-880.

[5] a) A. Narita, X. Feng, Y. Hernandez, S. A. Jensen, M. Bonn, H. Yang, I. A. Verzhbitskiy, C. Casiraghi, M. R. Hansen, A. H. R. Koch, G. Fytas, O. Ivasenko, B. Li, K. S. Mali, T. Balandina, S. Mahesh, S. De Feyter and K. Müllen, *Nature Chem.* **2014**, *6*, 126-132; b) T. H. Vo, M. Shekhirev, D. A. Kunkel, M. D. Morton, E. Berglund, L. Kong, P. M. Wilson, P. A. Dowben, A. Enders and A. Sinitskii, *Nat. Commun.* **2014**, *5*, 3189; c) T. H. Vo, M. Shekhirev, D. A. Kunkel, F. Orange, M. J. F. Guinel, A. Enders and A. Sinitskii, *Chem. Commun.* **2014**, *50*, 4172–4174; d) A. Narita, I. A. Verzhbitskiy, W. Frederickx, K. S. Mali, S. A. Jensen, M. R. Hansen, M. Bonn, S. De Feyter, C. Casiraghi, X. Feng and K. Müllen, *ACS Nano* **2014**, *8*, 11622-11630; e) M. G. Schwab, A. Narita, Y. Hernandez, T. Balandina, K. S. Mali, S. De Feyter, X. Feng and K. Müllen, *J. Am. Chem. Soc.* **2012**, *134*, 18169-18172.

[6] a) J. Cai, P. Ruffieux, R. Jaafar, M. Bieri, T. Braun, S. Blankenburg, M. Muoth, A. P. Seitsonen, M. Saleh, X. Feng, K. Müllen and R. Fasel, *Nature* **2010**, *466*, 470-473; b) Y.-C. Chen, T. Cao, C. Chen, Z. Pedramrazi, D. Haberer, D. G. de Oteyza, F. R. Fischer, S. G. Louie and M. F. Crommie, *Nature Nanotech.* **2015**, *10*, 156-160; c) H. Huang, D. Wei, J. Sun, S. L. Wong, Y. P. Feng, A. H. C. Neto and A. T. S. Wee, *Sci. Rep.* **2012**, *2*, 983.

[7] A. Narita, X. Feng and K. Müllen, *Chem. Rec.* **2015**, *15*, 295-309.

[8] a) A. N. Abbas, G. Liu, A. Narita, M. Orosco, X. Feng, K. Müllen and C. Zhou, *J. Am. Chem. Soc.* **2014**, *136*, 7555-7558; b) U. Zschieschang, H. Klauk, I. B. Müller, A. J. Strudwick, T. Hintermann, M. G. Schwab, A. Narita, X. Feng, K. Müllen and R. T. Weitz, *Adv. Electron. Mater.* **2015**, *1*, 1400010; c) K. T. Kim, J. W. Lee and W. H. Jo, *Macromol. Chem. Phys.* **2013**, *214*, 2768-2773; d) K. T. Kim, J. W. Jung and W. H. Jo, *Carbon* **2013**, *63*, 202-209; e) M. El Gemayel, A. Narita, L. F. Dössel, R. S. Sundaram, A. Kiersnowski, W. Pisula, M. R. Hansen, A. C. Ferrari, E. Orgiu, X. Feng, K. Müllen and P. Samori, *Nanoscale* **2014**, *6*, 6301-6314.

[9] a) B. Obradovic, R. Kotlyar, F. Heinz, P. Matagne, T. Rakshit, M. D. Giles, M. A. Stettler and D. E. Nikonov, *Appl. Phys. Lett.* **2006**, *88*, 142102; b) J. Wang, R. Zhao, M. Yang and Z. Liu, *J. Chem. Phys.* **2013**, *138*, 084701; c) S. Osella, A. Narita, M. G. Schwab, Y. Hernandez, X. Feng, K. Müllen and D. Beljonne, *ACS Nano* **2012**, *6*, 5539–5548.

[10] X. Yan, Y. Cui, Q. He, K. Wang, J. Li, W. Mu, B. Wang and Z.-c. Ou-yang, *Chem.—Eur. J.* **2008**, *14*, 5974-5980.

[11] J. Heyd, G. E. Scuseria and M. Ernzerhof, *J. Chem. Phys.* **2003**, *118*, 8207-8215.

[12] V. A. Rassolov, M. A. Ratner, J. A. Pople, P. C. Redfern and L. A. Curtiss, *J. Comput. Chem.* **2001**, *22*, 976-984.

[13] K. L. Chan, M. J. McKiernan, C. R. Towns and A. B. Holmes, *J. Am. Chem. Soc.* **2005**, *127*, 7662-7663.

[14] J. P. Hill, W. Jin, A. Kosaka, T. Fukushima, H. Ichihara, T. Shimomura, K. Ito, T. Hashizume, N. Ishii and T. Aida, *Science* **2004**, *304*, 1481-1483.

[15] C. D. Simpson, J. D. Brand, A. J. Berresheim, L. Przybilla, H. J. Räder and K. Müllen, *Chem.—Eur. J.* **2002**, *8*, 1424-1429.

[16] a) D. Wasserfallen, M. Kastler, W. Pisula, W. A. Hofer, Y. Fogel, Z. Wang and K. Müllen, *J. Am. Chem. Soc.* **2006**, *128*, 1334-1339; b) M. Kastler, W. Pisula, D. Wasserfallen, T. Pakula and K. Müllen, *J. Am. Chem. Soc.* **2005**, *127*, 4286-4296.

[17] J. Wu, W. Pisula and K. Müllen, *Chem. Rev.* **2007**, *107*, 718-747.

[18] W. Pisula, Ž. Tomović, C. Simpson, M. Kastler, T. Pakula and K. Müllen, *Chem. Mater.* **2005**, *17*, 4296-4303.

[19] L. Dössel, L. Gherghel, X. Feng and K. Müllen, *Angew. Chem. Int. Ed.* **2011**, *50*, 2540-2543.

[20] a) A. D. Schlüter, *J. Polym. Sci. Part A: Polym. Chem.* **2001**, *39*, 1533-1556; b) W. H. Carothers, *Trans. Faraday Soc.* **1936**, *32*, 39-49.

[21] K. Martin, J. Spickermann, H. J. Räder and K. Müllen, *Rapid Commun. Mass Spectrom.* **1996**, *10*, 1471-1474.

Entry for the Table of Contents (Please choose one layout)

COMMUNICATION

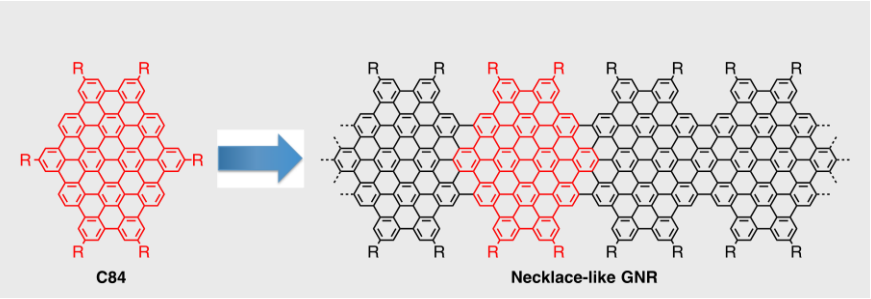

Graphene nanoribbons (GNRs) with an unprecedented “necklace-like” structure was synthesized through a bottom-up solution synthesis approach, together with a polycyclic aromatic hydrocarbon **C84** as a model compound. The necklace-like GNRs revealed a bandgap of ~1.4 eV, which has not been attained with other GNR structures.

Matthias Georg Schwab, Akimitsu Narita, Silvio Osella, Yunbin Hu, Ali Maghsoumi, Alexey Mavrinsky, Wojciech Pisula, Chiara Castiglioni, Matteo Tommasini, David Beljonne, Xinliang Feng, and Klaus Müllen**

Page No. – Page No.

Bottom-Up Synthesis of Necklace-Like Graphene Nanoribbons

Meeting the challenging magnetic and electronic structure of thiophene-based heterophenoquinones

Francesco Tampieri[A], Letizia Colella[B,C], Ali Maghsoumi[B], Javier Martí-Rujas[D], Emilio Parisini[D], Matteo Tommasini[B], Chiara Bertarelli*[B,D], Antonio Barbon*[A]

[A] Dipartimento di Scienze Chimiche - Università degli Studi di Padova,Via Marzolo 1, 35131 Padova, Italy

[B] Dipartimento di Chimica, Materiali e Ing. Chimica "G. Natta", Politecnico di Milano, Piazza L. Da Vinci 32, 20133 Milano, Italy

[C] INAF, Osservatorio Astronomico di Brera, via Bianchi 46, 23807 Merate, Italy

[D] Center for Nano Science and Technology@Polimi, Istituto Italiano di Tecnologia, Via Pascoli 70/3, 20133 Milano, Italy

KEYWORDS biradical, thiophene-based heterophenoquinones, open-shell molecule, EPR

ABSTRACT: Two thiophene-based heterophenoquinones, representing a family of molecules that exhibit biradicaloid character, have been studied by a combination of Electron Paramagnetic Resonance (EPR), Nuclear Magnetic Resonance (NMR), Raman, Infrared (IR) and X-ray diffraction measurements. This combined approach resolved and provided a detailed picture of the so far bleared electronic structure of the molecules in terms of two nearby states: a closed-shell diamagnetic state and a nearby biradical state, which is thermally populated.

INTRODUCTION

Conjugated quinoidal molecules are used in molecular electronics and optoelectronic devices for a wide range of applications because of their intriguing, non-trivial electronic properties.[1] For instance they have been used as a hole donor in an organic photodetector for polymer optical fibers.[2] Interestingly, thiophene-based heteroquinones have shown also to enhance photovoltaic activity. It has been reported that the addition of a small quantity (0.6 wt%) of 5,5'-bis(3,5-di-*tert*-butyl-4-oxo-2,5-cyclohexadiene-1-ylidene)-5,5'-dihydro-2,2'-bithiophene (QBT) to classical bulk heterojunction P3HT:PCBM (poly-3-hexylthiophene:fullerene) cells results in 47% increase in power conversion efficiency.[3] An interesting improvement of the photovoltaic performance was also observed in a standard poly(3-hexylthiophene)/1-(3-(methoxycarbonyl)propyl)-1-1-phenyl)-(6,6)C_{61} solar cell upon the addition of the 3 wt% of galvinoxyl radicals as a third active component. In this case the efficiency increased by 18% and the enhancement was attributed to a conversion of the polaron pair spin state from singlet to triplet mediated by the paramagnetic molecule.[4] In both cases[3,5] the third active component is characterized by the presence of unpaired electrons, since an unexpected radicaloid character was reported for QBT and its derivatives.[5] Henceforth, the increase in photovoltaic efficiency could be related to the paramagnetic character of these compounds. For this reason, in this work we address in details the unprecedented characterization of selected thiophene-based heterophenoquinones by electron paramagnetic spectroscopy. This investigation is corroborated by NMR, quantum chemical calculations, vibrational spectroscopy and X-ray diffraction.

Molecules in an open shell state with an even number of electrons normally exhibit high energy and therefore they are highly reactive;[6] although open shell states with two unpaired spins can be created by the promotion of an electron from one electronic state to another, this is an energy-demanding process that requires photoexcitation with visible or UV light. There are only few cases of isolated open-shell molecules in the ground-state, among them are non-Kekulé molecules, carbenes, nitrenes and few others.[7] Owing to their proximity, the interaction between the two electrons is rather strong (normally much higher than 1 cm^{-1}). These systems are properly called diradicals.[6]

When two unpaired spins with $S = 1/2$ localized on the same molecule are coupled by electron-electron interaction, two types of states are generated: a singlet and a triplet state (this latter being triply degenerate in the absence of dipolar interactions), whose energy difference is given by twice the spin exchange interaction J.[8] This energy difference is associated to an equivalent spin Hamiltonian,[9] normally described as $H = -2JS_1S_2$, but it is worth noting that the interaction is electrostatic in nature.

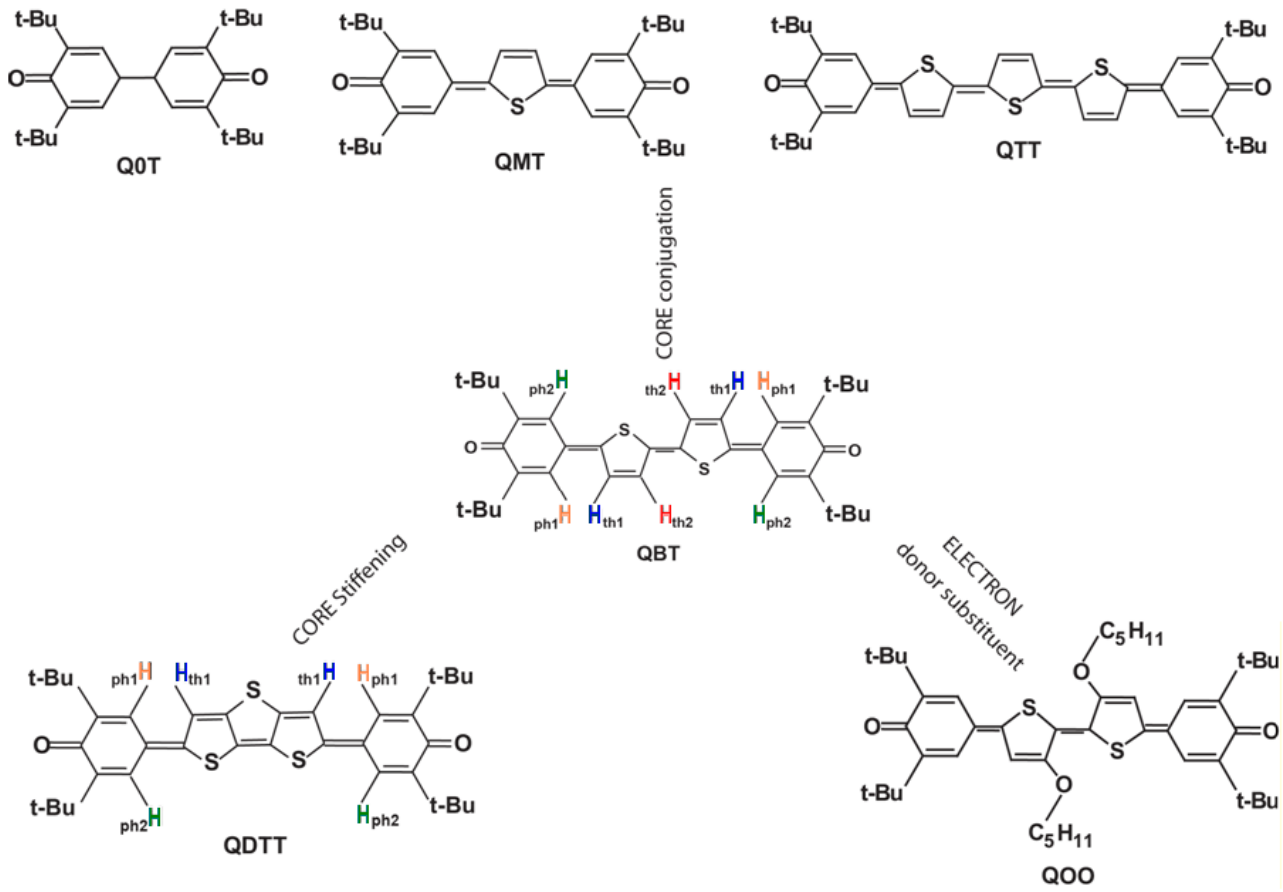

Figure 1. An overview on the studied quinoidal molecules. The colored atoms refer th1 (blue), th2 (red), ph1 (orange) and ph2 (green) protons.

The theory of spin exchange has been well described (for the case of the hydrogen molecule see ref 5); an extension of the model to polyatomic systems leads the exchange interaction to be written in a similar manner as: $J = 2\beta S + K$, where β is a resonance integral, S is an overlap integral and K is the classical electronic exchange integral.[10] The sign of J depends on the relative weight of the two terms: $2\beta S$ and K. The first term gives an antiferromagnetic contribution as $2\beta S < 0$, whereas the second one gives a ferromagnetic contribution, as $K > 0$, thus the ground state is the singlet if $J < 0$. In this case, the fraction of molecules in the excited triplet state (p_T) can be obtained from the statistical thermodynamics as $p_T = 3e^{2J/kT}/\left(1 + 3e^{2J/kT}\right)$.[8]

A pursued method to overcome the problem of the stability of open shell molecules, while at the same time limiting the exchange interaction, is to construct a molecule by connecting two radicals through a spacer that keeps them far apart; such molecules are termed biradicals. The major difference with the diradicals is that, normally, in biradicals a close shell ground state is not formed as the pairing of the two electrons in one of the two singly-occupied molecular orbitals (SOMO) is thermodynamically unfavorable due to the strong electron-electron interaction that would rise the energy of the system.

When the interaction between the two electrons is almost negligible, the triplet and the singlet states can be considered degenerate, and the behavior of the molecule is equivalent to that of two independent radicals (in this case the degeneracy of the state is four). Molecules with diradicaloid character have been observed in a number of systems: polyaromatic hydrocarbons and graphene,[11] hydrocarbons with non-Kekulé structutes. For some of these systems EPR spectra have been recorded, but either with featureless lineshape[12,13] or with a lineshape typical of triplet or higher states (diradical)[6,14,15].

To our knowledge, the only observed systems that exhibit real biradicaloid character are oligothiphenes[13], even if in the EPR spectrum well resolved hyperfine interactions are not observed.

So far, the description of biradical states is mostly done by considering the real state as a combination of biradicaloid and non biradicaloid states, estimated on the basis of the natural orbital occupation number (NOON). In a multiconfigurational approach, the state is a linear combination of the ground state and the excited state configurations. The occupation number of the LUMO orbital is a direct computational measure of the amount of biradical character[16,17]. In this framework, the systems that we have studied, namely thiophene-based heterophenoquinones, have unusual nontrivial behavior. Infact, they are closed-shell molecules in the ground state, but they possess biradicaloid character in the excited state; this is a quite an uncommon property because this open-shell state is at relatively low energy, and because the state is not a diradical state (no exchange interaction), as described later.

These systems were firstly synthesized by Takahashi and coworkers,[18] and they consist of dihydrothiophenediylidene moieties capped with two phenoquinones, namely (4-oxo-cyclohexa-2,5-dien-1-ylidene). For these molecules it is formally possible to write two resonance forms, a close-shell with quinoidal character, and an open-shell with aromatic phenyls. In our case phenoquinones are

substituted with tert-butyl groups in meta- positions, thus enhancing the solubility and the stability of the molecules. Despite of their short length, these materials are characterized by a very low band gap. The effective conjugation increases as the number of dihydrothiophenediylidenes increases, four being the maximum number of thienylene rings obtained so far.[18] Although this family of materials have been widely characterized in the past, highlighting intense absorption bands and peculiar amphoteric behavior,[19] a definite description of their electronic nature has never been reported.

Recently, the role of the π-conjugation length on the occurrence of a biradical ground state has been demonstrated within a homologous series of thiophene-based heterophenoquinones (2,6-di-tert-butylcyclohexa-2,5-dienone). Specifically, a combined experimental and theoretical study showed that by increasing the number of thiophenes, from one (**QMT**) to two rings (**QBT**), a biradicaloid character was stabilized (Figure 1).[20] By following the same approach, it has later been shown that this electronic character could be tuned not only by increasing the conjugation length, but also by the presence, nature, and position of electroactive groups linked to the molecular skeleton.[21] Therefore, the introduction of substituents is a convenient molecular tool that enables a separate control over the optical band gap and the electronic character of the ground state.

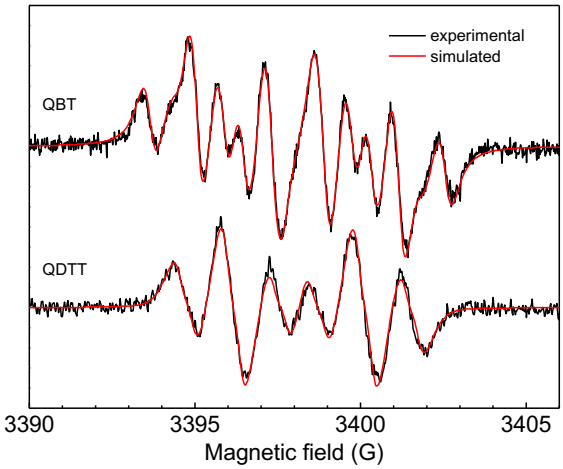

Figure 2. cw-EPR spectra of samples **QBT** (top) and **QDTT** (bottom) in toluene recorded at room temperature (black lines) together with their simulations (red lines).

This work is aimed at studying the paramagnetic character of two members of the family of bithiophenes substituted with cyclohexadienones, as it was deduced indirectly in previous studies[5] and to mark the differences with respect to the diamagnetic ground state. Here we report a detailed EPR investigation that, by combining the measurement of the spin distributions and hyperfine coupling constants (hfccs) with calculated DFT values, demonstrates the actual occurrence of a biradical state in **QBT**.

Indeed we show that the unpaired electrons act as two isolated 1/2 spins, each localized on one half of the molecule. Hence, the diradicaloid character for the paramagnetic state is ruled out. Moreover, it is here demonstrated that the biradicaloid state is a low-lying excited electron state, and not the electronic ground state, as previously thought, which is destabilized by introducing electron-donating OR substituents, like for **QOO** (see Figure 1). IR, Raman and NMR measurements clearly support our findings.

Finally, by considering also the influence of the **QBT** cis-trans isomerization versus the stiffening of the central conjugated thienilenic core, the bithienylene central unit was replaced by fused rings. Dithieno[3,2-b:2′,3′-d] thiophene was chosen because it is characterized by the same number of π-electrons as bithiophene, demonstrating that the electronic distribution is not influenced by the isomers forms, but it is ruled by the conjugation of the backbone.

RESULTS AND DISCUSSION

4,4'-(dithieno[3,2-b:2',3'-d]thiophene-2,6-di-yl)bis(2,6-di-tert-butylcyclohexa-2,5-dienone), namely **QDTT** (see Figure 1), has been synthesized following mainly the same route reported for **QBT**.[5] The quinoidal molecule is the result of the oxidation, using $K_3Fe(CN)_6$, of the corresponding aromatic compound, which is obtained through a Suzuki coupling between tris[3,5-di(*tert*-butyl)-4-(trimethylsilyloxy)phenyl]bo-roxine and 2,6-dibromo-dithieno[3,2-b:2`,3`-d]thiophene (see Supporting Information).

The continuous wave (cw)-EPR spectra of samples **QBT** and **QDTT** in toluene were recorded at room temperature and are shown in Figure 2 together with their simulations. We also tried to record the EPR spectrum for a **QOO** (see Figure 1) solution, but no signal was detected. This observation confirms what already been described in the literature[5], namely that the presence of electron-donor groups (in this case alkoxy groups) linked to the thiophene core, stabilizes the quinoidal character of the molecule completely suppressing the biradicaloid one. The spectra of samples **QBT** and **QDTT** are relative to radical species interacting with a few sets of protons: there is no possibility of simulating the spectra using models of diradical species (two interacting electrons with coupled protons), rather, we obtained an excellent simulation of the experimental spectra by considering a simple radical model. The hyperfine interactions and the number of equivalent protons obtained from the fitting of the cw-EPR spectra, are collected in Table 1. Both the number of the sets of coupled protons, and the number of equivalent protons in each set, give two major information: first, the function describing each of the unpaired electrons is extended only to one half of the molecule, where the monomer is the cyclohexandienone-thiophene unit, with one or two links between them, and second there is no interaction with the partner electron localized on the other side of the molecule.

From the hfccs a values we can make an estimate of the spin distribution at selected sites, in fact, by using the McConnel equation $a_i = Q\rho_i$,[22] in aromatic radicals the hyperfine coupling constant of a proton bound to the *i*-th carbon is proportional ($Q = 22$ G ca) to the spin density $\rho_i$resinding on the *i*-th carbon of the π-system. It results that around ¼ of the spin density is located on the carbons bound to protons ph1, ph2 and th1 (see Figure 1 for the labels).

We note that the spectra of both samples are due to two components with ratio of about 85:15 with the same structure, but with slightly different hfccs values. Whereas for **QBT** the second components might be explained by considering the *cis/trans* isomerization effect, for the rigid **QDTT** this is not possible. Instead, we opt for invoking the tendency of these molecules to form stacks, a feature that has also been observed by NMR spectroscopy (see further). Unfortunately, we could not detect the expected subtle changes of the EPR spectra with the changing of the experimental conditions (sample dilution or temperature variation) due to the low experimental signal-to-noise ratio.

In order to provide further evidence that the system is in an excited biradical state rather than in a pure radical state, we recorded the EPR spectra while changing the temperature. The variation of the EPR intensity for **QBT** in the 215 K - 320 K temperature range is reported in Figure 3; sample **QDTT** shows a similar behavior (not shown). For both samples, the EPR intensity decreases with the temperature.

The observation that, in our systems, the exchange interaction is negligible is a quite surprising result. However, it can be explained in terms of the contributions to this interaction: $2\beta S$ and K (calculated over the molecular orbital containing the two unpaired electrons), which have opposite sign. We have to deduce that in this particular case the two terms are comparable in module.

Overall, the combination of the EPR experimental data confirm the existence of an excited non-zero spin state with unusual behavior. The interpretation of the data is not trivial, as from this type of measurements routinely gives information on the exchange interaction J.[5] In the present case a correct interpretation of the data can be done by assuming that, in the studied molecules, there are two thermally accessible states: a closed shell ground state, and a biradical paramagnetic (P, two independent radicals) excited state. The energy difference between them has been estimated for **QBT** by the fitting of the EPR intensity, which is proportional to the sample magnetization[22], as function of the temperature (Figure 3). In our model, the paramagnetic state is an excited n-times degenerate state, whereas the ground state is not degenerate. The generalization of the statistical model in the Introduction leads to the fraction of molecules in the paramagnetic state calculated as

$$p_P = \frac{N_P}{N_{TOT}} = \frac{g_P}{Z} = \frac{n \cdot e^{-E_P/k_BT}}{1 + n \cdot e^{-E_P/k_BT}} \approx n \cdot e^{-E_P/k_BT} \qquad (1)$$

where N_P and N_{TOT} are the number of molecules in the excited and in the ground state, Z is the partition function, E_P is the excitation energy and k_B the Boltzmann constant; for room temperature $E_P \gg k_BT$, and the second term of the denominator is negligible. In a magnetic field, the magnetization is proportional to the small difference distribution of the population within the spin manifold, so that the magnetic susceptibility is

$$\chi \propto \frac{p_P}{T} \approx \frac{n \cdot e^{-E_P/k_BT}}{T} \qquad (2)$$

Table 1. Parameters obtained from the simulation of the cw-EPR spectra of **QBT** and **QDTT** samples in toluene recorded at room temperature: g-factor, the linewidth, the number of equivalent protons and their hfccs (a) and attribution.

Molecule		g-factor	Linewidth (G)	Number of equiv. H	a (G)	Attribution
QBT	Specie 1 (50%)	2.0035	0.47	1	3.86	H_{th1}
				2	1.38	H_{ph}
				1	0.72	H_{th2}
	Specie 2 (50.%)	2.0035	0.40	1	3.87	H_{th1}
				2	1.42	H_{ph}
				1	2.22	H_{th2}
QDTT		2.0048	0.37	1	3.98	H_{th1}
				2	1.40	H_{ph}

The fitting of the data with the function in equation (2) allowed the determination of the excitation energies E_P of 2130 ± 30 K (17.7 ± 0.2 kJ/mol). Note that this value is independent from the degeneracy of the state. The E_P value is fully consistent with quantitative EPR measurements: a determination of the number of spins was done for a $1 \cdot 10^{-3}$ M solution of **QBT** in chloroform at 300 K prepared by weighting. As reference a $1 \cdot 10^{-4}$ M solution of TEMPO ((2,2,6,6-tetramethylpiperidin-1-yl)oxyl, g = 2.0058) in toluene was used. By comparing the double integral of the EPR spectrum[22] we determined that the fraction of molecules in the biradical state is $(2.0 \pm 0.7) \cdot 10^{-3}$. This number is in a good match (within the error) with the fraction of molecules in paramagnetic state that can be obtained from the E_P value, in fact, by using equation (1), the result is $p_p = (3.3 \pm 0.3) \cdot 10^{-3}$ at 300 K. For the calculation the value of $n = 4$ was used, as the paramagnetic excited state is a biradical state.

The EPR measurement suggests that the two states differ not just for the spin function, but also in the electronic part. The hypothesis could not be verified by a full calculation, as the biradical molecules are far too large to enable the use of appropriate computational methods (i.e. CASSCF[5], that is particularly indicated in the presence of low-lying excited states).

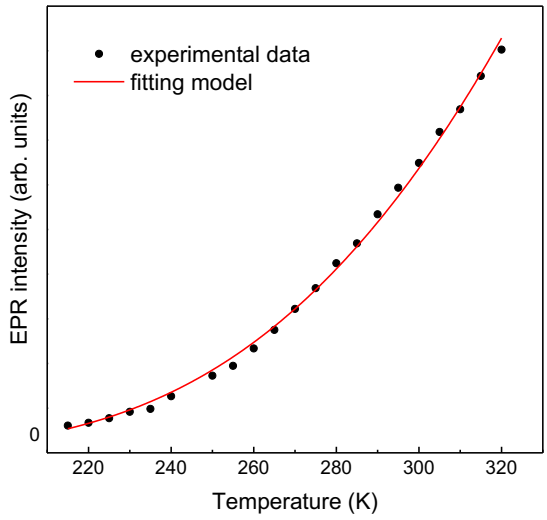

Figure 3. Plot of the EPR intensity of sample **QBT** as function of the temperature and the fitting of the data (red line) by using equation 2.

Table 2. Calculated hfccs for the cis/trans isomers of **QBT** molecule in a doublet state and for the half molecule (monomer end-capped with a proton (-H) or with a methyl group (-Me).

Proton	a (-H, G)	a (-Me, G)
H_{ph1}	1.98	1.81
H_{ph2}	2.02	1.87
H_{th1}	-4.07	-3.94
H_{th2}	0.94	0.83

Nevertheless, for **QBT**, based on EPR results, we tested the assertion that the two electrons act independently, and that they are localized on different halves of the molecule, interpreting the molecule as a combination of two monomers linked by the thiophene-thiophene bond. We have then obtained an estimation of the proton hfccs by DFT methods, which are instead extensively used in the case of monoradicals,[23] for the single radical monomer end-capped with a methyl group or a hydrogen atom. Indeed, calculations were in a very good agreement with the experimental values (compare Tables 1 and 2), thus suggesting that the electronic distribution obtained from this calculation is appropriate. Because of the good matching between the experimental and the calculated hfccs, we decided to study by EPR also the torsional flexibility of the phenyl groups about the thiophene-phenyl moiety. Incidentally, we observed a NMR line broadening effect that can likely be explained by this motion, as described later. This was done by calculating the hfccs for various phenyl rotation angles. The calculations (see Supporting Information) showed that the hfccs of the phenyl protons vary with the out-of-plane torsion from 1.81 to 2.43 G, for th1 protons from -3.90 to -0.90 G and for th2 protons from 0.83 to 0.95 G. The good agreement with the experimental values is lost upon with a 10-15 degrees from planarity. This tolerance is within the tilt angle found from X-ray data (see further).

The same calculation was also done for **QDTT**, although in this case, the presence of a bridging sulfur atom in the molecule was expected to introduce some difference with respect to **QTT**. We did the calculation by considering two fused thiophene rings, and we tested the results obtained when the terminal thiophene was substituted by methyl groups or hydrogen atoms. Indeed most of the π density is located on the phenyl-thiophene system, and the results of the hfccs are very similar to those of **QBT**.

Because of the relatively low energy difference between the ground state and the excited state, a multi-configurational approach for the molecules can be adopted[16,17]. We used NMR, Raman and FT-IR to observe anomalous behavior that might be indication of a biradicaloid contribution to the ground state.

With Raman and FT-IR we used the approach to show peculiar experimental features which stand out compared to the results from DFT models. In fact this quantum mechanical method is robust for closed shell molecules, but in the presence of contributions from biradical states it cannot properly treat the electronic structure of the molecule and consequently account for the peculiar molecular structure[5]. However, as a practical way to partially overcome these limitations of the DFT method, it has been shown that by carefully relaxing the molecular geometry along the Effective Conjugation Coordinate (ECC, also named Я coordinate)[5] it is possible to amend the most dramatic deviations of the simulated Raman spectra from experimental observation, at a computational cost that is more convenient than that associated with more appropriate but computationally much more demanding multi-configuration approaches.

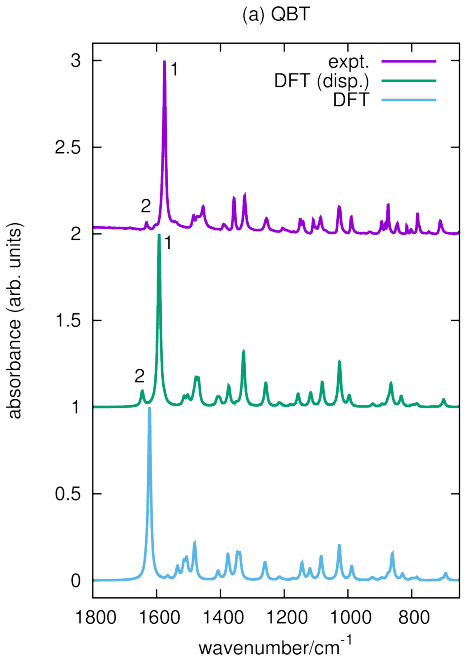

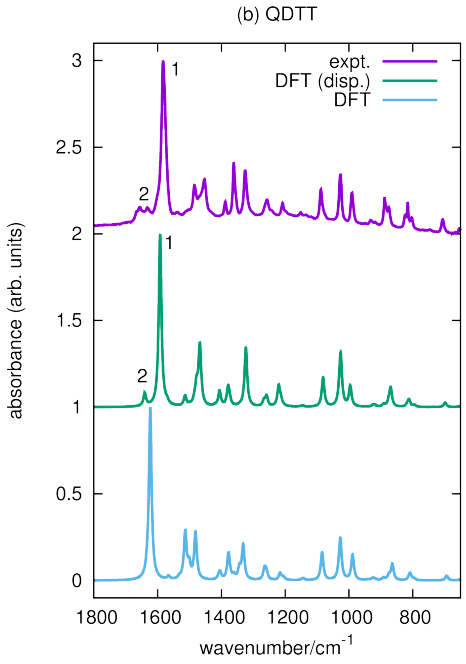

Figure 4. IR spectra of (a) **QBT** and (b) **QDTT** recorded with micro-IR setup (violet line). The IR spectra simulated with DFT methods (B3LYP/6-31G(d,p), frequency scaled by 0.98) are displayed with light blue and green lines. See text for details.

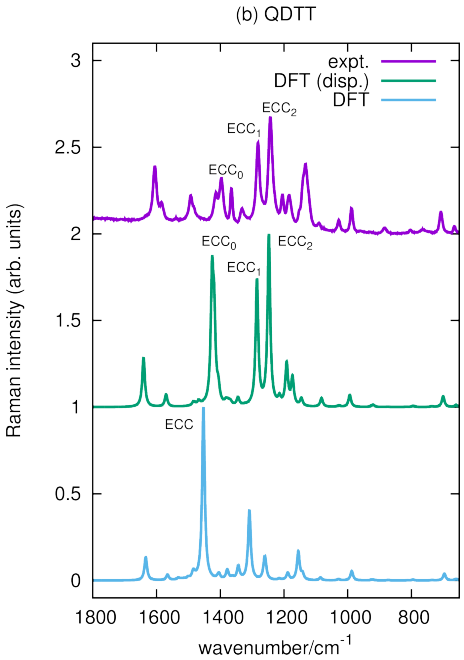

Figure 5. Raman spectra of (a) **QBT** and (b) **QDTT** recorded with 632.8 nm excitation (violet line). The Raman spectra simulated with DFT methods (B3LYP/6-31G(d,p), frequency scaled by 0.98) are displayed with light blue and green lines. See text for details.

Hence, we have followed the procedure introduced by Canesi *et al.*[5], and we displaced by $\Delta Q = 0.15$ Å amu1/2 the geometry of both **QBT** and **QDTT** starting from the geometry optimized at B3LYP/6-31G(d,p) level. The mode chosen for displacing the geometry was selected as the one displaying the largest Raman intensity at the optimized geometry. This ensures that the mode with largest electron-phonon coupling is considered: in fact, the strong electron-phonon coupling is a characteristic feature of the ECC (see for instance the work of Tommasini *et al.*[24] and references therein).

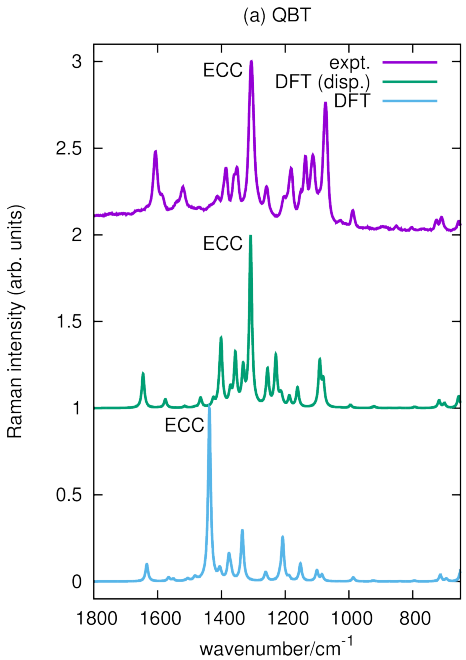

As shown in Figure 4, this kind of geometry displacement is able to significantly improve the simulation of the IR spectra of **QBT** and **QDTT**. While at the B3LYP/6-31G(d,p) equilibrium structure the simulated IR spectra do not capture correctly the features (1, 2) in the vicinity of 1600 cm^{-1} correctly, at the displaced geometry (for both **QBT** and **QDTT**) these two features emerge nicely in the simulated IR spectra. These can be assigned to the anti-symmetric C=O stretching (1) and to the anti-symmetric ring stretching (2) of the quinoid end groups of each molecule. Based on DFT calculation, IR intensity of the anti-symmetric C=O stretching (1625 cm^{-1}, unscaled DFT) is really strong (2448 km/mol in **QBT** and 2322 km/mol in **QDTT**) and it dominates over the whole mid-IR range (see Figure 4), in agreement with experimental spectra (see Figure S3 in Supporting Information for the graphical representation of the associated normal modes).

As for the Raman spectra of the two compounds (see Figure 5) their intense Raman features, associated to collective CC stretching vibrations involving the ECC (see Figure S4 in Supporting Information), are not correctly simulated by adopting the optimized B3LYP/6-31G(d,p) structure.

However, for the simulated spectra at displaced geometries, the intense ECC Raman features fall in the correct spectral range observed (see Supplementary Information for a graphical representation of the ECC modes selected for geometry displacement and of the ECC modes computed for the displaced geometries). We conclude that the "displaced geometry" approach provides an easy way to account for both IR and Raman observations.

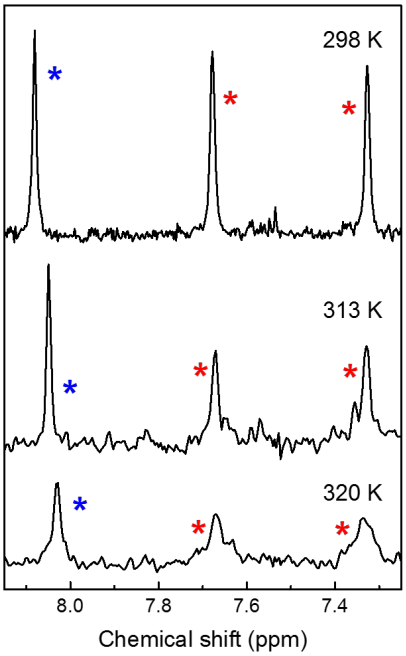

Figure 6. ^{1}H-NMR (600 MHz) spectra of sample **QDTT** (1 mM) in deuterated acetone at different temperatures in the aromatic region. The blue asterisks refer to proton th1 and the red asterisks to protons ph1 and ph2.

From NMR spectroscopy, possible indication of the biradicaloid presence could be line broadening and line shift.[25]

Since **QBT** suffers from a line broadening effect that is associated with conformational changes, we first present the NMR spectra of the more rigid **QDTT** molecule. The spectra were obtained in deuterated acetone, a low viscosity solvent which does not interfere with intramolecular motion, and shows no solvent signals (like in the case of $CDCl_3$) in the region of the thiophene and phenyl protons. We also used a rather low sample concentration in order to exclude band broadening due to stacking effects (observed for concentrations higher than 1 mM).

The ^{1}H-NMR spectra in the aromatic region of sample **QDTT** in deuterated acetone at different temperatures are collected in Figure 6, and indeed at 298 K these lines are narrow. The spectra show three distinct peaks, which are attributed to the thiophene protons th1 (blue asterisks in Figure 6) and to the phenyl protons ph1 and ph2 (red asterisks) by comparison with those of parent molecules.[18,19] With the rising of the temperature above room temperature, the increasing contribution of the paramagnetic state might lead to line broadening and shift and this might explain the experimental observation.

Unfortunately this mechanism cannot unambiguously be determined as responsible of the broadening, as another possible mechanism might be the presence of a thermally activated vibrational motion. The observations in favour of this mechanism is the separation between the phenyl protons (red starred lines) which decreases from 0.35 ppm at 298 K to 0.33 ppm at 320 K moreover the linewidth broadening of the relative lines is more pronounced,

For **QBT** analogous results have been obtained; we focus on the behavior of the NMR spectra above room temperature as the NMR of this species has been already properly studied[19] at room temperature and below. The spectrum in acetone is characterized at room temperature by four narrow lines in the aromatic region as due to a fast interconversion between *cis* and *trans* isomers. On rising of the temperature, the broadening of the lines of the phenyl protons is observed (see Supporting Information).

NMR results confirm that the bonds between the phenyls and the central thiophene core are not single bonds as there is not free rotation about them. However, some degree of limited flexibility has been observed. The partial double bond character is a further indication that the quinoidal structure is not fully appropriate to describe the electronic distribution.

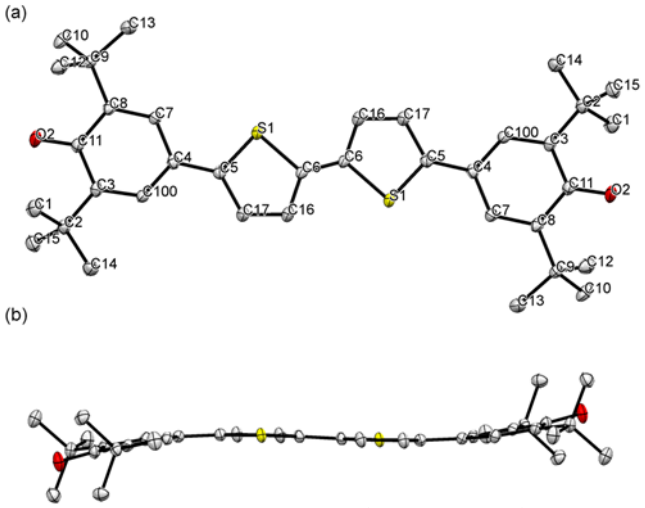

Figure 7. Molecular structure of QBT, a) Top view and b) side view.

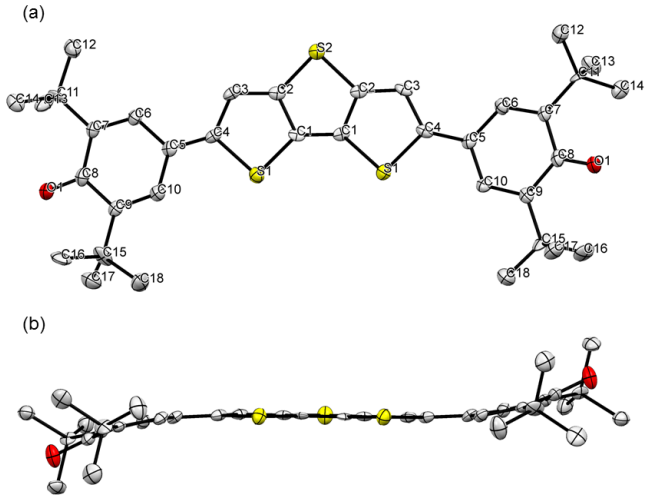

Figure 8. Molecular structure of **QDTT,** a) Top view and b) side view.

While for **QDTT** (Figure 8), the structure is almost completely planar, as the phenyl rings show a 179.7(9)° and -172.4(7)° torsion angles with the central core of the molecule (see Tables S6, S7 and S9 in Supporting Information).

The length of the bond between C4 and C5 is 1.40(3) and 1.39(1) Å for **QBT** and **QDTT** respectively. These lengths are consistent with a partial double bond character, supporting the NMR data.

CONCLUSION

We have characterized the paramagnetic state of two thiophene-based heterophenoquinones, **QBT** and **QDTT**, by EPR spectroscopy. From the simulation of the EPR spectra, we determined that their paramagnetic state is not diradical (triplet state), as previously believed. Instead, we showed that both molecules are biradicals. The two unpaired electrons are localized in different parts of the molecules and are not coupled with each other. This was also confirmed by DFT calculations of the hyperfine coupling constants of the unpaired electrons with the protons in the molecules.

Another major finding of this paper is that the paramagnetic biradical state is not the ground electronic state. The temperature-dependent EPR measurement led to the conclusion that the ground state is diamagnetic; the biradical state is an excited electron state, thermally accessible at room temperature.

These results have also enabled to highlight that the biradical state, and therefore the possibility to image the molecule as two unconnected portions, is not favored by the possible rotation around thiophene-thiophene bond of **QBT** and therefore by the presence of the isomers. Indeed the analysis of **QDTT** reveals that stiffening the central moiety, therefore excluding the possible splitting of the molecule in two parts, the molecule is characterized by the same electronic biradicaloid distribution. We demonstrated that the conjugation rules the electronic character of these structures, neglecting any geometrical interaction.

On the basis of the measurement on **QOO**, lacking an EPR signal, we confirm that electron-donor groups (in this case alkoxy groups) linked to the thiophene core destabilizes the paramagnetic biradical state.

EXPERIMENTALS

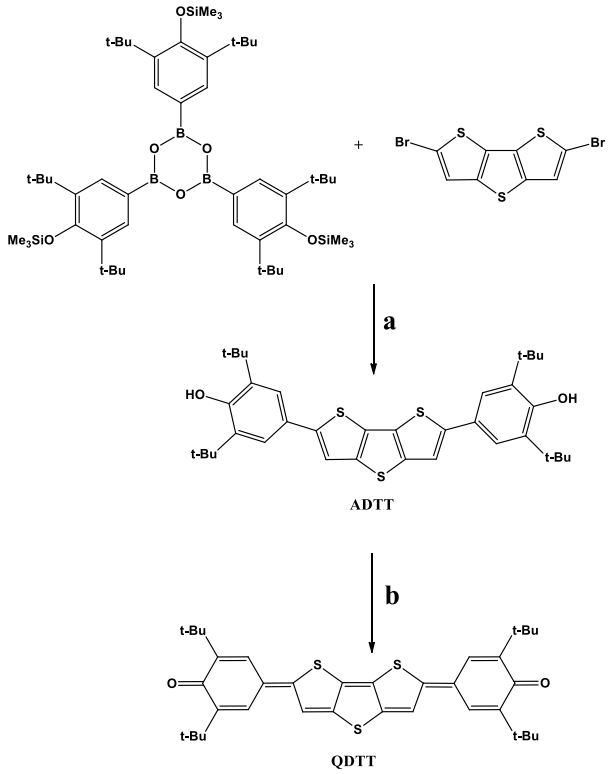

Scheme 1. Synthesis of **QDTT** : a) $Pd(PPh_3)_4$, DME, Na_2CO_3, H_2O ; b) $K_3Fe(CN)_6$, DCM, KOH, H_2O.

EPR measurements were obtained with a Bruker ECS106 spectrometer working at X-band and equipped with a 4108 TMH high sensitivity resonator; the temperature of the sample was controlled by a VT100 system. Solution for EPR measurements were prepared by dissolving weighted amount of the powders in toluene. Once transferred in quartz tubes, the samples underwent few freeze-pump-thaw cycles to remove dissolved gasses, and were sealed under vacuum.

^{1}H-NMR spectra were obtained on 1 mM solution in deuterated acetone, in tubes of 3 mm i.d. after the same freeze-pump-thaw cycles to remove dissolved gasses, and were sealed under vacuum. The NMR spectrometer was a 600-MHz Bruker Avance, where the temperature at the sample was controlled by means of a thermostated nitrogen flow. Typically, a total of 64 acquisitions were obtained for each NMR spectrum. The FID (free induction decay) signal was zero filled to 65 K and exponentially multiplied with a line broadening of 0.5 Hz before Fourier transformation. Phase and baseline were corrected manually.

The Raman spectra have been recorded with a Jobin-Yvon Labram HR800UV spectrometer equipped with the 632.8 nm excitation of a He-Ne laser. The laser power at the sample was always of the order of a few mW to prevent (or reduce as possible) laser-induced effects on the samples; care has been adopted to verify the reproducibility of the spectra. Samples were analyzed in a back-scattering geometry on glass slides by using the microscope with the 50× objective. The intensity of the reported Raman spectrum has been corrected with white light calibration.

Micro FT-IR measurements were carried out with Nicolet Nexus equipment coupled with a Thermo-Nicolet Continuμm infrared microscope and a cooled MCT detector (77 K). The spectra of the **QBT** and **QDTT** samples (as powders) were acquired by using the diamond anvil cell technique with a 15× infrared objective (256 scans, 2 cm^{-1} resolution, 650 – 4000 cm^{-1} spectral range).

Quantum chemical calculations have been carried out within Density Functional Theory. The selected method, B3LYP/6-31G(d,p), proved to be a good compromise between accuracy and computational costs in simulating the vibrational properties of compounds[5] similar to those investigated in this work. Gaussian09 rev. D.01[26] was employed to carry out all calculations here reported.

X-ray data collection. Single crystal data collection of **QBT** was done at 100 K using synchrotron radiation ($\lambda = 0.77489$ Å) at the BL-13-Xaloc Beamline[27] at Alba-CELLS Synchrotron, Barcelona under the Proposal Number 2013100590. Single crystal data collection of **QDTT** was done at 100 K using a Bruker X8 Prospector APEX-II/CCD diffractometer equipped with a microfocusing mirror (Cu-*Ka* radiation, $\lambda = 1.54178$ Å). The structures were determined using direct methods and refined (based on F2 using all independent data) by full-matrix least-square methods (SHELXTL 97). All non-hydrogen atoms were located from different Fourier maps and refined with isotropic displacement parameters.

The structures have been deposited in the Cambridge Crystallographic Data Center (CCDC), accession numbers **QBT**: 1436973 and **QDTT**: 1436972.

REFERENCES

1. Ribierre, J.; Watanabe, S.; Matsumoto, M.; Muto, T.; Hashizume, D.; Aoyama, T. Thickness. *J. Phys. Chem. C* **2011**, *115*, 20703-20709.

2. Agostinelli, T.; Caironi, M.; Natali, D.; Sampietro, M.; Dassa, G.; Canesi, E.; Bertarelli, C.; Zerbi, G.; Cabanillas-Gonzalez, J.; De Silvestri, S. *J. Appl. Phys.* **2008**, *104*, 4508.
3. Kan, Z.; Colella, L.; Canesi, E. V.; Lerario, G.; Kumar, R. S. S.; Bonometti, V.; Mussini, P. R.; Cavallo, G.; Terraneo, G.; Pattanasattayavong, P. *Solar Energy Mater. Solar Cells* **2014**, *120*, 37-47.
4. Zhang, Y.; Basel, T. P.; Gautam, B. R.; Yang, X.; Mascaro, D. J.; Liu, F.; Vardeny, Z. V. *Nature commun.* **2012**, *3*, 1043.
5. Canesi, E. V.; Fazzi, D.; Colella, L.; Bertarelli, C.; Castiglioni, C. *J. Am. Chem. Soc.* **2012**, *134*, 19070-19083.
6. Abe, M. Diradicals. *Chem. Rev.* **2013**, *113*, 7011-7088.
7. Dougherty, D. A. Spin control in organic molecules. *Acc. Chem. Res.* **1991**, *24*, 88-94.
8. Ruitenbeek, M.; Barbon, A.; Van Faassen, E.; Geus, J. *Catal. Lett.* **1998**, *54*, 101-104.
9. Ashcroft, N. W.; Mermin, N. D. Introduction to Solid State Physics; *Saunders, Philadelphia,* 1976.
10. Kollmar, C.; Kahn, O. *Acc. Chem. Res.* **1993**, *26*, 259-265.
11. Sun, Z.; Zeng, Z.; Wu, J. *Acc. Chem. Res.* **2014**, *47*, 2582-2591.
12. Das, S.; Lee, S.; Son, M.; Zhu, X.; Zhang, W.; Zheng, B.; Hu, P.; Zeng, Z.; Sun, Z.; Zeng, W. *Chem. Eur. J.* **2014**, *20*, 11410-11420.
13. Takahashi, T.; Matsuoka, K.; Takimiya, K.; Otsubo, T.; Aso, Y. *J. Am. Chem. Soc.* **2005**, *127*, 8928-8929.
14. Kubo, T.; Sakamoto, M.; Nakasuji, K. *Polyhedron* **2005**, *24*, 2522-2527.
15. Shultz, D. A.; Bodnar, S. H.; Lee, H.; Kampf, J. W.; Incarvito, C. D.; Rheingold, A. L. *J. Am. Chem. Soc.* **2002**, *124*, 10054-10061.
16. Doehnert, D.; Koutecky, J. *J. Am. Chem. Soc.* **1980**, *102*, 1789-1796.
17. Shimizu, A.; Hirao, Y.; Matsumoto, K.; Kurata, H.; Kubo, T.; Uruichi, M.; Yakushi, K. *Chem. Commun.* **2012**, *48*, 5629-5631.
18. Takahashi, K.; Suzuki, T. *J. Am. Chem. Soc.* **1989**, *111*, 5483-5485.
19. Takahashi, K.; Gunji, A.; Yanagi, K.; Miki, M. *J. Org. Chem.* **1996**, *61*, 4784-4792.
20. Fazzi, D.; Canesi, E. V.; Negri, F.; Bertarelli, C.; Castiglioni, C. *ChemPhysChem* **2010**, *11*, 3685-3695.
21. Colella, L.; Brambilla, L.; Nardone, V.; Parisini, E.; Castiglioni, C.; Bertarelli, C. *Phys. Chem. Chem. Phys.* **2015**, *17*, 10426-10437.
22. Weil, J. A.; Bolton, J. R. *Electron paramagnetic resonance: elementary theory and practical applications;* John Wiley & Sons, 2007.
23. Barone, V. *Computational strategies for spectroscopy: from small molecules to nano systems;* John Wiley & Sons, 2011.
24. Tommasini, M.; Longhi, G.; Abbate, S.; Zerbi, G. *J. Raman Spectrosc.* **2014**, *45*, 89-96.
25. Machonkin, T. E.; Westler, W. M.; Markley, J. L. *Inorg. Chem.* **2005**, *44*, 779-797.
26. Gaussian 09, Revision **D.01**, Frisch, M. J.; Trucks, G. W.; Schlegel, H. B.; Scuseria, G. E.; Robb, M. A.; Cheeseman, J. R.; Scalmani, G.; Barone, V.; Mennucci, B.; Petersson, G. A.; Nakatsuji, H.; Caricato, M.; Li, X.; Hratchian, H. P.; Izmaylov, A. F.; Bloino, J.; Zheng, G.; Sonnenberg, J. L.; Hada, M.; Ehara, M.; Toyota, K.; Fukuda, R.; Hasegawa, J.; Ishida, M.; Nakajima, T.; Honda, Y.; Kitao, O.; Nakai, H.; Vreven, T.; Montgomery, J. A., Jr.; Peralta, J. E.; Ogliaro, F.; Bearpark, M.; Heyd, J. J.; Brothers, E.; Kudin, K. N.; Staroverov, V. N.; Kobayashi, R.; Normand, J.; Raghavachari, K.; Rendell, A.; Burant, J. C.; Iyengar, S. S.; Tomasi, J.; Cossi, M.; Rega, N.; Millam, J. M.; Klene, M.; Knox, J. E.; Cross, J. B.; Bakken, V.; Adamo, C.; Jaramillo, J.; Gomperts, R.; Stratmann, R. E.; Yazyev, O.; Austin, A. J.; Cammi, R.; Pomelli, C.; Ochterski, J. W.; Martin, R. L.; Morokuma, K.; Zakrzewski, V. G.; Voth, G. A.; Salvador, P.; Dannenberg, J. J.; Dapprich, S.; Daniels, A. D.; Farkas, Ö.; Foresman, J. B.; Ortiz, J. V.; Cioslowski, J.; Fox, D. J. Gaussian, Inc., Wallingford CT, 2009.
27. Juanhuix, J.; Gil-Ortiz, F.; Cuni, G.; Colldelram, C.; Nicolás, J.; Lidón, J.; Boter, E.; Ruget, C.; Ferrer, S.; Benach, J. *J. Synchrotron Radiat.* **2014**, *21*, 679-689.

Table of contents:

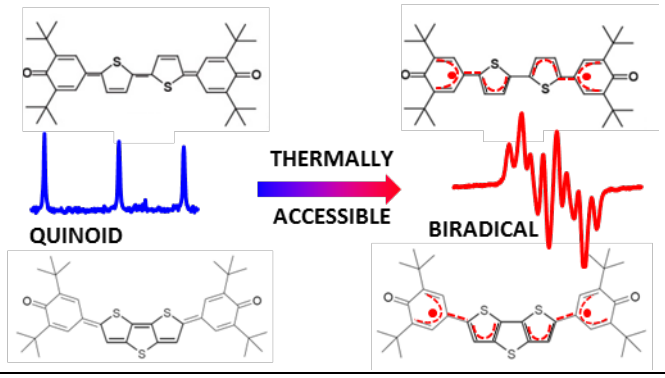

The unconventional electronic and vibrational properties of thiophene-based heterophenoquinones are due to the mixing of the closed-shell ground state and a thermally accessible biradical state.